A LATTICE MODELLING FRAMEWORK WITH APPLICATIONS ON REINFORCED CONCRETE AND AUTOCLAVED AERATED CONCRETE MASONRY INFILL WALLS

A THESIS SUBMITTED TO
THE GRADUATE SCHOOL OF NATURAL AND APPLIED SCIENCES
OF
MIDDLE EAST TECHNICAL UNIVERSITY

BY

BEYAZIT BESTAMİ AYDIN

IN PARTIAL FULFILLMENT OF THE REQUIREMENTS
FOR
THE DEGREE OF DOCTOR OF PHILOSOPHY
IN
CIVIL ENGINEERING

NOVEMBER 2022

Approval of the thesis:

A LATTICE MODELLING FRAMEWORK WITH APPLICATIONS ON REINFORCED CONCRETE AND AUTOCLAVED AERATED CONCRETE MASONRY INFILL WALLS

submitted by **BEYAZIT BESTAMİ AYDIN** in partial fulfillment of the requirements for the degree of **Doctor of Philosophy** i**n Civil Engineering, Middle East Technical University** by,

Prof. Dr. Halil Kalıpçılar
Dean, Graduate School of **Natural and Applied Sciences** _____

Prof. Dr. Erdem Canbay
Head of Department, **Civil Engineering** _____

Prof. Dr. Barış Binici
Supervisor, **Civil Engineering, METU** _____

Prof. Dr. Kağan Tuncay
Co-Supervisor, **Civil Engineering, METU** _____

Examining Committee Members:

Prof. Dr. Hakkı Polat Gülkan
Civil Engineering, Başkent Üniversitesi _____

Prof. Dr. Barış Binici
Civil Engineering, METU _____

Prof. Dr. Erdem Canbay
Civil Engineering, METU _____

Prof. Dr. Yalın Arıcı
Civil Engineering, METU _____

Assoc. Prof. Dr. Alper Aldemir
Civil Engineering, Hacettepe Universitesi _____

Date: 21.11.2022

I hereby declare that all information in this document has been obtained and presented in accordance with academic rules and ethical conduct. I also declare that, as required by these rules and conduct, I have fully cited and referenced all material and results that are not original to this work.

Name Last name : Beyazıt Bestami Aydın

Signature :

ABSTRACT

A LATTICE MODELLING FRAMEWORK WITH APPLICATIONS ON REINFORCED CONCRETE AND AUTOCLAVED AERATED CONCRETE MASONRY INFILL WALLS

Aydin, Beyazıt Bestami
Doctor of Philosophy, Civil Engineering
Supervisor : Prof. Dr. Barış Binici
Co-Supervisor: Prof. Dr. Kağan Tuncay

November 2022, 181 pages

The heterogeneous nature and the mixture rules of concrete result in complex behavior at different domain levels as micro, meso and macro scales. Cracks evolve randomly from the micro to the macro level and result in nonlinear response of structures. Predicting the nonlinear response of concrete is directly related to the performance assessment of reinforced concrete (RC) structures, which is becoming more important, given the observed of aging infrastructure and the need for sustainability. Strength and deformation capacity estimations along with crack width predictions appear to play a key role for structural engineers in the design and assessment of structures. Another quasi-static material mostly used in structures after the concrete is the masonry elements. Masonry walls consist of different materials and exhibit complex responses similar to concrete. A combination of walls and reinforced concrete (RC) frames create infill walls. Significant infill wall damage in RC frame buildings was observed in past earthquakes. Collapse of these walls may cause loss of life. Still, understanding RC frame-infilled wall interaction is

challenging, while the nonlinear behavior has been investigated in different scales by many researchers.

Despite significant developments, the computational modeling of concrete and masonry fracture initiation and propagation is still under development. Many different numerical approaches have been used in the past. Recent studies in the last decade in this field have focused on using particle-based simulation methods (such as the discrete element method, lattice-based methods, smoothed particle hydrodynamics, etc.) to capture the local character of the fracture phenomenon. The advantages of these tools are the relative ease of modeling and the simulation of crack propagation using a few key parameters with the ability to bridge various scales from micro to macro levels.

In this work, a practical two-dimensional lattice approach at the mesoscale level is proposed, where the continuum is discretized using truss elements extending over a predefined horizon, similar to the concept used in peridynamics with static and dynamic solution techniques for nonlinear problems. The compression response of concrete is critically reviewed and explained as an indirect tension failure by using the proposed lattice approach with a novel calibration technique that employs the magnitude of grid perturbation. Promising numerical results show that compression failure can be estimated with lattice models with tension-only failure envelopes. Simulation results of RC beams, columns, walls, and frame tests with different failure types focusing on the influence of the mesh size, horizon, and softening functions on the sensitivity of results are in good agreement with the experimental results based on estimating crack patterns, spacings, and overall monotonic load-deflection response. An explicit time integration technique with a novel proportional-integral-derivative control is used to efficiently simulate the response under monotonic loading in quasi-static manner. The proposed approach is then applied to simulate the response of unreinforced aerated autoclaved concrete (AAC) masonry-infilled RC frames. Two AAC-infilled walls were tested to have a benchmark for comparison purposes. The wall components used in these tests were

used for characterization tests of AAC masonries in order to determine the mechanical properties of such behavior. The results were used to calibrate the model. In addition to the tests conducted, two other tests from the literature were used for further validation. The proposed lattice model was capable of estimating crack propagation in the infill walls with reasonable accuracy. The frame-infill wall interaction was successfully simulated by providing a realistic representation of strut formation. Finally, a parametric study was conducted to examine contact length and strut width as a function of lateral deformation. The results show that the infill wall-frame contact length is significantly dependent on the lateral deformation demand levels and properties of the interaction region. It can be stated that all simulation results demonstrate the ability of accurately predicting the direction of crack propagation and the flowing force over the structure with the proposed modeling approach, with a rather simple and intuitive method.

Keywords: Concrete, Masonry, Infill Wall, Fracture, Modeling

ÖZ

BETONARME VE GAZ BETON DOLGULANMIŞ BETONARME ÇERÇEVELERİN ÜZERİNDE UYGULAMALAR İLE BİR KAFES MODELİ SİSTEMİ

Aydın, Beyazıt Bestami
Doktora, İnşaat Mühendisliği
Tez Yöneticisi: Prof. Dr. Barış Binici
Ortak Tez Yöneticisi: Prof. Dr. Kağan Tuncay

Kasım 2022, 181 sayfa

Betonun farklı bileşenlerden oluşan doğası ve karışım kuralları, mikro, mezo ve makro ölçekler gibi farklı etki alanı seviyelerinde karmaşık davranışlara neden olur. Çatlaklar, mikro seviyeden makro seviyeye rastgele gelişir ve yapıların doğrusal olmayan tepkisine neden olur. Betonun bu tepkisini tahmin etmek, yaşlanan altyapı ve sürdürebilirlik ihtiyacı göz önüne alındığında daha önemli hale gelen betonarme yapıların performans değerlendirmesi ile doğrudan ilgilidir. Mukavemet ve deformasyon kapasitesi ile çatlak genişliği tahminleri, yapıların tasarımında ve değerlendirilmesinde yapı mühendisleri için önemli bir rol oynamaktadır. Yapılarda betondan sonra en çok kullanılan diğer bir yarı statik malzeme ise yığma elemanlardır. Yığma duvarlar farklı malzemelerden oluşur ve betona benzer karmaşık tepkiler sergiler. Duvarlar ve betonarme çerçevelerin kombinasyonu ise dolgu duvarları oluşturur. Geçmişteki depremlerde betonarme çerçeveli binalarda önemli dolgu duvar hasarı gözlemlenmiştir. Bu duvarların çökmesi can kaybına neden olabilir. Yine de, betonarme çerçeve ve dolgu duvar etkileşimini anlamak

zordur, ancak doğrusal olmayan davranış birçok araştırmacı tarafından farklı ölçeklerde araştırılmıştır.

Önemli gelişmelere rağmen, beton ve yığma çatlağın başlaması ve yayılmasının sayısal modellemesi hala gelişme aşamasındadır. Geçmişte birçok farklı hesaplama yaklaşımı kullanılmıştır. Bu alanda son on yılda yapılan çalışmalar, kırılma olgusunun lokal karakterini modelleyebilmek için parçacık tabanlı simülasyon yöntemlerinin (ayrık elemanlar yöntemi, kafes tabanlı yöntemler, düzleştirilmiş parçacık hidrodinamiği, vb.) kullanmaya odaklanmıştır. Bu araçların avantajları, göreceli modelleme kolaylığı ve mikrodan makro seviyelere kadar çeşitli ölçekleri bağlama yeteneği ile birkaç önemli parametre kullanarak çatlak yayılımının simülasyonudur.

Bu çalışmada, doğrusal olmayan problemler için statik ve dinamik çözüm teknikleri ile peridinamikte kullanılan kavrama benzer şekilde, sürekliliğin önceden tanımlanmış bir ufuk boyunca uzanan kafes elemanları kullanılarak parçalandığı, orta ölçekli düzeyde pratik bir iki boyutlu kafes yaklaşımı önerilmiştir. Betonun sıkışma davranışı, kafes sistemi örgüsü karıştırmasını kullanan yeni bir kalibrasyon tekniği ile önerilen kafes yaklaşımı kullanılarak dolaylı bir çekme gerilim kırılması olarak ciddi derecede gözden geçirilir ve açıklanır. Umut verici sayısal sonuçlar, yalnızca gerilim kırılma özeliğine sahip kafes modelleri ile sıkışma çatlağının tahmin edilebileceğini göstermektedir. Ağ boyutu, ufuk ve yumuşama fonksiyonlarının sonuçların duyarlılığı üzerindeki etkisine odaklanan farklı göçme tiplerine sahip betonarme kirişler, kolonlar, duvarlar ve çerçeve testlerinin simülasyon sonuçları, çatlak dağılımları, aralıkları ve genel monotonik davranışı tahmini açısından deneysel sonuçlarla iyi bir uyum içindedir. Monotonik yükleme altındaki statik davranışı doğru bir şekilde simüle etmek için yeni bir orantılı-integral-türev kontrolüne sahip açık zaman entegrasyon tekniği kullanılmıştır. Önerilen yaklaşım daha sonra, donatısı otoklavlanmış gazbeton duvar dolgulu betonarme çerçevelerin tepkisini modellemek için kullanılır. İki gazbeton dolgulu duvar, karşılaştırma amacıyla test edilmiştir. Bu tür davranışların mekanik özelliklerini belirtmek için

otoklavlanmış gazbeton duvarların karakterizasyon testleri için bu testlerde kullanılan duvar bileşenleri kullanılmıştır. Sonuçlar modeli kalibre etmek için kullanılmıştır. Yapılan testlere ek olarak, daha fazla doğrulama için literatürden iki test daha kullanıldı. Önerilen kafes modeli, dolgu duvarlarda çatlak yayılımını makul bir doğrulukla tahmin edebilmiştir. Çerçeve-dolgu duvar etkileşimi, basma bölgesi oluşumunu gerçekçi bir temsili sağlanarak başarılı bir şekilde simüle edilmiştir. Son olarak, yanal deformasyonun bir fonksiyonu olarak temas uzunluğu ve basınç bölgesi genişliğini incelemek için parametrik bir çalışma yapılmıştır. Sonuçlar, dolgu duvar-çerçeve temas uzunluğunun, etkileşim bölgesinin yanal deformasyon talep seviyelerine ve özelliklerine önemli ölçüde bağlı olduğunu göstermektedir. Tüm simülasyon sonuçlarının, oldukça basit ve sezgisel bir yöntemle, önerilen modelleme yaklaşımı ile yapı üzerindeki çatlak ilerleme yönünü ve akan kuvveti doğru bir şekilde tahmin etme yeteneğini gösterdiği ifade edilebilir.

Anahtar Kelimeler: Beton, Yığma, Dolgu Duvar, Çatlama, Modelleme

To My Family

ACKNOWLEDGMENTS

I want to express my profound gratitude to my advisor Prof. Dr. Barış Binici, and co-advisor Prof. Dr. Kağan Tuncay, whose knowledge, criticism, patience, and support enabled me to develop the ideas behind this dissertation. From them, I have learned not only how to become a researcher but also how to have a strong character. I will always admire their attitude towards their students and carry the honor of working with them all my life. They will always be my advisors.

The value of ideas that emerged from our conversation with Prof. Dr. Yalin Arici and Assoc. Dr. Alper Aldemir is invaluable for the development of this study. I would like to thank him for his availability.

My special thanks go to my eternal mentorship İsmail Ozan Demirel. I think it was one of my luckiest times in my life when I had the chance to meet him because he proved me that good and unselfish guys still exist.

My thanks go to my office mates and friends. I will never forget them with pleasure the inspiring discussions and activities we had.

I would like to express my sincere gratitude to my beloved mother and father, Hatice Aydın and Kadir Aydın for their eternal love, encouragement, and trust.

It is the gospel truth that Gizem Yaz Aydın was and will support me in good times and in bad times in sickness and in health as my lovely wife.

This work is partially funded to continue some part of my studies in TU Delft by the Scientific and Technological Research Council of Turkey (TUBİTAK) as 2214A International Doctoral Research Fellowship under application number 1059B141900037. I would like to thank TUBİTAK for supporting my studies.

TABLE OF CONTENTS

ABSTRACT v

ÖZ viii

ACKNOWLEDGMENTS xii

TABLE OF CONTENTS xiii

LIST OF TABLES xvi

LIST OF FIGURES xvii

CHAPTERS

1 INTRODUCTION 1

1.1 General 1

1.2 Literature Review 2

1.2.1 Concrete Material 3

1.2.2 Numerical Approaches for Concrete Materials 5

1.2.3 Masonry Infilled Walls 19

1.2.4 Numerical Modeling for Infill Walls 20

1.2.5 Nonlinear Solution Schemes 23

1.2.6 Motivation of Research 24

1.3 Objective and Scope 25

2 MATERIAL MODELING WITH LATTICE NETWORKS 29

2.1 Lattice Topology and Nodal Interaction 29

2.2 Elastic Properties 32

2.3 Justification of the Approach 34

2.4 Tension Modeling 37

2.5 Compression Modeling 40
2.5.1 Compression Response 41
2.5.2 Methodology 43
2.5.3 Validation of Perturbed Mesh for Concrete and Masonry 57
2.6 Reinforced Concrete Modeling 71
2.7 Discussion of the Model 74
2.8 Bi-material (Reinforced Concrete+AAC) Modeling 79
2.9 Solution Procedures 81
2.10 Summary of Calibration of Modeling 85
3 REINFORCED CONCRETE AND MASONRY STRUCTURE MODELING AND VALIDATION 87
3.1 Reinforced Concrete Members 87
3.1.1 Column Simulations 90
3.1.2 Beam Simulations 95
3.1.3 Wall Simulations 102
3.1.4 Parametric Studies 106
3.1.5 Discussion of Results 111
3.2 Reinforced Concrete Structures (Portal Frame Simulations) 114
4 AAC INFILLED FRAME TESTS AND VALIDATIONS 119
4.1 AAC Infilled Frames Experiments 119
4.1.1 New Tests in This Study 119
4.1.2 Tests in Literature 124
4.2 AAC Infilled Frames Simulations 125
4.2.1 Infilled Frame (Binici et al. 2019) 126

4.2.2 Infilled Frames in This Study 127
4.2.3 Pavia Test 131
4.2.4 Discussion of Results 133
4.3 Parametric Study 134
5 CONCLUSION 139
5.1 Summary 139
5.2 Concluding Remarks 140
5.3 Future Works 143
REFERENCES 145
APPENDICES
A. Residual Bond Strength Parameter 177
CURRICULUM VITAE 179

LIST OF TABLES

TABLES

Table 2.1. Specimen Properties for Compression Simulations 58
Table 2.2. Jansen and Shah (1997) Results 59
Table 2.3. Strut Efficiency Factor for Laughery and Pujol (2015) and Brown et al. (2006) 63
Table 2.4. Material Properties of AAC Masonries 68
Table 2.5. Results for AAC Masonry Diagonal and Uniaxial Compression Experiments and Simulations 69
Table 3.1. Properties of the Test Specimens of Reinforced Concrete Members 88
Table 3.2. Information regarding Time Step, CPU Time, and Lattice data for the Results Presented in This Study 89
Table 3.3. Belgin and Sener (2007) Results 102
Table 3.4. Parameters Values for Sensitivity Analysis 108
Table 3.5. Summary of the Comparison between the Computed and Experimental Results 113
Table 3.6. Material Properties of Concrete and Steel for Portal Frames 114

LIST OF FIGURES

FIGURES

Figure 1.1. Concrete at Different Scales 4
Figure 1.2. Concrete Response 5
Figure 1.3. Macro-scale Numerical Methods 7
Figure 1.4. Finite Element Methods with Maximum Principal Strains and Cracks . 9
Figure 1.5. Particle Based Modeling 12
Figure 1.6. Lattice Modeling 13
Figure 1.7. Crack Pattern for Direct Tension Simulations (Schlangen and Qian, 2009) 14
Figure 1.8. Nonlinear Lattice Modeling (Bazant et al. 1990) and Lattice Discrete Particle Model (Cusatis et al. 2011) 16
Figure 1.9. Lattice Approach Proposed by Aydin et al. (2018) with Different Horizons 17
Figure 1.10. Numerical Modeling for Masonry Elements 22
Figure 2.1. Lattice Model for (a) δ = 1.5d and (b) δ= 3.01d 30
Figure 2.2. Topology of Lattice Model for (a) Boundary Conditions and (b) Grid Types 31
Figure 2.3. Poisson's Ratio Variations 34
Figure 2.4. Assumed Material Behavior Force-Strain Diagram for Concrete Elements 39
Figure 2.5. Workflow for Constitutive Model Calibration for Only Tension (Test Specimen Drawn Using Data from Cornelissen et al. 1986) 40
Figure 2.6. Compression Response for Two Boundary Conditions (van Vliet and van Mier 1996) 43
Figure 2.7. Uniaxial Material Behavior of Lattice Member in Compression 44
Figure 2.8. Compression Test Results of a Cube Specimen with Dimensions of 100 mm for Uniform Mesh 45

Figure 2.9. Simulation of Rectangular Specimens Tested by Kupfer (1969) with Initial Crookedness (%7) 47
Figure 2.10. Compression Test Simulation and Experimental Results of a Cube Specimen with Dimensions of 100 mm for Random Mesh (van Mier 1997) 49
Figure 2.11. Model Parameter Calibration for Both Tension and Compression 51
Figure 2.12. Compressive Strength from Simulations 52
Figure 2.13. Work-Flow for Compression Calibration of AAC Masonry Structures 53
Figure 2.14. Convergence Results for (a) Batch 1 (METU) and (b) Batch 2 (Pavia) 54
Figure 2.15. Convergence Results for Different Concrete Materials and Boundary Conditions 55
Figure 2.16. Mesh Objectivity and Size Effect Results 57
Figure 2.17. Comparisons with Test Results (Jansen and Shah 1997) for (a) Test Specimens (Dimensions in mm); (b) Relative Stress-Strain Curve And (c) Crack Patterns 60
Figure 2.18. Simulation Results of Compression Strut Tests (Brown et al. 2006; Laughery and Pujol 2015) (a) Typical Specimen Dimensions; (b)Simulation Results; and (c) Experimental Cracking of Laughery and Pujol (2015); (d) Brown et al. (2006) and (e) All Results 62
Figure 2.19. Compression and Diagonal Test Experiments and Simulations of Batch 1, METU Experiments 66
Figure 2.20. Cracks in Simulations and Experiments for Uniaxial and Diagonal Compression Tests of Batch 1 67
Figure 2.21. Representation of Three Types of Lattice Elements (Dimensions in Millimeter) (Acun and Sucuoglu 2010) 71
Figure 2.22. Assumed Material Constitutive Models for (a) Steel and (b) Bond elements 74
Figure 2.23. Overview of the modeling approach: element types and corresponding constitutive models 80

Figure 2.24. Application of the SLA for Tension Response of Lattice Elements .. 82
Figure 2.25. PID Control Kinematic Representation and Example 85
Figure 3.1. Full Scale Reinforced Concrete Column Simulation: (a) Dimensions and Details of Test Specimen (Dimensions are given in mm); (b) Observed Crack Pattern; (c) Load-Deflection Comparison (Acun and Sucuoglu 2010)..... 92
Figure 3.2. Full Scale Reinforced Concrete Column Simulation: (d) Cracking and Rebar Strains at about 2.5% Drift Ratio for d=17.5 mm, $\delta = 1.5d$; (e) d=17.5 mm, $\delta = 1.5d$; (f) d=35 mm, $\delta = 1.5d$; (g) d=17.5 mm, $\delta = 3.01d$ (Amplification Factor = 10 for (d)-(g)) (Acun and Sucuoglu 2010). 93
Figure 3.3. Representation of Lattice Model (Dimensions in millimeter) (Ozcebe and Saatcioglu 1987)..... 94
Figure 3.4. Column Specimen (U4) Simulation: (a) Dimensions and Details of Test Specimen (Dimensions are Given in mm); (b) Load-Deflection Comparison; (c) Observed Crack Pattern; (d) $\delta = 1.5d$; (e) $\delta = 3.01d$ (Amplification Factor = 3 for (d) and (e)) (Ozcebe and Saatcioglu 1987). 95
Figure 3.5. Deep Beam Simulation: (a) Dimensions and Details of Test Specimen (Dimensions are given in mm); (b) Load-Deflection Comparison; (c) Observed Crack Pattern; (d) d=10 mm, $\delta = 3.01d$; (e) d=10 mm, $\delta = 1.5d$; (f) d=20 mm, $\delta = 1.5d$ (Amplification Factor = 10 for (d)-(f)) (Foster and Gilbert 1998). 97
Figure 3.6. Representation of Lattice Model (Dimensions in millimeter) (Foster and Gilbert 1998)..... 98
Figure 3.7. Reinforced Beam Simulation: (a) Dimensions and Details; (b) Load-Deflection Comparison; (c) d = 25 mm; (d) d = 12.5 mm (Walraven 1978)..... 99
Figure 3.8. Representation of Lattice Model (Dimensions in millimeter) (Walraven 1978). 100
Figure 3.9. Simulation Results of Overreinforced Beams (Belgin and Sener, 2008): (a) Test Specimens and Crack Patterns; (b) Uniform Mesh (L11x30); (c) L11x30. 101
Figure 3.10. Slender Reinforced Concrete Wall (i.e. aspect ratio 1:3) Simulation: (a) Dimensions and Details of Test Specimen (Dimensions are given in mm); (b)

Load-Deflection Comparison; (c) Observed Crack Pattern; (d) $\delta = 1.5d$; (e) $\delta = 3.01d$ (Amplification Factor = 10 for (d) and (e)) (Thomsen and Wallace 1995,2004). 103
Figure 3.11. Representation of Lattice Model (Dimensions in millimeter) (Thomsen and Wallace 1995,2004). 104
Figure 3.12. Reinforced Concrete Wall Simulation: (a) Dimensions and Details of Test Specimen (Dimensions are given in mm); (b) Load-Deflection Comparison; (c) Observed Crack Pattern; (d) $\delta = 1.5d$; (e) $\delta = 3.01d$ (Amplification Factor = 10 for (d) and (e)) (Aldemir et al. 2017). 105
Figure 3.13. Representation of Lattice Model (Dimensions in millimeter) (Aldemir et al. 2017) 106
Figure 3.14. Deterministic Sensitivity Analysis Results for Model Parameters ... 109
Figure 3.15. Deterministic Sensitivity Analysis Results for Concrete Constitutive Material Parameters 109
Figure 3.16. Lateral Load – Top Displacement Curves in Different Loading Rates 110
Figure 3.17. Simulation Comparisons With Respect To Lattice Rotation 111
Figure 3.18. Dimensions of Portal Frames for (a) METU Frame (Batch 1) (Binici et al. 2019) and (b) Pavia Frame (Batch 2) (Calvi and Bolognini 2001) 115
Figure 3.19. Reinforced Concrete Portal Frame Simulations: (a) Load-Deflection Comparison; Observed Crack Pattern for the Residual Bond Parameter ($\boldsymbol{a}$) Values of (b) 0.7 and (c) 0.3 (Binici et al. 2019). 117
Figure 3.20. Reinforced Concrete Portal Frame Simulations: (a) Load-Deflection Comparison; (b) Observed Crack Pattern (Calvi and Bolognini 2001). 118
Figure 4.1. Specimen Dimensions and Installed Instrumentations of the AAC Infilled Frames 121
Figure 4.2. Global and Local Response Curves and Cracking of Specimens SP1, Cracks at Different Drift Ratios and (b) Lateral Displacement-Base Shear and Interface Opening Responses for Corresponding LVDT Labels for the Specimen SP1 122

Figure 4.3. Global and Local Response Curves and Cracking of Specimens SP2, Cracks at Different Drift Ratios and (b) Lateral Displacement-Base Shear and Interface Opening Responses for Corresponding LVDT Labels for the Specimen SP2 and (c) Drift-Base Shear Curve Comparisons for Bare Frame and Infill Walls as Binici et al. (2019), SP1, SP2 123
Figure 4.4. Experiment and Simulations Results of Infill Test (Binici et al. 2019): (a) Base Shear – Top Displacement Responses, and Cracks (b) in Experiment at Positive (3.0% Drift Ratio) and Negative (3.5% Drift Ratio) Directions, (C) in Simulation at 1.32% and 4.00% Lateral Drift Ratios with Observed Experimental Cracks 127
Figure 4.5. Experiment and Simulation Results of SP1: (a) Base Shear – Top Displacement Responses and (b) Interface Openings of Corresponding Lvdts and (c) Cracks in Simulation at 1.39% And 2.92% Lateral Drift Ratios with Observed Experimental Cracks at Different Drift Ratios and DIC Results 129
Figure 4.6. Experiment and Simulation Results of SP2: (a) Base Shear – Top Displacement Responses and Interface Openings of Corresponding Lvdts and (b) Cracks in Simulation at 1.60% and 4.00% Lateral Drift Ratios with Observed Experimental Cracks at Different Drift Ratios 130
Figure 4.7. Experiment and Simulation Results of Pavia Infill Test (Penna and Calvi 2006): (a) Base Shear – Top Displacement Curve and (b) Cracks for Two Simulations at 0.66% and 1.11% Lateral Drift Ratios with Observed Experimental Cracks at Directions 132
Figure 4.8. Masonry Infilled Wall and RC Frame Assemblage 134
Figure 4.9. Contact Length in Columns and Drift Ratio Curves for Different Length Scales (L/H) And Interface Properties of (a) SP1 (Only Upper Side Foam), (b) Binici et al. (2019) (All Sides Foam), (c) Pavia Test (2006) (No Foam) 136

CHAPTER 1

INTRODUCTION

1.1 General

Structures are essential parts of a nation's economy. People are usually not aware of structures as a live environment until there is a problem in structural performance. Structures are the key elements of modern civilized life. Problems on infrastructures have significant effects on modern economies. For example, 2 trillion dollars is allocated for the USA nation's infrastructure upgrade (New York Times 2021). On the other hand, earthquake can lead to significant damage on poor infrastructure that is hard to recover psychologically and economically. According to Word Bank, the cost of the 1999 earthquake in Turkey was in the order of 12-17 billion dollars, most of which was spent to repair the damaged structures. Thus, sustainable structures and performance assessment of existing buildings become more and more important for urban life.

Decision on the performance of moderately damaged structures, whether the structure has been heavily damaged or should be strengthened, is a very challenging issue. For reinforced concrete structures, the issue is related to understanding the fracture and nonlinear concepts of materials and structures. Since a significant portion of the built environment is made from concrete, the behavior of concrete under extreme loading requires special attention. However, understanding the fracture and load response of concrete is a challenging task due to its highly nonlinear quasi-brittle behavior. Due to its heterogeneous nature (Mehta 1993), concrete exhibits complex behavior at the micro, meso, and macro scales (Wittmann, 1983). Cracks evolve from the micro level to the macro level randomly and cause nonlinear response of structure. On the other hand, after concrete, the other mostly used component in the built environment is masonry elements. Masonry walls exhibit

complex responses similar to concrete due to consisting of a variety of materials, such as brick and mortar. Previous earthquakes have caused significant damage on masonry-infilled walls of RC frame buildings. The collapse of these infilled walls may cause loss of life in buildings. Understanding RC frame-infilled wall interaction plays a crucial role in assessing the inter-story response of a building and is still challenging.

The performance assessment of reinforced concrete structures which is becoming more important due to the aforementioned reasons is directly related to prediction nonlinear response of concrete and masonry walls. Strength and deformation capacity estimations along with crack width predictions appear to play a key role for structural engineers in the design and assessment of structures. Many researchers have investigated the nonlinear behavior of these materials in different scales. In this context, robust modeling techniques that can exhibit good engineering accuracy with minimum number of input parameters are still needed.

This work has been conducted to develop a practical and efficient approach to describe the nonlinear behavior of the heterogeneous cementitious nature of concrete material for RC members and structures, autoclaved aerated concrete (AAC) masonry and infill walls. In this chapter, a detailed explanation of concrete and masonry-infilled walls and the literature review of numerical approaches are presented. After briefly explaining nonlinear solution schemes and research motivation, objectives and scope are given.

1.2 Literature Review

In this section, firstly, the literature on the complex behavior of concrete is explained. Extensive work on corresponding the modeling approaches in different scales, from macro to micro-scale, is summarized. While explaining these topics, concrete material models in compression are briefly reviewed. Then, masonry-infilled walls and numerical approaches for them are mentioned. In order to solve nonlinear

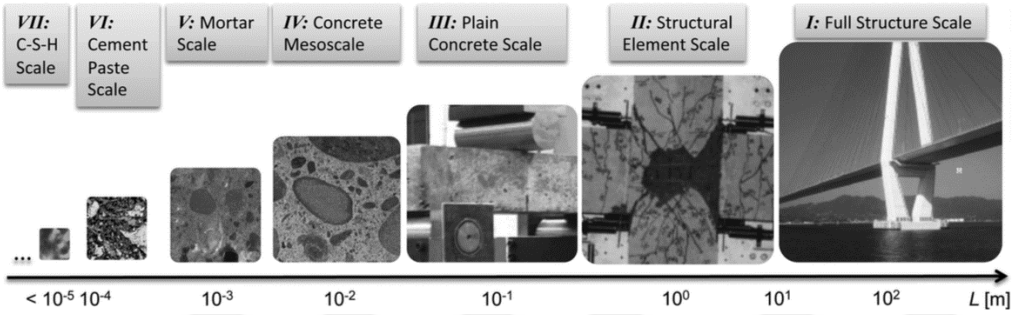
behavior, used nonlinear solutions schemes were introduced by emphasizing sequentially linear analysis and dynamic solution schemes. Finally, research motivation is stated.

1.2.1 Concrete Material

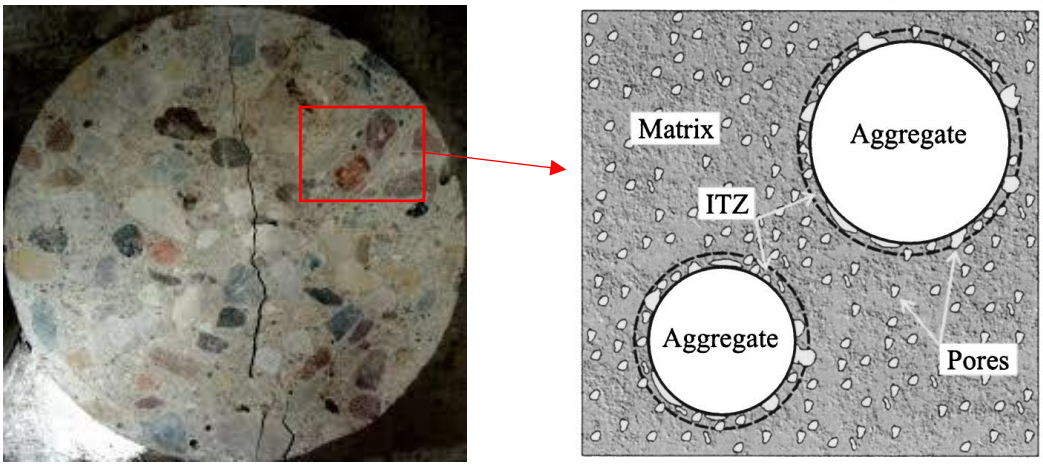
Understanding cracking in concrete is a challenging task due to its heterogonous nature. It is a mixture of cement, sand and aggregate. The material should be investigated at from the micro and to the macro level in order to understand crack propagation in concrete (Figure 1.1). Concrete media is composed of three constituents at the mesoscale: cement as the binder, aggregate as the filler and ITZ as the interfacial transition zone from cement to aggregate (Figure 1.1). The weakest micro parts of concrete can be exhibited as the region surrounded the aggregates (Interfacial Transition Zone) and matrix filled between them. Cracks tend to bridge and local failure generally occurs in these zones. The cracks affect the global load-deflection response of concrete. The nonlinearity is obtained due to the crack propagations usually along ITZ and cement paste for normal strength concrete.

Concrete, when subjected to tension, has a nearly elastic response until cracking and exhibits softening after cracking (Figure 1.2a) (Chen and Han, 2007). The pioneering works of Hillerborg et al. (1976), Bazant and Oh (1983), Hordjik et al. (1991) led to a better understanding toward modeling concrete in tension by incorporating tensile fracture energy as a material parameter. On the other hand, concrete exhibits a very complex response in compression. Failure in uniaxial uniform compression for concrete was explained with different theories on different aspects. Many cylindrical test specimens with different aspect ratios were compressed uniformly by Jansen and Shah (1997) (Figure 1.2b), concluding crushing is a localized failure in experiments, and the required energy to exhibit compression failure is independent of length scales. However, the specimens were not lubricated at the ends, so the boundaries affecting the compression response were laterally restrained in these tests. On the other hand, damage zones were separated as splitting micro and macro cracks by

Markeset and Hillerborg (1995). Bazant and Xiang (1997) explained the failure with the buckling of the portion between two cracking regions (Figure 1.2c). In short, the uniaxial compression behavior of concrete is nonlinear beyond about 40% of the ultimate strength, and follows a softening regime beyond ultimate strength due to micro and macro cracking. Although named as the compressive strength, several researchers have argued that compression is merely an indirect tensile failure, followed by material instability (Kendall, 1978; Willam et al., 1989; Bazant et al., 1993; Fantilli et al., 2002; Birck et al., 2016). Modeling of the compression response of concrete is covered in detail in subsequent sections of this work.

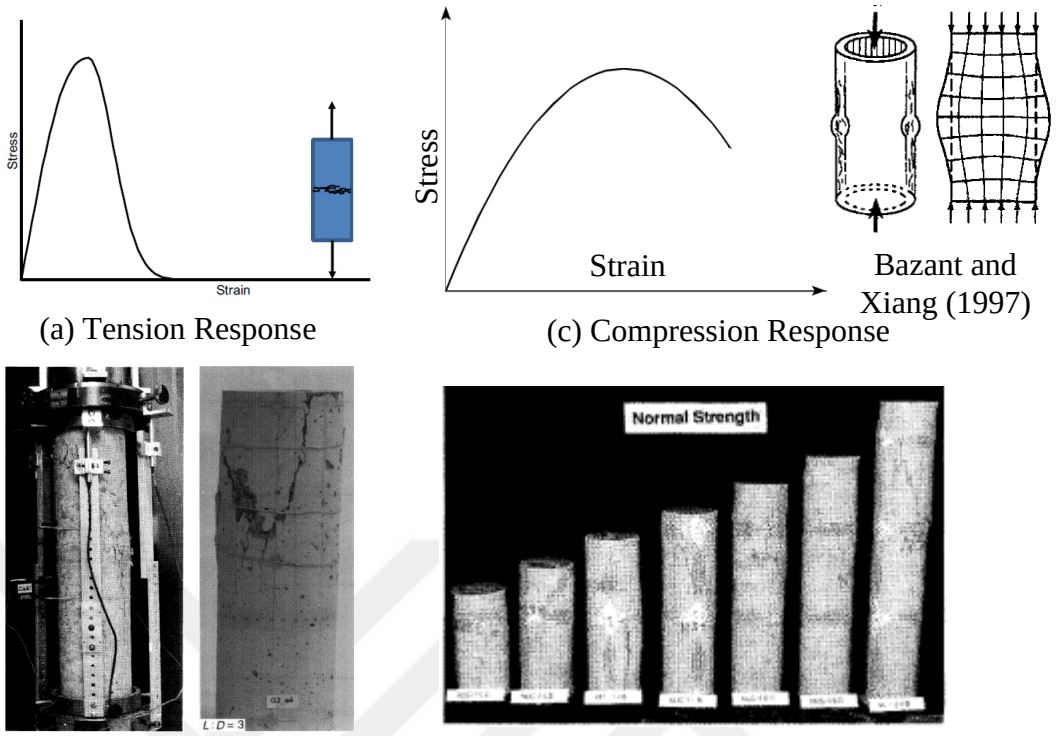


Concrete Material at Different Scales



Concrete at Mesoscale

Figure 1.1. Concrete at Different Scales



(a) Tension Response (c) Compression Response

(b) Jansen and Shah (1997)

Figure 1.2. Concrete Response

1.2.2 Numerical Approaches for Concrete Materials

Although explaining the complex behavior of concrete in tension and compression is challenging, many numerical approaches have been proposed for simulating the behavior of concrete and reinforced concrete members at different scales with mesh or mesh-free methods in order to define typical response. Homogeneous material modeling is used for macro-scale simulations, whereas inhomogeneity is incorporated at micro-scale and mesoscale level, which are more involved but less practical (Figure 1.1). While the elements used in the microscale simulations are in the few millimeters order, macroscale models are employed with larger element sizes.

1.2.2.1 Macro-models

Lumped and spread of plasticity over the length of a macro-element (Figure 1.3a,b, respectively) with beam-type formulations were studied by many researchers (Clough and Johnston 1966; Giberson 1969; Li and Jirsa 1998; Lee and Elnashai 2001; Elwood 2004; Mostafaei and Vecchio 2008; Scott and Fenves 2006). In these models, nonlinearity was defined at the specific sections in the element. In general, these sections are called the plastic hinge regions at the reinforced concrete (RC) members. While easy to implement and formulate, micro behavior of concrete cannot be obtained with such scale models. For example, these models are incapable of capturing strain-softening response of concrete despite some efforts for regularization (Coleman and Spacone 2001).

Distributed nonlinearity with multi-fiber models is another macro-scale approach for modeling concrete (Figure 1.3c)(Takayanagi and Schnobrich 1979; Taucer et al. 1991; Neuenhofer and Filippou 1997; Guner and Vecchio 2011; Limkatanyu and Spacone 2002; Spacone et al. 1996; Mazars et al. 2006). It should be noted that this model is different from distributed plasticity. In these models, the element has sections with multiple fibers, representing the cross-section of RC member. The nonlinear stress-strain responses of these fibers are defined according to their material response. These sections are compatible with the rotation of element with the assumption of plane sections remaining plane. Thus, the softening response can be simulated with special techniques. The main disadvantage of the model is the incapability of representing shear-related effects. Although some existing techniques were proposed to handle this problem, such as using ASFI (Mostafaei and Vecchio, 2008; Saritas and Filippou, 2009), they are either hard to implement or limited in their application.

One of the most popular and practical macro-model approach is the strut and tie model (STM) (Figure 1.3d). The model enables the representation of the complex stress distribution in the structure in a simple way by discretizing with struts, ties, and nodes. These elements are based on the truss analogy. The strut and tie model

becomes a very useful approach for modeling shear critical structures after Schlaich et al. (1987). Many researches used the method to design different types of members, such as deep beams, inverted-T beams, shear walls, bridges, etc. (Brown et al. 2002-2006, Birrcher et al. 2006-2009, Williams et al. 2009-2012, Larson et al. 2009-2013, Wing and Gustavo 2003, Liang et al. 2002). The method was introduced into ASCE-ACI (1998), AASHTO LRFD (1994 2016), (FIP 1996) and ACI 318-02 (2002) provisions. While it offers to explain complex behavior in a simple manner, there is no common consensus about the mechanical properties to be used for STM nodes/elements. Stiffness and strength properties are especially hard to define if the goal is to obtain the load-deformation response (Leu et al. 2006; Yun 2000; Tjhin and Kuchma 2002).

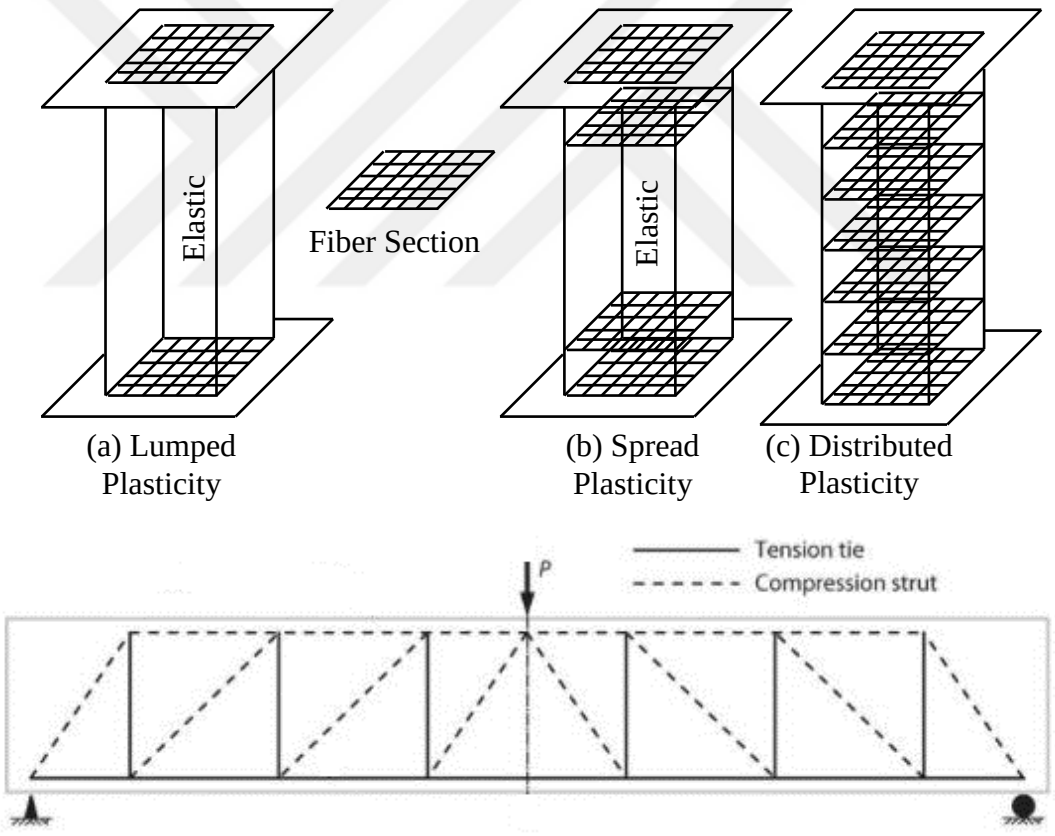


Figure 1.3. Macro-scale Numerical Methods

1.2.2.2 Micro and Meso Scale Models

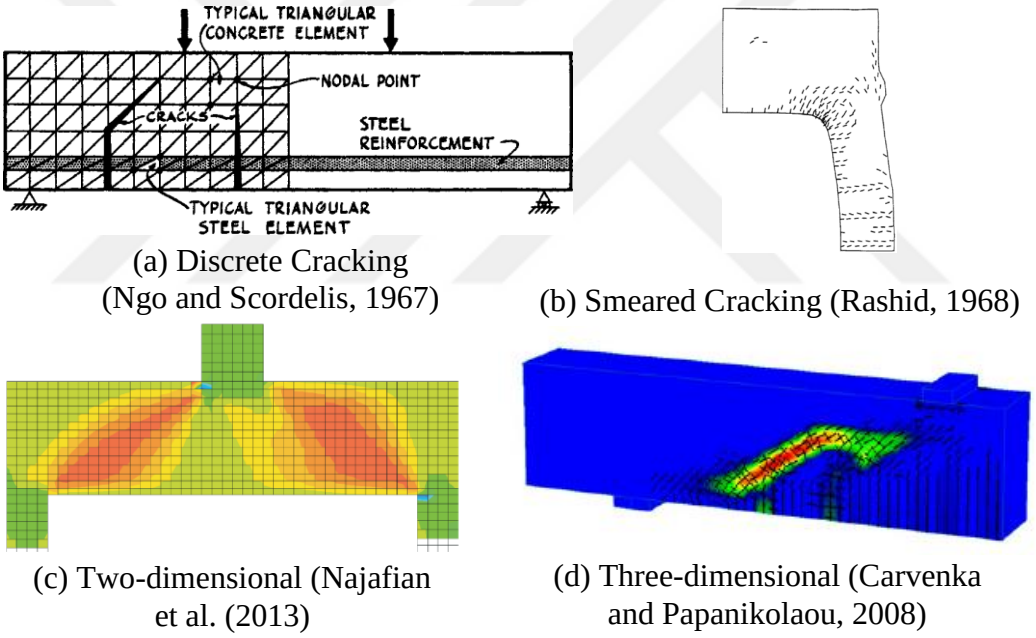
Although macro models are computationally efficient and reasonable for large structural estimations, estimating the properties of the macro elements is challenging as the response parameters are hard to predict. Micro and meso scale elements are capable of simulating the crack pattern and widths, reinforcement response and its interaction with concrete with bond response and the force flow over the members. In this section, numerical studies in micro and meso scale conducted to explain concrete response are summarized under two main headings as finite element models and particle-based and lattice models. The effect of micro and meso structural modeling on macroscopical behavior is discussed.

1.2.2.2.1 Finite Element Models

Since the 1960s, the finite element method (FEM) has been the preferred choice to simulate the concrete fracture and response of reinforced concrete members. Starting with Ngo and Scordelis (1967) and Rashid (1968), discrete crack and smeared crack models and approaches as two mainstream directions were often employed within the finite element framework (Figure 1.4a,b). Continuum-based smeared crack finite element modeling represents crack opening with strain localization (Carol et al. 1997; Rots et al. 2008; Slobbe et al. 2014). The main drawback of continuum-based finite element modeling is the difficulty of employing the actual separation due to cracking. On the other hand, discrete crack finite element approaches require identifying crack locations à priori, and remeshing. Pre- and post-processing difficulty, and necessitate different constitutive models for the cracks and continuum part are the other disadvantages.

One-dimensional frame element models (Clough and Johnston, 1966; Roufaiel and Meyer, 1987; Spacone et al., 1996; Lee and Elnashai, 2001; Elwood, 2004; Scott and Fenves, 2006), two and three-dimensional shell or solid elements (Balan et al., 1997; Lura et al., 2002; Tan et al., 2005; Cervenka and Papanikolaou, 2008; Koutromanos

and Shing, 2012; Najafian et al., 2013) have been adapted to modeling of members and structures (Figure 1.4c,d). The application of FEM in mesoscale for concrete, as given by Roelfstra et al. (1985), represented mortar with finite elements, which were in turn connected to aggregate elements. More recently, the classical approach of modeling concrete ingredients separately was attempted by using the FEM (Wang et al., 1999; Kwan et al., 1999; Caballero et al., 2006; Wriggers and Moftah, 2006; Lopez et al., 2008a;b). Moreover, the heterogeneous nature of concrete was modeled with a uniform grid in previous studies (Zohdi and Wriggle, 2001; Hafner et al., 2006; Lee and Park, 2008). All the aforementioned studies are important toward understanding the behavior of concrete and developing numerical models. However, these results have found limited application in practice.



(a) Discrete Cracking (Ngo and Scordelis, 1967)

(b) Smeared Cracking (Rashid, 1968)

(c) Two-dimensional (Najafian et al. (2013)

(d) Three-dimensional (Carvenka and Papanikolaou, 2008)

Figure 1.4. Finite Element Methods with Maximum Principal Strains and Cracks

1.2.2.2.2 Particle-based and Lattice Models

In 1821, Navier proposed a theory based on dynamic equilibrium for analyzing objects using forces according to Isaac Newton's second law. The theory claimed

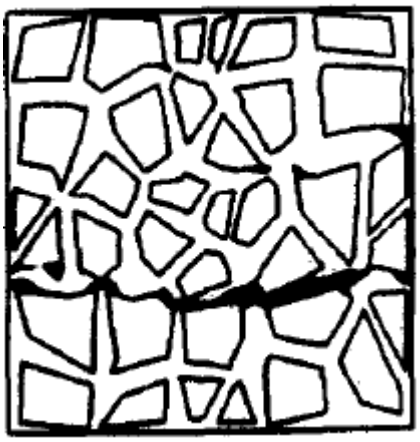
summation of the forces should always be considered at a point since the concept of stress was not known yet. About ten years later, the concept of stress was proposed (Cauchy 1828). The particle-based methods (PBM) focus on the equilibrium in the points. The increase in computational power led to the development of modern particle-based methods for the simulation of fracture at the micro and meso scales. There has been an increasing interest in employing particle-based simulation techniques for fracture simulations of concrete as mesoscale PBMs are very attractive to represent the individual behavior of the ingredients of concrete, namely, mortar, aggregates, and the interfacial transition zone. For this purpose, Stankowski (1990) proposed the model in which the elastic aggregates are connected with inelastic mortar phase (Figure 1.5a). Such small-scale models may overcome the drawbacks of the FEM approaches, such as the need for remeshing upon fracture and simulating the crack opening explicitly. Moreover, the particle models were further used to simulate the behavior of different concrete types, such as fiber-reinforced concrete (Figure 1.5b) (Schauffert and Cusatis, 2012; Schauffert et al., 2012; Ceccato et al., 2017 etc.).

The particle-based method of Silling (2000), the so-called peridynamics (PD) and smoothed particle hydrodynamics (Lucy 1977) with similar mathematical backgrounds (Ganzenmüller et al. 2015) are two of the attractive methods due to the ease of model definition and implementation. The bond-based PD allows each point to interact with neighboring points with a pairwise force function, while the damage is incorporated by defining a nonlinear function for the force-elongation response (Figure 1.5c) (Silling 2000; Gerstle and Sau 2004). It is well known that this approach has a limitation on matching arbitrary Poisson's ratios in the linear elastic range (Nayfeh and Hefzy 1978; Beale and Strolovitz 1988; Donze et al. 1995). In order to overcome this restriction, different solution techniques were implemented. The state-based peridynamics approach of Silling et al. (2007) can address all possible Poisson's ratios by considering the states of the connected points to a node instead of just two node interactions. With this modification, it is not necessary to obtain an equal magnitude of the interaction between two material nodes and the

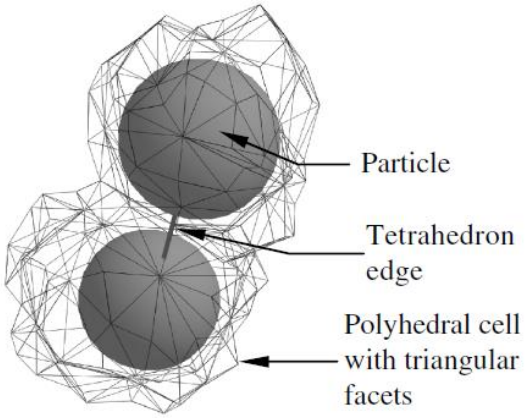
interaction depends on the state of connected nodes in volume (dV_i and dV_j in Figure 1.5c). The state-based peridynamics was applied successfully to simulating crack nucleation (Silling et al. 2010; Littlewood 2011), impact damage (Seleson and Parks 2011, Tupek et al. 2013), polycrystal fracture (Askari et al. 2008), crystal plasticity (Sun and Sundararaghavan 2014), concrete fracture (Gerstle 2015, Nikravesh and Gerstle 2018), geomaterial fragmentation (Lai et al. 2015), and dynamic blast loading (Littlewood 2010). However, due to its conceptual simplicity, the use of few input parameters, and the success in modeling fracture (and the complexity of state-based models), the bond-based model is still commonly preferred for nonlinear simulations (Figure 1.5d) (Kilic et al. 2009; Ha and Bobaru 2010, 2011; Hu et al. 2012; Oterkus et al. 2012; Bobaru et al. 2012; Shen et al. 2013; Ghajari et al. 2014). Summarily, bond-based peridynamics simulate the interaction of nodes with axial forces in connections in a specified horizon region, while volumetric interaction is obtained in state-based peridynamics.

Another popular particle method similar to the bond-based peridynamics is the lattice approach in which the continuum is discretized with nodes connected to each other by means of structural elements such as springs, trusses or beams (Figure 1.6). In order to induce heterogeneity, mechanical properties such as stiffness or strength of the elements are randomized (Hrennikoff, 1941; Schlangen and van Mier, 1992; Schlangen 1993; Lilliu and van Mier, 2003; Cusatis and Pelessone, 2006; Grassl and Jirasek, 2010). Truss-based lattice models were used owing to the advantage of computational efficiency and ease of calibration (Burt and Dougill, 1977; Bazant et al., 1990; Bazant and Planas, 1997; Schlangen and Garboczi, 1997; van Mier, 2013; Birck et al., 2016). The greatest disadvantage of the truss-based lattice network is the limitation on the Poisson ratio similar to the bond-based PD (1/3 in 2D and 1/4 in 3D) (Silling et al., 2007). The limitation on the Poisson ratio was overcome by using shear springs (Kawai, 1978; Zubelewicz and Bazant, 1987; Griffiths and Mustoe, 2001; Cusatis et al., 2003), beam elements (Lilliu and van Mier, 2003; Karihaloo et al., 2003; Liu et al., 2007; Gerstle et al., 2013; Aziz, 2014), spring birth (Caldarelli et al., 1999; Parisi and Caldarelli, 2000), Kirkwood–Keating springs (Monette and

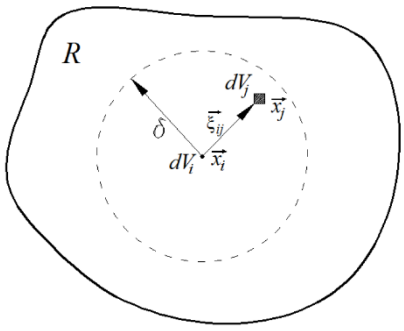
Anderson, 1994; Ostoja-Starzewski et al., 1996) and the artificial force concept (Baudet et al., 2007). It should be reminded that while the use of beam elements was criticized by Cusatis et al. (2006), the spring-based models were found insufficient by Schlangen and van Mier (1992). As no consensus is available with the particle-based approaches, and the choice of modeling often depends on which engineering parameter should be estimated accurately (elasticity or plasticity parameters, deflection/vibration calculations, visuals of crack patterns, crack widths). The literature shows that it is quite acceptable to choose a modeling approach to accurately simulate certain engineering demand parameters while accepting model limitations for go accurate simulation of other parameters.



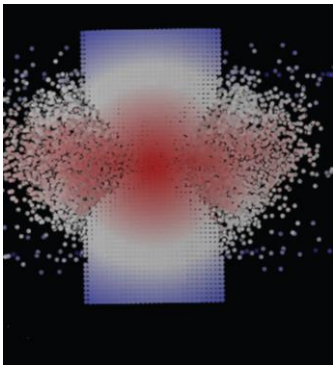
(a) Stankovski (1990)



(b) Schauffert and Cusatis (2011)

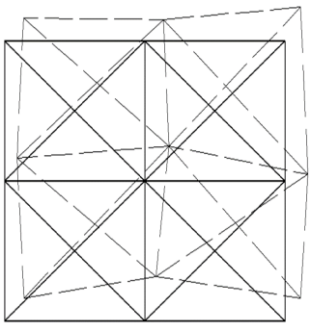


(c) Kinematic of peridynamics

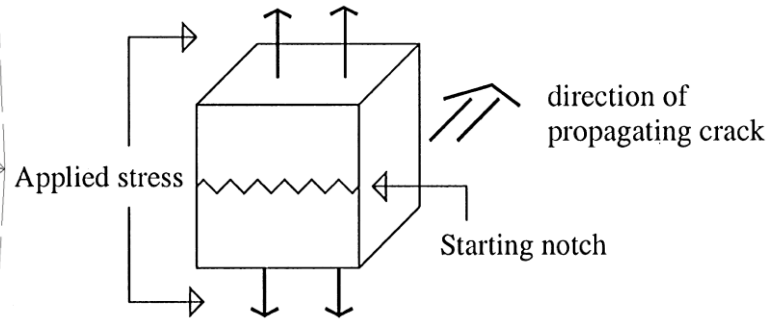


(d) Shen et al. (2013)

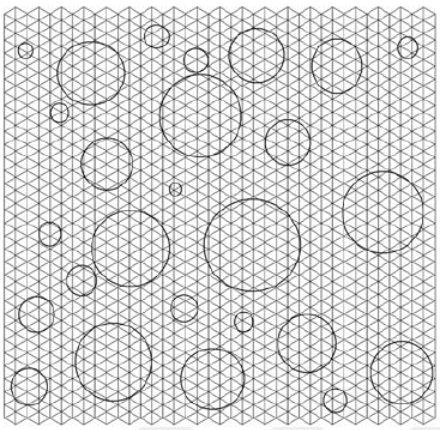
Figure 1.5. Particle Based Modeling



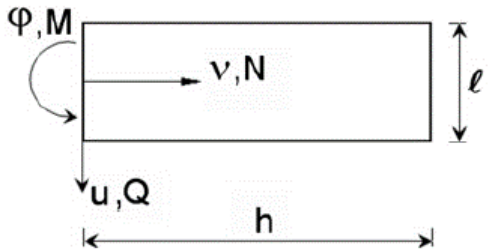
Hrrenikoff (1941)



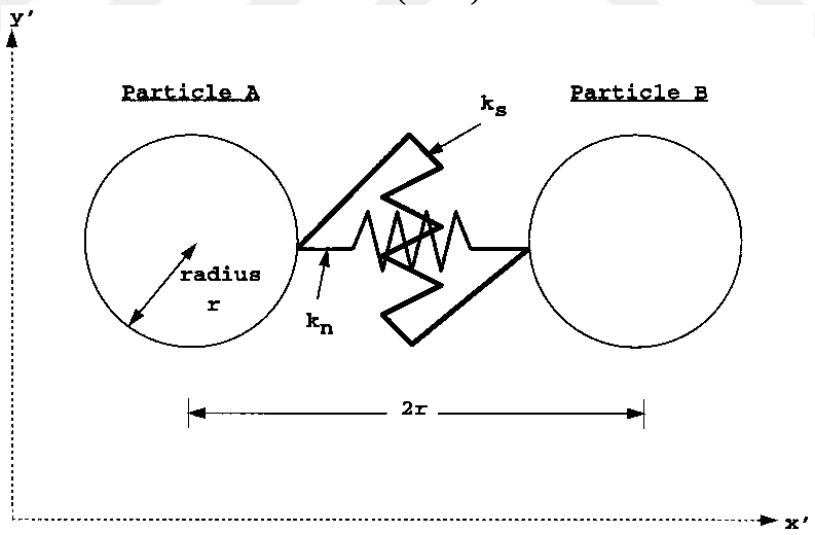
Parisi and Caldarelli (2000)



Liu et al. (2007)



Kinematics and statics of a beam



Griffiths and Mustoe (2001)

Figure 1.6. Lattice Modeling

Schlangen and Qian (2009) introduced a beam network with a brittle response. The model was used to simulate the uniaxial tension tests of cylinder specimens (Figure

1.7). Spherical particles with the different material models were embedded into the homogeneous material model (mortar) to create “model concrete”. Also, random material models distributed over the lattice domain were simulated for comparison. It should be pointed out that tensile fracture energy was not a parameter in that model, and even though it was considered at the local level later, the model could not capture the global tensile fracture energy value for direct tension simulations (Figure 1.7).

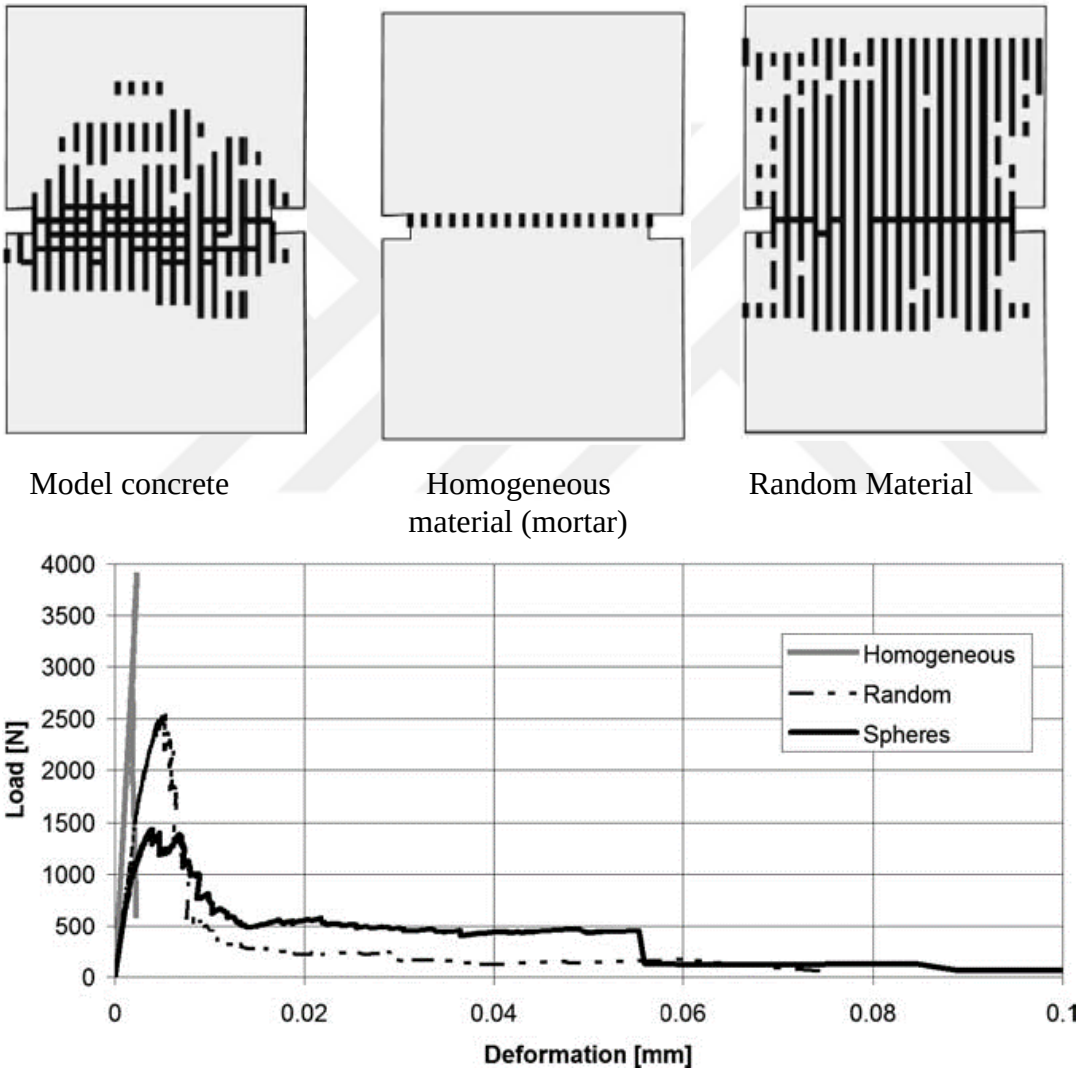
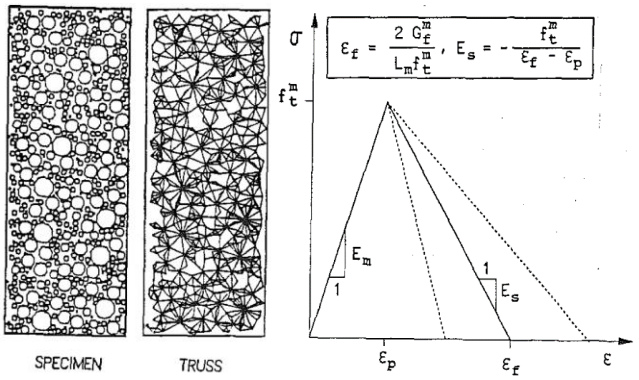
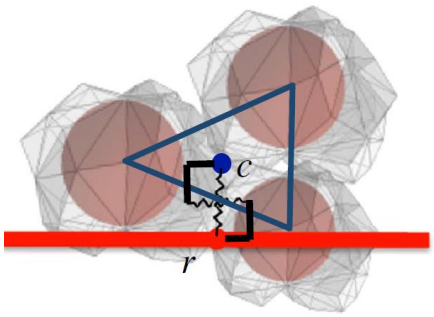


Figure 1.7. Crack Pattern for Direct Tension Simulations (Schlangen and Qian, 2009)

The nonlinear constitutive models have been employed for truss members in recent lattice models (Bažant et al. 1990; Schlangen and van Mier 1992; Jirásek and Bažant 1995) (Figure 1.8a). The approach of Cusatis et al. (2003) added a confinement-sensitive shear element in addition to the axial element and explicitly modeled aggregates, cement paste and interfacial transition zones separately with different material constants. Cusatis et al. (2006) later extended this approach to mixed-mode crack propagation in concrete. The developed model accounts for fracture and cohesion at the mesoscale. More recently, Cusatis et al. (2011a, b) proposed the Lattice Discrete Particle Model (LDPM) which basically integrates the confinement shear lattice and discrete particle models to replicate the connection of the coarse aggregate particles distributed all over the domain with mortar lattice elements (Figure 1.8b,c). Lu and Panagiotou (2013) developed a three-dimensional cyclic model for nonplanar reinforced concrete walls in which nonlinear Euler-Bernoulli fiber-section beam elements were used to represent steel and concrete in the vertical direction, and nonlinear truss elements were used to represent the steel and concrete in the horizontal direction and the concrete in the diagonal directions. A similar approach was followed by Moharrami et al. (2015) who presented a nonlinear truss model for the analysis of shear-dominated reinforced concrete columns subjected to cyclic loading. Most lattice models defined at the mesoscale use uniform spatial node/element distribution. Yip et al. (2005) developed a methodology that allows irregular lattice distribution and applied it to load balancing of prestressed concrete beam. Nagai et al. (2014) simulated the failure of anchorage bars using a three-dimensional lattice model using irregular lattice distribution. Although their model was defined at the mesoscale, the full geometry of steel bars was considered in the simulations. An application of lattice model to glass fiber-reinforced polymer beams was presented by Fascetti et al. (2016), who used a random lattice model to predict cracks pattern. It was claimed that random lattice models are less dependent on the mesh.



(a) Truss Lattice Model (Bazant et al. 1990)



(b) Lattice Discrete Particle Model (LDPM)

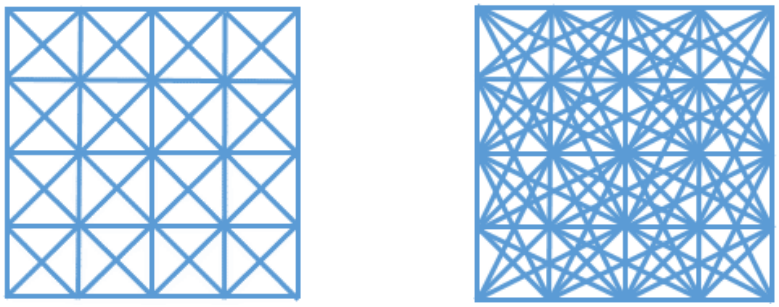


(c) LDPM for L11x30 Specimen

Figure 1.8. Nonlinear Lattice Modeling (Bazant et al. 1990) and Lattice Discrete Particle Model (Cusatis et al. 2011)

The recent work by Aydin et al. (2018) combined the horizon concept of PD with a classical lattice approach as a mesoscale concrete fracture simulation tool. In that study, the continuum was discretized with the overlapping lattices by employing simple rules for the force deformation response of the truss elements (Figure 1.9). However, the end result is dictated by the complicated connectivity and damage sequence of the truss elements. Being a mesoscale approach (i.e. an element size of the order of a few millimeters), the force-displacement responses of the concrete ingredients are needed to relate the meso- and macro-scale response. It is possible to model the mesoscale response of cement-paste, aggregates, and interfacial transition zone by using the overlapping lattice model (OLM). Despite its potential of capturing the crack propagation better within the cement paste, such an approach requires many parameters to be able to describe the geometry and mesoscale ingredients. Instead of attempting to link the mesoscale response to the concrete medium, an engineering approach was preferred, where the truss elements were assumed to have similar force-deformation response curves representing a homogenized continuum.

In this way, a more practical modeling approach capable of simulating concrete fracture with reasonable engineering accuracy was achieved for plain concrete members. Thus, homogeneous material properties were assumed to imitate heterogeneous material, i.e., concrete, so as to preserve practicality. Tensile softening parameters of the concrete lattice elements and bond elements were used to simulate plain concrete fracture. Tension calibration of lattice elements was conducted by matching the average response within characteristic length. The crack opening can be represented with strain-localization in this model similar to smeared crack model of FEM. The compression model is assumed as elastic. In short, the lattice model of Aydin et al. (2018) with a nonlinear tension and elastic compression model is shown to be a practical engineering tool to simulate direct and indirect tension failure under bending for concrete. Figure 1.9 shows the topology of the overlapping approach created by Aydin et al. (2018). However, the performance of this approach in compression remains unclear. Moreover, the validation problems were conducted for plain concrete and limited reinforced concrete members with no emphasis on reinforced concrete in detail. The approach will be reviewed in detail in the next chapter.



(a) $\delta = 1.5d$ (b) $\delta = 3.01d$

Figure 1.9. Lattice Approach Proposed by Aydin et al. (2018) with Different Horizons

In this literature section, the modeling approaches in different scales to describe the concrete response, their advantages and disadvantages were discussed. In addition to the element types used in these approaches, different constitutive models used in

these elements were also mentioned to describe the heterogeneous nature of concrete. The concrete material models in compression emphasizing the relation with the tensile response are discussed in the next section.

1.2.2.3 Concrete Material Models in Compression

All these explained models in different scales were used by many researchers to define complex response of concrete in compression, as explained based on experimental observation before. According to Iskander and Shrive (2018), the concrete compression models can be categorized into three groups: 1- Energy based fracture models (Kaplan, 1961; Glucklich, 1963; Hsu et al., 1963; Kendall, 1978; Sih, 1974; Wang and Shrive, 1995), 2- Stress based fracture models (Griffith, 1924; Lajtai, 1971; Dzik and Lajtai, 1996), 3- phenomenological compressive behavior models (Hognestad, 1951; Mirza and Hsu, 1969; Popovics, 1973; Collins and Mitchell, 1991). The third approach is the most popular choice for modeling concrete in compression for macro-scale engineering simulations due to its practicality. Reinforced concrete design guidelines (for example TEC, 2019; Eurocode 2, 2002) provide simple empirical relations between the tensile and compressive strengths of concrete. Hence, it is well-accepted that compressive failure is merely related to tension failure. However, this phenomenon has not been simulated successfully as few researchers attempted to simulate the compressive strength by using tension-only mesoscale material models (Schlangen and Qian, 2009; Qian, 2012, Roth et al., 2015; Wang and Waisman, 2016; Birck et al., 2016). For example, the beam elements in the network conducted by Schlangen and Qian (2009) have brittle behavior, and when the only tensile stress exceeds its strength, the elements break. However, a compressive failure for the interface elements was defined to obtain reasonable simulation results in compression for fiber concrete. The compressive capacity of the specimen would be considered an elemental strength in the later development of their model. Thus, it can be concluded that clear success has not been achieved in this regard.

1.2.3 Masonry Infilled Walls

Masonry walls are primary components of many historical buildings while the combination of walls made of masonry components such as aerated autoclaved concrete (AAC) is used worldwide to separate spaces in reinforced concrete frames in many structures and these components have similar mechanical characteristic behavior with cementitious materials. Infill walls are considered as non-structural elements in structural design; however, they improve the rigidity and lateral strength of the structural system. Past earthquakes (Van, Kocaeli, Bingol, Messina, Carlentini, L'Aquila, Wenchuan, Abruzzo, Northridge, Emilia Earthquakes) have shown infill walls may sustain considerable damage under moderate to severe ground motions. Nevertheless, the collapse of infill walls may create asymmetry in structures, might trigger heavy-damage and may cause loss of life. Significant degradation in structures' performance has been noted due to the infill wall damage (Penna et al. 2014; Braga et al. 2011; Vicente et al. 2012; Ricci et al. 2011; Binici et al. 2012). Hence, the performance limit states of infill walls should be predicted accurately.

Infill walls are generally not included in the analysis and design of frame buildings. This practical approach ignores the interaction between the infill walls and the frame. The observed damage on the infill walls after the earthquakes indicates that the energy absorption and the contribution of the infill walls to the lateral load-carrying capacity can be significant. Understanding the frame-infill interaction has been the subject of numerous studies since the 1950s (Polyakov 1950), including experimental studies (Klingner and Bertero 1976; Smith 1966; Asteris et al. 2011; Alwashali 2019) and analytical investigations (Asteris 2003; Papia et al. 2003; Cavaleri et al. 2009; Mohebkhah and Tasnimi 2012). However, the interaction could not be fully understood due to the dearth of detailed simulations and the presence of several parameters, such as the mechanical properties of mortar, the wall geometry, and the space between the frame and infill affecting the prediction of the response

(Tarque et al. 2015). Hence, explaining the force flow over the infill walls is necessary in order to define the effect of walls on global response.

1.2.4 Numerical Modeling for Infill Walls

Macroscale, mesoscale and microscale models were also used to model the infill wall behavior. The generally used macroscale model is placing one or more struts for the walls (Polyakov 1960; Chrysostomou et al. 2002; El-Dakhakhni et al. 2003; Galli 2006; Amato et al. 2008; Kadysiewski and Mosalam 2009; FEMA 356 2000) (Figure 1.10a). The contact regions between the frames and the infill walls are assumed stationary at the corners in most of these models. The key disadvantage of these models is the difficulty of estimating strut properties. The existing strut models in American (MSJC 2011) and Canadian (CCMPA 2009) codes cannot accurately predict the rigidity, strength, and ductility properties of infill walls, as shown by Turgay et al. (2014). Furthermore, strut behavior becomes unpredictable when openings in the wall. The strut-based macro models do not provide information on the local behavior, interface opening and cracking.

In order to overcome these deficiencies, finite element models (FEM) were employed by many researchers in micro and mesoscales (Mehrabi and Shing 1997; Mosalam et al. 1997; Sutcliffe et al. 2001; Asteris et al. 2013; Milanesi et al. 2018; Fenerci et al. 2016) (Figure 1.10b). Two different finite element approaches were employed, in which the wall units (brick, autoclaved aerated concrete (AAC) and mortar) were either modeled separately (microscale) or homogenized (mesoscale) (Lotfi and Shing 1994; Giambanco and Di Gati 1997; Gambarotta and Lagomarsino 1997; Oliveira Lourenço 2004; Alfano and Sacco 2006; Fouchal et al. 2009; Pari et al. 2021). While they can provide a more realistic response estimation for crack propagation and damage patterns, the pre- and post- processing difficulties due to the interface elements between individual bricks, computational inefficiencies and limited applications in practice are major drawbacks (UDEC 2004). Calibration of the mesoscale constitutive models involving a combination of different elements and

description of the interaction region are significant challenges for these classes of models (Negro and Colombo 1997). Also, the finite element methods are incapable of representing the response of different parts together after loading (Mohebkhah et al. 2008). Although the interface elements are used to handle a few discontinuities in the FEM at micro-scale, the model is not able to model a large number of them.

Discrete element method (DEM) is another micro-scale approach to modeling the infill walls (Figure 1.10c). The model, firstly proposed by Cundall (1971) as UDEC (Universal Distinct Element Code) software, was used in rock mechanics (Chrysostomou and Asteris 2012) and masonry structures (Barbosa and Ghaboussi 1990; Dialer 1992; Lemos 2007; Sarhosis and Shen 2014). In this method, the blocks are connected with mortars and interfaces. Thus, DEM has a similar conceptual structure to the micro-scale FEM concept with small differences. However, the model is capable of changing contact size and contact mapping, unlike FEM. Hence, larger number of discontinuities can be modeled with the mortar and interface elements.

Particle-based and lattice simulations were proposed in the last few decades to overcome the disadvantages of FEM to estimate the fracturing and damage for concrete and RC structures in micro and mesoscale, as mentioned. The application of LDPM developed by Cusatis and co-workers (Cusatis et al. 2011a,b) for concrete and RC members was explained before. They also utilized the model to simulate mortar (Pathirage et al. 2019; Han et al. 2021), masonry and masonry interaction with mortar (Angiolilli et al. 2020; 2021; Mercuri et al. 2020) with a good accuracy in order to simulate multi-materials and multi-material domains (i.e., masonry) as a particle-based model. On the other hand, the application of lattice models for multi-material domains is very limited (Rizvi et al. 2018). Modeling the anisotropic behavior of masonry units and multi-material media with a lattice network is the key difficulty in these models.

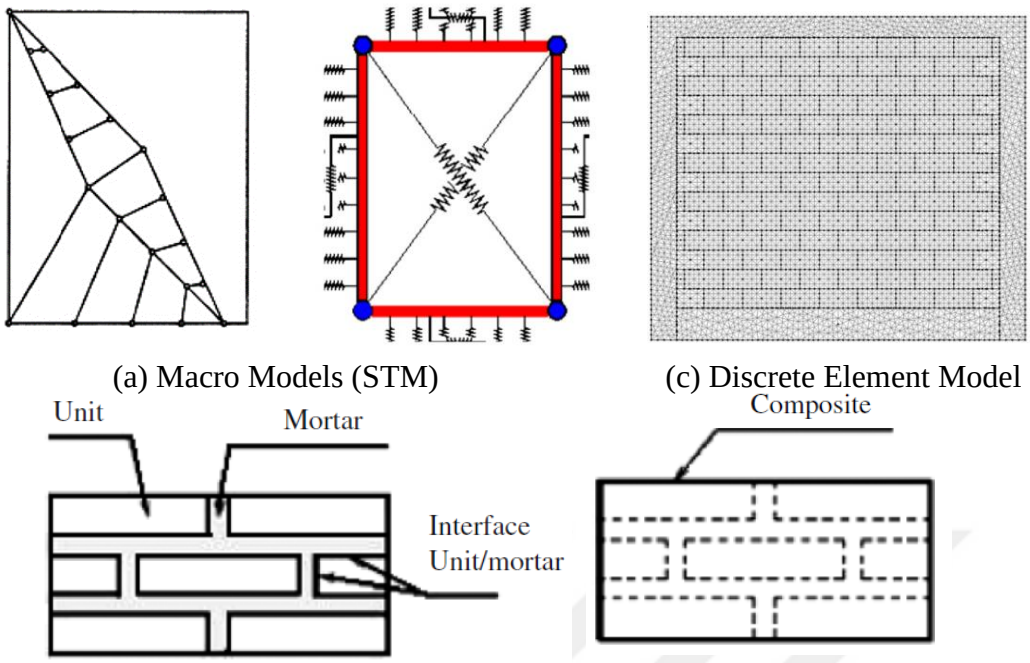


Figure 1.10. Numerical Modeling for Masonry Elements

The aforementioned models are generally used for brick-type walls by introducing anisotropic or isotropic behavior since such walls are widely used. On the other hand, AAC is used increasingly for both structural and nonstructural purposes due to the insulation, fire resistance and its light weight. The glue used to contact the AAC units is generally stronger than the AAC blocks so the AAC masonry walls exhibit strong continuity. None of the lattice models mentioned above was utilized for the application of AAC masonry and infilled walls in the literature, considering the inherent strong continuity due to the strength of glue. More experimental studies and numerical simulations should be implemented to exhibit the characteristic properties of the materials used in AAC walls for such a new infill material due to limited experimental and numerical results.

1.2.5 Nonlinear Solution Schemes

Prediction of limit states due to cracking requires complex nonlinear analysis. The solution is required for static and dynamic loads. Newton-Raphson and arc length methods in addition to many different types of static solutions are commonly used to aid with the convergence problems for quasi-brittle materials in static loading. On the other hand, convergence problems can be overcome by using techniques like sequentially linear analysis (SLA) (Rots 2001) always yielding positive stiffness. This technique (Rots 2001, Rots et al. 2006, 2008) was employed with the PD methodology to simulate plain concrete fracture by Aydin et al. (2018). As the technique uses the ratio of the strength and governing force to find the multiplier of the applied external unit load, it is not able to simulate non-proportional loading, the general case of loading in structures, efficiently (Pari et al. 2020). Almost every loading patterns are non-proportional in real life. The most famous one is the dead load which is obtained for every structure. Extensive work was proposed by many researchers to handle this restriction (Dejong et al. 2008; Yu et al. 2016; Alfaiate et al. 2018), however, it is still an open issue.

For prescribing dynamic loads' equilibrium, explicit and implicit time integration can be used. With a very slow loading rate to vanish inertial forces, these techniques can be used to solve the nonlinearity in static load cases. The performance of these two time integration methodologies is different for specific problems, with different computational costs and stability issues. Although the critical time step limitation is the most important disadvantage of the explicit time integration technique, it generally provides a fast solution. For many different cases, explicit solution scheme was recommended for the solution of nonlinear material properties for quasi-brittle materials due to its advantage of no instep iterations (Yang 2019).

1.2.6 Motivation of Research

The current state of the art has a large number of sophisticated models (such as finite element modeling with smeared or discrete cracking, particle-based and lattice approaches with aggregate-cement paste-ITZ modeling or wall units, mortar, interface modeling) and simpler design oriented approaches (i.e strut and tie models) to replicate the behavior of concrete and masonry wall members and structures as explained above. Lattice models are well suited for simulating nonlinearity; however, their use was very limited in the modeling of fracture of plain concrete and infill structures. In this sense, a simple modeling technique based on latttice model, that can exhibit good engineering accuracy with minimum number of input parameters, is still needed.

In addition, while the inter-story drift limits are given in the codes to examine performance limit states of infill walls, the damage limit states are not detailed for both fragile and deformable components. Thus, estimating damage limit state of infill walls at different deformation levels is essential. In this context, the lattice model should be improved to simulate such responses.

In the light of information from many research studies, the outcomes demonstrate that the main focus to represent the damage for quasi-brittle materials is shifting to particle and lattice-based models. The lattice model proposed by Aydin et al. (2018) is an effective and efficient approach, with a good prediction of the actual crack patterns and response for plain concrete with tension-only modeling strategy. The model has not been tested for reinforced concrete members, structures, masonry and masonry-infilled wall applications; the performance of the model in compression is limited. As the solution technique is based on SLA method, it cannot be used for non-proportional loading. Thus, a robust solution methodology should include solution of nonlinearity for quasi-brittle materials for the lattice model in this study.

1.3 Objective and Scope

The main goal of this study is to propose an effective but relatively simple methodology to simulate non-linear response of RC and AAC-infilled frame structures under monotonic loading. The objectives of the study are given as follows:

- To propose a simple lattice model for simulating nonlinear behavior of concrete and AAC masonry walls with calibrated constitutive models
- To implement novel proportional-integral-derivative (PID) algorithm instead of SLA method into explicit time integration methodology
- To demonstrate the compression failure in lattice approach as local material instability induced by splitting due to indirect tensile failure
- To show compression failure with tension-only behavior for concrete and AAC masonry walls
- To validate the proposed model for prediction of crack propagation and response in RC members and structures with different horizon sizes.
- To validate the robustness of the model by investigating the uncertainties in the model
- To investigate the effect of interaction behavior and wall openings on the global response of two AAC infilled frames tests
- To validate the model for crack propagation and response in AAC-infilled frames (bi-material)
- To study the contact behavior for different aspect ratios of infilled frames as a function of lateral deformation

The two-dimensional (2D) mesoscale truss-based lattice approach to simulate the plain concrete, RC, AAC masonry members, and structures and AAC masonry infilled frames (bi-material) response by using an explicit time integration analysis scheme with proportional-integral-derivative (PID) control tailored for monotonic loading excluding any cyclic damage rules is employed. Explicit time integration methodology with novel proportional-integral-derivative (PID) algorithm instead of SLA method has not been implemented into the lattice framework by any researcher.

One of the important goals of the present research is to explain the concrete and masonry compression response as an indirect tension failure by using tension-only plasticity with mesh randomization. The length scale and grid dependency of the model are investigated numerically. The accuracy of the hypothesis is validated with the compression strut and over-reinforced concrete beam experimental results.

The validation studies on RC structures presented herein include three columns, two beams, two walls, and two RC portal frames tested previously by other researchers. Upon presenting the results on the comparisons of simulation and test results, a parametric study including deterministic sensitivity analysis, loading rate and grid rotation effects were conducted in order to present the feasibility of the model for RC simulations. It is aimed that the truss-based lattice approach with the extensive calibration techniques is introduced to estimate flexural and shear crack propagation, crack widths and spacing, unconfined compression failure with tension-only modeling, load-deflection response and capacity demands for such members and structures as a practical simulation platform.

The proposed lattice network has a great potential to simulate AAC infilled wall structures as well as a practical and easy-to-implement, enabling modelling of the strong continuity exhibited by the AAC masonry walls. The lattice models of four unreinforced AAC masonry-infilled RC frames was developed. A consistent modelling approach employing bi-material idealization in the lattice models for AAC and concrete with a special emphasis on the interface between these materials was used. Two single-bay and single-story half-scaled AAC-infilled portal frames were tested in Middle East Technical University's structural laboratory to investigate the effect of interaction behavior and wall openings on the global response by comparing the lattice simulation results and to validate the proposed approach along with the two additional frames taken from the literature (Binici et al. 2019; Penna and Calvi 2006).

The scope of the study is limited to simulating the monotonic response and load-deformation characteristics of RC and infill structures by using a lattice model in

two-dimensional domain. In this context, the goal was to develop a two-dimensional practical modeling tool that can be used by practicing engineers interested in obtaining the response of structures under distress.

The study is organized as follows. After this introductory section, the details of the lattice model are explained in Chapter 2. Concrete, RC and bi-material modeling are discussed in detail. A demonstration of compression failure as an indirect tensile failure and validation of these findings is presented. In Chapter 3, the validation of the lattice model for several structural experiments in literature for both RC members and structures is presented. In Chapter 4, details and results of two AAC-infilled frame tests are shown followed by contact length estimations for different aspect ratios compared with the existing analytical formulations. Then, the corresponding lattice model is presented. Finally, in chapter 5, conclusions are drawn.

CHAPTER 2

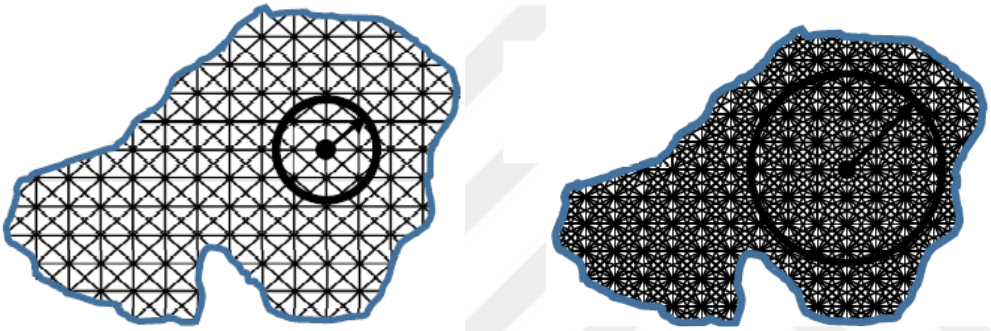
MATERIAL MODELING WITH LATTICE NETWORKS

In this chapter, the lattice approach used in this study is explained in detail along with the constitutive model calibrations. The model for tension by using a multilinear piecewise softening function is introduced. The perturbation of the mesh to model the compressive response with tension-only failure is discussed. The failure approach is validated with simple material tests. The model is described in this section in terms of its geometric and elastic properties, nonlinear tension and compression modeling constitutive models and definition of its parameters utilized with calibration, validation studies of compression modeling, bond and reinforcement implementation and bi-material behavior and static and dynamic loading solution scheme.

2.1 Lattice Topology and Nodal Interaction

Nonlocal theories consider the effects of long-range interactions in solid materials. Their applications to problems of solid and fracture mechanics have been studied in depth by Kröner (1967), Eringen (1992), and Kunin (1982). It is a challenging issue to define fracturing for the classical continuum theory which evolves from partial differential equations, resulting in singularity at crack surfaces. Instead, constitutive relations are typically written in an integral form which can be expanded in a series of spatial derivatives of strain accounting for gradients and higher gradients of strain. The term ‘nonlocal’ indicates that stress at a point depends on strain as well as gradients of strain at the same point. In order to acquire nonlocality for particle and lattice-based models, peridynamics theorem proposed an interaction pattern in the domain called as horizon concept which allows accounting for the nonlocal effects in the medium, i.e., the effect on a point from the immediate surrounding points. A

similar concept is employed for the presented lattice model in this study. Each node interacts with the points within a predetermined distance called the horizon (δ). In the two-dimensional lattice model, a structured grid is created with uniformly distributed nodes separated by a certain grid size (d) in the two directions (Figure 2.1). The connected points are those within a circle for a selected horizon distance (δ) as shown in Figure 2.1. For example, a node located away from the boundaries is connected to 8 and 28 nodes for horizon values of $1.5d$ and $3.01d$, respectively for the two-dimensional models. The lattice with a horizon of $1.5d$ corresponds to the classical lattice geometry of Hrennikoff (1941).



(a) Horizon (δ) = $1.5d$ (b) Horizon (δ) = $3.01d$

Figure 2.1. Lattice Model for (a) δ = $1.5d$ and (b) δ= $3.01d$

In the model used in this study, unstructured grid distribution was also used to perturb the lattice grid by R between zero and R_{max} at a random angle of θ (Figure 2.2b) between zero and 360 degrees both with uniform probability distributions in order to exhibit compression failure, which is explained in Section 2.5 in detail. The perturbation of the mesh is employed only for the δ=$1.5d$ in this study.

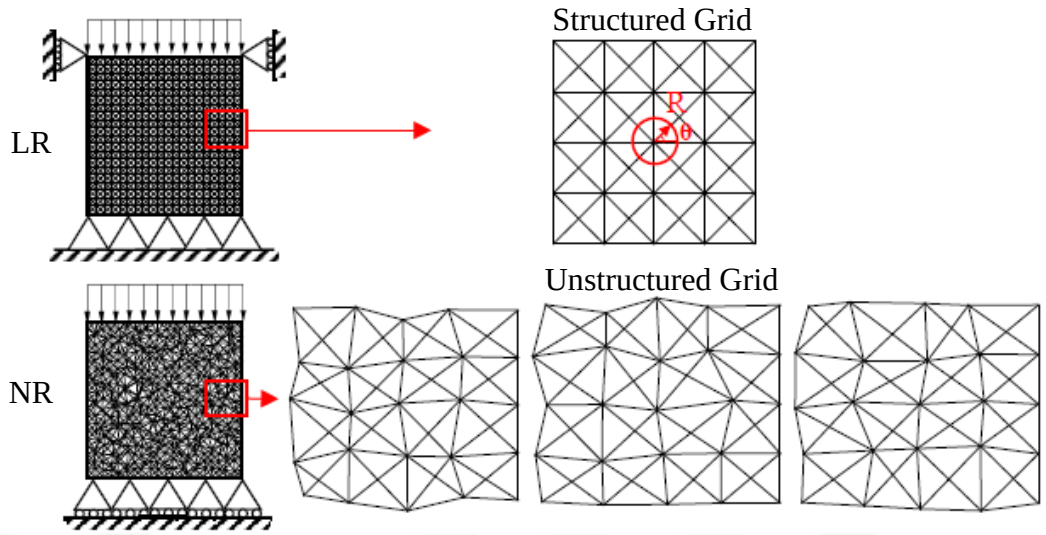


Figure 2.2. Topology of Lattice Model for (a) Boundary Conditions and (b) Grid Types

The interaction type of the nodes in the horizon region is the main concern in peridynamics such that bond-based peridynamics are related to node-to-node interaction instead of volume-to-volume as opposed to state-based, as mentioned before. In bond-based peridynamics, the force between two nodes is acting axially, and nodal equilibrium is considered. In fact, classical two-node truss elements are employed in the lattice model between the nodes to treat the interaction forces as a classical structural analysis similar to the bond-based peridynamics of Macek and Silling (2007). Each point is initially connected to all points within its horizon via truss elements which can only transfer axial load. In other words, only translational degrees of freedom at the nodes were utilized since the presented lattice model is composed of a truss network, which means the elements in the model are only able to transfer load effect via axial deformation. The shear transmission and rotation in a region is available for a lattice unit rather than a single element. While the diagonal elements provide the shear resistance, rotation is represented within the mesoscale translational motions. The shear and rotational degrees of freedoms are mimicked with only translational motions thanks to the topology of the lattice unit. In short,

only translational motion is utilized for each element while shear transmission and rotation in a region are available for a lattice unit rather than element-wise. At the boundaries, the lattice does not have the same mesh density as the inside region when the horizon is greater than $1.5d$. However, one should not expect the same stiffness at the boundaries due to local weaknesses. Each node with a lumped mass is connected to the neighboring nodes within its horizon via truss elements.

2.2 Elastic Properties

In order to obtain the elastic properties of the lattice model, the total elastic energy of the system subjected to a uniform strain field is equated to the total elastic energy of the lattice model and the modulus of elasticity times the cross-sectional area of truss elements ($E_t A_t$) is determined. Further detail was explained in Aydin et al. (2018). For different horizons, $E_t A_t$ values can be obtained in closed form. For this purpose, first strain fields in both regions (i.e. ε_x and ε_y) are introduced. Following Hooke's Law and assuming same stresses in both directions strains can be found as:

$$\varepsilon_x = \varepsilon_y = \varepsilon = \sigma\left(\frac{1-\nu}{E_t}\right) \tag{2.1}$$

Then the energy stored in the region can be written as:

$$\int \frac{\varepsilon_x \sigma_x}{2} + \frac{\varepsilon_y \sigma_y}{2} dV = \int \frac{\varepsilon\sigma}{2} + \frac{\varepsilon\sigma}{2} dV = \varepsilon\sigma w A = \varepsilon^2 \left(\frac{E_t}{1-\nu}\right) wA \tag{2.2}$$

where w is thickness and A is the volume per unit thickness area with wA being the volume. This total elastic energy must equal to the total strain energy stored by the considered lattice elements as given below:

$$\sum_{i=1}^{n} \frac{1}{2}\left(\frac{{N_i}^2}{2E_t A_t} L_i\right) = \frac{E_t A_t \varepsilon^2}{4} * \sum_{i=1}^{n} L_i \tag{2.3}$$

Where N is axial force in the element, L is the length of the element and n is the number of element in the region. Equating Eqs. (2.2) and (2.3), one may find the elastic properties of the lattice elements.

$$E_t A_t = \frac{4E_t A w}{(1-\nu)\sum_{i=1}^{n} L_i} = C\, E_t d w \tag{2.4}$$

It is noted that ν is 1/3 for 2D lattice mesh (Hrennikoff 1941) and A can be taken as d^2. The difference in $E_t A_t$ values for lattice models with different horizon values between the horizon sizes results from the summation term in Eq. (2.4). For a horizon value of $3.01d$, 28 elements are connected at a node with the lengths of d, $d\sqrt{2}$, $2d$, $d\sqrt{8}$, $3d$ (4 elements each) and 8 elements with the length of $d\sqrt{5}$. For a horizon value of $1.5d$, a node has 8 elements consisting of 4 elements with the length of d and $d\sqrt{2}$. By using these lengths, the C values are observed as 0.102 and 0.621 for $3.01d$ and $1.5d$ horizons, respectively. Thus, for horizon values of $3.01d$ and $1.5d$, it can be shown that $E_t A_t$ can be obtained in closed form as $0.102E_t dw$ and $0.621E_t dw$, respectively. In addition, it should be clarified that the same elasticity modulus for tension and compression was used to preserve isotropy.

The Poisson's Ratio values were computed for two different horizons (1.5δ and 3.01δ) of the square grid and hexagonal grid (honeycomb) in order to investigate the change of Poisson's Ratio based on the axis of rotation (Figure 2.3). It can be seen that the rectangular grid with a horizon of $1.5d$ does not produce a constant Poisson's Ratio upon rotation of the deformation axis. The Poisson's ratio of a truss-based square lattice mesh with $1.5d$ horizon changes between 0.26 and 0.42 depending on the rotation of the loading axis. The axis of rotation versus the computed Poisson's Ratio plot is shown in Figure 2.3. It should be noted that despite the possible change in the Poisson's ratio, the change in shear modulus is only in the order of 10%. Upon increasing the horizon to $3.01d$, the Poisson's ratio varies between 0.31 and 0.35 and it can be considered as about 0.33 irrespective of the direction. Choosing the horizon value as $1.5d$ significantly decreases the number of truss elements and speeds up the computations at the expense of creating directional dependency. As

shown by Gerstle (2015), the truss-based hexagonal lattice model performs as expected yielding a Poisson's Ratio of 0.33 irrespective of axis rotation (Figure 2.3). In addition, varying Poisson's ratio can be obtained, as shown by Rahman (2012) and Aziz (2014), and Gerstle (2015), by using the beam elements. However, using beam elements results in much more computational effort in addition to the other disadvantages. The reason for selecting only axial interaction in this study instead of employing rotational behavior in mesoscale with square mesh is discussed in detail in section 2.3.

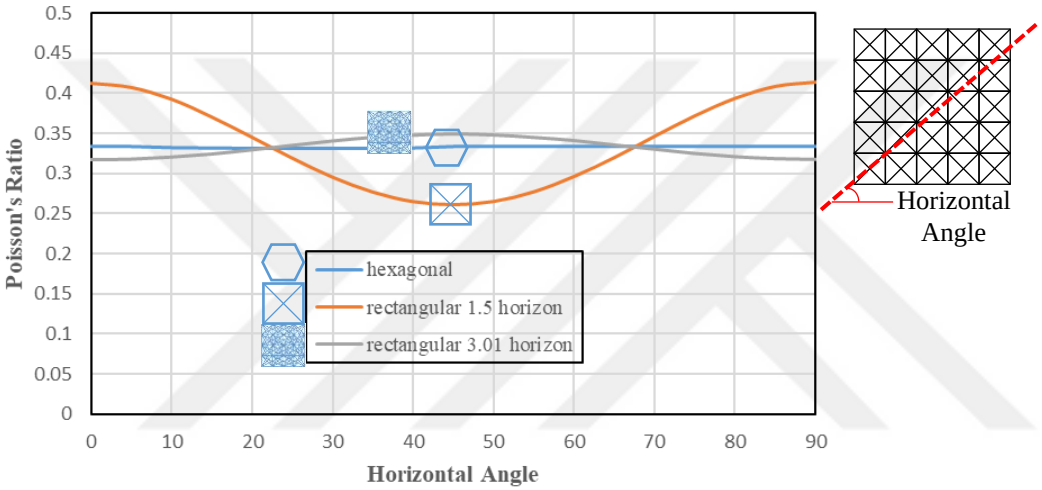


Figure 2.3. Poisson's Ratio Variations

2.3 Justification of the Approach

A square truss network with different horizon distances were employed throughout the study because of the following reasons: i- A square grid truss network is easily applied from the point of view of mesh generation, programming, and runtime. ii- The increasing of the horizon distance allows approaching the theoretical Poisson's Ratio of 0.33 for the lattice models. iii- There is vast amount of experience in modeling reinforced concrete members with strut and tie models with a rectangular truss network at macro scale (Schlaich et al. 1987; Liang et al. 2000; Scott et al. 2012). Hence engineers are used to defining load transfer with truss elements. iv-

Upon using a rectangular lattice grid, reinforcement definition is simplified, since the reinforcement is usually placed vertically or horizontally in RC simulations. v- Lattice mesh structures with number of edges more than four (such as hexagonal mesh) would contain unequal number of horizontal and vertical lattice elements that may introduce direction bias in the nonlinear compression regime. vi- With a square grid, mesh boundary zigzags can be avoided naturally and it allows modeling of the straight boundaries with ease.

It should be clarified that although the mesh density decreases at the boundaries when the horizon size is greater than $1.5d$, thanks to the square grid and availability of adjusting the horizon distance, this effect could be reduced and consequently, it does not have any unexpected deformation effects at the boundaries.

Estimating the linear elastic behavior accurately in an objective manner is quite important from a mechanics point of view and such an estimation plays a crucial role in predicting the response of structures under serviceability conditions. However, it is of secondary importance while estimating the near collapse state (i.e., strength and deformation capacity) of structural elements in the nonlinear regime. The Poisson's ratio of concrete, although initially starts from about 0.2, rapidly changes upon cracking and damage accumulation. The variable nature of Poisson's ratio in the nonlinear response beyond about 30% of its compressive strength was shown experimentally by Kupfer et al. (1969) and Mirmiran and Shahawy (1997), among others. In this regard, a number of variable Possion's ratio models were proposed in the literature (Blacklock and Richard 1969; Binici 2005; Lim and Ozbakkaloglu 2015). Based on these studies, although important (Rahman 2012), adherence elastic Poisson's ratio is not treated as a prerequisite to simulate concrete fracture and damage state at high deformation demands in this study. The following arguments could be put forward to justify the simple lattice approach of this thesis;

i- With this perspective, the proposed lattice approach can be placed in the class of simple models (i.e. strut and tie, truss, bond-based peridynamics, spring network models) that are widely used in structural engineering. These models have seen wide acceptance in the engineering community and they cannot match the Poisson's Ratio.

ii- Increasing the model complexity to match the Poisson's Ratio may hinder the wide spread use of the model by the engineers. This argument is supported by the following statements from Cusatis (2011) and Nikravesh and Gerstle (2018):

"The full Poisson's ratio range can be obtained by introducing the volumetric/deviatoric decomposition of the normal component. The same approach could be used for Lattice Discrete Particle Model (LDPM)-type formulation; however in this way, the LDPM capability of correctly simulating splitting failure under compression (this being one of the unique features of LDPM) would be completely lost." (Cusatis 2011)

"While we recognize that the State-Based Peridynamic Lattice Model (SPLM) is not absolutely objective in the sense of tensor mathematics and continuum mechanics, the SPLM approach "exploits an engineer's tolerance for imprecision" (to paraphrase a quote by Zadeh [Zadeh (1973)]. It is reasonably objective, is physically realistic, and is more computationally efficient than other computational models presented in the literature of which we are aware" (Nikravesh and Gerstle 2018).

It is well known that simpler strut and tie models, which have common properties with the presented lattice model, are in design codes, however state-based peridynamic models are still not used by practicing structural engineers.

iii- The proposed model, although not matching the Poisson's Ratio in the linear elastic range, is robust and insensitive to modeling in the nonlinear range as shown in Section 3.1.4.1.

iv- Despite significant change in Poisson's Ratio, the change in shear modulus is only in the order of 10%, as mentioned.

In short, the proposed model is not claimed to be perfectly valid within the range of linear elastic behavior until collapse; but rather a simple engineering approach that can approximate the response with reasonable accuracy is devised. In addition, simulating the nonlinear response of reinforced concrete elements with the lattice approach, which will be shown to be one of the key topic of the paper, is insensitive to estimating the Poisson's Ratio with a high degree of accuracy as shown by the case studies in the study.

Each mathematical model should be evaluated with its accuracy and complexity. The lattice model developed in this study is simple with few parameters, not capable of perfectly matching the Poisson's Ratio perfectly however it can simulate the nonlinear response with a reasonable degree of accuracy. On the other hand, the state-based approach is more complicated: it can match the Poisson's Ratio and depending on the choice of numerous parameters it is capable of simulating the nonlinear response with the appropriate choice of many non-linear response parameters (i.e., shear, tension, compression and combined loadings). The peridynamic literature has constantly been growing in the last decade and a major part of it is still employing bond-based models, as mentioned before. It can be stated that the application area of bond-based models is not likely to disappear in the near future as its applications for polymers, glass and other brittle materials grow.

2.4 Tension Modeling

The force in the truss elements is assumed to behave linear elastically until the critical strain ε_{cr} is reached. The complicated connectivity of the lattice network along with the computed damage sequence enables the simulation of crack propagation with few parameters. As concrete exhibits tension softening, beyond a critical strain, the element can transfer further tension by a piecewise linear softening function as shown in Figure 2.4. Although an exponential softening function seems to be more practical, a trilinear force-displacement function was preferred owing to the flexibility offered by it while matching the "exact" force-displacement relationship in tension by adjusting the tension softening parameters. Detailed comparisons of the lattice model with experimental data were presented in and earlier publication based on the master thesis of Aydin (2018). The unloading rules are origin oriented for the tension model as shown in Figure 2.4. The stress-displacement model of Hordijk (Cornelissen et al. 1986) is employed as the "representative" test result for the softening part. The parameters, a_1, a_2 and a_3 of the uniaxial tensile behavior are free parameters and found such that lattice simulation matches the

uniaxial stress-average displacement response of the Hordijk Model. The Hordijk's Model directly provides the stress ($\sigma(\delta)$) - crack opening displacement (δ) relationship and the tensile fracture energy as a function of maximum crack opening displacement (δ_{max}) and tensile strength (f_t) with the equations given below:

$$\sigma(\delta) = f_t\left(1 + 3\left(\frac{\delta}{\delta_{max}}\right)^3 \exp\left(-6.93\left(\frac{\delta}{\delta_{max}}\right)\right)\right),\ \delta_{max} = 5.136G_f/f_t \qquad (2.5)$$

While using the Hordijk Model, the tensile fracture energy and tensile strength were used to compute the ultimate crack opening displacement. In order to use the Hordijk Model as a benchmark result for the average stress-displacement relation measured over a gauge length (l_o) with given tensile strength and tensile fracture energy and tensile strength, first δ_{max} was computed from the above equation from the tensile fracture energy G_f, and tensile strength f_t (Aydin et al. 2018). Afterward, the average displacement was computed by adding the δ to the elastic displacement occurring over l_o i.e. $\delta_e = \frac{\sigma(\delta)}{E} l_o$, which means the crack opening displacement was added to the elastic displacement occurring over the selected gauge length to obtain the benchmark stress-average displacement curve. In this way, a general solution for any gauge length could be obtained. This inverse method of finding the model parameters was preferred over the approach of assigning the Hordijk model directly to the lattice elements. Because the computed crack could be spanning more than one lattice element at different orientations and the dissipated energy is not known as a priori. The flowchart of the concrete tensile constitutive model calibration, a sort of inverse analysis, is shown in Figure 2.5. In the process of softening parameter calibration, the tension test of a specimen is simulated and the parameters are adjusted until the energy error is reduced below a threshold value. This calibration procedure for concrete lattice elements was conducted prior to all simulations described in this study. Then, simulations of the test specimens as can be seen in validation sections were conducted as blind predictions with the calibrated parameters rather than post-dictation.

The energy under the stress-strain diagram is regularized by using the element size and the fracture energy concept (Bažant and Oh 1983). Isotropic behavior on tensile fracture energy was obtained by utilizing constitutive models of elements based on their lengths. Thus, the crack propagation in any direction can be obtained objectively. The softening parameters are based on the displacement instead of strain values so that the necessary energy to open a unit area of crack of all elements is kept constant. This means that the area under the stress displacement curve should be the same for all elements over the domain. This tensile fracture energy regularization approximately enables the model mesh independent and robust as can be seen at validation problems.

AAC masonry walls indicate uniform behavior because of their strong glue so that strong continuity is obtained. Thus, an isotropic response can be simulated in the same manner as the concrete element. In this study, AAC stress-strain behavior is similar to concrete elements obviously employing its own material properties. Detailed discussion is in section 2.8.

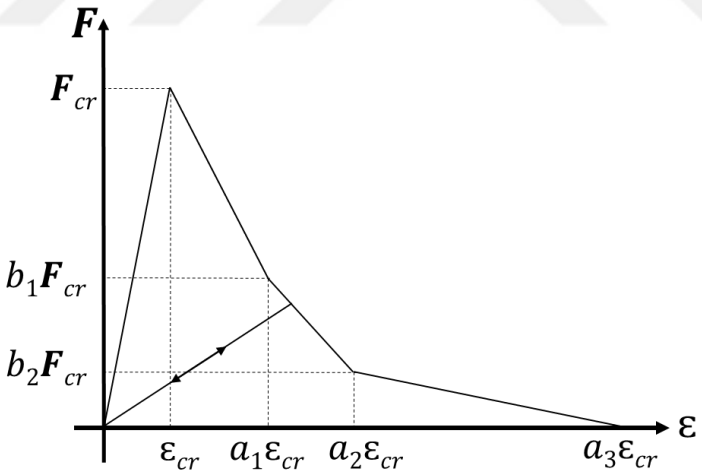


Figure 2.4. Assumed Material Behavior Force-Strain Diagram for Concrete Elements

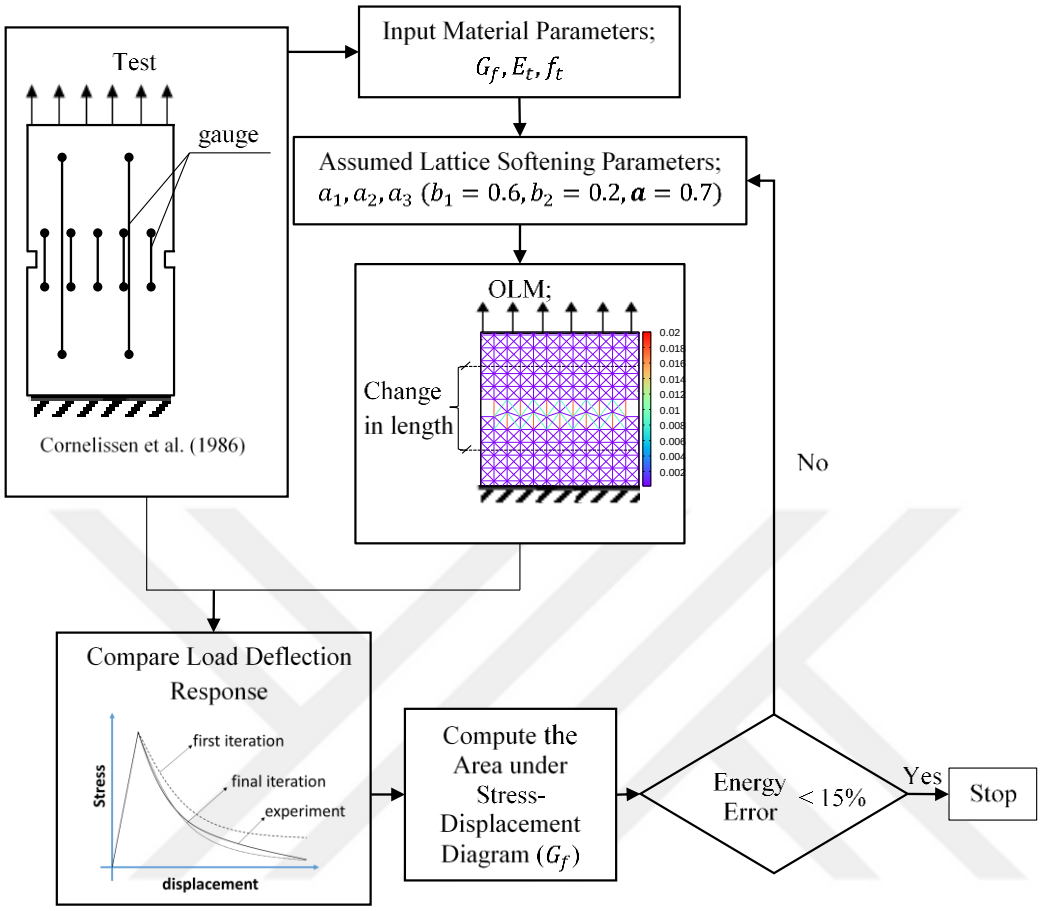


Figure 2.5. Workflow for Constitutive Model Calibration for Only Tension (Test Specimen Drawn Using Data from Cornelissen et al. 1986)

2.5 Compression Modeling

Concrete compressive strength is a key material parameter for the design and analysis of reinforced concrete structures. Past research and current practice usually consider the modeling of concrete behavior in uniaxial compression empirically based on test results. In this section, a lattice modeling approach with only nonlinear tension-softening and linear elastic compression behavior was developed to demonstrate that the compressive failure (strength) is merely an indirect tensile failure followed by material instability. Perturbation of the grid distribution is

described to overcome compressive locking problem of structured grid topology. Finally, the validity of such a modeling was tested in the comparisons of simulations with concrete and AAC masonry test results. Uniaxial compression simulations were performed to investigate the relationship between tensile and compressive strengths.

2.5.1 Compression Response

It is very challenging issue to understand the reason of nonlinearity in the compression of quasi-brittle material such as concrete. Nonlinearity is associated with fracturing behavior, rather than compressive crushing (Schlangen and van Mier 1992). This fracturing was explained in different aspects by many researchers so that splitting cracks and cover spalling due to compression can be considered as a result of instability of local area (Kendall 1978; Bažant et al. 1993; Bažant and Xiang 1997). The focus of the current research is not only the fact that compressive strength is merely an indirect tensile failure followed by material instability, but also this phenomenon was simulated by using only nonlinear tensile modeling while the compressive response is modeled as a linear elastic material. There exist no defined compressive constitutive model of elements but linear, as mentioned. Although there are many studies stating this fact, only a few numerical simulation studies were able to simulate compression failure without using a phenomenological model for the compression response.

It is important to understand the regions of the uniaxial load-deflection curve of concrete in compression (Figure 2.6a). Linear elastic response up to 30-40% of f_c, where stiffness does not change, implies that there exists no cracks or very micro-cracks formed at the weakest parts such as ITZ. Elastic rigidity begins to change when the micro-cracks start to occur. At the beginning of the nonlinearity of the stress-strain relationship, since the number and width of micro cracks are few and small, a stable cracked system exists. After cracks are observed in the matrix and the micro-cracks join with each other to form macro cracks, and the specimen becomes rather unstable. Failure is obtained due to rapid propagation of the cracks in the

matrix and transition zones, rapid increase in the strain and unstable crack system. While the splitting cracking is observed with increasing uniaxial compressive loading in the first stage, the major cracks are obtained at the end.

The failure in compression is usually named as crushing at the macro level but it is actually a splitting induced failure mode in the micro-scale Figure 2.6c,d. Vertical cracks resulting from splitting motion are obtained due to radial stresses in uniaxial compression response. Thus, the compression capacity is connected with the loss of the stability. Also, the softening can be attributed to the lateral instability of the specimen. This complex behavior can be related to the tensile response indirectly.

The cracking response in uniaxial compression tests is highly affected with end zone conditions. While the vertical cracks are observed if the end zone effect is eliminated, the lateral load due to restrained condition at the ends causes the diagonal cracks. Also, the end condition influences the load-deflection response. Van Vliet and van Mier (1996) stated that the compression response especially softening behavior in compression is directly related with the boundary condition of the specimen. The more softened response is observed for the higher restrained conditions. Thus, the softening in compression is obtained as resulting from the restrained condition in concrete Figure 2.6b. This is the close idea with that the confinement of concrete increase the softening. Even the compressive strength of the same concrete batch is influenced with the boundary conditions. The representative cracking pattern in two extreme boundary conditions are shown in Figure 2.6c, and d.

The area under the stress-displacement curve is an indicator of the energy required for the final major cracks. It is usually called as “compressive fracture energy” similar to the concept with the tensile fracture energy. However, while the required energy to completely open the cracks does not change with the lateral restriction in tension, the compressive fracture energy can change with end conditions. It is a difficult question, in which boundary condition should be considered to determine the compressive fracture energy. This is the same question that compressive fracture energy is determined by diagonal cracks or splitting cracks.

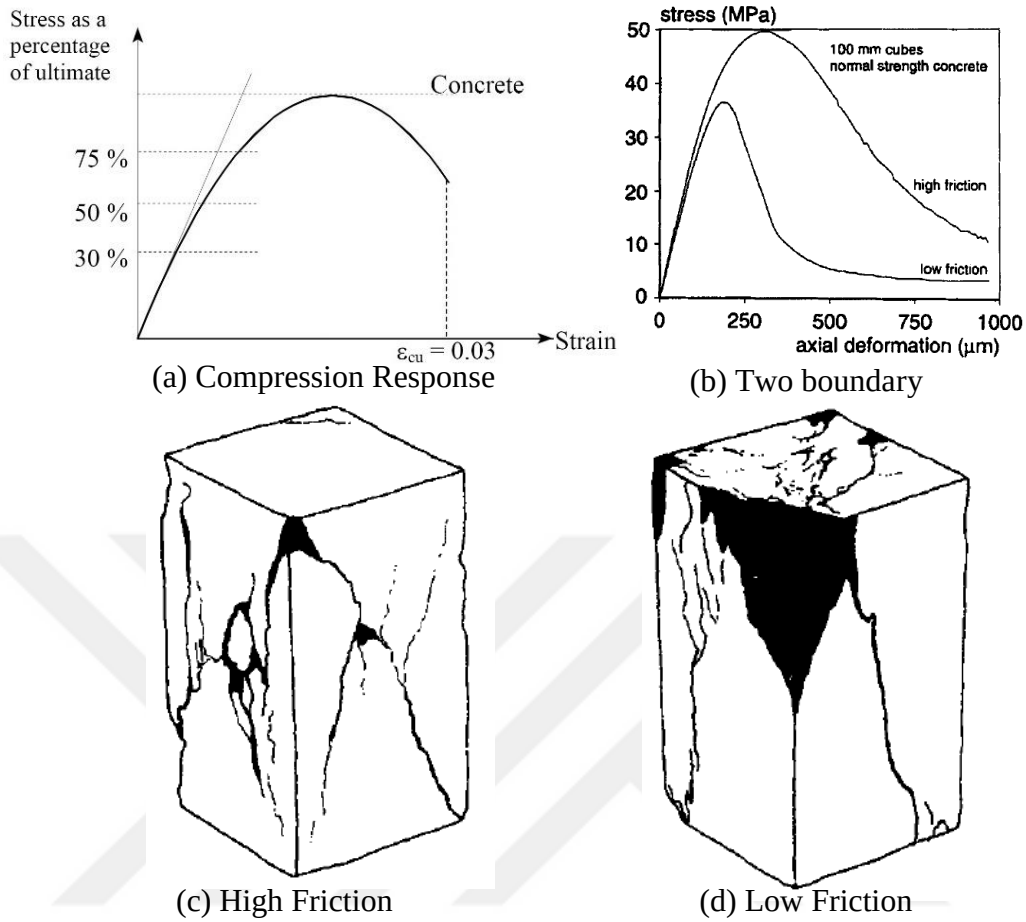


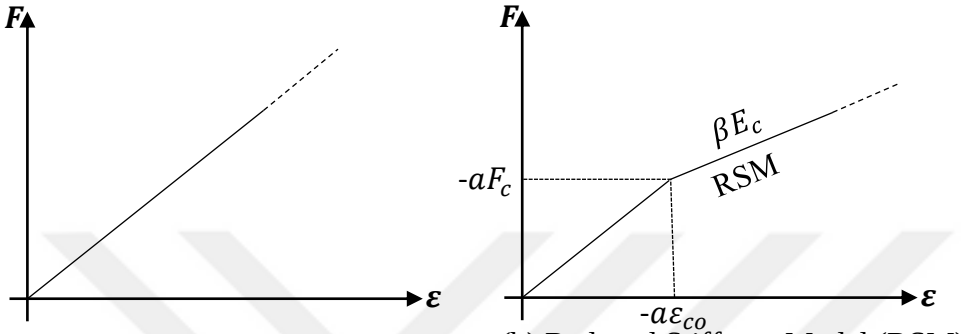
Figure 2.6. Compression Response for Two Boundary Conditions (van Vliet and van Mier 1996)

In the light of this information, the compression behavior is explained with only tension response in this study. Such a vision was previously stated by Bazant et al. (1993) and Kendall (1978). After calibrated tensile fracture energy of the lattice network, the cracking and failure in compression is an outcome of the indirect tension failure and loss of the local and global stability of the lattice system.

2.5.2 Methodology

The lattice approach presented herein does not use any nonlinear constitutive model in compression (Figure 2.7a). It is postulated that lattice elements are capable of

modeling tension and compression as an indirect tensile failure due to the local instability of lattice elements. This chapter explains the direct relationship between tensile and compressive strengths for lattice model for only 1.5d horizon sizes. An explicit time integration method for all simulations mentioned for compression validation studies was used and explained in section 2.9 in detail.

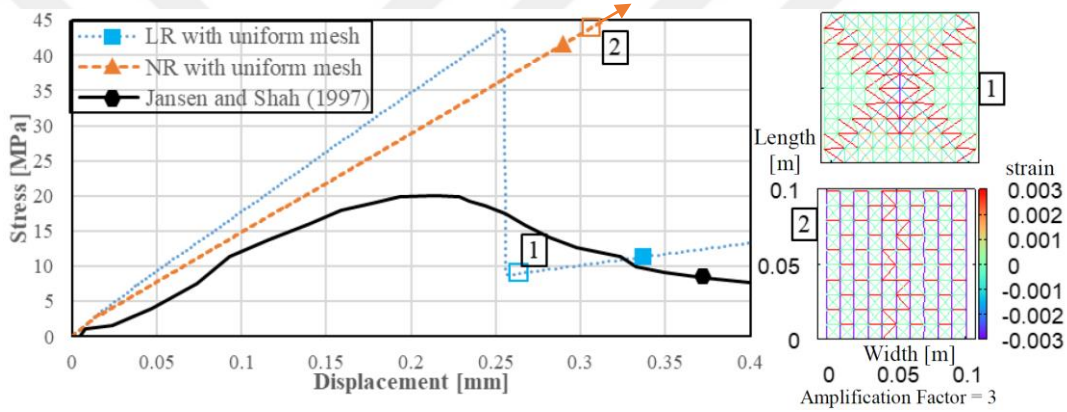


(a) Linear Model (b) Reduced Stiffness Model (RSM)

Figure 2.7. Uniaxial Material Behavior of Lattice Member in Compression

The uniaxial compression response of the lattice model with structured grid and linear compressive response was studied by simulating the compression testing of a 100 mm x 100 mm x 100 mm cube specimen (Figure 2.2). The compressive strength (f_c) and the tensile fracture energy (G_f) of the specimen were chosen as 20 MPa and 50 N/m, respectively. The tensile strength (f_t) and modulus of elasticity (E_c) were calculated from the equations given in ACI 318-19 (2019) by using the uniaxial compressive strength. The tension test was simulated and the softening parameters of the tension model were calibrated by matching the numerical tension test result to the Hordijk model (Cornelisssen et al. 1986) as described in the previous section. Uniaxial compression simulations were conducted with a regular grid size of 10 mm. The effect of boundary conditions on a uniaxial test was studied by van Mier (1997) following that two different boundary conditions: i-laterally restrained (LR) by using pin supports at the bottom nodes, and roller support at the top nodes, ii- no lateral restraint (NR) by placing only roller supports at bottom nodes and leaving the top nodes free (Figure 2.2.a). Uniform displacement was imposed on the uppermost

nodes at a sufficiently slow speed to simulate a quasi-static test with the dynamic explicit integration solution scheme. The simulation results are presented in Figure 2.8. For the specimen with NR boundary conditions, the first splitting cracks (i.e. tensile strains in the softening region) were observed in the horizontal elements resulting in a stiffness reduction of around 3.5 MPa. After this point, the vertical elements transferred the forces from the top to the base. With increasing load, the splitting cracks completely opened in the horizontal elements. The analysis was conducted until a compressive stress of 45 MPa and no strength decrease was observed, since the vertical lattice elements could carry axial forces due to their linear elastic compressive behavior.



(a) Stress-Displacement Curve (b) Crack Pattern

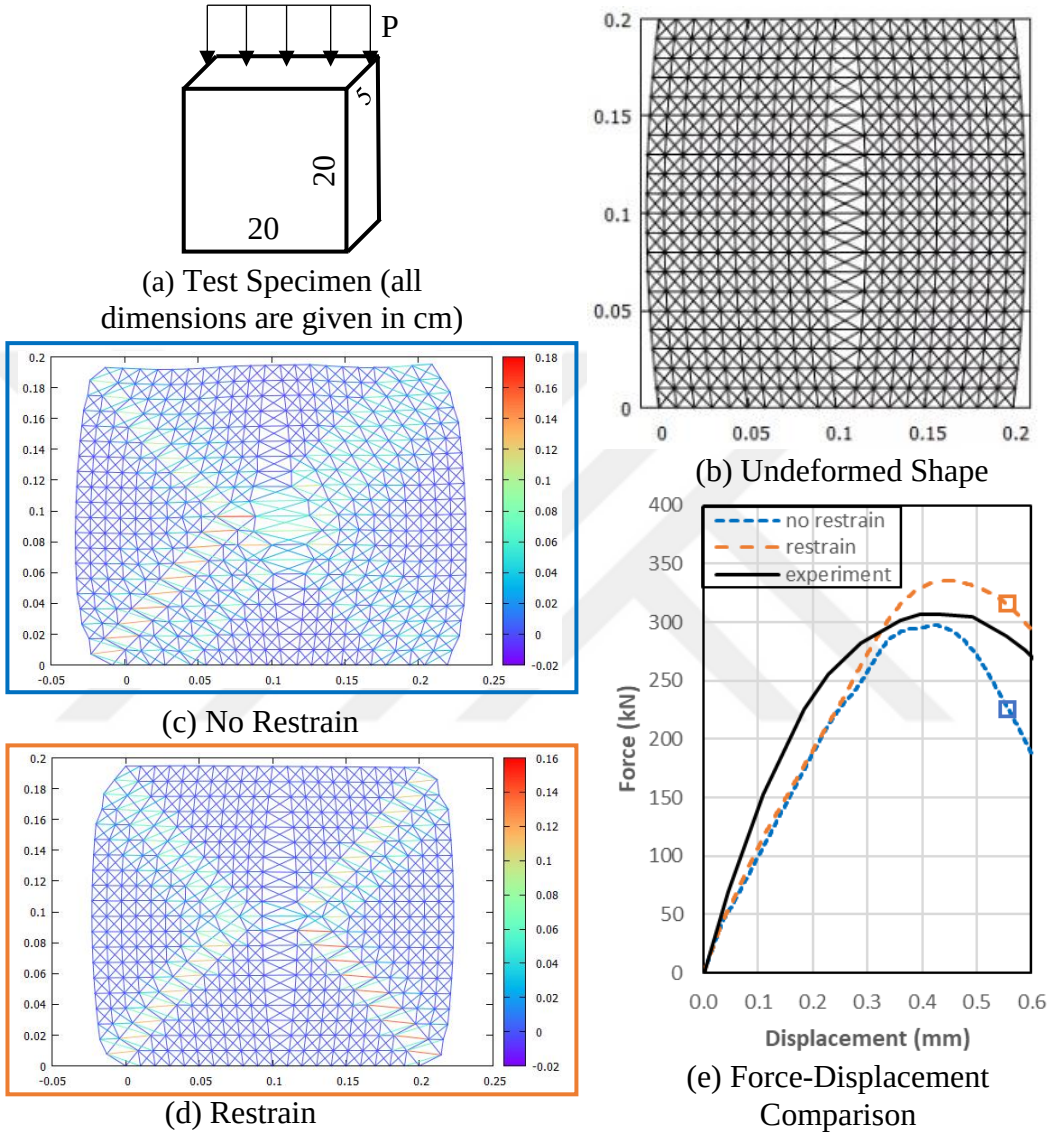
Figure 2.8. Compression Test Results of a Cube Specimen with Dimensions of 100 mm for Uniform Mesh

For the LR boundary condition, cracking was observed along the two diagonals due to the lateral restraint along the boundaries. Although the vertical lattice elements carried the axial forces, instability occurred due to the shear force imposed along the crack directions resulting in a compressive strength of 43 MPa, which was about two times the compressive strength of the selected concrete grade. These results show that the end conditions significantly affect the compressive strength (Choi et al., 1996) simulations, and uniform grid lattice simulations are incapable of simulating the compression response.

The compression test conducted by Kupfer (1969) on a rectangular specimen was simulated in order to discuss this problem of vertical locking, as shown in Figure 2.9a. The specimen size was 20 x 20 x 5 cm. An initial crookedness was assigned to the vertical truss elements in the compression test specimen to initiate instability. Initial crookedness with the value of %7 (7 mm in the middle) was placed at the mid-vertical line, as can be seen in the Figure 2.9b. The grid size was taken as 10 mm. The top boundary moved downward at a velocity of 0.001 m/s (this velocity was found to be sufficiently small so that computational results were independent of inertial effects). Two different boundary condition sets were used: no friction (shown as 'no restrain' in the figure) and perfect contact (shown as 'restrain' in the figure). E_t and f_t were taken as 31870 MPa and 2.78 MPa, respectively. By using the maximum aggregate size and the compressive strength which were reported as 15 mm and 30 MPa, respectively, G_f was found as 75 N/m. Then, the corresponding softening parameters were calibrated using the methodology presented in the previous section. Displacement was measured from the middle point of the top of the specimen. The amplification factor for the displacements is shown in the same figure. The results presented below show that the lattice modeling approach can provide a reasonable approximation of the average stress-strain curve in compression by using an only tension modeling approach for the lattice elements Figure 2.9c-e. However, if the uniform mesh was used, compressive strength could not be determined due to the elastic response. Although this result can be estimated as the evidence of that the compression capacity can be handled with a random mesh model, assigning the crookedness in the loading axis is not a practical solution.

This problem of vertical locking can be circumvented by inducing grid heterogeneity, which has been done by using Voronin diagrams or Fuller curve based mesh generations to incorporate aggregate distributions (Bolander and Sukumar, 2005; van Mier et al., 2002; Wriggers and Moftah, 2006). Since the model herein is a homogenous media model (i.e. the differentiation between paste and aggregate is not made during mesh generation for the purposes of practicality), it was preferred to perturb the lattice grid by R at a random angle of θ (Figure 2.2.b) as a practical

method. R_{max} was selected to be 0.6 mm and 0.75 mm for the NR and LR boundary conditions for cube specimen, respectively. A detailed discussion on how to select the values of R_{max} is given later in this section.



(a) Test Specimen (all dimensions are given in cm)

(b) Undeformed Shape

(c) No Restrain

(d) Restrain

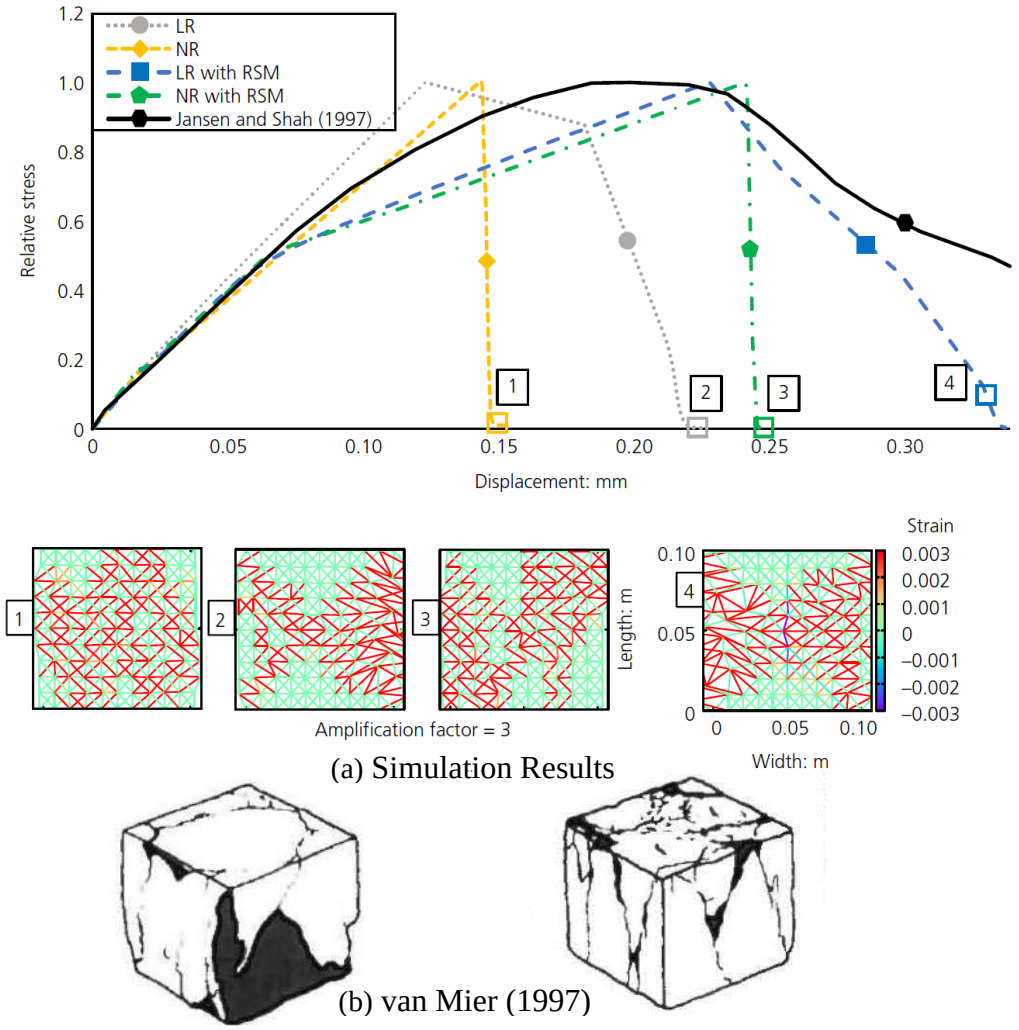
(e) Force-Displacement Comparison

Figure 2.9. Simulation of Rectangular Specimens Tested by Kupfer (1969) with Initial Crookedness (%7)

The simulation results of the cube specimen with dimensions of 100 mm in a disturbance sample are shown in Figure 2.10a. It is observed that the strength of the specimen is captured with this simple grid modification. The loss of stability in the

vertical elements occurred for specimen NR at 20 MPa with a sharp decrease in the load carrying capacity. For the case of the LR specimen, after the formation of diagonal cracks, loss of stability of vertical load resisting elements took place slightly below the desired compressive strength level, exhibiting some softening. Although the simulations captured the strength values, these simulations did not provide a good match of the post-cracking stiffness and ultimate strain at peak stress. These two problems are related to the stiffness of the compressive load carrying lattice members. It is well known that, upon lateral cracking, the stiffness of concrete in compression reduces (Vecchio and Collins, 1982; 1986; Hsu and Mo, 2010 etc.). This phenomenon is introduced for the laterally cracked lattice nodes carrying compressive forces by using the reduced stiffness model (RSM) in compression as shown in Figure 2.7b. Parameters α and β were taken as 0.4 and 1/3 based on the assumption of 40% stiffness reduction at a strain of 1/3 of concrete strain at peak stress, ε_{co} (i.e. $\varepsilon_{co} = 2f_c/E_c$) . The revised simulation results with this compressive model are shown in Figure 2.10a. It can be observed that this model captures the pre-peak compressive behavior with good accuracy while underestimating the softening region slightly. For these two boundary conditions, the crack patterns are consistent with experimental results obtained by van Mier (1997), as can be seen in Figure 2.6c,d for rectangular prism and Figure 2.10b for cube with dimensions of 10 cm. As stated before, boundary conditions affect the softening regime of compression behavior significantly. Steeper softening is observed with decreasing friction at the boundaries. In the case of NR, the specimen exhibited a sharp drop after reaching the peak strength as observed with a beam lattice simulation by Chang et al. (2019). In the case of LR, the softening response is more likely to be obtained, as the diagonal cracks mostly control the post-peak behavior. Orthogonal elements to force flow direction in a lattice unit provide the internal friction with calibrated model for the tensile fracture energy and mesh perturbation, which allows triggering of the instability initiated by internal cracking thanks to the topology of the used rectangular lattice unit. In short, Figure 2.10 shows that models without the reduced compressive stiffness approach cannot predict the failure displacements. However,

the failure displacement was captured with sufficient accuracy upon using the reduced compressive stiffness approach, while the post-cracking response up to peak strength was underestimated. This underestimation could be overcome by gradually reducing the compressive stiffness as a function of lateral strain (Vecchio and Collins, 1982; 1986; Hsu and Mo, 2010 etc.). However, such fine tuning was not attempted in order to preserve the practicality of the model.



(a) Simulation Results

(b) van Mier (1997)

Figure 2.10. Compression Test Simulation and Experimental Results of a Cube Specimen with Dimensions of 100 mm for Random Mesh (van Mier 1997)

2.5.2.1 Selection of Mesh Disturbance Parameters

The key parameter to simulate the compressive strength in a tension-only lattice model is the grid perturbance magnitude, R_{max}. It is assumed that upon selecting the concrete tensile strength (f_t) and tensile fracture energy (G_f), the concrete compressive strength (f_c) and modulus of elasticity (E_c) can be computed from empirical equations such as those given in TS 500 (2000) and ACI 318-19 (2019). Afterwards, the work-flow discussed for tension calibration in Section 2.4 is extended by employing the iterative procedure outlined in Figure 2.11 to determine the model parameters (a_1,a_2,a_3,b_1,b_2, R_{max}/d). It should be noted that R_{max}/d is not used in the calibration of the tension model parameters, as tension behavior is found to be insensitive to this parameter. It should also be noted that the tension model parameter calibration procedure is similar to that explained in the previous section and the compression model parameter calibration is the new feature that converges with five simulations for concrete to the correct R_{max} until the desired compressive strength is achieved. It is well known that concrete compressive strength may show significant variations (Wight 2016) and its mean strength estimation depends on the number of tested specimens. Based on engineering judgement and relative importance of the compressive strength in member strength estimations, it was decided to employ 10% error margin for mean strength to be a reasonable computational efficiency.

Furthermore, the reduced stiffness parameters α (0.4) and β (0.33) were kept constant throughout the study in order to obtain objective results while using RSM in the simulations. Due to the inherent randomness of the modeling approach, successive simulation results are different. This is similar to the uncertainty one would obtain from testing and requires a statistically meaningful number of simulations must be conducted.

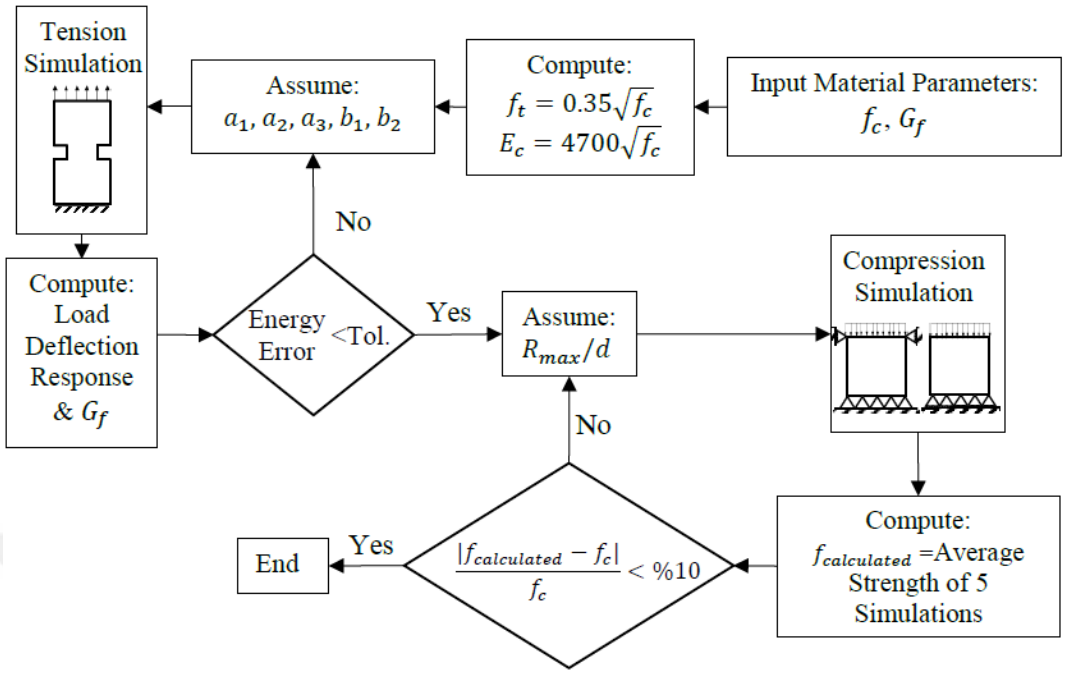
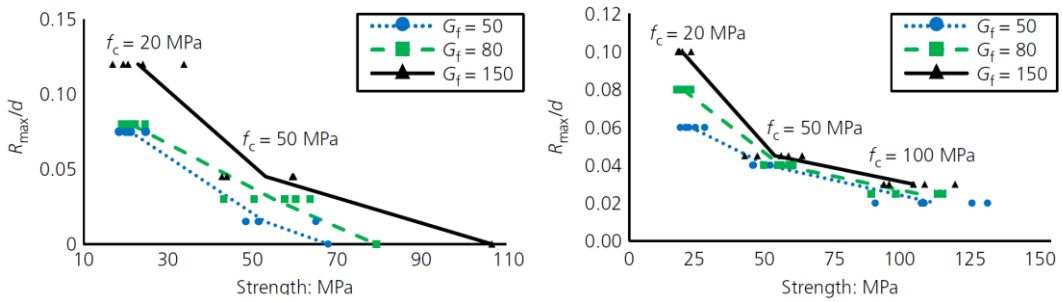


Figure 2.11. Model Parameter Calibration for Both Tension and Compression

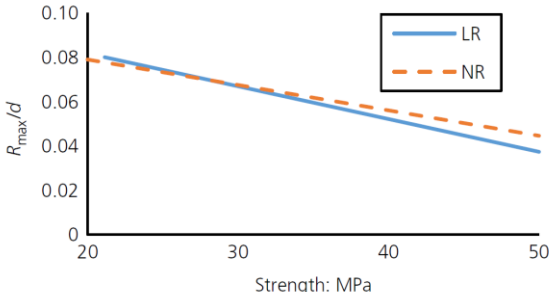
The flowchart for both tension and compression was employed for 100 mm x 100 mm x 100 mm test specimens modeled with a grid size of 10 mm and subjected to uniaxial compression for f_c values of 20 MPa, 50 MPa, and 100 MPa along with three different G_f values of 50, 80, and 150 N/m for each f_t. These fracture energy values were chosen since they are close to the values obtained from CEB-FIB Model Code 1990 (1993) by assuming the maximum aggregate size value of 12 mm. For each parameter set, five different simulation sets were performed until convergence of the model parameters was achieved. The results are plotted in Figure 2.12.a and b for two different boundary conditions. The trend lines shown in Figure 2.12.a and b are plotted based on the average of five simulations. These curves can be thought of as a guide in selecting the R_{max} value for a given tensile strength, fracture energy and desired boundary condition. It can be observed that for the selected parameters, a uniaxial concrete compressive strength of 20 to 100 MPa can be simulated for the LR boundary conditions. Compressive strength values above 100 MPa would require a tensile strength larger than 3.5 MPa, irrespective of the tensile fracture energy.

Larger R_{max} values are needed for NR simulations in order to achieve a similar compressive strength compared to LR. Another interesting result is the fact that compressive strength appears to be more sensitive to G_f for LR than NR conditions. As expected, larger R_{max} results in lower compressive strength for both boundary conditions. Moreover, the curve of G_f value of 80 N/m for two different boundary conditions until 50 MPa indicates that R_{max} values are not so different than each other (Figure 2.12.c).



(a) LR

(b) NR



(c) G_f=80 N/m

Figure 2.12. Compressive Strength from Simulations

The calibration of the R_{max}/d values were slightly modified for AAC masonry walls (Figure 2.13). The R_{max}/d value was calibrated by comparing the average compression strength of 100 compression simulations, with 100 different grid perturbation instances, with the mean value of the compressive strength from uniaxial compression AAC masonry tests with an acceptable error of 10% based on engineering judgement and computational efficiency. Furthermore, the effect of the number of simulations was studied, as shown in Figure 2.14. Simulations were

employed for the uniaxial and diagonal compression experiments tested by Todorovic et al. (2019) and for this study as described in section 2.5.3.2. It can be observed that uniaxial compression tests converge at about 50 iterations, whereas diagonal compression tests require about 100 simulations to achieve accurate results. Standard deviations of related simulation results are listed in Table 2.5. Hence, based on preliminary simulations, it was found that 100 cases should be simulated in order to obtain accurate results for material strength estimations for AAC masonry calibration simulations. Thus, 100 simulations were selected for all calibration studies for AAC masonry. However, for any other compressive strength level, the simulations should be repeated to find the optimal R_{max}/d. Therefore, 100 simulations act as a calibration simulation rather than a validation study for AAC masonry calibration.

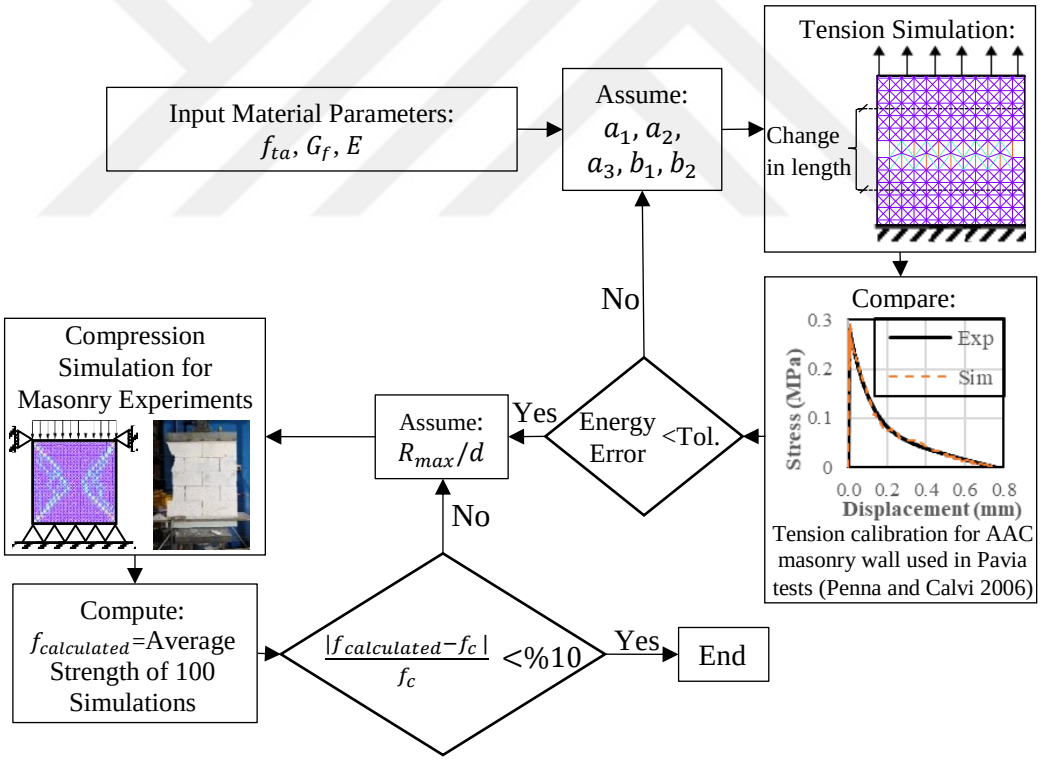
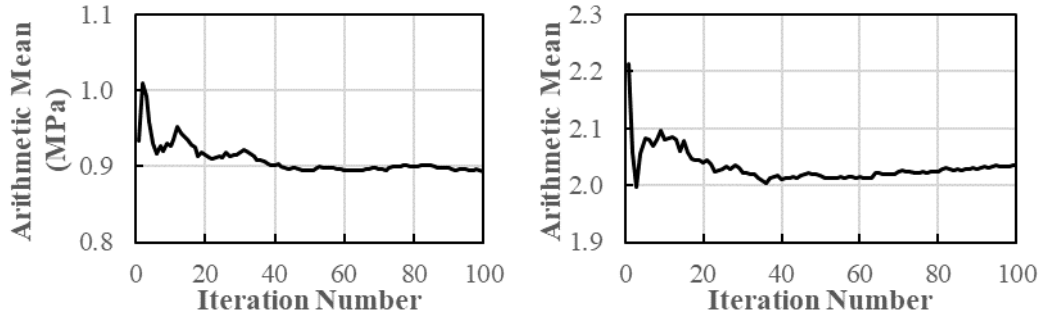
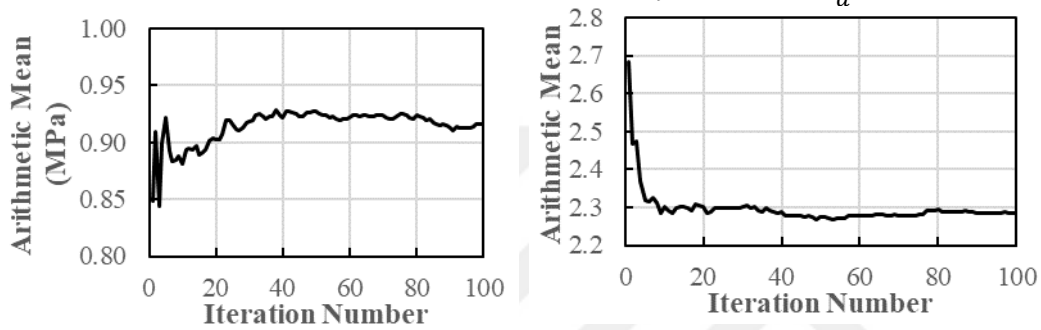


Figure 2.13. Work-Flow for Compression Calibration of AAC Masonry Structures



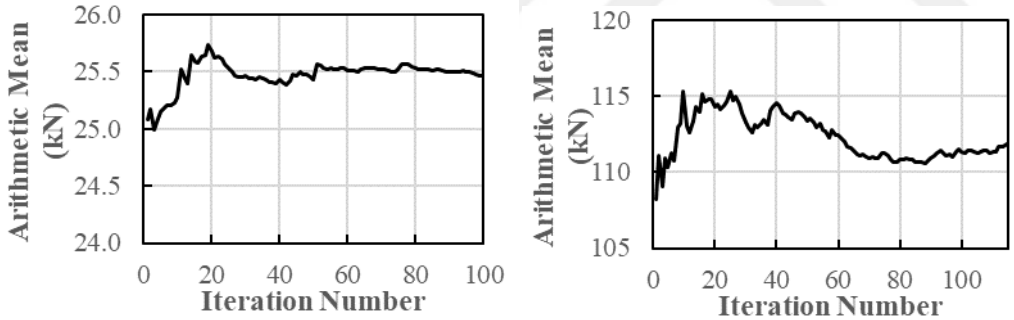
Uniaxial compression test simulation in this study

Uniaxial compression test simulation with G_f=56.7 N/m, $\frac{R_{max}}{d}$=0.067



Uniaxial compression test simulation (Todorovic et al. 2019)

Uniaxial compression test simulation with G_f=56.7 N/m, $\frac{R_{max}}{d}$=0.05



Diagonal compression test simulation

(a)

Diagonal compression test simulation

(b)

Figure 2.14. Convergence Results for (a) Batch 1 (METU) and (b) Batch 2 (Pavia)

On the other hand, for concrete, it can be noted that five simulations were used to determine R_{max}/d value. The same study was conducted for concrete to obtain the effect of iteration number. The simulation results which can be shown in Figure 2.12 were used to create the curves in Figure 2.15 for some different f_c, G_f and boundary conditions. It can be concluded that the alteration in compressive strength of concrete

is much lower than AAC masonry, since the R_{max}/d value is much smaller, and the error margin is acceptable according to Wight's (2016) observation.

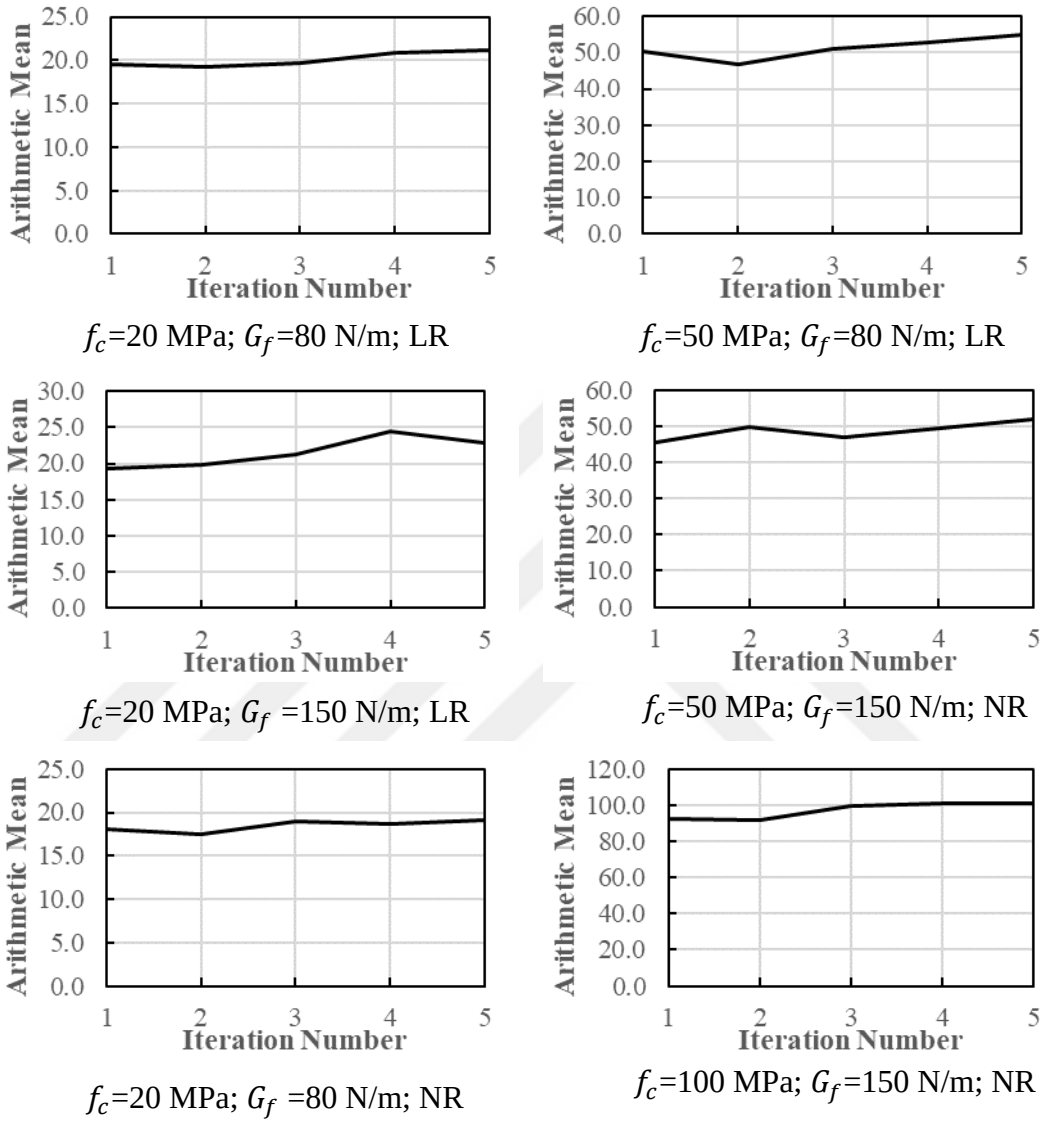
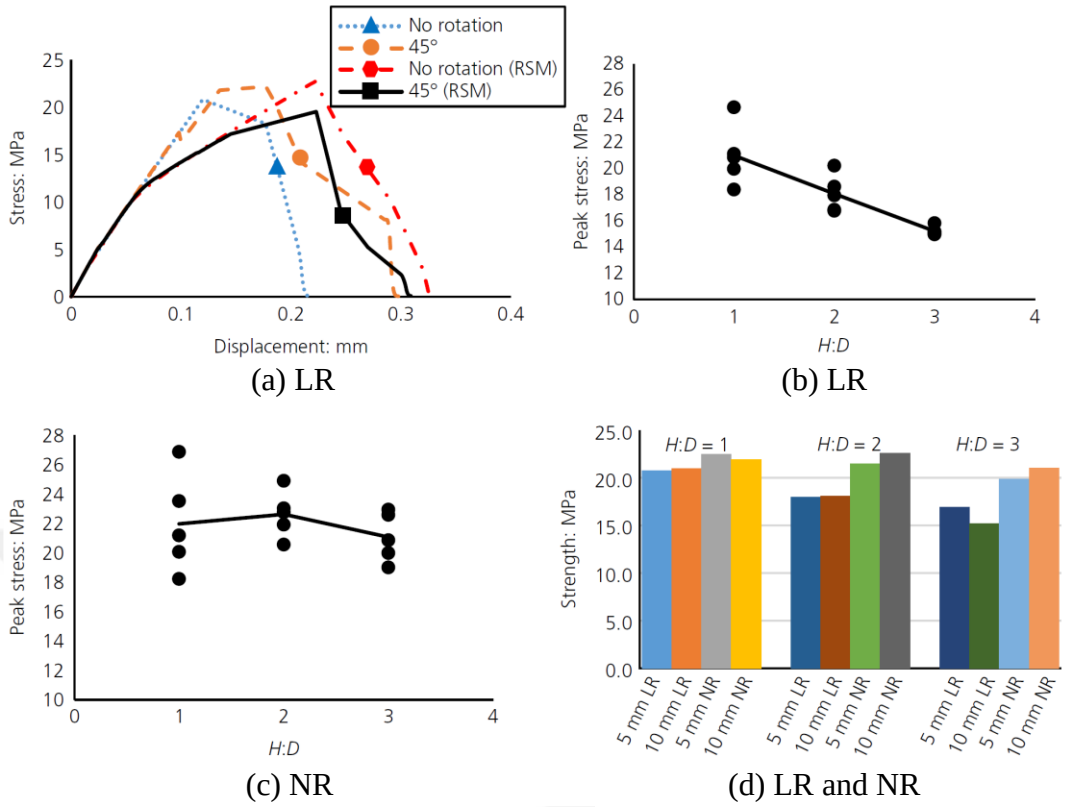


Figure 2.15. Convergence Results for Different Concrete Materials and Boundary Conditions

2.5.2.2 Sensitivity Analysis of Mesh Disturbance

The sensitivity of the results to grid size and orientation were studied by performing analyses of the cube compression tests with two different grid sizes and two different grid orientations. For the grid density study, 5 mm and 10 mm grid spacings were used for the simulations, whereas an orthogonal grid and a grid rotated 45 degrees were selected for the purposes of investigating the grid isotropy by using a 10 mm grid spacing. Simulation results are shown in Figure 2.16.a. It can be observed that results are not sensitive to the grid refinement based on general pattern of the load displacement response owing to the regularization achieved with the use of tensile fracture energy. Despite some slight variation upon applying the stress with a rotated coordinate system, one can say that rotation effects are not critical for simulating the compression behavior with a lattice model.

In order to understand the behavior of the lattice model's size effect, the same specimen is simulated with different H:D ratios without introducing any reduced stiffness model (RSM) for compression. For this purpose, values for H:D are chosen as 2 and 3 in addition to 1. The strength values were obtained for LR and NR. The average values of 5 simulations were determined as 21, 18, and 15 MPa for H:D values of 1, 2, and 3 of LR, respectively. The strength values decrease with higher H:D values, which is in line with the observations from tests due to slenderness effects, as shown in Figure 2.16.b (Choi et al., 1996). On the other hand, there is no observed decreasing trend for peak stresses by increasing H:D values for NR as suggested by Choi et al. (1996) (Figure 2.16.c). A similar response is observed for the 5 mm grid size, meaning that the R_{max}/d value is nearly constant (Figure 2.16.d). Although decreasing stiffness in the elemental level results in better representation at the global level for the simulation of the uniaxial compression test, for the rest of the simulations, RSM was not used to preserve the practicality since the main aim is to capture compressive strength and failure as an indirect tension failure rather than the complete response in compression.



(a) LR (b) LR

(c) NR (d) LR and NR

Figure 2.16. Mesh Objectivity and Size Effect Results

2.5.3 Validation of Perturbed Mesh for Concrete and Masonry

The perturbation of the grid leads to desired instability in local regions of the domain. Thus, creating a weak zone through the strut affects the compressive strength of concrete. In this part, this effect is used for simulating the behavior of both concrete and AAC masonry. Uniaxial compression and compression strut tests were used to validate the proposed lattice model in compression response for concrete members in this section. In context, simulation results of the over-reinforced beam is explained in Section 3.1.2. Furthermore, the performance of the model for AAC wall tests was investigated. Thus, the model was calibrated for compression to use in the simulation of AAC infill walls in this study.

2.5.3.1 Concrete

As the first validation study, the experiments conducted by Jansen and Shah (1997) were simulated using the proposed lattice model. The tests were conducted on cylinders; however, the simulations were conducted on prisms with the same aspect ratio and same cross-sectional area (Figure 2.17.a). The ends of the specimen were not lubricated in the tests, so they were assumed to be LR specimens. The cylindrical compressive strength was reported as 45 MPa, and the maximum aggregate size (d_{max}) was 9 mm, resulting in a G_f of 80 N/m. The proposed algorithm to estimate the required R_{max} value was determined by applying the procedure in Figure 2.11. The properties of the specimens that are used for simulation can be seen in Table 2.1.

Table 2.1. Specimen Properties for Compression Simulations

Properties	**Specimens**		
	Jansen and Shah (1997)	**Laughery and Pujol (2015)**	**Brown et al. (2006)**
	H:D=4.5 & 2.0	**B1 & B3**	**Specimens**
Thickness (mm)	79	200	102
f_b (MPa)	45.0	30.0	26.4
f_c (MPa)	53[a]	37[a]	31[a]
f_t (MPa)	2.55[b]	2.13[b]	1.95[b]
E_c (MPa)	34217[c]	28589[c]	26211[c]
d_{max} (mm)	9	25	-
G_f (N/m)	80[d]	86[d]	50
a_1	1.5	1.5	1.5
a_2	60	70	40
a_3	300	440	270
v (mm/s)	0.1	0.1	0.4
d (mm)	10		
R_{max}/d for LR	0.040	0.055	0.050
R_{max}/d for NR	-	0.050	-

[a]*These values are found by using ACI 318-11(American Concrete Institute 2011).*

[b]*These values are found by using TS 500 (TSE 2000) (i.e. $f_t = 0.35\sqrt{f_c}$)*

[c] *These values are found by using ACI 318-11(American Concrete Institute 2011)(i.e. $E_c = 4700\sqrt{f_c}$)*

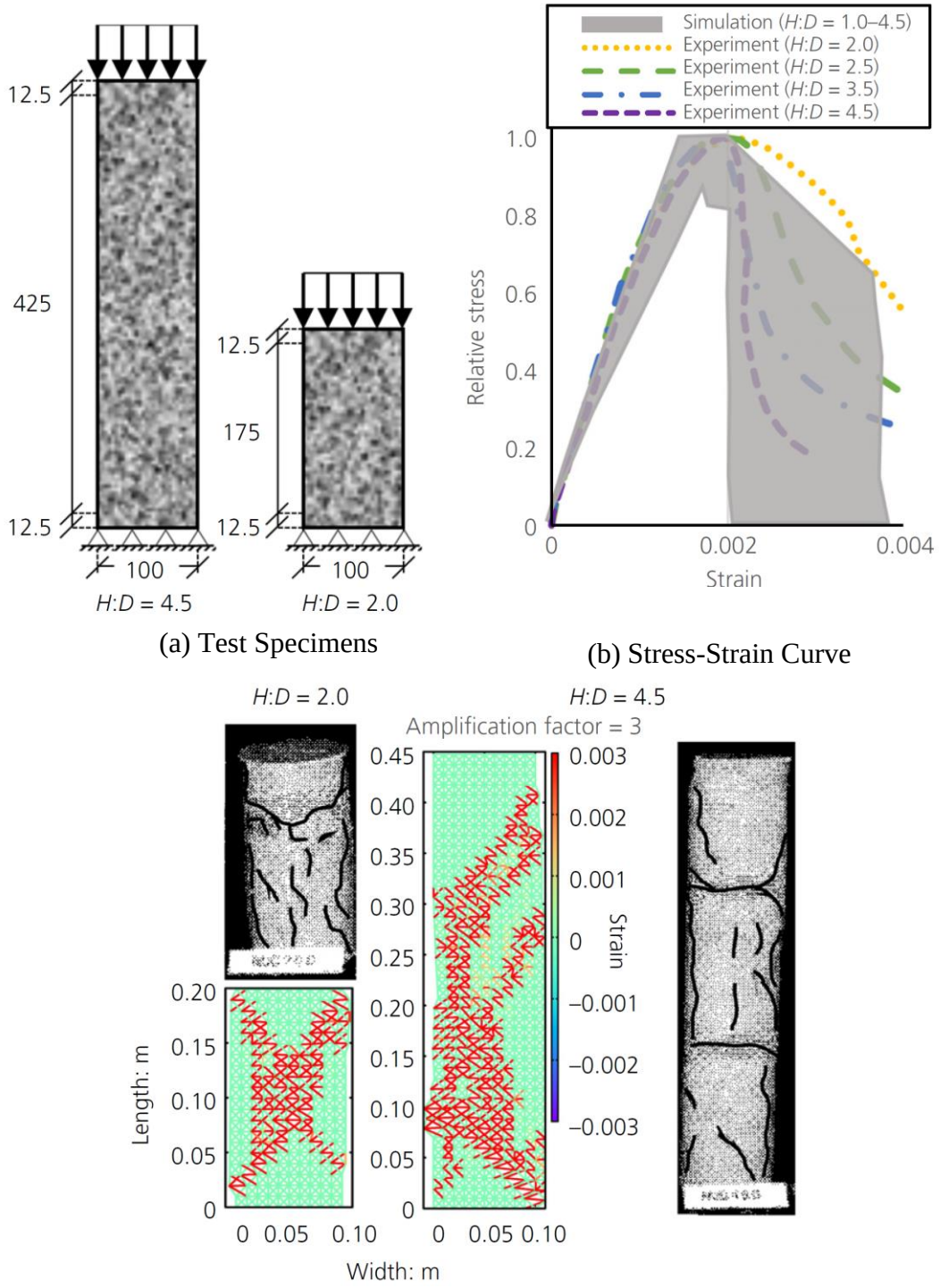
[d]*These values are found by using CEB-FIP model code 1990 (1993).*

The specimens with H:D of 1.0, 2.0, and 4.5 were simulated and the results are presented in Figure 2.17.b. The estimated damage patterns at the end of the simulations by showing strain distribution (positive is tensile values) can be seen in Figure 2.17.c. The uniaxial compressive strength from the experiments (an average of 3 and 2 specimens for H:D of 2.0 and 4.5, respectively) was 49.1 MPa and 47.2 MPa, whereas the average compressive strengths from 5 simulations were 43.45 MPa and 43.05 for H:D of 2.0 and 4.5, respectively. (Table 2.2). The initial stiffness of the load-deflection curve was in perfect agreement with the test results, whereas the softening regime of the deformation response was slightly underestimated. This can be attributed to the difference between the cylinder and prism response in addition to the lack of direct compression softening control in the tension-only lattice modeling. The estimated strength values are consistent with the results observed from the tests.

A number of researchers have studied the strength of compression struts in the literature. The key difference in the strut behavior is the fact that the force flows from the loaded points to the supports as a prismatic or bottle-shaped strut depending on the loaded area to specimen width. In order to examine this behavior, tests on plain concrete struts loaded in uniaxial compression were simulated by the lattice model.

Table 2.2. Jansen and Shah (1997) Results

Trial	**Strength (f_c) [MPa]**					
	H:D=4.5		**H:D=2.0**		**H:D=1.0**	
	Experiment	**LR**	**Experiment**	**LR**	**Experiment**	**LR**
1	46.7	47.35	42.8	43.74		51.80
2	47.7	41.42	55.6	47.78		54.99
3		45.67	49.0	43.69	-	57.08
4		40.14		35.18		66.23
5		40.68		46.87		42.92
Average	**47.2**	**43.05**	**49.1**	**43.45**	**-**	**54.60**



(a) Test Specimens

(b) Stress-Strain Curve

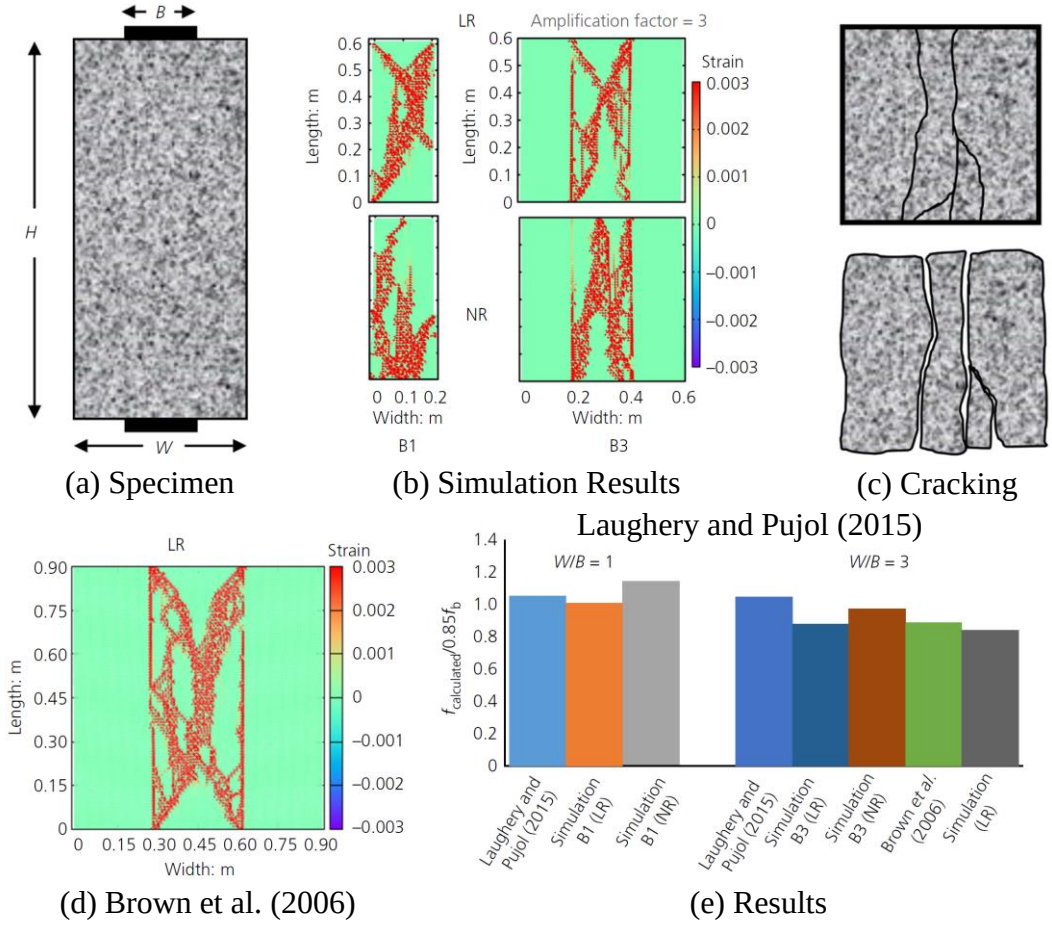
(c) Crack Patterns

Figure 2.17. Comparisons with Test Results (Jansen and Shah 1997) for (a) Test Specimens (Dimensions in mm); (b) Relative Stress-Strain Curve And (c) Crack Patterns

The first validation study was conducted by simulating the specimens tested by Laughery and Pujol (2015). The dimensions (width W and length H), of the simulated specimens B1 and B3 were 200x600 mm and 600x600 mm, respectively (Figure 2.18.a). The plate widths and thickness of the loaded platens were 200 mm so that the loading was applied at the full width of specimen for B1 and 1/3 width of specimen B3. The cylindrical strength (f_b) for the B series was about 30 MPa. The parameters used in the simulations are shown in Table 2.1. The grid size was chosen as 10 mm for simulations. The R_{max}/d value computed based on the flowchart in Figure 2.11 was 0.055 and 0.050 for LR and NR, respectively. Laughery and Pujol (2015) did not report any load-deflection curves; however, the strut efficiency was determined as shown in Table 2.3. Furthermore, the restraining effects along the loaded end plates were not reported. Hence simulations were conducted for both the LR and NR cases. Computed and reported strut efficiency factors are presented in Table 2.3, and the crack patterns are given in Figure 2.18.b. The estimated strut efficiency factors were within about 10% of the test results. The highest strut efficiency differences are observed from the B1 specimen experiment and NR. This can be attributed to the tensile strength value that was not reported for this specimen. In addition, the reduction of strength was observed in the simulations due to a decrease in the H:W ratio. In all simulations, diagonal cracks first appeared, followed by splitting cracks and shear cracking. The only picture from the test is shown in Figure 2.18.c. It can be observed that vertical cracking followed by the loss of stability of the disintegrated parts is similar to the results obtained from the simulations.

Similar tests were conducted by Brown et al. (2006) to examine the strut efficiency factors. A square prism with dimensions of 900x900 mm was tested. The bearing area was 1/3 of the width of the specimens. The properties are shown in Table 2.1. There is no reported data for d_{max} so G_f was taken as 50 N/m. The grid size was chosen as 10 mm. The same procedure as explained for the specimens of Laughery and Pujol (2015) was conducted. Only the LR condition was considered since the

same failure type, at the interface between the node and strut of the model, was reported even though extra confinement was implemented.



(a) Specimen (b) Simulation Results (c) Cracking Laughery and Pujol (2015)

(d) Brown et al. (2006) (e) Results

Figure 2.18. Simulation Results of Compression Strut Tests (Brown et al. 2006; Laughery and Pujol 2015) (a) Typical Specimen Dimensions; (b)Simulation Results; and (c) Experimental Cracking of Laughery and Pujol (2015); (d) Brown et al. (2006) and (e) All Results

The crack pattern is given in Figure 2.18.d, and the efficiency factors from both experimental and lattice-based simulations are shown in Table 2.3 and Figure 2.18.e. The estimated efficiency factor is consistent with the experimental result. In particular, the results from the two experiment series were the same as each other, but the boundary conditions affected the results. In other words, it is more likely that boundary conditions of Laughery and Pujol (2015) were NR, whereas the boundary

conditions of Brown et al. (2006) were LR based on the closeness of the estimated results to the experimental ones. This result indicates the importance of boundary conditions while investigating the strength of struts when using strut and tie modeling.

Table 2.3. Strut Efficiency Factor for Laughery and Pujol (2015) and Brown et al. (2006)

Strut Efficiency Factor=$f_{calculated}/0.85f_b$								
Trial	Laughery and Pujol (2015)						Brown et al. (2006)	
	B1 [H=600, W=200, B=200 mm]			B3 [H=600, W=600, B=200 mm]			Specimens [H=900, W=900, B=300]	
	Experiment	LR	NR	Experiment	LR	NR	Experiment	LR
1	1.06	1.00	1.06	1.03	0.84	0.97	1.01	0.87
2	1.02	0.98	1.15	1.02	0.90	0.97	0.76	0.80
3	1.07	1.04	1.14	1.09	0.91	0.86		0.84
4		0.98	1.25		0.89	0.94		0.91
5		1.03	1.12		0.86	0.92		0.78
Average	**1.05**	**1.01**	**1.14**	**1.05**	**0.88**	**0.93**	**0.89**	**0.84**

2.5.3.2 AAC Masonry

After the validation studies on tests from the literature on concrete, laboratory experiments were performed in the METU Structural Laboratory for the application of the model for AAC. Three AAC masonry wallettes have been tested to obtain uniaxial compression response in order to calibrate the models in this section. Later, the calibration of the proposed model for AAC wallettes from different experimental campaign performed by Costa (2007) additional to these tests to use calibrated values to use for infill wall simulations as shown in chapter 4. Also, the simulation results are presented with the use of different R_{max}/d and G_f values.

Firstly, uniaxial compression tests of three AAC masonry wallettes with a thickness of 10 cm, sampled from the infill wall specimens tested in this study, are explained in this part. The wallettes were performed in METU Structural Laboratory. It should

be mentioned that "batch" term refers to a set of one AAC wall and one RC frame in this study, as described in detail in Section 4.1. The specimens were prepared according to TS EN 1052-1 (2000). The dimensions and installed instrumentations are shown in Figure 2.19a. It should be mentioned that additional three AAC masonry wallettes with the width value of 450 mm and the same dimensions for height and thickness were tested by fixing the plates at the upper side. It results in undesired rotation to the specimen. Thus, ball joints providing to rotate the end plates at the top of the upper side were used to avoid undesired moments. AAC units used in this study were the same as the units used in Todorovic et al. (2019) (Figure 2.19b).

Digital image correlation (DIC) was conducted to observe the local strain concentrations during all tests conducted for this study. For this purpose, small black points were created randomly on a single face of the specimens. The average diameter of the black dots is around 0.6 mm. The spacing of these points ranges from 1.5 mm to 3.5 mm for DIC results in this study. The photographs were taken with a 24-megapixel camera. A single camera was used to obtain in-plane cracking response for the tests conducted in-plane load, which is the scope of this study. Accurate results were obtained by using only one camera for in-plane infill experiments by many researchers (Ramos et al. 2015; Korswagen et al. 2019; Furtado et al. 2015; Kumar et al. 2019). However, according to Mojsilovic and Salmanpour (2016), error can be introduced by out-of-plane motion of the specimen in 2D DIC, and this error is proportional to the ratio of the out-of-plane motion to the distance of the camera from the specimen. For this purpose, the camera was placed at the closest distance. Also, it was ensured that the rods were placed at the top of the infill wall specimens in order to prevent out-of-plane deformation or distortion. Moreover, it should be noted that the main aim was to visualize cracking patterns with DIC since a relatively large area was photographed. Thus, crack width and strain measurements were beyond the limitation of the camera resolution.

Test setup and DIC results are shown in Figure 2.19c. Color contours represent the displacement of the points in lateral direction and major strain distribution obtained from DIC, overlapping with the crack patterns on the same image. Compressive

strength values of the specimens with fixed plate are 1.74, 1.60, and 1.14 MPa. A higher strength was noticed in those specimens, probably since the specimens were exposed to an undesired moment as a result of the boundary conditions. Thus, they are not taken into account in the calculations. The compressive strength results of three tests with rotated plates were determined as 1.20 MPa, 0.90 MPa, and 0.87 MPa. Todorovic et al. (2019) found that the mean compressive strength of five masonry prisms with dimensions (width x thickness) of 300 x 100 mm was 0.97 MPa, while the average value obtained from our tests was 0.99 MPa. Compressive stress and average displacement measured from left and right Linear Variable Differential Transformers (LVDT), and the crack pattern at the end of the experiment for specimen 2 are shown in Figure 2.19d and e. A brittle response with sudden drop after peak load and higher capacity than the other two specimens was exhibited by Test 1. The softening portion of that specimen could not be obtained due to the malfunctioning of LVDT controlling the induced displacement. The maximum compressive strength in that test was also obtained in this experiment among 8 tests, including specimens tested by Todorovic et al. (2019) additional to our tests. Furthermore, it should be noted that the compression calibration of the model is conducted according to the mean strength of 8 tests, including those tested in this study and Todorovic et al. (2019).

Uniaxial and diagonal compression experiments for two AAC masonry batches are simulated for different G_f and R_{max}/d values and capacity results are summarized in Table 2.5. While the brittle response in tension was assumed for the METU experiments, a tensile fracture energy of 56.7 N/m was used for batch 2, the Pavia experiments, as suggested by Milanesi et al. (2018). The tension softening parameters were found by executing the flow-chart using provided tensile fracture energy (G_f) values, as explained in previous. All mechanical properties of AAC masonries and corresponding tension softening parameters determined based on the procedure explained in Section 2.4 are listed in Table 2.4.

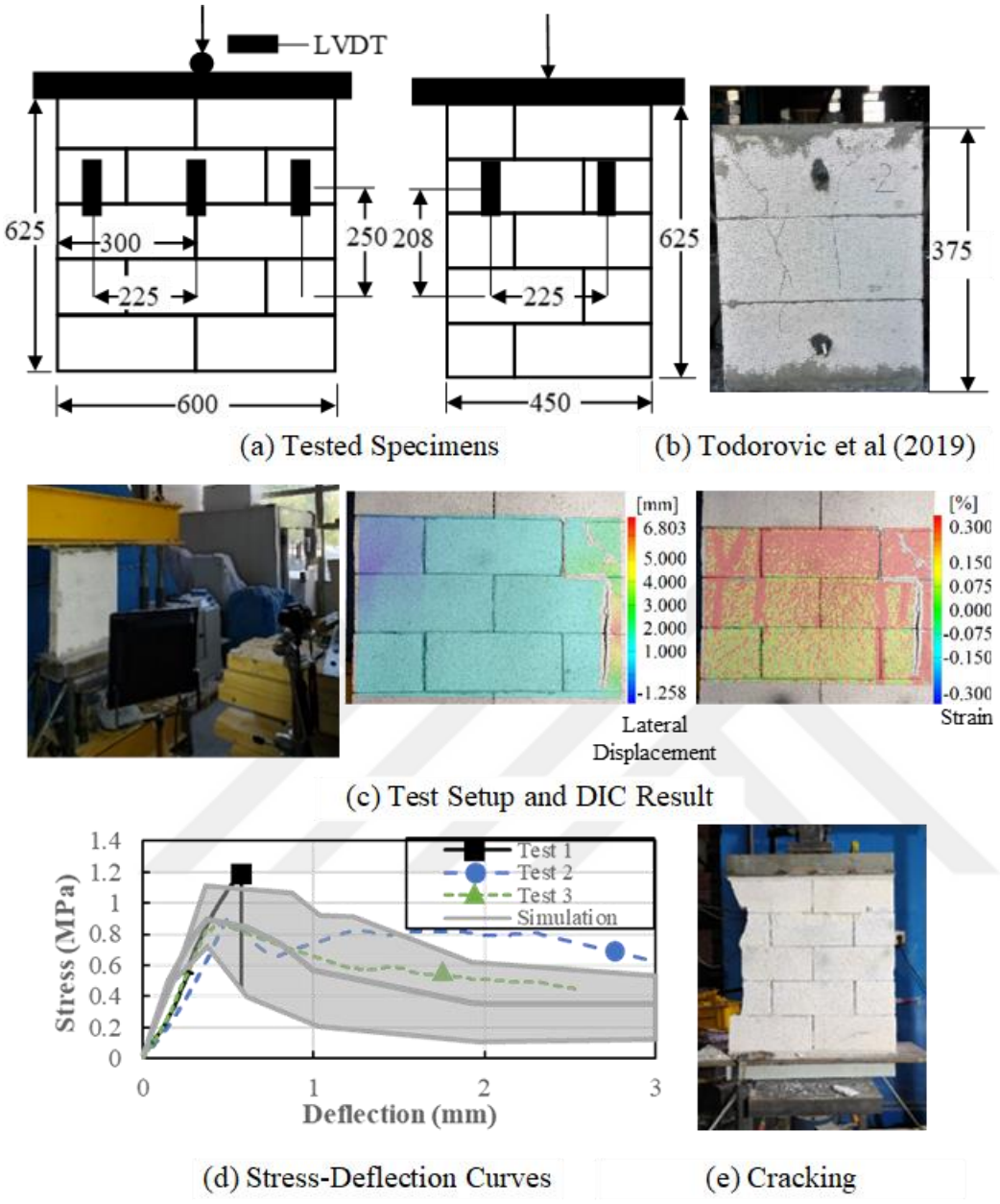
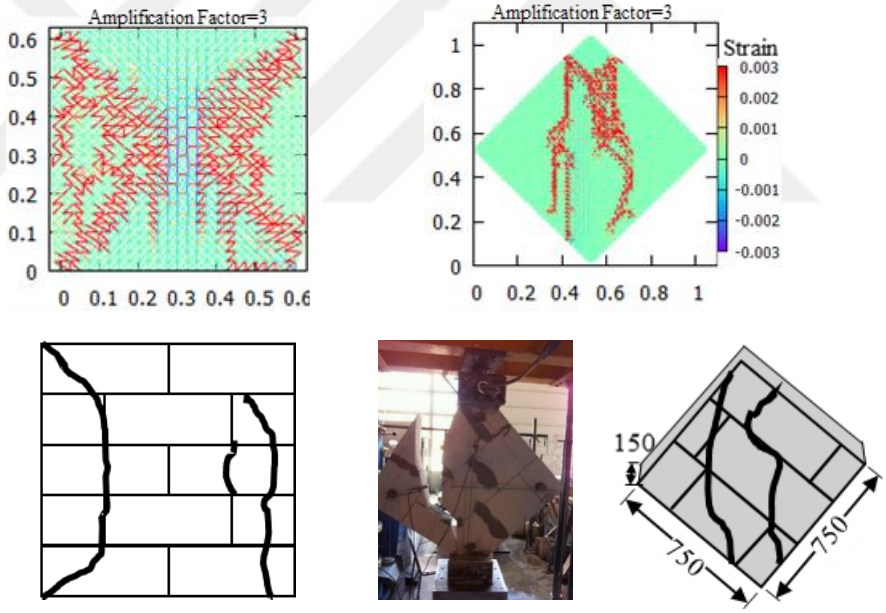


Figure 2.19. Compression and Diagonal Test Experiments and Simulations of Batch 1, METU Experiments

The randomness values were found by matching the uniaxial compression strength of masonry with the test results (Figure 2.13). The compression calibration procedure was applied and R_{max}/d was found as 0.125 for the AAC walls for both tests of batch 1. The range and mean of load-deflection responses of 100 simulations, the

comparisons of experimental and numerical results, and crack patterns from experiments and simulations are summarized in Figure 2.19d, Table 2.5, and Figure 2.20. In Figure 2.20, color contours denote the strain values of the lattice elements, and lines on the specimen represent the cracking observed in experiments. The experimental results appear to be in the range of 100 simulation results.

On the other hand, Costa (2007) performed six uniaxial compression tests for the AAC wallettes for batch 2, Pavia experiments. Three of each were tested in different orientations (vertical and horizontal, with 90^o rotated). The dimensions (length x width) of these two specimens were 940x1250 mm and 1000x940mm for vertical and horizontal specimens. The mean compressive strength of AAC masonries was reported as about 2.07 MPa. The same calibration procedure was performed, and R_{max} value was found as 2.0 mm for the grid size (d) of 30 mm.



(a) Cracking of Uniaxial Compression Test (b) Cracking of Diagonal Test

Figure 2.20. Cracks in Simulations and Experiments for Uniaxial and Diagonal Compression Tests of Batch 1

The performance of the calibrated model (i.e., for R_{max}/d and G_f) was first examined with the diagonal tests. Two and seven specimens with the dimensions

(length x width x thickness) of 750x750x150 mm (Figure 2.20b) and 630x750x300 mm were compressed diagonally for batch 1 and batch 2, respectively (Costa 2007; Demirel et al. 2015). According to ASTM E519-10 (2010), two steel loading shoes were used, and the length and height of the bearing of the loading head were determined to be about 150 mm and 100 mm, respectively. Thus, the top and bottom boundary nodes are restrained in both directions. The determined capacities from simulations and experiment results, and crack patterns can be found in Table 2.5 and Figure 2.20b.

Table 2.4. Material Properties of AAC Masonries

Properties (AAC)	**Batch 1 (METU)**	**Batch 2 (Pavia)[a]**
Thickness (mm)	10	30
Modulus of Elasticity (MPa)	1000	1498
Density (kg/m^3)	350	484
Tension Strength (MPa)	0.300[b]	0.278
Compression Strength (MPa)	0.9	2.0
Tensile fracture energy (N/m)	(Brittle)[b]	56.7
a_1[c]	1.50	1.50
a_2	1.51	140.00
a_3	1.52	600.00
R_{max}/d	0.125	0.067

[a] *Values were taken from Milanesi et al. (2018)*

[b] *Calibrated values from tests*

[c] *Tensile fracture energy parameters were found for d=5 mm*

While the capacity estimation for G_f and R_{max}/d values of 56.7 N/m and 0.067, respectively, agrees with the test results for batch 2, capacity results were found to be slightly lower than expected for batch 1. The reason may be partly attributed to the limited (two) number of experiments. Using a lower randomness value and a higher tension softening increases the uniaxial and diagonal compression capacity. The unique combination of R_{max}/d and G_f should be determined to employ

sufficiently accurate capacity estimations for both diagonal and uniaxial tests. Thus, in the case G_f value is not available, diagonal test results additional to uniaxial compression test results can be used to calibrate both values. Based on these calibrations and validations at the material level, the G_f, a_1, a_2 a_3 and R_{max}/d values were established for AAC masonry, as shown in Table 2.4.

Table 2.5. Results for AAC Masonry Diagonal and Uniaxial Compression Experiments and Simulations

	Batch 1 (METU)			**Batch 2 (Pavia)**			
	Uniaxial Compression Test						
		Simulation (d = 25 mm)			**Simulation (d = 30 mm)**		
		Brittle, $\frac{R_{max}}{d}$=0.125					
Results (MPa)	**Exp**	**Todorovic et al. (2019)**	**In this Study**	**Exp**	**Gf=56.7 $\frac{R_{max}}{d}$=0.067**	**Brittle $\frac{R_{max}}{d}$=0.05**	**Gf=56.7 $\frac{R_{max}}{d}$=0.05**
Number	8	100	100	6	100	100	100
Min.	0.87	0.65	0.70	1.98	1.70	1.39	1.93
Max.	1.20	1.20	1.13	2.25	2.50	2.21	2.88
Mean	0.98	0.92	0.90	2.07	2.04	1.84	2.29
Standard Deviation	0.10	0.11	0.09	0.10	0.16	0.15	0.16
	Diagonal Test						
Results (kN)	**Exp**	**Simulation (d = 20 mm)**		**Exp**	**Simulation (d = 30 mm)**		
Number	2	100		7	100	100	100
Min.	33.11	23.94		91.06	90.48	54.83	103.76
Max.	48.85	32.80		146.47	150.36	107.58	162.05
Mean	40.98	25.47		114.56	111.32	71.88	131.74
Standard Deviation	-	1.18		18.98	12.97	13.09	13.65

2.5.3.3 Discussion of Results for Compression Validations

The problem of locking is overcome by inducing grid perturbation with a novel calibration technique that allows one to select the magnitude of grid perturbation as

a function of the compressive strength and tensile fracture energy. The following conclusions can be drawn based on the results:

- The compressive strength was estimated with a reasonable accuracy by using mesoscale lattice models without a predefined nonlinear compression behavior.
- Compressive strength is dependent on the boundary conditions (LR and NR) even when the same perturbed grid is used in the simulations. This is in line with experimental evidence in the literature.
- While the use of tensile fracture energy approximately handles mesh sensitivity, it is observed that results are slightly dependent on grid orientation for uniaxial compression simulations.
- The model is able to capture the compressive behavior, including the slenderness effect for specimens subjected to pure compression.
- A mild softening in the uniaxial compression test is obtained. However, as the softening depends on boundary conditions in experiments, more tests are required to understand tensile fracture energy for compression, boundary conditions and compressive strength relations.

With the feature of representing compressive behavior with indirect tension response, the proposed modeling approach differs significantly from the available body of models, in which tension response was calibrated for material constitutive models to match the average response within the characteristic length and compression behavior was simulated with a phenomenological approach. It is demonstrated that compressive behavior can be estimated by using appropriate cracking models leading to compression failure as and indirect tension failure due to material instability rather than a plasticity-based constitutive model. This fundamental finding has the potential to offer new frontiers in modeling concrete structures under loading to failure.

In short, one of the important novelty of the present research is to simulate the concrete and masonry uniaxial compression response as an indirect tension failure

by using a homogenized lattice model modeling only the tensile behavior of concrete and AAC masonry and mesh randomization. Concrete in compression is assumed to be elastic. However, due to the mesoscale nature of modeling, splitting cracks and cover spalling due to compression are simulated as indirect tensile failures followed by lattice in the proposed lattice approach making it an attractive model with few parameters with the perturbation of the grid distribution.

2.6 Reinforced Concrete Modeling

Two additional element types for reinforced concrete (RC) simulations are needed in addition the concrete lattice network; the steel and bond elements. Thus for the reinforced concrete modeling, three element types are utilized as concrete, steel and the bond connecting concrete and steel nodes in the lattice network. The element representations for the simulation of a column specimen tested by Acun and Sucuoglu (2010) are shown in Figure 2.21.

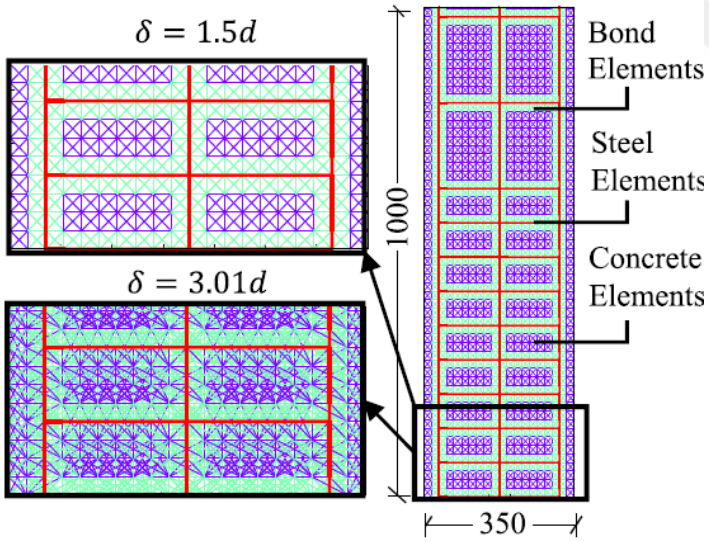


Figure 2.21. Representation of Three Types of Lattice Elements (Dimensions in Millimeter) (Acun and Sucuoglu 2010)

Steel reinforcing bars are represented with lattice elements at their centroid and they are assumed to have an elastic perfectly plastic load-strain response (Figure 2.22a).

In RC member simulations, two different horizon values, $1.5d$ and $3.01d$, were chosen. Within the horizon of the reinforcement lattice nodes, bond elements are used to connect steel nodes to concrete nodes. For the bond an elastic brittle response with a residual strength is used as shown in Figure 2.22b. The bond-slip constitutive models, e.g., the one by Murcia Delso and Shing (2015), divides the bond-slip resistance into two components, bearing and friction. The residual is equal to the frictional bond which is about 0.25 of maximum bond strength. However, the frictional bond coefficient should be thought within the scope of the modeling approach. With the two-dimensional lattice modeling, the number of lattice members acting as bond links should be thought together with the bond strength. The preliminary studies on the beam simulation were conducted by Aydin et al. (2018) for the constitutive model of bond elements. In that study, the bond strength was varied from 40% to 130% of the tensile strength of concrete elements. For smaller residual bond coefficient, premature bond failure was observed. Bond strength values higher than 70% were found to be successful in reflecting the slip behavior in RC simulations of different type of experimental, such as tension stiffening experiments. Thus, it can be concluded that 0.7 appears to be the optimum value of the bond coefficient. Therefore, the residual bond strength parameter ($\boldsymbol{\alpha}$) is chosen as 0.7 for RC member simulations to ensure that the deformed bar residual bond strength is reflected accurately. On the other hand, it should be noted that the number and lengths of bond elements increase as the horizon is increased. If the d value is large, for $\delta = 3.01d$, bond elements connecting steel nodes to concrete nodes are physically too far (increasing both stiffness and strength), hence, a slight strength enhancement due to increased bond is observed in all the conducted simulations, although the more isotropic response is conducted as shown in Section 2.1. This can be remedied by reducing the bond strength for $3.01d$ horizon, and adjusting constitutive law for the bond elements as a function of the horizon and minimum distance between nodes.

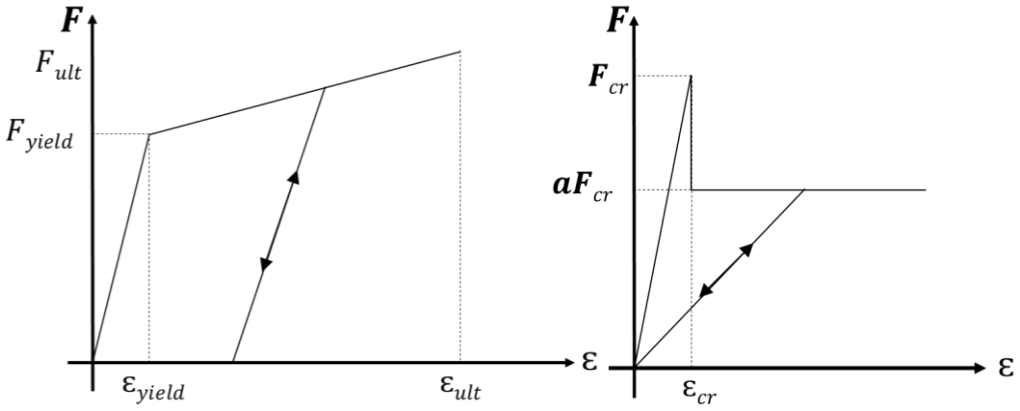
While the constant $\boldsymbol{\alpha}$ value is practical to define the overall interaction behavior of deformed bars with concrete for simulations, the actual bond behavior is affected by

rebar diameter and concrete mechanical properties. In this context, $\boldsymbol{\alpha}$ can be defined by considering that the ultimate bond force by calculating residual bond strength should be equal to the bond forces obtained by bond elements in the lattice network. Thus, the residual bond strength parameter ($\boldsymbol{\alpha}$) can be defined with the following formulation;

$$\boldsymbol{\alpha} = \frac{\tau_b \pi d_b}{0.621 w f_t \sqrt{2}} \tag{2.6}$$

Where τ_b is the residual bond strength, d_b is longitudinal bar diameter, f_t is the tensile strength of concrete, w is the member thickness. The free-body-diagram and the deriving formulations are shown in Appendix A. The $\boldsymbol{\alpha}$ value obtained from the equation was used for only the RC frame and AAC infilled frame simulations, as explained in Section 3.2 and Chapter 4 in order to exhibit the effect of bond strength on the simulation results.

The bond element unloading branch, origin-oriented, is the same with concrete elements. On the other hand, residual force after unloading with the initial stiffness of steel is introduced for the steel elements. However, it should be pointed out that all elements are monitored during the simulations whether unloading behavior is obtained. While none of the steel elements is unloaded, unloading responses for some of the concrete and bond elements can be obtained rarely in the stress localization zones due to redistribution of loading during the simulation. These parts become the non-load bearing zones, which means there would be no reloading on these elements that would have no contribution to the global response. Also, it can be concluded that there exist no unloading branch in the elements at the functional parts since the element responses were monitored during the simulations.



(a) Steel (b) Bond

Figure 2.22. Assumed Material Constitutive Models for (a) Steel and (b) Bond elements

2.7 Discussion of the Model

FEM-based approach is conducted in two mainstream directions as smeared and discrete models, as mentioned before. The main drawback of the smeared finite element modeling is the inability of demonstrating the actual separation due to cracking and having to operate with average strains across a gauge length rather than with actual crack openings. On the other hand, the issues on identifying crack locations as à priori, remeshing, pre- and post-processing, and the necessity of defining different constitutive models for the cracks and continuum parts are the key disadvantages of discrete crack models. In the defined approach in this study, the disadvantages in the discrete model such as remeshing are handled with the continuum approach as a single-phase medium. The crack propagation is presented directly and easily with calibrated truss network compared with the FEM-based damage plasticity. Cracking was modeled directly without conducting average approaches as in FEM. Also, the compression response was utilized as linear while the compression capacity was determined by perturbing mesh, which results in no need for nonlinear response in compression. Although there are a number of proposed macroscopic constitutive models to successfully simulate concrete

behavior with the FE methods (Balan et al., 1997; Lura et al., 2002; Tan et al., 2005; Cervenka and Papanikolaou, 2008; Koutromanos and Shing, 2012; Najafian et al., 2013), as mentioned before, these approaches require calibration of tension, compression, softening, hardening and failure surface evolution parameters. Thus, while great effort and careful implementation are needed for successful applications in FE methods, the lattice approach requires less parameters, easier implementation, and post-processing since cracking is represented with lattice elements, cracks are simulated in a discrete manner, which is an advantage over the continuum-based approaches.

The key differences of the lattice model in this study from the approaches of Cusatis (2011a) Bolander and Sukumar (2005) and Elias et al. (2013) are:

1) Calibration of lattice material properties to match the average response within the characteristic length rather than assigning standard material properties. This allows a much more practical lattice approach removing the need of modeling aggregate distributions and cement pastes.

2) assumption of homogeneous media for discrete lattice elements by providing calibrated multilinear softening parameters and randomization through mesh perturbation controlled with R_{max}/d in compression for the treatment of inhomogeneity so as to preserve practicality. This allows using simple 1D constitutive models.

3) Compression failure is treated as an indirect tension failure in this study, whereas other aforementioned works employed a plasticity-based constitutive model for concrete in compression.

The proposed lattice model and the strut and tie modeling share the common basis of using truss members to express the force flow; the strut and tie modeling is a macro model, whereas the lattice simulation is a mesoscale approach. Accordingly, struts in the nonlinear strut and tie models employ an average nonlinear stress-strain curve for concrete in compression. On the other hand, lattice simulation handles the

compression response with mesoscale lattice members that can simulate micro cracks leading to compression failure.

Recently, Moharrami et al. (2015) proposed a nonlinear strut and tie model to estimate the response of reinforced concrete columns. In their approach, ties are represented by nonlinear tension softening uniaxial models, whereas struts are modeled as nonlinear compression elements. In addition, the angles of the diagonal elements were arranged by considering aggregate interlock for shear induced failure of RC columns to overcome the restriction. The lattice approach in this thesis differs from classical nonlinear strut and tie models as the compression response is modeled with a tension-only model by using a mesoscale unstructured grid. In this way, it was possible to capture compression failure in the shape of an indirect tensile failure, which is a key novelty of the proposed approach. Nonlinear strut and tie models may provide practical methods to simulate the complicated response of reinforced concrete at the macro-scale level. However, the proposed lattice-based approach may provide further insight into concrete cracking and crushing with simpler uniaxial tensile constitutive models while requiring more computational effort.

Gerstle et al. (2013) used an alternating node connection scheme for the rebars to define reinforcement connection to a grid. On the other hand, the lattice model created for this study is a mesoscale approach where the grid size is kept in the millimeter scale. The grid spacing is small enough to represent the reinforcement at their correct locations, as a result of the square grid selection in this study. Owing to the mesoscale nature of the proposed lattice model with grid size in the order of several millimeters, such a match came naturally with the approach. Hence, a reinforcement decoupling as applied by Gerstle et al. (2013) was not deemed necessary. However, if the approach is extended as a macro model with lattice grids spaced at several centimeters, decoupling the reinforcing bar configuration from the lattice grid layout should be employed.

It should be noted that reinforcement running in the direction of the lattice and spaced at multiples of the lattice spacing can be modeled. Reinforcement locations should

be carefully selected while choosing the grid sizes. Also, reinforced concrete elements are conventionally reinforced with horizontal and vertical bars. Hence, the proposed lattice approach, without loss of generality, can handle almost all practical problems. For inclined reinforcement, one must use stepped reinforcing bars in the lattice model.

No special confinement model was employed. The confinement effect was due to the lateral restraining effect of the stirrups. It is completely related with indirect expansion of the beam and column. The model gives so close results with each other even mesh is rotated as 45 degrees, as discussed further in section 3.1.4.3. However, the two-dimensional lattice approach has obviously limited capability in modeling confinement imposed by the stirrups. For a more accurate representation of the column confinement and capturing confinement efficiency (Saatcioglu and Razvi, 1992), completely, a three-dimensional lattice approach is needed, which is beyond the scope of the study.

The crack directions did not align with the lattice directions, the principle direction of the mesh, for plain concrete simulations in a previous study by Aydin et al. (2018). Reinforcement patterns used in the experimental studies create a number of high stiffness and high strength lines in the proposed two-dimensional computational domain. In addition, although the problem is inherently three-dimensional, in order to remain practical within the scope of the thesis, the model is kept two-dimensional. The bond elements that connect steel and concrete nodes have a residual strength value, as discussed earlier. As a consequence of this, the computational results in the next chapter show inelastic strains concentrating around the reinforcement lines. Basically, due to the presence of reinforcement and bond elements, a more significant concentration of cracks was observed around the reinforcement regions. This may appear as a disadvantage of the lattice model to clearly present the crack locations; however, such micro-cracking, usually not visually observed in the tests, may actually exist at small scales. In fact, although we are not able to observe it directly in experimental studies, there is high degree of damage around the reinforcing bars due to bond transfer. As the results obtained from the simulations

can be seen as width-averaged quantities which are not the same as cracks observed in the experiments; hence, naturally, reinforcement pattern is reflected in damage patterns.

Two-dimensional mathematical modeling, as opposed to a three-dimensional model, is proposed since all the test cases presented in the study (except cylindrical specimens) have an axis of symmetry along the loading direction and were subjected to in-plane loading only and there is no out-of-plane load in any of the simulated cases. These limitations allow 2D modeling of the problem as opposed to more computationally demanding 3D models. Thus, two-dimensional modeling is conducted instead of using three-dimensional models for the sake of computational efficiency. This study can be thought as an extension of those 2D-oriented models with a different approach in terms of material modeling.

The lattice modeling approach in this study establishes a balance between model complexity and engineering accuracy for damage estimations. The model keeps a good balance between the simplicity of implementation/calibration with the sophistication of its behavior and capabilities. It was not preferred to use complicated plasticity, damage or frictional slip concepts within the scope of the study such that practicing engineers interested in obtaining the response of RC elements under distress could employ the approach by using any standard finite element software platform.

The simple lattice modeling approach herein is easy to implement in the available engineering software or research-oriented analysis platforms by conducting the exhibited calibration procedures with the basic two force elements. This is a feature expected to increase the impact of the proposed of the approach both in research and practice. While it would be ineffective for the analysis of the entire structure with a mesoscale lattice network by using very long elements, which is the nature of mesoscale approaches, a more realistic response is obtained, and detailed understanding of the nature of nonlinearity is provided. Instead, the nonlinear part of

the structures can be conducted such as plastic hinge region of columns, anchorage, bond, etc.

2.8 Bi-material (Reinforced Concrete+AAC) Modeling

For infill walls subjected to combine in-plane and out-of-plane loadings, 3D approach is a must for modeling. Meso-scale models can indeed be two-dimensional and they are capable of simulating AAC masonry and masonry infilled wall behavior as presented past studies (Milanesi et al. 2018, Dolatshahi and Aref 2011, Khojasteh 2017). The lattice approach in this study was used by introducing bi-material modeling to simulate AAC masonry-infilled RC frame simulations. Two additional element types, in addition to the reinforced concrete model, were defined. The first one represents the AAC masonry elements, which also adopts the concept of a piecewise linear softening diagram for the tensile regime as same with the concrete elements. The softening parameters, a_1, a_2, a_3 of the tensile behavior of AAC elements were found to be similar to the concrete elements such that lattice simulation result of global tensile stress deflection curve, area of which is tensile fracture energy, matches the uniaxial stress-average displacement response of the tension test result within a specific gauge length. In the absence of reliable test data, the model of Cornelissen et al. (1986) is employed as the "correct" test result to calibrate the input parameters for softening part. Secondly, a special interface element, called "foam element", was introduced to simulate the interaction regions filled with foam between the wall and reinforced concrete frame members. The behavior of the interface elements connecting the AAC wall and concrete elements with foam material is selected as hyperelastic in compression, while the capacity is assumed as zero in tension (top left in Figure 2.23). The compressive modulus of elasticity multiplied by the cross-sectional area of foam elements is formulated as;

$$EA(\varepsilon) = (EA)_i + (EA)_i(m_t - 1)(-\varepsilon)^{n-1} \text{ for } \varepsilon \leq 0 \qquad (2.7)$$

Where ε is the strain, $(EA)_i$ is the initially defined modulus of elasticity multiplied by the cross-sectional area, n is the parameter adjusting the polynomial degree and m_t is the multiplication value of initial $(EA)_i$ at strain value of -1. The same formulation is applicable for the unloading branch so that no energy dissipation can occur. In the interface region, the diagonal elements of the lattice framework were removed due to the very low shear resistance of the foam or leveling mortar. Geometric nonlinearity was incorporated for all the elements except the interface elements so that only interaction in the normal direction was considered.

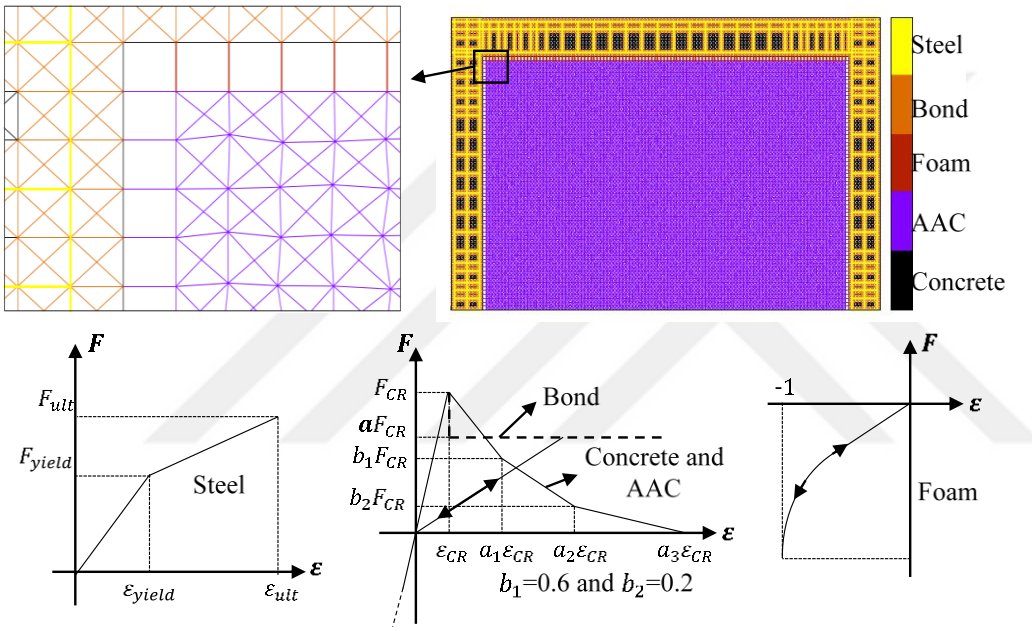


Figure 2.23. Overview of the modeling approach: element types and corresponding constitutive models

All element types that are used in this study and their respective constitutive models are shown in Figure 2.23. It seems that the nature of both concrete and AAC is inhomogeneous. However, treatment of such inhomogeneity at the mesoscale level requires modeling of components such as aggregates, cement pastes, and pores. This would further complicate the computational approach and make the calibration process very challenging due to the uncertainty in material parameters. Hence, homogeneous material properties were assumed by calibrating multilinear softening

curve in tension to represent the behavior within characteristic length and applying randomness through mesh perturbation controlled with R_{max}/d in compression for the treatment of inhomogeneity due to preserving practicality.

2.9 Solution Procedures

In this study, two different solution schemes were used. Firstly, Sequentially Linear Analysis (SLA) (Rots 2001, Rots et al. 2006, 2008) was employed for the material calibration of the model in tension. The procedure evolves a saw-tooth curve, and the sequence of the analysis is determined by the damage of the elements instead of force or displacement increments. Basically, after applying unit load to the defined places, linear elastic analysis is employed, and then the internal forces obtained in all elements are determined. According to the critical element closest to its capacity, the scale factor is captured and applied to the discretized system. Thanks to a series of linear elastic solutions inherently, SLA is a simple solution algorithm to solve nonlinear problems with obtained any convergence problems even if snapback behavior is desired during the nonlinearity. Using always positive stiffness enables to simulate a constitutive model, which is steep function like a multi-linear softening curve, easily. Aydin et al. (2018) used this solution algorithm successfully by emphasizing its simplicity and functionality. The application of the SLA for the constitutive response of concrete elements can be seen in Figure 2.24. However, the main disadvantage of using saw-tooth curve is the difficulties when conducting non-proportional loading (Pari et al. 2020). This type of loading is obtained in almost every structure. For this reason, this solution methodology was conducted for only tension calibration.

Secondly, explicit time integration methods have the advantage of being non-iterative, suitable for parallel programming, and simulating large deformations and local instabilities without any convergence problems, which are very crucial for the nature of the model with the way of capturing compression failure. Therefore, an

explicit time integration method was used to solve the equation of motion for the lattice models.

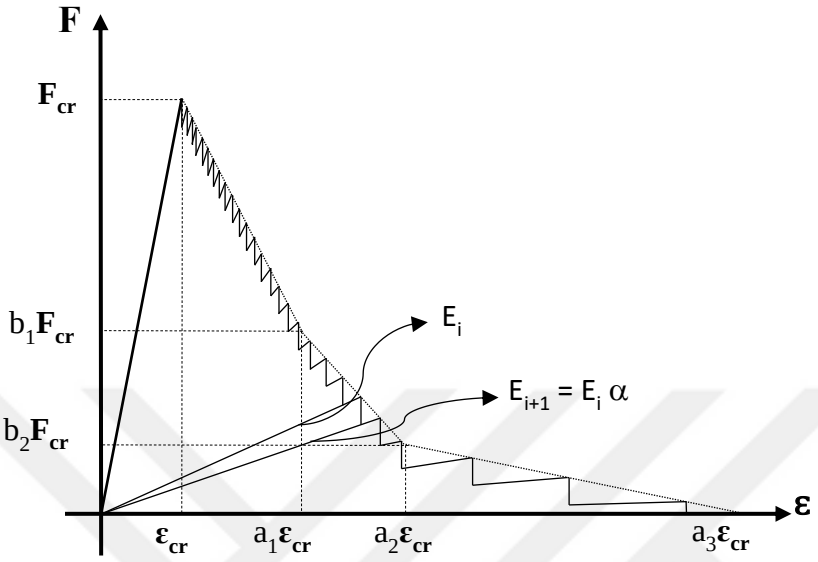


Figure 2.24. Application of the SLA for Tension Response of Lattice Elements

An explicit numerical integration is used to solve the equation of motion given in Eq. (2.8), where a lumped diagonal mass matrix, $\boldsymbol{m}$, along with a mass proportional damping matrix, $\boldsymbol{c}$ are employed.

$$\boldsymbol{m}\,\boldsymbol{a_i} + \boldsymbol{c}\,\boldsymbol{v_i} + \boldsymbol{r_i} = \boldsymbol{F_i} \tag{2.8}$$

Above $\boldsymbol{r_i}$ is the restoring force vector, $\boldsymbol{a_i}$, $\boldsymbol{v_i}$ are the acceleration and velocity vectors, respectively, and $\boldsymbol{F_i}$ is the forcing function vector at time *i*. Damping matrix was approximated using Rayleigh damping (5%) in all the simulations. The velocity of all the simulations conducted in this study was sufficiently small to vanish inertial effects, which means the damping matrices were always multiplied with very small values. The equation of motion was solved by using the method of Chung and Lee (1994) with the steps summarized below:

1) Read the restoring force ($\boldsymbol{r_i}$) and current displacements ($\boldsymbol{u_i}$).

2) Compute the acceleration at time i+1: $\boldsymbol{a_{i+1}} = \boldsymbol{m}^{-1}(\boldsymbol{F_i} - \boldsymbol{c}\,\boldsymbol{v_i} - \boldsymbol{r_i})$

3) Compute the displacements at time step i+1: $\boldsymbol{u_{i+1}} = \boldsymbol{u_i} + \Delta t \boldsymbol{v_i} + \beta_1 \boldsymbol{a_i} + \beta_2 \boldsymbol{a_{i+1}}$

4) Compute the velocities at time step i+1: $\boldsymbol{v_{i+1}} = \boldsymbol{v_i} + \gamma_1 \boldsymbol{a_i} + \gamma_2 \boldsymbol{a_{i+1}}$

5) Repeat all steps for the incremental time steps.

Above $\beta_1, \beta_2, \gamma_1, \gamma_2$ are the coefficients of integration and Δt is time step. In order to calculate the coefficients of integration, integration parameter, β, is chosen as 1.01 such that it is between 1 and $28/27$ (Chung and Lee 1994). Coefficients β_1, β_2, γ_1, and γ_2 used in the time stepping are a function of the time increment as given below:

$$\beta_1 = \Delta t^2 (\frac{1}{2} - \beta), \beta_2 = \Delta t^2 \beta, \qquad \gamma_1 = -\Delta t/2, \qquad \gamma_2 = 3\Delta t/2 \qquad (2.9)$$

An explicit dynamic finite element analysis program was prepared by using truss elements that are capable of undergoing large deformation using an updated Lagrangian scheme. P-delta effect (from geometric nonlinearity) can also be simulated with this way. The loading durations were kept sufficiently small to simulate quasi-static loading conditions and to eliminate dynamic amplification effects and minimize the kinetic energy.

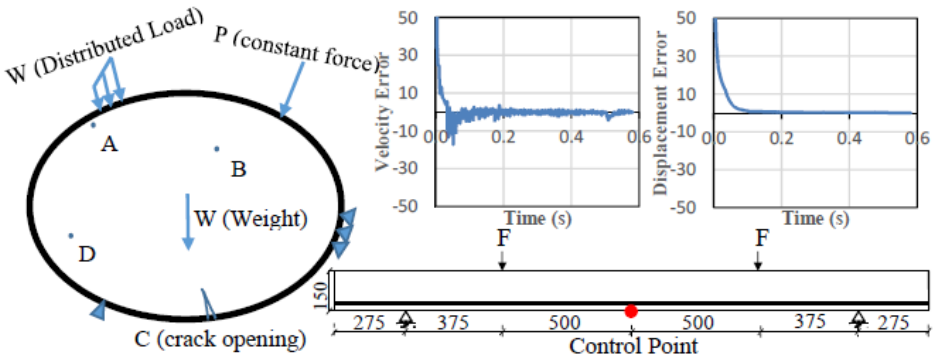
In order to extend the capability of the explicit dynamic analysis platform to perform inelastic static analysis, a PID control algorithm was implemented. Most of the simulations in this study were tested by using a displacement-controlled approach using the feedback from a Linear Variable Differential Transducer (LVDT). In order to simulate such specimens with an explicit time integration a PID control scheme is used inspired from mechanical control systems. In fact, most of the testing equipment uses the PID algorithm to control the hydraulic equipment. By adapting the PID control in the explicit time integration we were able to exactly simulate the testing conditions. If explicit integration were used without any control algorithm, it would not be possible to obtain the softening region of the specimens tested in a displacement-controlled manner. Furthermore, if dynamic tests are simulated, using just explicit dynamics analysis would be more physically realistic. In general, a PID

controller is a loop feedback controller used in various industrial control systems. The algorithm can be expressed as:

$$\dot{F}(t) = K_p e(t) + K_i \int_0^t e(t)dt + K_d \frac{de}{dt} \quad (2.10)$$

Above, $e(t)$ represents the tracking error, K_p is the proportional gain coefficient, K_i is the integral gain coefficient and K_d is the derivative gain coefficient. Since the formulation is used for displacement or load control in structural analysis in this study, while the left-hand side of the equation is assumed as the rate of the forcing function $F(t)$, the right-hand side is the function of the error function $e(t)$. In our problem, assuming the control variable be $u(t)$ which is the desired displacement value at time t and the displacement from the computational model be $u_p(t)$, the error function can be defined as $e(t) = u(t) - u_p(t)$. On the other hand, the same manner should be implemented for the derivative component of the equation by using differences for desired and calculated velocity values at time t. Desired velocity value at time t is calculated with the user-defined desired displacement value at time t. Since acceleration is not desired at any t value, the integrated part of $e(t)$ is a function of acceleration calculated from the computational model. Thus, the rate of $F(t)$ is defined by the integro-differential equation as a function of $e(t)$ as in Eq. (2.7). Eq. (2.7) was solved at each step of the explicit integration to update the value of $F(t)$. For an arbitrary system shown in Figure 2.25(a), the rate of $F(t)$ can be controlled in multiple ways. Some examples of control are displacement rate at point A, relative displacement rate between points A and B, crack width rate of change at C, rate of stress or strain change at D. Control target can easily be changed during the history of loading. Upon transition from elastic to an inelastic state $\dot{F}(t)$ assumes negative values resulting in the ability of capturing the softening response with sufficient accuracy. PID constants were selected based on the classical work of Ziegler and Nichols (1942). Selected parameters and control scheme for each simulation are presented later. This PID control scheme was implemented within the lattice simulation platform and employed in the solution of the problems presented in the next sections. The example of control method is shown in Figure 2.25(b) for

the beam tested by Walraven (1978) which is also the example provided in the next section with 12.5 mm grid size and 3.01 horizon. The point which is controlled by the PID is the velocity of the bottom point of the midspan section of the beam. The errors are calculated as (computed-desired)/desired x100. The numerical solutions show that PID has good accuracy in controlling the velocity and the corresponding displacement of the chosen location. In short, an explicit dynamic numerical integration is used; and PID feedback is implemented to solve a quasi-static problem with a dynamic solver. Lattice models in this study were solved by using this solution methodology instead of SLA except direct tension test to calibrate softening parameters.



(a) Arbitrary System (b) Beam Test (Walraven 1978)

Figure 2.25. PID Control Kinematic Representation and Example

2.10 Summary of Calibration of Modeling

Tensile softening parameters of the concrete and AAC lattice elements, bond elements, interface elements in the mesh, and perturbation of nodes are the key parameters of the model. First, with the input parameters of concrete as f_t, G_f and E_t, tension curve of corresponding material with softening parameters should be created by using the flowchart in Figure 2.5. Then, with using f_c value addition the other parameters, R_{max}/d value is determined with 5 and 100 simulation results by

applying compression calibration, explained in Figure 2.11 for concrete and Figure 2.13 for AAC masonry, respectively, to handle compressive failure in the system. In short, for concrete and AAC masonry members, the model has only 3 input parameters (f_t, G_f and E_t) in tension to calibrate tension softening function parameters and 1 input parameter (f_c) in compression to determine the perturbation value of the nodes for concrete and AAC masonry members, although it does not match Poisson's Ratio in the linear elastic range. For RC simulations, steel elements are placed in the appropriate location at the discretized domain, and steel nodes are connected to the nearest concrete nodes by using bond elements. F_{yield}, ε_{yield} and ε_{ult} values are used to construct the constitutive model of steel elements as shown in Figure 2.22a. For bond elements, the material model is assumed as shown in Figure 2.22b. Finally, AAC masonry walls and RC frames can be connected with special interface elements, as mentioned in Section 2.8. An overview of all element types and corresponding constitutive models can be seen in Figure 2.23. The stand-alone computational framework of the presented lattice approach capable of all mentioned properties of the model was prepared scratch in Fortran programming language.

CHAPTER 3

REINFORCED CONCRETE AND MASONRY STRUCTURE MODELING AND VALIDATION

Seven reinforced concrete member and two portal frame simulations were conducted to validate the accuracy of the lattice modeling for RC members and structures within the scope of this study. Reinforced concrete column, beam, wall, and portal frame tests conducted by different researchers were compiled for this purpose. Specimens failing in shear and/or flexure were selected to test the ability of the lattice analysis in capturing the member load-deformation response. Also, over-reinforced beams were simulated in order to investigate the performance of the model on the concrete crushing response so that it is in the same manner with the uniaxial compression response. A discussion of the results and their comparisons are presented below for the three groups of members. After validation problems for the RC concrete members, two RC portal frame tests were simulated.

3.1 Reinforced Concrete Members

In this part, the lattice truss model is validated for numerous RC members, i.e., columns, beams and walls failing under different modes. The presented results compare the experimental cyclic and monotonic force-displacement response of RC beams, columns and walls, with the monotonic backbone response obtained using the proposed lattice model. The summary of the test specimens, material properties, constitutive model, and solution control parameters for members are presented in Table 3.1. Tests were selected based on their failure modes and acceptance of the results in the engineering community. The column studies are already in the well-recognized PEER Database. In these column tests, compressive strength was always reported, while the tensile strength was not since it has little bearing for the column

behavior. In fact, the influence of tensile strength was studied with deterministic sensitivity studies later in this chapter. Material properties, whenever available, were taken from reported values and they were based on relevant standards if not given.

Table 3.1. Properties of the Test Specimens of Reinforced Concrete Members

Parameters	Column		Beam				Wall	
	Acun and Sucuoglu (2010)	Ozcebe and Saatcioglu (1987)	Foster and Gilbert (1998)	Walraven (1978)		Belgin and Sener (2008)	Thomsen and Wallace (1995, 2004)	Aldemir et al. (2017)
				Grid 1	Grid 2	S5x7 L11x30		
f_t (MPa)	1.78[b]	1.917[b]	6.2	2.5		1.57 1.72	2.03	1.85[b]
f_c (MPa)	25.9	30	80	-		20 24	42.8	28
E_t (GPa)	23.92[c]	25.743[c]	47.7	25.0		21.019 23.025	31.03	24.87[c]
G_f (N/m)	75	81[d]	117[d]	60		50[d]	75	75
f_y (MPa)	454	448	460	440		530 514	414	360
E_s (GPa)	200		210			200		
N (kN)	632	600	-	-		-	378	-
d (mm)	17.5 35	25	10 20	12.5	25	5 20	19	20
K_px10^9	1.0		1.0	6.00		1.0		
K_ix10^7	10		1.0	3.00		10		
K_dx10^4	1.0		1.0	1.35		1.0		
a_1[a]	1.5	1.5	1.5	1.5		1.5 1.5	1.5	1.5
a_2	80	70	20	30		60 60	80	70
a_3	350	350	100	200		320 300	350	360
R_{max}/d	-					0.080 0.075	-	

[a]*These values are for δ=1.5d and d=5 mm. For δ=3.01d, a_1 is taken as 3.01.*

[b]*These values are found by using TS 500 (TSE 2000).*

[c] *These values are found by using ACI 318-11(American Concrete Institute 2011)(i.e. $E_c = 4700\sqrt{f_c}$)*

[d]*These values are found by using CEB-FIP model code 1990 (CEB-FIP 1993).*

Tensile softening parameters (a_1, a_2, a_3) were calibrated by using the workflow for all concrete specimens explained in Section 2.4. One can expect the value of "a_2" to

be increased while G_f increases from left to right for the column specimens in the table. Parameter a_2 is not the only parameter to control G_f. In fact a_3 plays a crucial role in this regard. It is observed that parameter a_2 mainly controls the softening region just beyond the peak strength. Simulation data for column, beam and wall simulations are presented in Table 3.2. The velocity of the lateral loading point was taken as about 0.025 m/s for all the simulations.

Table 3.2. Information regarding Time Step, CPU Time, and Lattice data for the Results Presented in This Study

Simulations	d (mm)	δ	Time Steps (sec.)	Durations Per 10000 Steps (sec.)	Number of Particles	Number of Elements	Max. Disp. (mm)
Column							
Acun and Sucuoglu (2010)	17.5	1.5	2.5 x 10^{-8}	8.78	2667	10226	105
		3.01		24.94		33096	
	35	1.5	1.0 x 10^{-7}	2.28	704	2593	
Ozcebe and Saatcioglu (1987)	25	1.5	8.0 x 10^{-8}	2.14	675	2522	110
		3.01		6.42		8388	
Foster and Gilbert (1998)	10	1.5	5.0 x 10^{-8}	69.04	20841	82100	11
		3.01		214.22		284202	
	20	1.5	1.0 x 10^{-8}	16.82	5301	20570	
Beam							
Walraven (1978)	12.5	1.5	1.0 x 10^{-8}	7.45	2405	9028	11.5
		3.01	4.0 x 10^{-8}	23.04		30124	
	25	1.5	2.5 x 10^{-8}	2.00	651	2306	
		3.01	2.5 x 10^{-7}	5.72		7332	
Wall							
Thomsen and Wallace (1995, 2004)	19	1.5	1.0 x 10^{-8}	41.72	12998	51211	72
		3.01		120.21		162903	
Aldemir et al. (2017)	20	1.5	5.0 x 10^{-8}	66.88	20385	80684	20
		3.01		208.09		280260	

Note: The computer has Intel(R) Core(TM) i5-4590 Processor and 8 GB Installed Memory (RAM)

An effort was made to distinguish the cracks based on their strain values in the strain distribution figures. In order to clearly demonstrate the crack patterns, the following steps were used to post-process crack locations: i- The highest elongation location in a crack region of the lattice network was determined. ii- The crack direction was calculated based on the crack width-weighted average of lattice element directions. iii- The neighboring lattice with the largest average elongation was selected as the next crack location. iv- Process was continued until an uncracked location was reached. Thus, the lines on the estimated strain distribution images in the figures are compared to the observed cracks during the tests.

3.1.1 Column Simulations

Lattice models were constructed by using different grid sizes (i.e., 17.5 mm and 35 mm) and horizons ($1.5d$ and $3.01d$) to test their effect on the response (Figure 2.21). In these models, three types of elements, as described in the Section 2.6, were used to model concrete, steel reinforcement, and bond. Bond elements were connected from the steel nodes to concrete nodes within the prescribed horizon. First, a full-scale reinforced concrete column tested by Acun and Sucuoglu (2010) was simulated (Figure 3.1a). The purpose of these series of tests was to observe the energy dissipation capacity of well-detailed RC columns subjected to different loading histories.

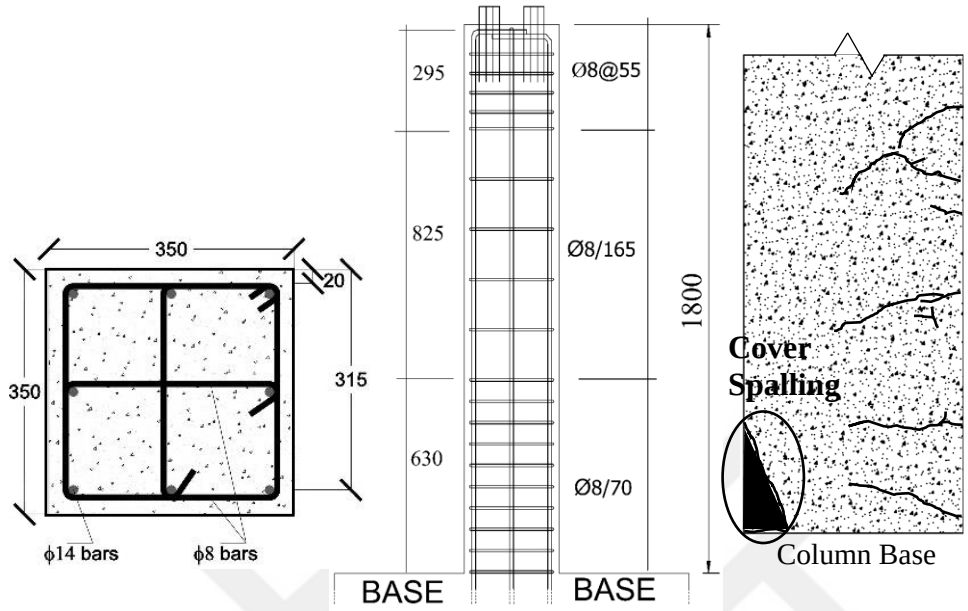
The column test specimen was first subjected to a constant axial load (632 kN) and then increasing cyclic lateral displacement excursions were applied. The specimen exhibited a ductile flexural failure mode with steel yielding followed by cover spalling. The grid sizes were taken as the integer dividers of the stirrup spacing in order to provide a uniform mesh size while placing the reinforcement at their exact locations. The foundation of the specimens and the strong floor were not modeled, and fixed supports were placed at the bottom boundary of the column. Lateral load and top displacement results and damage patterns from the simulations and the

experiment are shown in Figure 3.1 and Figure 3.2, respectively. In Figure 3.2, contours denote the strain values of the lattice elements.

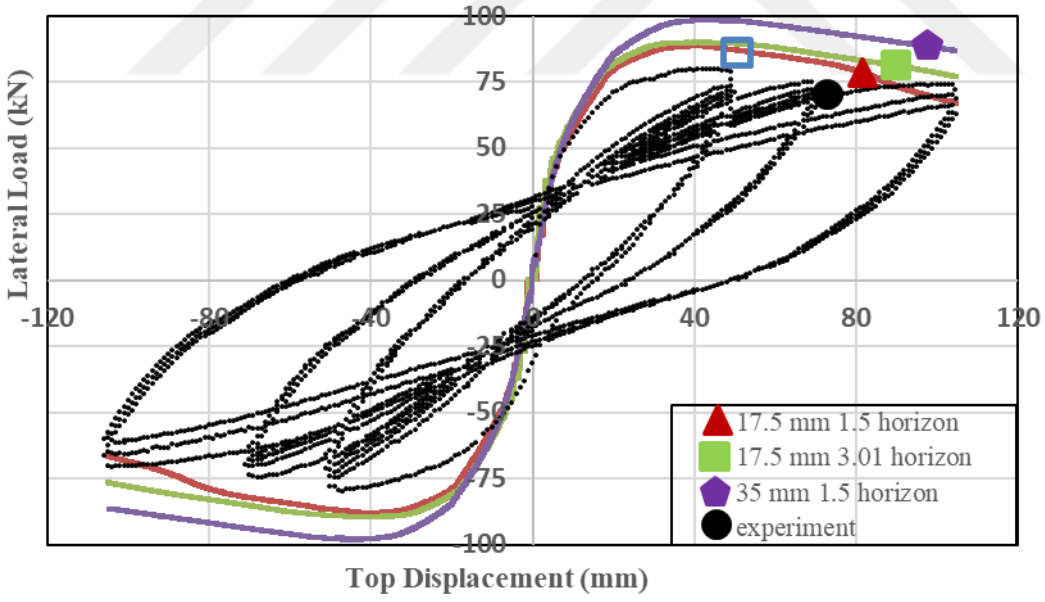
In the figures presented strain distribution in simulations, several close-up views are provided to clearly show concrete spalling. Also, it can be observed that there are multiple shear cracks in the test result. Similarly, the numerical simulation exhibits many inclined shear and flexural cracks. It was observed that the lateral load carrying capacity estimations from the simulation with the largest grid size had the largest error. Upon decreasing the grid size, a better agreement with the test result was observed. The lateral load carrying capacity of the test specimen was overestimated by about 10% for the $1.5d$ horizon with 17.5 mm grid spacing. The absence of cyclic modeling appeared to be the reason of the observed overestimation of the lateral load carrying capacity. The strength degradation after the peak was found to be more severe in the simulation than that observed in the test. Crack developments were not visually reported by Acun and Sucuoglu (2010) and Acun (2010). However, it was reported that flexural cracking extended 60 cm from the base of the column. Crack development and rebar strains at about 2.5% interstory drift ratio for the $1.5d$ horizon with 17.5 mm grid spacing model are shown in Figure 3.1d. It can be observed that the flexural cracking zone is approximately 60 cm from the base agreeing well with the experimental observation. The flexural crack spacing was approximately equal to the stirrup spacing. The computational rebar strains show significant yielding of both longitudinal and transverse rebars. The estimated flexural crack spacing of about 10 cm from the lattice simulation was similar to the flexural crack spacing from the experimental observations.

It should be noted that crack spacing was observed clearly for the $1.5d$ horizon with 17.5 mm grid spacing model, which gave the closest estimate of the capacity. The 17.5 mm with the $3.01d$ horizon lattice model estimated slightly higher lateral load carrying capacity compared to the $1.5d$ horizon case. Compression induced cover spalling was captured as a result of the local instability in the compressed lattice

elements. These results show the ability of the lattice modeling in capturing the response of a reinforced concrete member failing in a flexural mode.

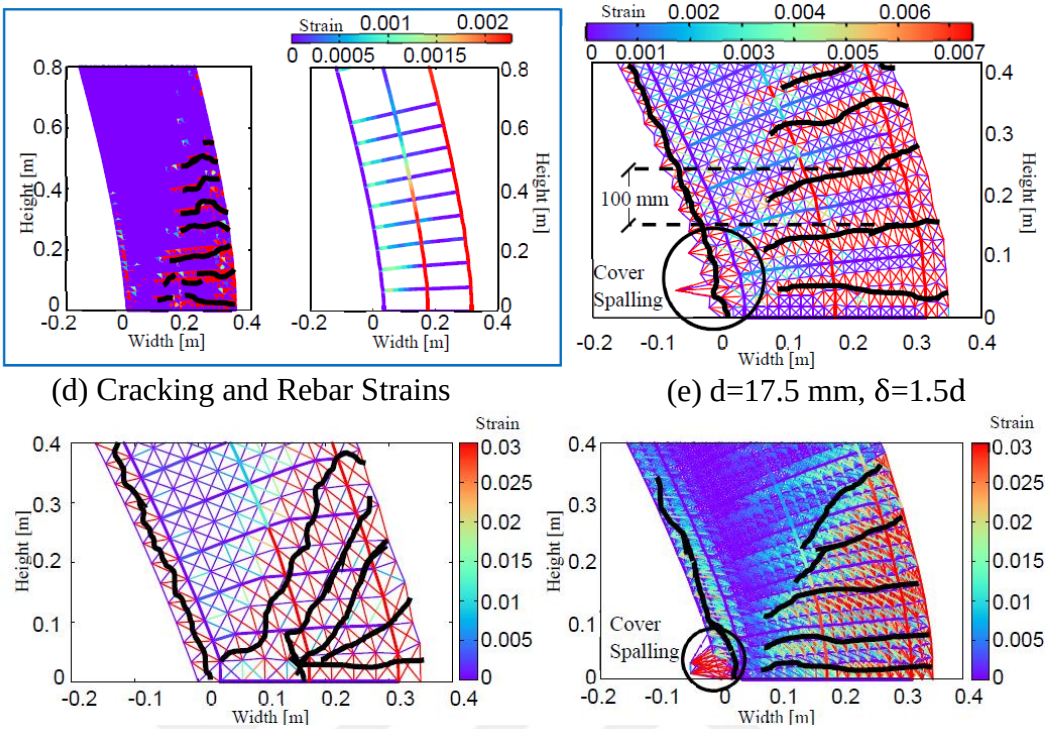


(a) Test Specimen (b) Cracking in Experiment



(c) Load-Deflection Curves

Figure 3.1. Full Scale Reinforced Concrete Column Simulation: (a) Dimensions and Details of Test Specimen (Dimensions are given in mm); (b) Observed Crack Pattern; (c) Load-Deflection Comparison (Acun and Sucuoglu 2010).



(d) Cracking and Rebar Strains (e) d=17.5 mm, δ=1.5d

(f) d=35 mm, δ=1.5d (f) d=17.5 mm, δ=3.01d

Figure 3.2. Full Scale Reinforced Concrete Column Simulation: (d) Cracking and Rebar Strains at about 2.5% Drift Ratio for d=17.5 mm, $\delta = 1.5d$; (e) d=17.5 mm, $\delta = 1.5d$; (f) d=35 mm, $\delta = 1.5d$; (g) d=17.5 mm, $\delta = 3.01d$ (Amplification Factor = 10 for (d)-(g)) (Acun and Sucuoglu 2010).

The full scale reinforced concrete column specimen (U4) from Ozcebe and Saatcioglu (1987), which exhibited a flexural-shear failure mode, was simulated by using the lattice modeling approach in a quasi-static monotonic manner. The lattice models and the details of the specimen and are shown in Figure 3.3 and Figure 3.4a, respectively. The lattice model was constructed by using a 25 mm grid size with $1.5d$ and $3.01d$ horizon sizes. A similar loading strategy to Acun and Sucuoglu (2010) test simulation was used (Figure 3.1a) i.e. first the axial load of 600 kN was applied and then lateral displacement with velocity control was induced at the top nodes. Lateral load and top displacement comparisons and the damage patterns from the experiment and simulations are shown in Figure 3.4b-e. It can be observed that the overall load-deformation response was simulated with a reasonable accuracy for the

$1.5d$ horizon lattice model. The strength degradation with increasing displacement demands was successfully duplicated with this model. The $3.01d$ horizon model over-estimated the lateral strength and the ductility of the column. The key reason could be attributed to the strengthening effect of the increased horizon in the regions of tensile stressed concrete and bond elements. The higher horizon size enabled slightly higher capacity estimation because residual forces at the bond regions for $3.01d$ are higher than the $1.5d$ horizon size since bond elements were connected the steel nodes to very far concrete nodes with same residual force for all elements individually, as mentioned in Section 2.6. On the other hand, the ductility of the column was related with the progressive compressive failure as indirect tension response with uniform mesh distribution. The perturbation effect of the higher horizon sizes is not the scope of this study. Similar to the result from the previous simulation, the cover spalling was captured by the lattice model in the form of lateral splitting followed by the lattice instability. In short, it can be stated that the classical lattice model (i.e. the $1.5d$ horizon case) was more successful compared to a larger horizon model in simulating the reinforced concrete shear response.

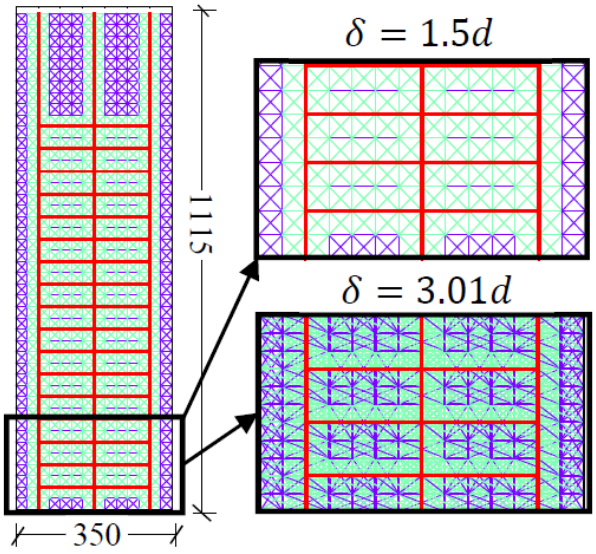
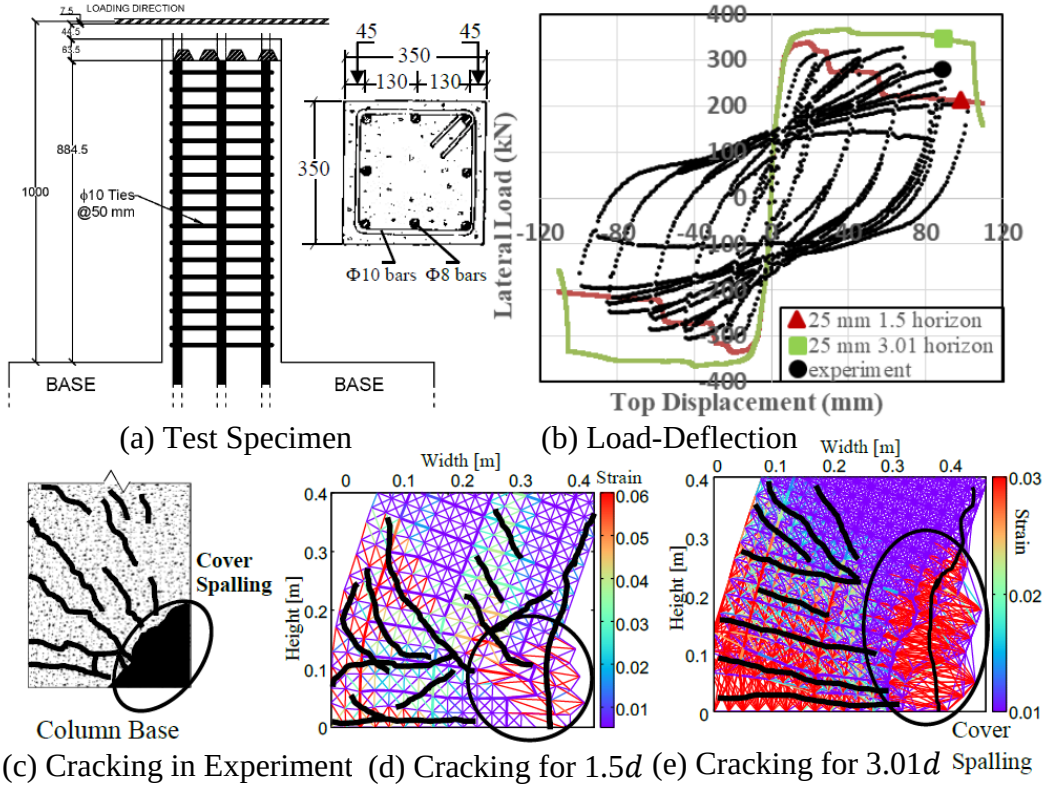


Figure 3.3. Representation of Lattice Model (Dimensions in millimeter) (Ozcebe and Saatcioglu 1987)



(a) Test Specimen (b) Load-Deflection

(c) Cracking in Experiment (d) Cracking for $1.5d$ (e) Cracking for $3.01d$

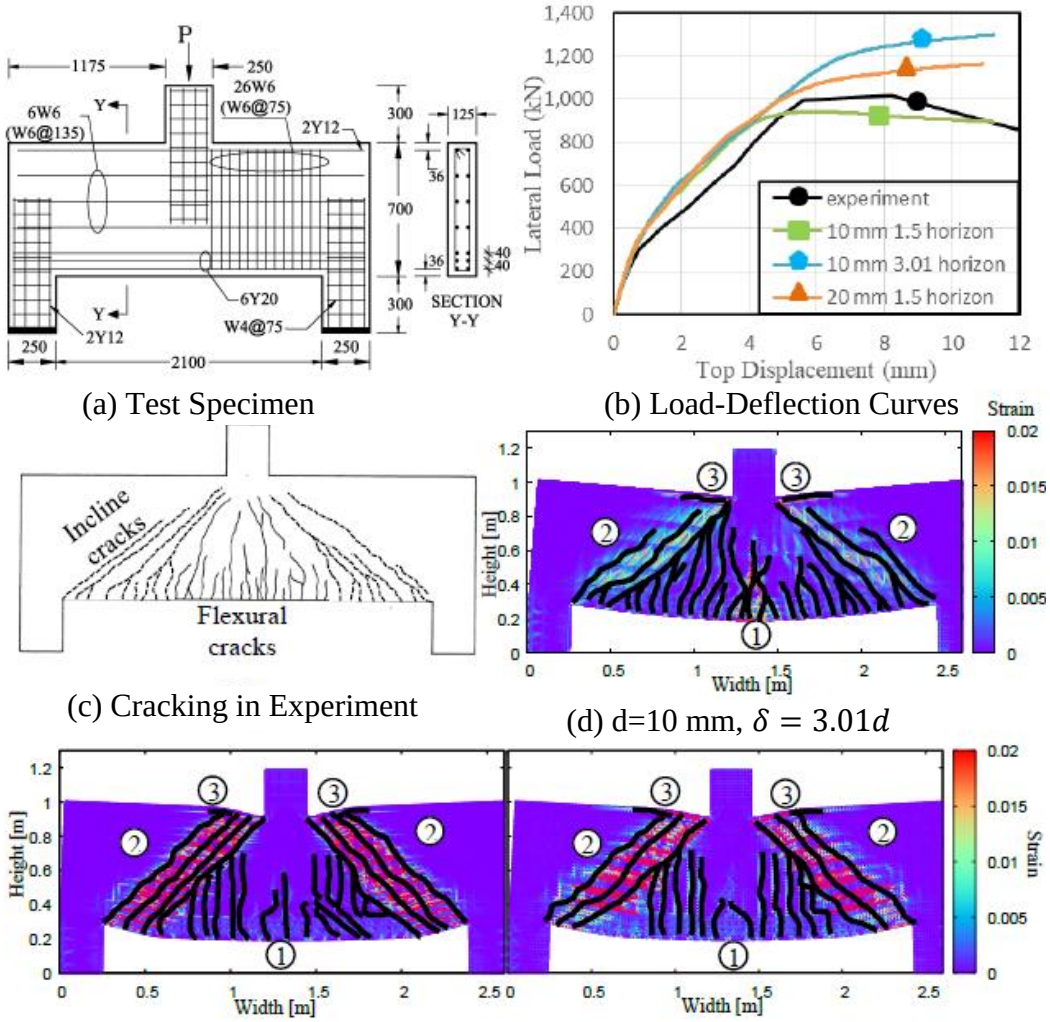
Figure 3.4. Column Specimen (U4) Simulation: (a) Dimensions and Details of Test Specimen (Dimensions are Given in mm); (b) Load-Deflection Comparison; (c) Observed Crack Pattern; (d) $\delta = 1.5d$; (e) $\delta = 3.01d$ (Amplification Factor = 3 for (d) and (e)) (Ozcebe and Saatcioglu 1987).

3.1.2 Beam Simulations

The reinforced high strength reinforced concrete deep beam tested by Foster and Gilbert (1998) shown in Figure 3.5a was simulated by using the lattice approach. The test specimen sustained damage first by flexural cracking followed by inclined shear cracking and compressive failure. Three lattice models were prepared with two uniform grid sizes (10 mm and 20 mm) and two horizons ($1.5d$, $3.01d$) as presented in Figure 3.5 and Figure 3.6. Load and midspan displacement results were obtained by plotting the total load versus the midspan deflection obtained by subtracting the average support displacements from the computed midspan

deflection (Figure 3.5b). The damage patterns mapped from the test specimen are shown along with the computed damage patterns from the three lattice analyses (Figure 3.5c-f). It can be observed that the lattice model with the $3.01d$ horizon significantly overestimated the response beyond a midspan deflection of about 4 mm. The larger horizon used in the lattice elements was thought to be the reason of the over-strength in the $3.01d$ horizon lattice model, similar to the column simulations. One reason is that a higher horizon size provides more connection between steel and concrete nodes by introducing higher residual bond strength, which means higher capacity estimation. Secondly, compression locking for the simulations with $3.01d$ horizon size results in higher load carrying capacity at the struts due to the uniform mesh distribution. On the other hand, the lattice models with $1.5d$ horizons provided a better estimate, where the ultimate strength of the model with the smaller grid size was only 5% different than the test result. The sequence of cracking is marked in Figure 3.5d-f. First, flexural cracking in the tension zone was observed followed by inclined shear cracks extending from the support to the loading plate. Finally, horizontal cracks appeared in the compression zone resembling a splitting failure. Flexural cracking followed by shear cracking and splitting of the compressed zone was captured in a reasonable manner by all the models. Foster and Gilbert (1996, 1998) reported only the final crack pattern and indicated that failure occurred when the shear cracks penetrated into the compression zone in a sudden manner. This observation agrees well with the simulation results.

For the second beam validation study, the reinforced concrete beam test (with no shear reinforcement) of Walraven (1978) shown in Figure 3.7a was simulated. The failed pictures of the specimen were not available for this test. The load carrying capacities based on flexural yielding of the reinforcement and shear strength of the section according to ACI 318-11 (American Concrete Institute 2011) were found as 56.48 kN and 46.56 kN, respectively. Based on this calculation and the observed ductility of the load-deformation response, flexural cracking followed by shear failure appears to be the failure mode of the specimen.



(a) Test Specimen (b) Load-Deflection Curves

(c) Cracking in Experiment (d) d=10 mm, $\delta = 3.01d$

(e) d=10 mm, $\delta = 1.5d$ (f) d=20 mm, $\delta = 1.5d$

Figure 3.5. Deep Beam Simulation: (a) Dimensions and Details of Test Specimen (Dimensions are given in mm); (b) Load-Deflection Comparison; (c) Observed Crack Pattern; (d) d=10 mm, $\delta = 3.01d$; (e) d=10 mm, $\delta = 1.5d$; (f) d=20 mm, $\delta = 1.5d$ (Amplification Factor = 10 for (d)-(f)) (Foster and Gilbert 1998).

Four lattice models using 25 mm and 12.5 mm grid sizes with $1.5d$ and $3.01d$ horizon sizes were employed (Figure 3.8). Load and midspan displacement results along with the obtained damage patterns and strain plots are shown in Figure 3.7b-d.

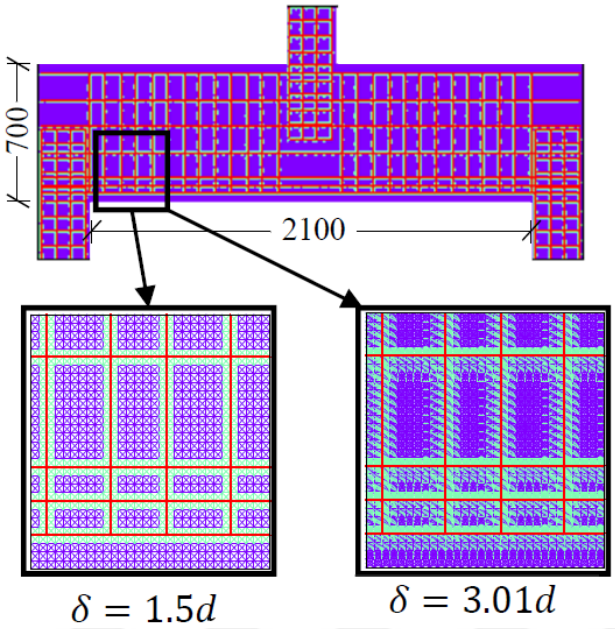


Figure 3.6. Representation of Lattice Model (Dimensions in millimeter) (Foster and Gilbert 1998)

The estimated crack spacing ranged between 80 to 100 mm, which appears to be reasonable based on engineering judgement. In the simulations, the beam experienced flexural yielding followed by shear failure. The three simulation results except 25 mm $1.5d$ horizon are quite similar to each other. Hence, it is not possible to claim the less mesh dependency or better results with increasing horizon values. The 25 mm $1.5d$ horizon simulation for Walraven (1978) test experience a combined bond and shear failure. This was not observed in the other simulations and there is no experimental evidence reported by Walraven (1978) on a possible bond failure. The slightly lower capacity observed in the 25 mm $1.5d$ horizon simulation can be attributed to the inability of transferring tensile stresses to the reinforcement upon shear cracking. It can be seen that shear failure took place in the support region and flexural cracking was observed in the middle region. In this regard, damage pattern is realistic as it is a combination of flexure and shear. The strength and load-deformation response of the beam was estimated almost perfectly along with the deformation capacity.

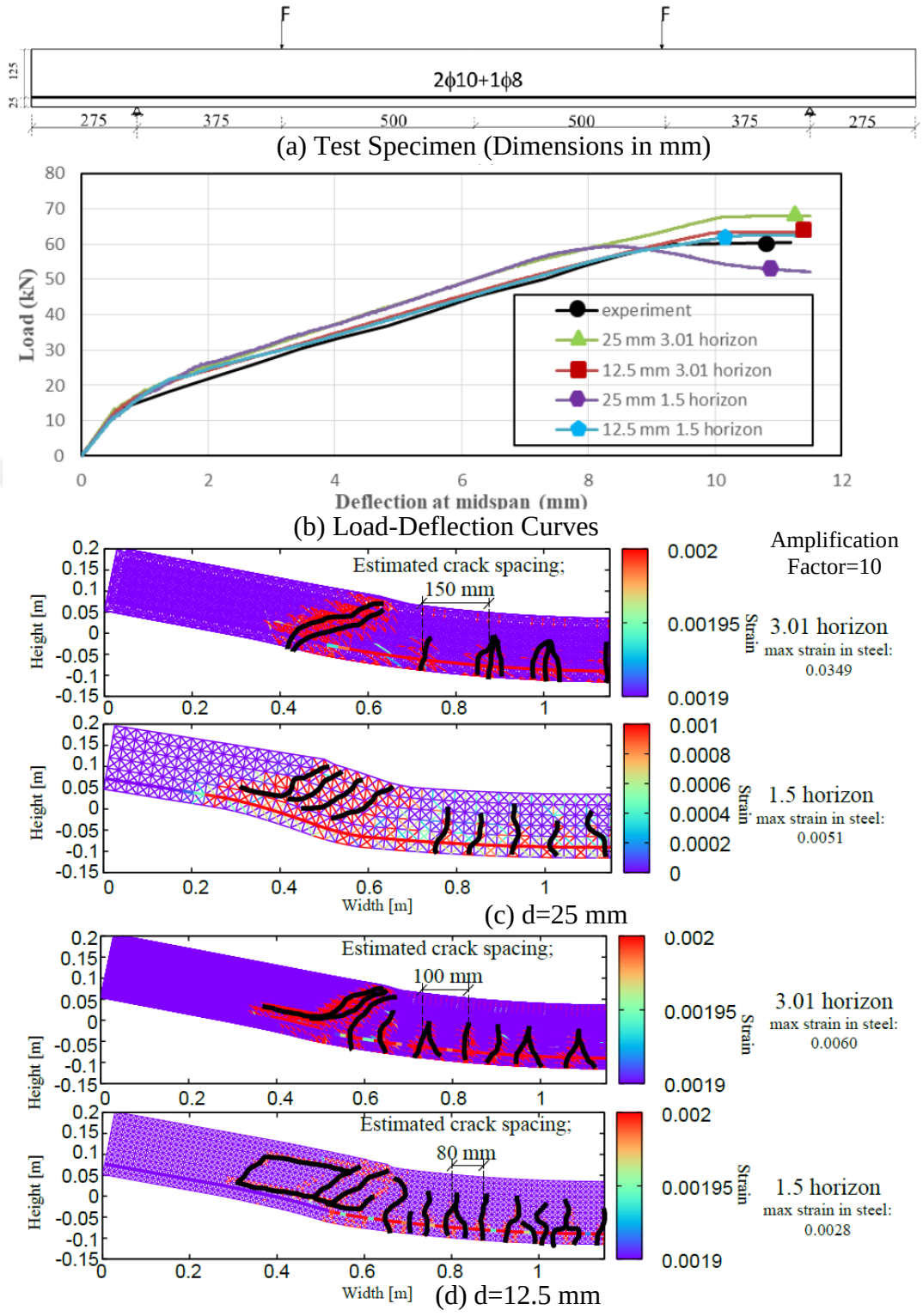


Figure 3.7. Reinforced Beam Simulation: (a) Dimensions and Details; (b) Load-Deflection Comparison; (c) d = 25 mm; (d) d = 12.5 mm (Walraven 1978).

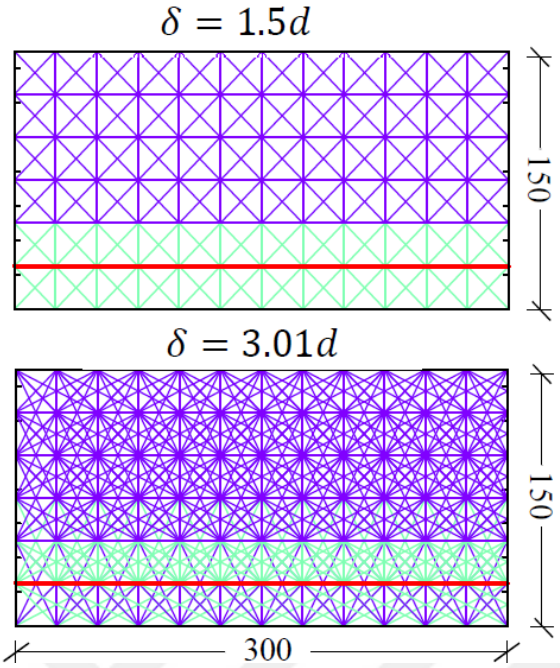
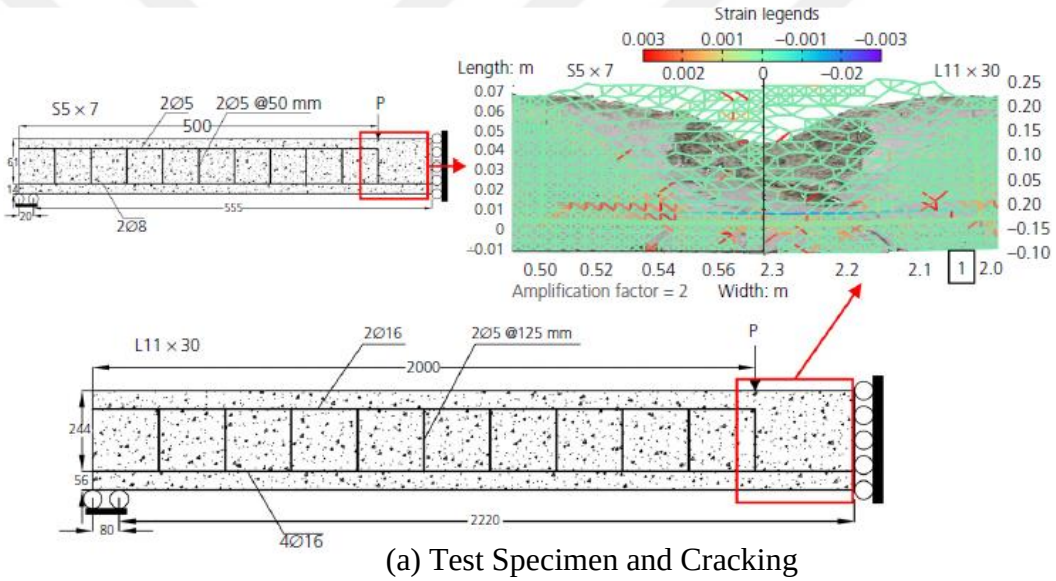


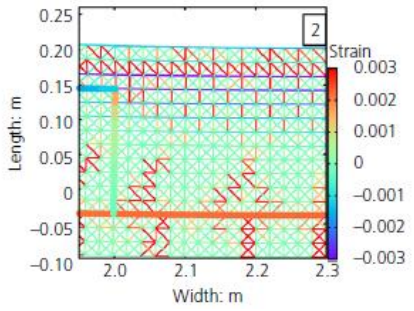
Figure 3.8. Representation of Lattice Model (Dimensions in millimeter) (Walraven 1978).

Four-point bending beam tests having only tension reinforcement (Belgin and Sener, 2008) were also simulated to test the ability of the lattice model in estimating concrete crushing response in structural members. Only $1.5d$ horizon size was used. The specimen details can be seen in Figure 3.9.a. Owing to symmetry, half of the specimens were modeled with a grid size of 5 mm and 20 mm for S5x7 and L11x30, respectively. It should be noted that both specimens were scaled versions of each other with a similar reinforcement ratio, ρ=3%. The damage results are presented for both tested beams to show the possible differences. The lattice simulations were conducted for a uniform grid and a perturbed grid with selected R_{max} based on the flowchart in Figure 2.11. The capacities of the experiments and simulations and also the ACI 318-14 (2016) and Lattice Discrete Particle Model (LDPM) (Alnaggar et al., 2019) are given in Table 3.3. The simulation results of estimated damage for both beams are shown in Figure 3.9.a. In the damage pattern, the elements with strain values higher than 0.003 are removed for better cracking representation. The crack pattern for uniform grid and load deflection curve along with the experimental results

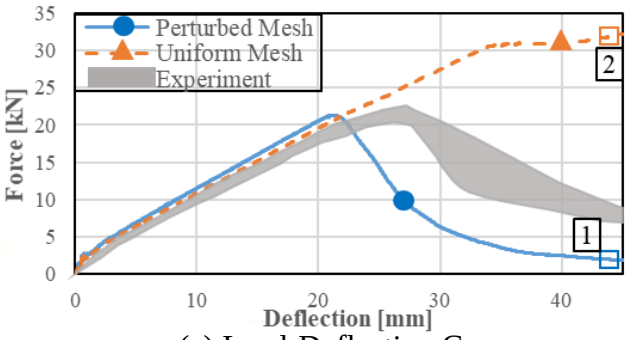
for the three L11x30 specimens, are shown in Figure 3.9.b and c. The load carrying capacity was not obtained accurately upon using a structured grid, due to compression locking (Figure 3.9.b). The upper horizontal concrete elements are carry so much of the compression that the capacity is determined by the yielding of the tension steel. Similar behavior is observed for the uniaxial compression simulations as mentioned. On the other hand, the estimated strength of the specimen was very close to the experimental result when an unstructured grid was used. The estimated cracking was in good agreement with the test results. First, flexural cracking was observed as was the case in the experiment. Then, the capacity was reached with the crushing of concrete, showing quite accurate simulation.



(a) Test Specimen and Cracking



(b) Uniform Mesh



(c) Load-Deflection Curves

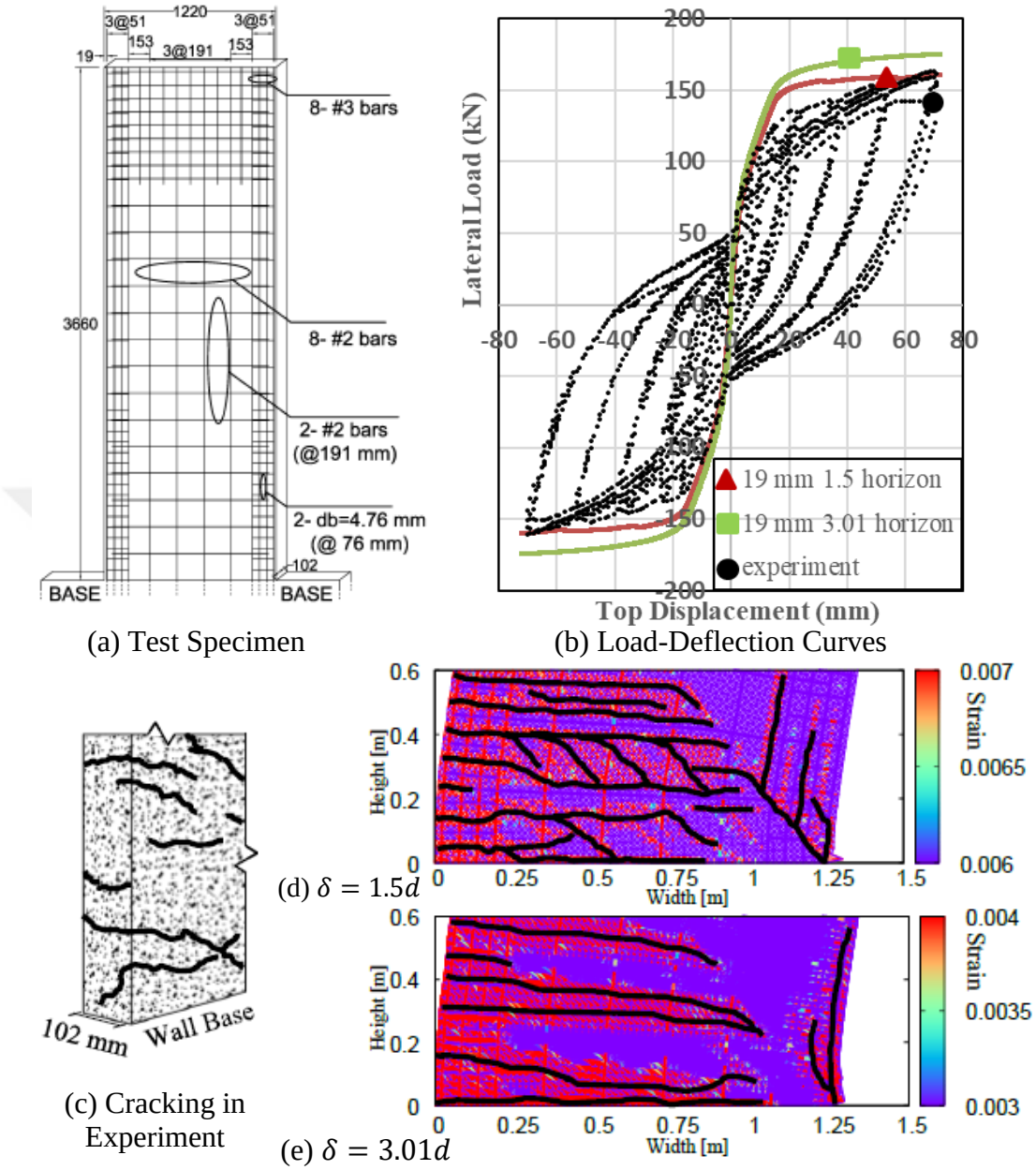
Figure 3.9. Simulation Results of Overreinforced Beams (Belgin and Sener, 2008): (a) Test Specimens and Crack Patterns; (b) Uniform Mesh (L11x30); (c) L11x30.

Table 3.3. Belgin and Sener (2007) Results

Capacity [kN]								
Trial	S5x7				L11x30			
	Experiment	Simulation	LDPM	ACI318	Experiment	Simulation	LDPM	ACI318
1	2.452	2.298	3.05	2.8	25.961	18.037	19.5	21.8
2	3.032	2.997			24.376	19.083		
3	2.877	2.186			25.807	21.247		
4		3.025				21.292		
5		2.330				19.208		
Average	**2.787**	**2.567**	**3.05**	**2.8**	**25.381**	**19.773**	**19.5**	**21.8**

3.1.3 Wall Simulations

A slender reinforced concrete wall (i.e. aspect ratio 1: 3) tested by Thomsen and Wallace (1995, 2004) under constant axial load and increasing cyclic lateral displacement excursions was simulated by using the lattice approach in a static monotonic manner (Figure 3.10a). Grid size was used as 19 mm with the $1.5d$ and $3.01d$ horizons (Figure 3.11). Estimated lateral load and top displacement result along with the experimental one are shown in Figure 3.10b. Damage patterns of the test and the numerical results corresponding to the end of the simulations are also shown in the same figure. It can be observed that the simulation result closely follows the envelope of the response with slight over-predictions of the post-cracking stiffness and strength. Although the initial stiffness and the ultimate strength of this specimen was accurately simulated an overestimation of the response in the post yielding region was noted. The horizon change did not significantly influence the response of the lattice model, while the larger horizon provided a clearer representation of the crack spacing. Based on the estimations from this model and that from Acun and Sucuoglu (2010) simulation result, one can state that the proposed lattice model appears to perform reasonably for members failing under flexural failure modes.



(a) Test Specimen

(b) Load-Deflection Curves

(c) Cracking in Experiment

(d) $\delta = 1.5d$

(e) $\delta = 3.01d$

Figure 3.10. Slender Reinforced Concrete Wall (i.e. aspect ratio 1:3) Simulation: (a) Dimensions and Details of Test Specimen (Dimensions are given in mm); (b) Load-Deflection Comparison; (c) Observed Crack Pattern; (d) $\delta = 1.5d$; (e) $\delta = 3.01d$ (Amplification Factor = 10 for (d) and (e)) (Thomsen and Wallace 1995,2004).

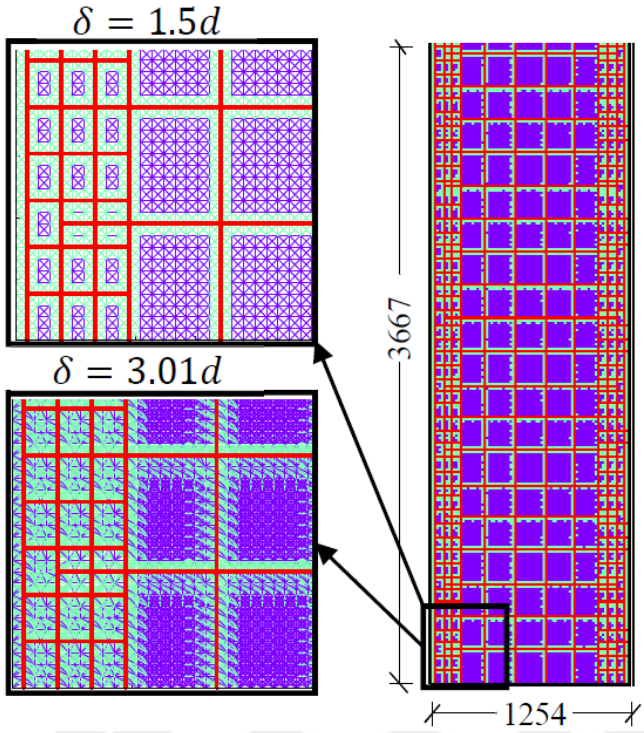
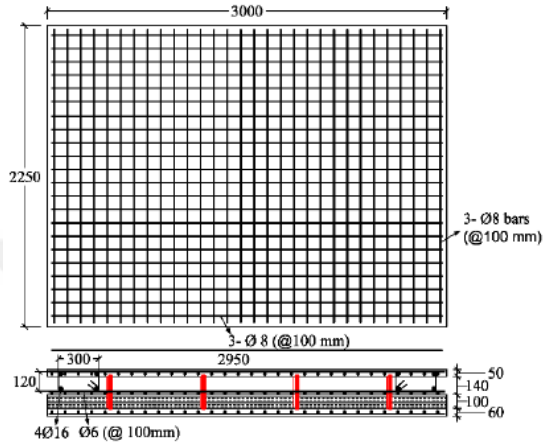


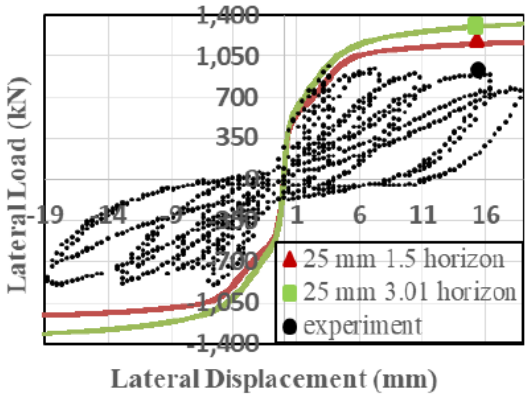
Figure 3.11. Representation of Lattice Model (Dimensions in millimeter) (Thomsen and Wallace 1995,2004).

The last test case was the simulation of a reinforced concrete wall tested by Aldemir et al. (2017) failing in a flexural-shear mode. The specimen was tested to observe the deformation capacity of a squat reinforced concrete wall designed to yield in shear. The specimen was tested up to about 1% drift ratio and did not sustain any strength degradation despite the severe inclined cracking. The details of the specimen and instrumentations on the specimen are shown in Figure 3.12a. Two lattice models were constructed by using 20 mm grid spacing and $1.5d$ and $3.01d$ horizon sizes (Figure 3.13). The response estimations and damage pattern observed in experiment and simulation are presented in Figure 3.12b-e. It can be observed that the ultimate strength and the deformation capacity of the model were simulated with a reasonable accuracy. The ultimate strength of the $1.5d$ horizon model was closer to the experimental result, whereas the larger horizon provided more lateral load carrying capacity. This result is consistent with the previous discussions on the effect of increasing horizon in increasing the lateral strength. In this simulation, the bond

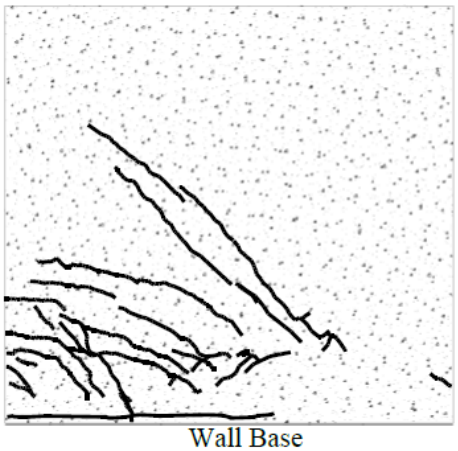
effect for higher horizon was more dominant. The damage patterns show that the combined flexural and shear cracking was captured by the numerical model. It can be concluded that the failure of the specimen was due to flexural-shear cracking for the last simulation whereas flexural failure mode was the dominant one for the test of Thomsen and Wallace (1995, 2004).



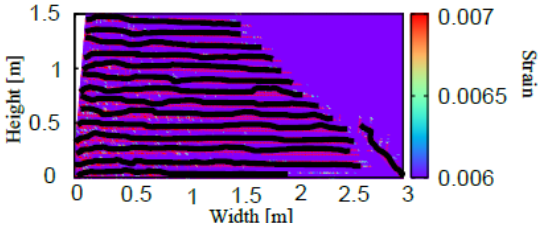
(a) Test Specimen



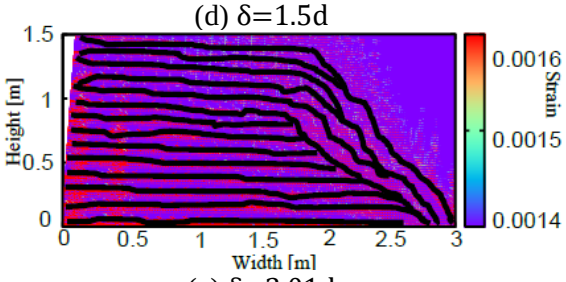
(b) Load-Deflection Curves



(c) Cracking in Experiment



(d) δ=1.5d



(e) δ=3.01d

Figure 3.12. Reinforced Concrete Wall Simulation: (a) Dimensions and Details of Test Specimen (Dimensions are given in mm); (b) Load-Deflection Comparison; (c) Observed Crack Pattern; (d) $\delta = 1.5d$; (e) $\delta = 3.01d$ (Amplification Factor = 10 for (d) and (e)) (Aldemir et al. 2017).

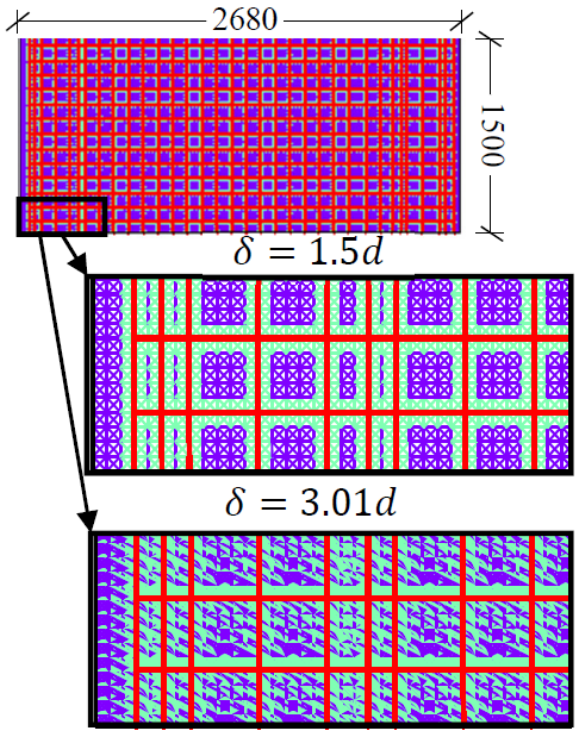


Figure 3.13. Representation of Lattice Model (Dimensions in millimeter) (Aldemir et al. 2017)

3.1.4 Parametric Studies

In this section, several parametric studies are conducted. First, the sensitivity of the results to the change in all parameters were examined with deterministic sensitivity analysis in order to propose the robustness of the model. Then, the effect of loading velocity on global response is discussed. Finally, the results with 45 rotated grids are presented and compared with the results obtained from no rotation.

3.1.4.1 Sensitivity Analysis

In order to understand the effect of uncertainty on the ultimate strength and energy absorption capacity estimations of the lattice results, a deterministic sensitivity study was conducted. For this purpose, the *tornado diagram* commonly used in decision

analysis (Clemen 1996), was used. The tornado diagram consists of a set of horizontal bars, referred to as swings, for each variable. The extreme values of the swings are computed by using the predefined upper and lower bounds of the variable (e.g. mean ± standard deviation as used in this study) while the other input variables are set to their best estimates such as their mean values. The length of each swing represents the variation in the output due to the variation in the respective random variable. Therefore, a variable with larger effect on the output has larger swing than those with smaller effects. In a tornado diagram, swings are displayed in the descending order of the swing size from top to bottom resembling a tornado to display clearly the most influential parameters.

The selected demand parameters were the ultimate strength and energy absorption capacity (i.e. area under the load-deflection curve). On the other hand, input parameters with possible uncertainties were selected as $E_t, f_t, G_f, f_y, \boldsymbol{a}$ and the loading velocity (v). Two validation cases, namely the Acun and Sucuoglu (2010) column test and Foster and Gilbert (1998) beam test were reanalyzed for the purposes of developing the tornado diagrams. The mean values of the variables were selected same as those values used in the simulations. The coefficient of variation of E_t, f_t, G_f, f_y were taken from Mirza and MacGregor (1979) and Mirza et al. (1979) whereas the coefficient of variation for $\boldsymbol{a}$ and the loading velocity were selected as 0.2 based on engineering judgement (Table 3.4).

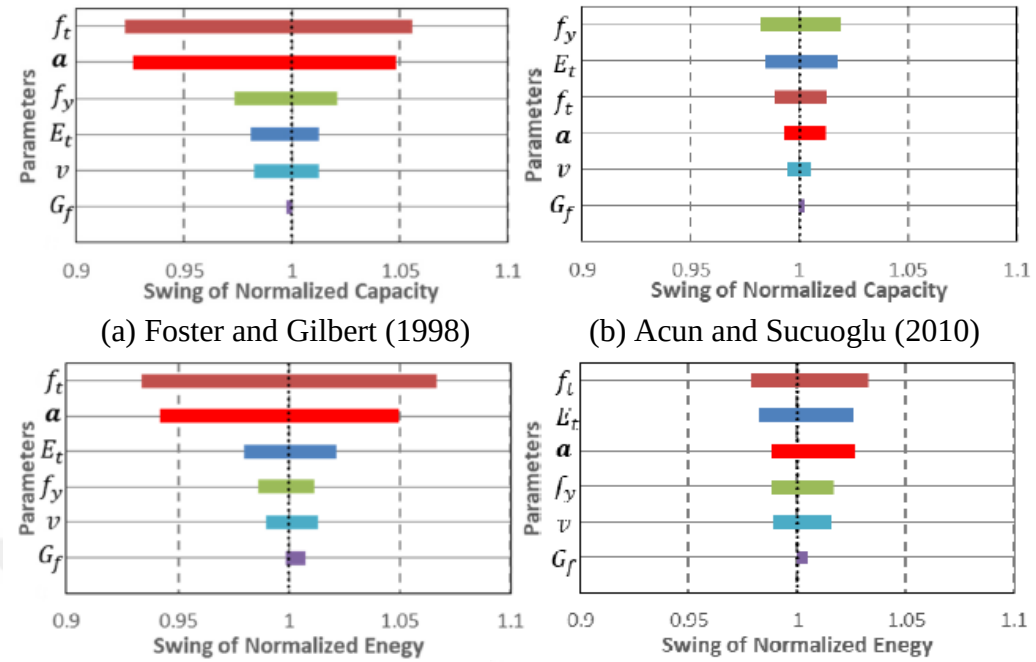
Tornado diagrams for the analyzed cases are presented in Figure 3.14. It is interesting to note that none of input parameters ($E_t, f_t, G_f, f_y, \boldsymbol{a}$ and the loading velocity (v)) considered in the parametric studies affected the strength or stiffness of the reinforced concrete element more than 8 %. This result showed the robust nature of the lattice approach and its ability of predictions without significant dependence on the uncertainty of the input parameters. It can be observed the parameters with the outmost importance were the concrete tensile strength and reinforcement yield strength for the strength estimation of RC members failing in flexure (Acun and Sucuoglu, 2010) and shear (Foster and Gilbert, 1998), respectively. On the other

hand, E_t, f_t and $\boldsymbol{a}$ were the most important parameters effecting the estimation of normalized energy for both cases. The least important parameter appeared to be G_f. It should be noted that upon changing G_f, the softening parameters of the tension model Figure 2.4 were calibrated separately for each simulation. This situation does not allow observing the influence of softening parameters on the demands. Hence a separate sensitivity study to examine the influence of variability in the softening parameters, namely a_1, a_2, a_3, b_1, b_2, was conducted.

Table 3.4. Parameters Values for Sensitivity Analysis

Parameters	Mean Values for Acun and Sucuoglu, 2010 Test	Mean Values for Foster and Gilbert, 1998 Test	Coefficient of variation
$\boldsymbol{E_t}$ **(GPa)**	23.92	47.7	0.12
$\boldsymbol{f_t}$ **(MPa)**	1.78	6.20	0.20
$\boldsymbol{G_f}$ **(N/m)**	75	117	0.20
$\boldsymbol{f_y}$ **(MPa)**	454	460	0.05
$\boldsymbol{v}$ **(m/s)**	0.25	0.025	0.20
$\boldsymbol{a}$	0.7	0.7	0.20

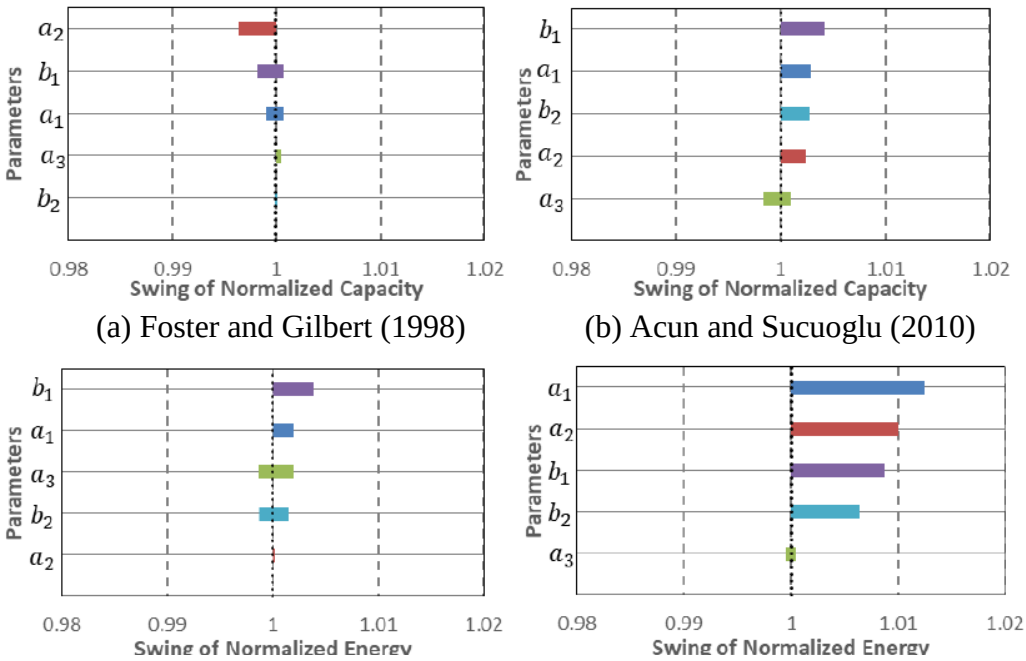
For this study, the coefficient of variation was chosen uniformly as 0.10 for all the parameters. The resulting tornado diagrams are shown in Figure 3.15. It can be observed that the maximum change in the demand parameters was up to 2% upon considering the uncertainty of the softening parameters. This result shows that the softening parameters that are calibrated consistently with the procedure given in Figure 2.11 can result in rational estimations with small uncertainties. Parameters a_1, a_3 and b_1 appear to be more influential on the uncertainity compared to the other parameters. In other words, the first point on the descending portion of the piece-wise linear softening function and the ultimate strain are the important parameters for the sensitivity. However, it should be reiterated that the uncertainties in the parameters are reflected in the outcomes in a much smaller manner, showing the robustness of the lattice approach.



(a) Foster and Gilbert (1998) (b) Acun and Sucuoglu (2010)

(c) Foster and Gilbert (1998) (d) Acun and Sucuoglu (2010)

Figure 3.14. Deterministic Sensitivity Analysis Results for Model Parameters



(a) Foster and Gilbert (1998) (b) Acun and Sucuoglu (2010)

(c) Foster and Gilbert (1998) (d) Acun and Sucuoglu (2010)

Figure 3.15. Deterministic Sensitivity Analysis Results for Concrete Constitutive Material Parameters

3.1.4.2 Loading Rates

The column specimen tested by Acun and Sucuoglu (2010) presented in "Column Simulations" section was simulated with different d and loading velocities (Figure 3.16). The change of loading rate for Acun and Sucuoglu (2010) test did not change the response estimations as shown in the figure. In all simulations, the loading rate was checked in terms of if smaller velocity changed the results. The results of RC member simulations, columns, beams and walls, are presented with a similar loading rate of 0.025 m/s.

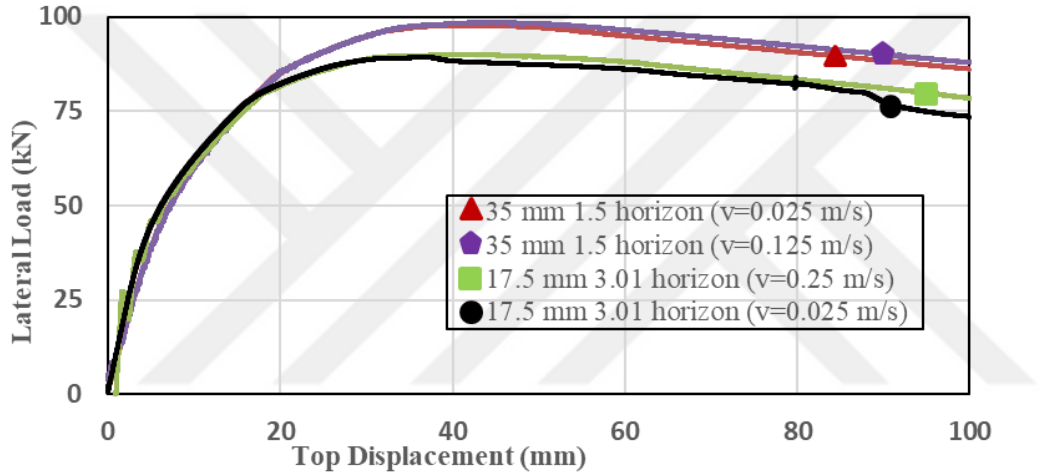


Figure 3.16. Lateral Load – Top Displacement Curves in Different Loading Rates

3.1.4.3 Grid Rotation

The effect of lattice rotation was studied by solving one of the example problems using two different lattice angles in order to ensure the objectivity of the model with respect to lattice rotation. Acun and Sucuoglu (2010) column test presented in the "Column Simulations" section was solved with the 0 and 45-degree lattice angles. The results are shown in the Figure 3.17. It can be seen that the load-deflection response and the crack patterns are almost unaffected by the lattice rotation. Also, Poisson's Ratio change for different lattice angles is shown in Figure 2.3.

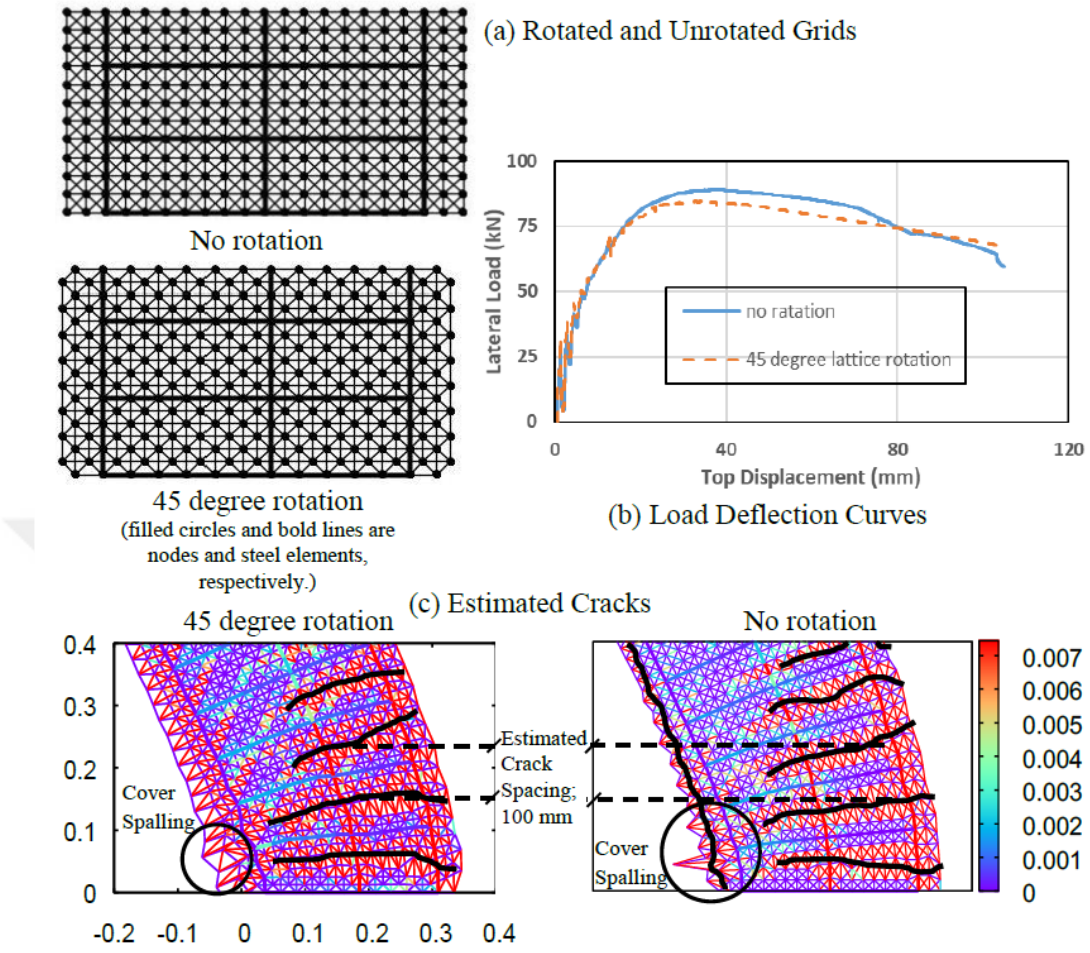


Figure 3.17. Simulation Comparisons With Respect To Lattice Rotation

3.1.5 Discussion of Results

A summary of the results is shown in Table 3.5. Initial stiffness and ultimate strength estimations are close to the experimental observation for all the analyzed cases. It can be stated that the overall load-deformation response, crack patterns and spacing estimations are in reasonable agreement. Reducing the grid size of the model appeared to result in more accurate estimations of strength and deformation capacity. Furthermore, smaller horizon is faster, but it is not perfectly isotropic as explained in Section 2.2 (also shown in Table 3.2). On the other hand, simulation results

pointed out that 1.5d horizon size seems to be the better choice for the response estimation of the RC members as opposed to 3.01d for brittle homogeneous materials (Silling and Askari, 2005). The absence of a compression model did not adversely affect the response estimations for the simulations conducted in these simulations. In most of the reinforced concrete tests, the failure was determined by concrete cracking in flexure or shear, and steel yielding. It should also be noted that the model was proven with the accurate estimation of the concrete cover spalling and rebar buckling failure in column and beam experiments due to instability in some of the simulations with only tension and compression calibration procedures. As can be seen in Figure 3.3 and Figure 3.4, lattice elements in the compressed portion of the columns undergo large later deformation indicating cover spalling. Moreover, validation study for over-reinforced beams (Belgin and Sener, 2008) shows that the proposed lattice model captures the compression failure as a local stability loss. Calculated load-deflection curves are in good agreement with the experimental results. Compression softening is observed, but it is slightly underestimated. This can be attributed to the absence of cohesion in the proposed lattice approach. Furthermore, there is a close relationship between tensile and compression softening behaviors. The results of the deterministic sensitivity analyses confirmed the robustness of the model. It was found that the expected uncertainty in the input parameters affected the response estimations by no more than about 10%. The most influential parameters related with strength and strain energy capacities are determined as concrete tensile strength and steel yield strength. Interestingly, the variation of the tensile fracture energy and tensile softening parameters appeared to exhibit insignificant differences for strength and energy absorption estimations in the reinforced concrete simulations. One of the most important reason of this robustness is the tensile fracture energy regularization of the model. In the light of information on mesh sensitivity in works conducted for concrete and RC members, it can be stated that tensile fracture energy regularization enables mesh independence in mesoscale. Thus, different grid sizes could be utilized with mesh objectivity. Mesh independency is also proven with the simulation results.

Furthermore, a simpler model such as beam elements with fiber section could be employed while use of fiber modeling approach is perfectly suitable for flexural failure modes; however, it is difficult to obtain shear response, crack width estimations and damage patterns. Finally, it can be stated that the simulation of various failure types including flexural, shear, tensile, compressive failures, and combination of them obtained in the experiments were exhibited with sufficiently accurate results by using proposed model.

Table 3.5. Summary of the Comparison between the Computed and Experimental Results

Simulations	***d*** **(mm)**	***δ***	**Initial Stiffness (kN/mm)**		**Maximum Force (kN)**	
			Experiment	Simulation	Experiment	Simulation
Column						
Acun and Sucuoglu (2010)	17.5	1.5	9.45	9.47	79.862	88.565
		3.01		9.48		89.748
	35	1.5		9.33		98.411
Ozcebe and Saatcioglu (1987)	25	1.5	87.47	85.81	324.614	337.053
		3.01		93.68		366.531
Beam						
Foster and Gilbert (1998)	10	1.5	553.90	553.14	1019	942.207
		3.01		578.10		1298.582
	20	1.5		598.06		1162.548
Walraven (1978)	12.5	1.5	23.91	21.91	60.38	62.303
		3.01		23.80		63.453
	25	1.5		23.00		59.386
		3.01		25.64		67.947
Belgin and Sener (2008) S5x7	5	1.5	0.85	0.94	2.787	2.567
L11x30	20		1.54	1.60	25.381	19.773
Wall						
Thomsen and Wallace (1995,2004)	19	1.5	35.19	32.26	163.284	169.834
		3.01		38.38		174.544
Aldemir et al. (2017)	20	1.5	1038.44	943.16	963.592	1164.413
		3.01		1052.37		1325.675

3.2 Reinforced Concrete Structures (Portal Frame Simulations)

Two single-bay and single-story portal bare frames with planar dimensions of 2750x4200 and 2500x1500 tested by Calvi and Bolognini (2001) and Binici et al. (2019) were compiled for reinforced concrete structure validation problems of the proposed lattice model within the scope of this study. The mechanical properties of concrete and rebar of portal frame specimens and dimensions and the details of the reinforcement used in test specimens are presented in Table 3.6 and Figure 3.18.

Table 3.6. Material Properties of Concrete and Steel for Portal Frames

Properties	**Batch 1 (METU)**	**Batch 2 (Pavia)[a]**	
Concrete		**Column**	**Beam**
Compression Strength [MPa]	27.94[b] 25.00[c]	29.32	34.56
Tension Strength [MPa]	1.85[d]	2.31	2.67
Density [kg/m^3]	2400	2500	
Modulus of Elasticity [GPa]	24.5[e]	24.3	25.5
Tensile fracture energy [N/m]	70[f]	94	97
a_1[g]	1.5		
a_2	80.5	50.0	40.0
a_3	350.0	300.0	270.0
Long. Reinforcement			
Modulus of Elasticity [MPa]	200000		
Yield Strength [MPa]	448[b] 456[c]	558	
Ultimate Strength [MPa]	535	649	
Ultimate Strain	0.1	0.023	
τ_b[MPa][h]	3.9	4.2	

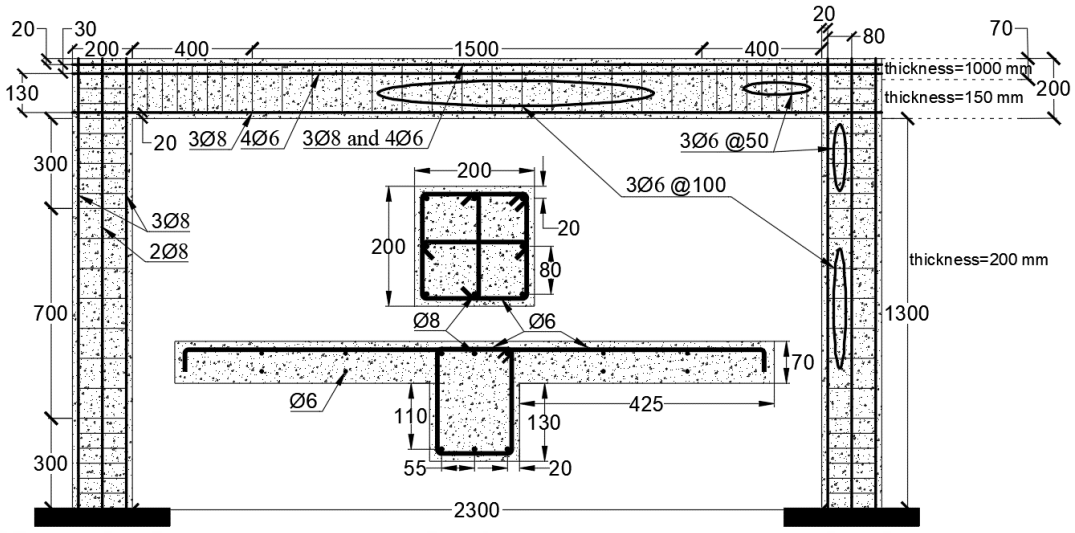
[a] *Values were taken from Milanesi et al. (2018);*

[b] *Binici et al. (2019);* [c] *In this study;* [d] *TS500 (2000)*

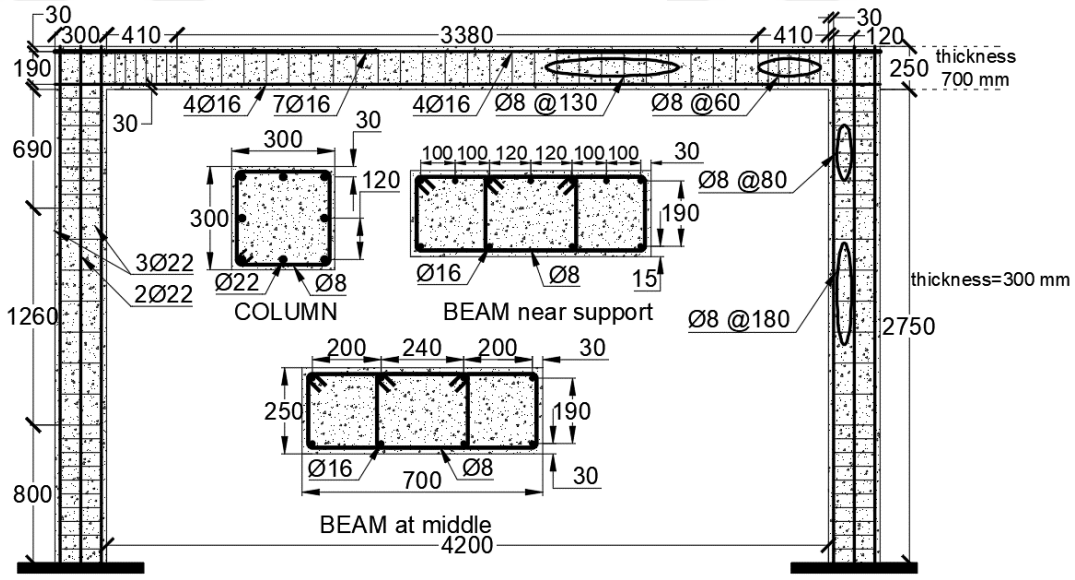
[e] *ACI 318 (2011);* [f] *CEB FIP Model Code 2010 (2012)*

[g] *Tensile fracture energy parameters were found for grid size (d)=5 mm*

[h] *Calculated as* $0.78\sqrt{f_c}$



(a) METU Frame



(b) Pavia Frame

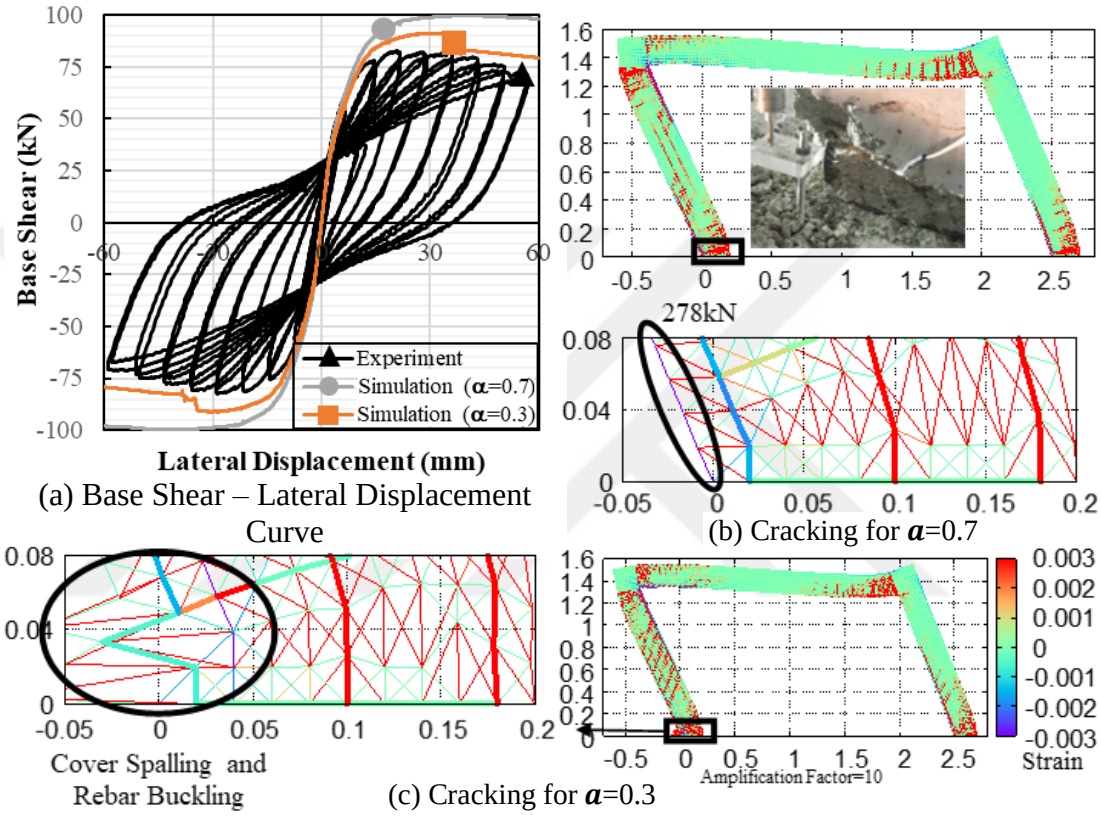
Figure 3.18. Dimensions of Portal Frames for (a) METU Frame (Batch 1) (Binici et al. 2019) and (b) Pavia Frame (Batch 2) (Calvi and Bolognini 2001)

Reported values, if available, were used for the simulation, while corresponding standards were used for the parameters that were not reported. In the models, three types of elements were used for steel, concrete, and bond, as mentioned in Reinforced Concrete Modeling section. The bottom of both columns was fixed. The lateral load was applied as a uniformly distributed load by using proportional integral derivative control to avoid stress localization after applying axial load on the related

top nodes. The grid sizes were adjusted in order to place the longitudinal reinforcements at their exact locations. Only $1.5d$ horizon size was used for these simulations for the sake of simplicity and also, better results are obtained for $1.5d$ horizon size compared with the higher horizon sizes as discussed for RC member simulations.

The bare frame tested in Middle East Technical University's structural laboratory by Binici et al. (2019) was a half-scale frame. The load-deflection curve from the simulations is shown in Figure 3.19a. Grid size (d) was chosen as 20 mm. Two different $\boldsymbol{\alpha}$ values, 0.7 and the value found by Eq. (2.8) as 0.3 as mentioned in Section 2.6, were chosen to investigate the effect of residual bond strength value on the global response. The initial stiffness from the simulation and experiments were close to each other for the $\boldsymbol{\alpha}$ value of 0.7. Also, the base shear simulation resembled the envelop of the experimental response until the displacement value of about 10 mm. However, the capacity was overestimated; the simulated lateral load-carrying capacity was 100 kN, versus an experimental capacity of 83 kN. Spalling was observed during the experiment after a 3% drift ratio at the column base (Binici et al. 2019) (Figure 3.19b). Figure 3.19b represents the strain values of concrete and steel elements near the end of the simulation. With a uniform surface grid, the concrete element on the outer part of the compression edge of the column sustained high forces due to linear response in compression. On the other hand, with an $\boldsymbol{\alpha}$ value of 0.3, as found by Eq. (2.8), the experimental load-deflection curve is sufficiently accurately duplicated (Figure 3.19c). Moreover, cover spalling following by rebar buckling was exhibited. The figure is enhanced by enlarging images and the region related with the cover spalling and rebar buckling is indicated in order to better representation. After sufficient relative displacement was reached on the bottom region of columns, elements at the cover region became unstable due to large deformations. The model incorporates the instability due to the updated-lagrangian approach. We refer to cover spalling and bar buckling when the stress drops to zero and stability is triggered.

From the simulations, it was observed that there is a unique relationship for the lattice unit due to tensile fracture energy and the randomness concept. While the maximum strain concept can be stated as the failure point for tensile response, material stability problem is the main subject in compression failure in the form of spalling or crushing.



(a) Base Shear – Lateral Displacement Curve

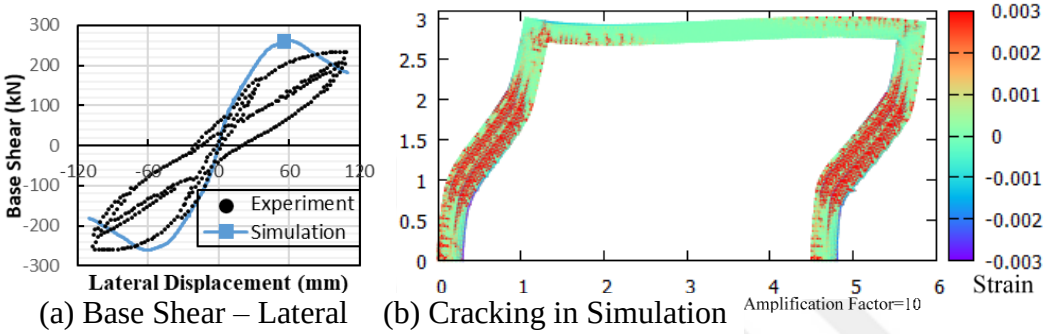
(b) Cracking for α=0.7

(c) Cracking for α=0.3

Figure 3.19. Reinforced Concrete Portal Frame Simulations: (a) Load-Deflection Comparison; Observed Crack Pattern for the Residual Bond Parameter (α) Values of (b) 0.7 and (c) 0.3 (Binici et al. 2019).

A full-scale frame conducted by Calvi and Bolognini (2001) (Pavia Frame) and used for AAC masonry infilled wall conducted by Penna and Calvi (2006) was subjected to an axial load of 400 kN on each column. The compressive strengths of concrete used in columns and beam were different. Lattice modeling with a grid size value of 30 mm was performed. α value is determined by using Eq. (2.8). Lateral load and top displacement comparisons and damage patterns from the simulation are shown

in Figure 3.20. Initial stiffness was accurately simulated. Although the lateral load-carrying capacity was estimated sufficiently accurate, the displacement demand at the capacity was obtained slightly lower in simulation. The reason for this higher rigidity can be attributed to the monotonic simulation instead of cyclic modeling. Also, strength degradation after the peak was captured with the lattice model. Crack developments were not visually reported in the experimental work. First, flexural cracking near the end of columns and beam was observed in the simulation. Then, splitting between steel and concrete occurred at high displacement demands.



(a) Base Shear – Lateral Displacement Curve (b) Cracking in Simulation

Figure 3.20. Reinforced Concrete Portal Frame Simulations: (a) Load-Deflection Comparison; (b) Observed Crack Pattern (Calvi and Bolognini 2001).

CHAPTER 4

AAC INFILLED FRAME TESTS AND VALIDATIONS

In this chapter, the experimental results of two AAC infilled frames tested for the purposes of this study are presented. The results of these two tests are discussed with the previous AAC infill wall specimen tested by Binici et al. (2019). Later, four AAC masonry infilled walls, including two specimens in this study, Binici et al. (2019) and Penna and Calvi (2006) were simulate with the proposed lattice model. Finally, a parametric study to estimate the contact length of the walls with different aspect ratios and properties of the interaction region was conducted.

4.1 AAC Infilled Frames Experiments

In this section, first, the specimens for two unreinforced AAC masonry infilled frames tested in METU Structural Laboratory within the scope of this study are described and test results are presented. Then, AAC-infilled frames tested by Binici et al. (2019) and Penna and Calvi (2006) are introduced

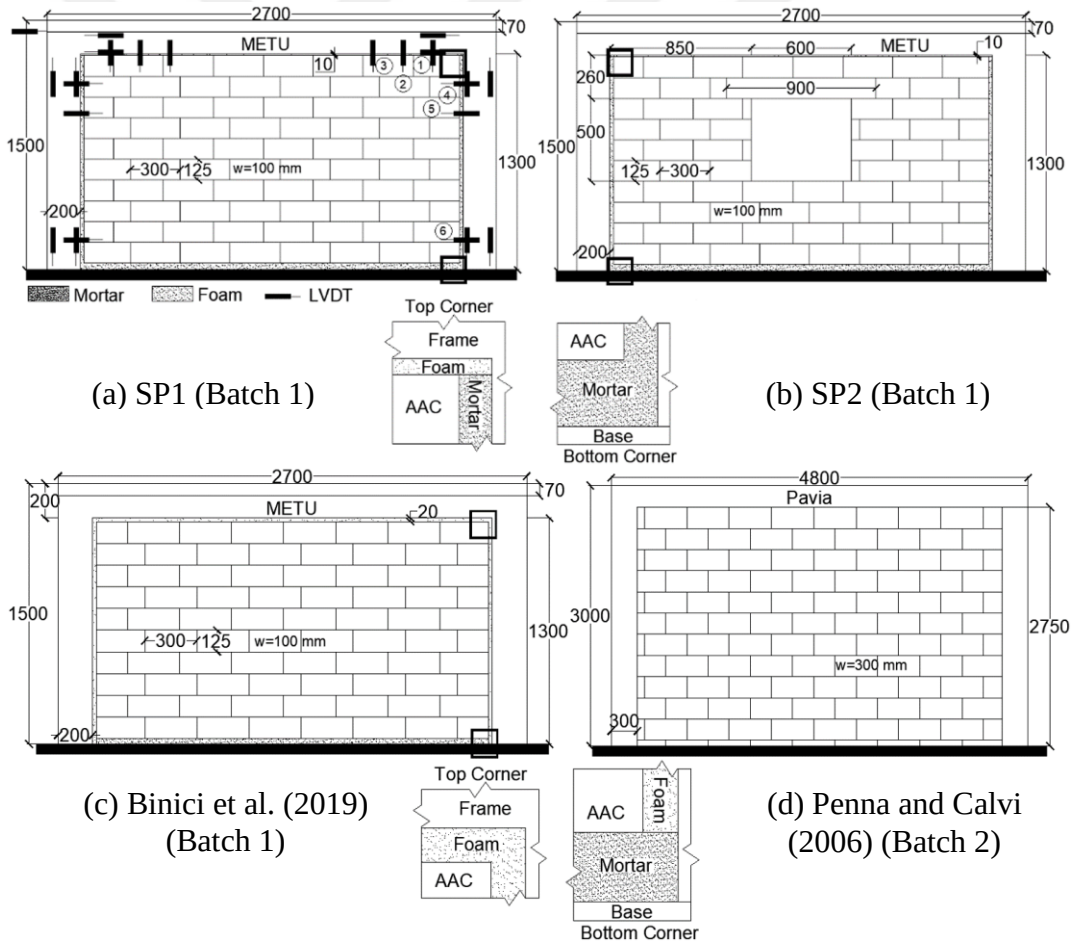
4.1.1 New Tests in This Study

Two single-bay and single-story half-scaled AAC-infilled portal frames were tested in the course of this experimental program. The presence of the opening in the infill wall and its effect on the compression strut in the wall were studied with these specimens. The details and dimensions of the specimens named SP1 and SP2 are shown in Figure 4.1a and b. The dimensions and reinforcement detailing of the test frame, used for SP1 and SP2, were previously shown in Figure 3.18a. The mechanical properties of concrete and rebar used for the frames are provided in Table 3.6. The water/cement ratio, cement type and the maximum aggregate size of the

concrete used in the experiments was as 0.65, CEM1 42,5R and 11.2, respectively, with a target cylindrical compressive strength of 25 MPa. Three uniaxial compression tests were conducted on 150 mm x 300 mm cylinders (ASTM C192 2002) on the test days to determine compressive strength of concrete. According to ASTM C617 (ASTM C617 2012), sulfur caps were placed at the both ends to achieve plane surface. The RC frames were designed following the Turkish Earthquake Design Code (2018) requirements. While the SP1 specimen had no opening, a window opening was placed in the wall for the SP2 specimen. The upper gap between the beam and the infill wall was adjusted as 1 cm and filled with foam for both specimens. On the other hand, leveling mortar was placed at the left and right interaction regions. Concentrated axial forces with a magnitude of 180 kN (0.18 × compressive strength (f_c) × gross section of columns) were applied on the columns with hydraulic actuators to simulate the axial forces from upper stories. Also, a distributed load was performed by placing steel blocks representing the dead plus reduced live loads (10.25 kN/m) on the slabs. The lateral load was then applied with a displacement control feedback. Lateral displacement reached positive and negative target drift ratios twice and drifts were increased by 0.5% at each cycle. The same loading procedure was applied for both infill wall specimens, SP1 and SP2.

Digital Image Correlation (DIC) was performed for the walls as similar to procedure explained in Section 2.5.3.2. The spacing of the dots to identify the locations was from 2.5 mm to 4.0 mm. The main aim of DIC procedure was just to visualize cracking pattern, as mentioned in Section 2.5.3.2. The lateral load and displacement responses, the local response measured with LVDTs (labels are shown in Figure 4.1a), and crack patterns at various drift ratios, 1.0% and 3.0% for positive and 3.0% for negative directions, are shown in Figure 4.2 and Figure 4.3 for SP1 and SP2. The plastic hinging of members is illustrated in the same figure by using the measured curvature values from the LVDTs located at the end sections. The lateral load carrying capacity of SP1 was found as 96.4 kN for positive and 105.4 kN for negative loading directions, respectively. The yield load carrying capacity was found at a lateral displacement value of about 16 mm, and no capacity drop was observed until

the 3.0% drift ratio, at which the experiment was finished for SP1. On the other hand, for SP2 a maximum load which was about 25% less than that observe in SP1 occurred at a displacement of about 50 mm until the end of the experiment (at a 4% drift ratio). Thus, strength degradation was not found for either of the specimens. The maximum crack width at the wall was measured as 0.75 mm and 1.5mm at the 0.35% drift ratio at which the first cracking was experienced for SP1 and SP2. First, cracks on the columns were observed for a drift ratio of 0.5%. The main crack was a diagonal crack with a shear sliding mode at the mid-region for SP1. With increasing deformation demands, additional cracks were observed, as shown in Figure 4.2. For specimen SP2, inclined cracks were observed on both sides of the opening, indicating the lack of formation of the diagonal compression strut (Figure 4.3).



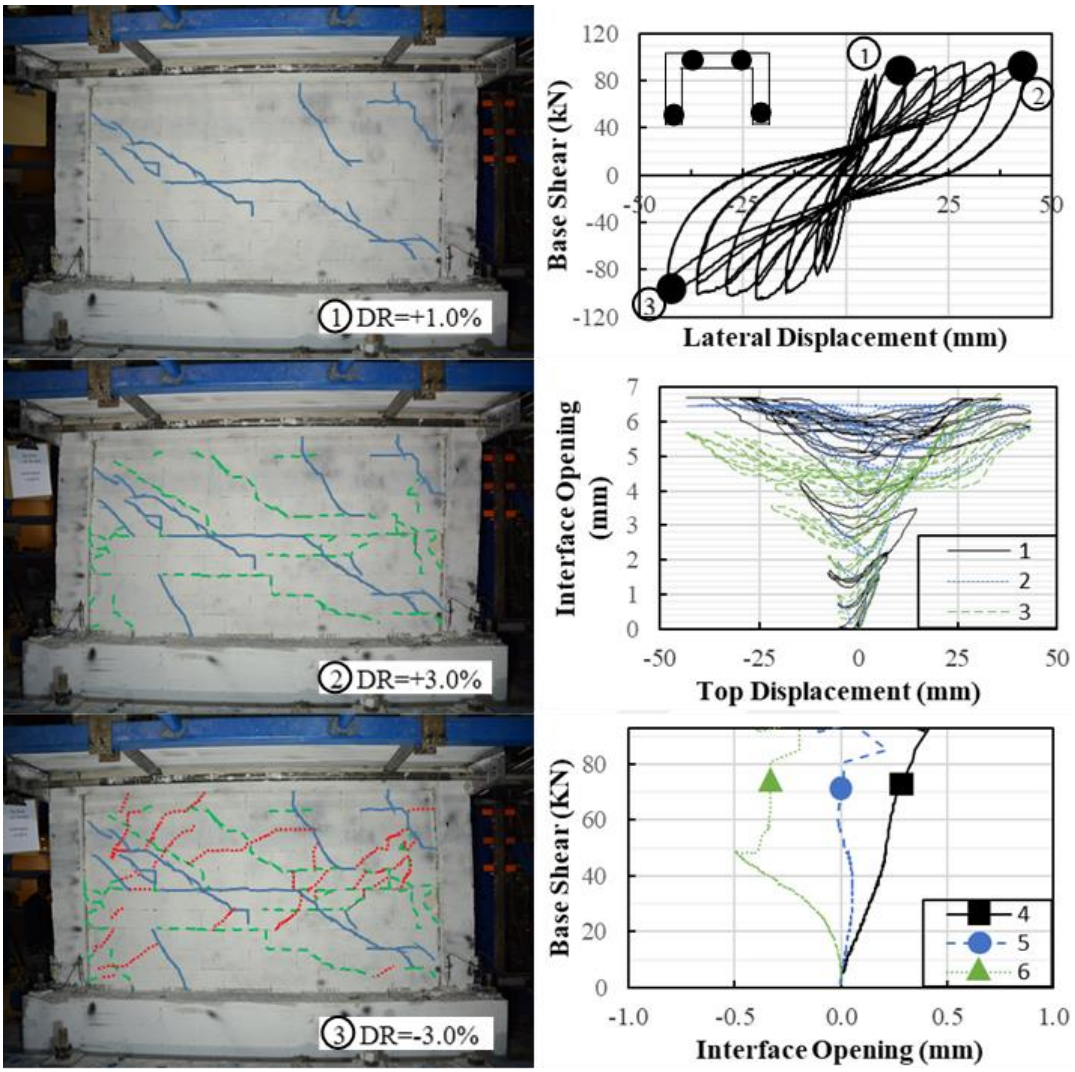
(a) SP1 (Batch 1)

(b) SP2 (Batch 1)

(c) Binici et al. (2019) (Batch 1)

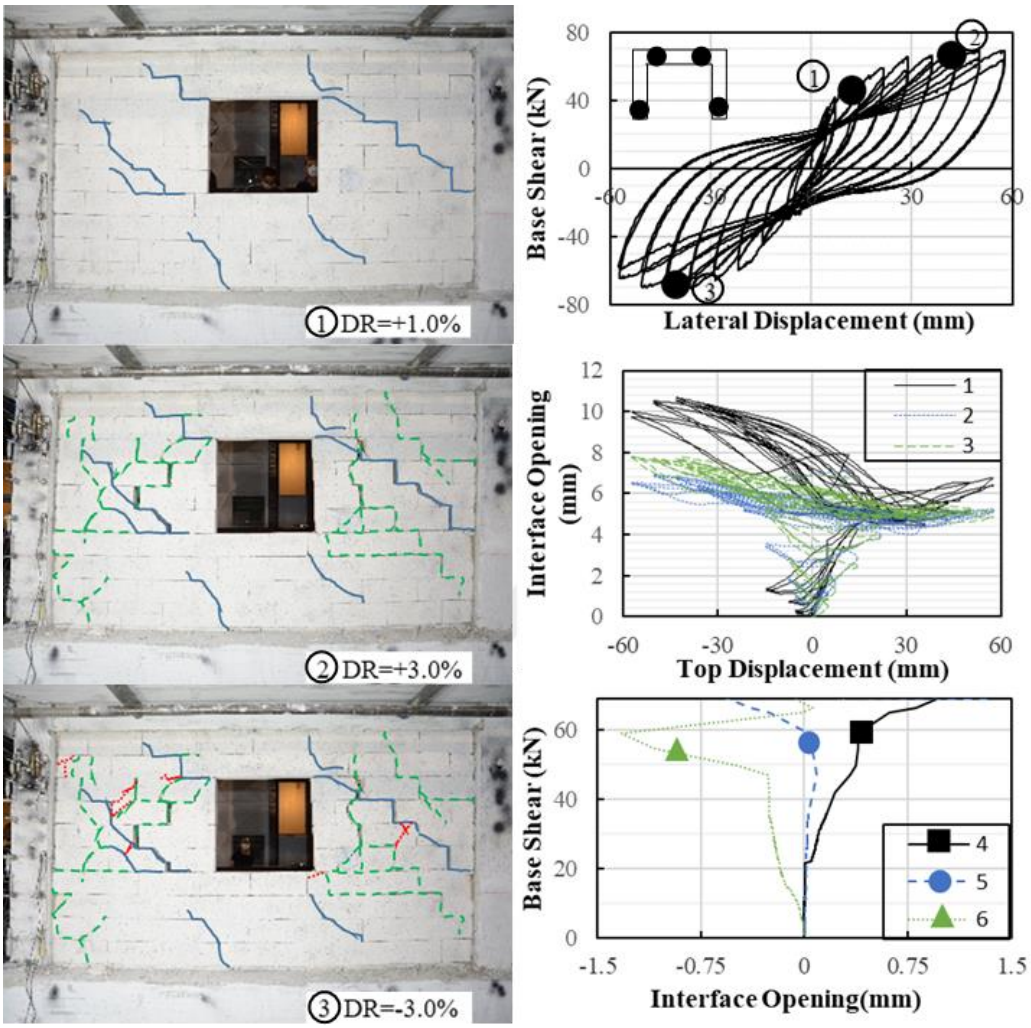
(d) Penna and Calvi (2006) (Batch 2)

Figure 4.1. Specimen Dimensions and Installed Instrumentations of the AAC Infilled Frames

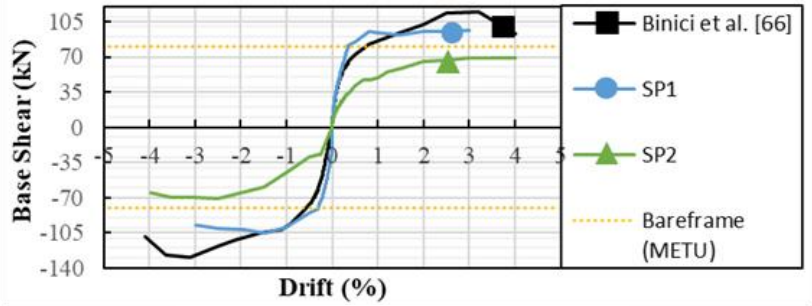


(a) Cracks at different drift ratios (b) Global and local responses

Figure 4.2. Global and Local Response Curves and Cracking of Specimens SP1, Cracks at Different Drift Ratios and (b) Lateral Displacement-Base Shear and Interface Opening Responses for Corresponding LVDT Labels for the Specimen SP1



(a) Cracks at different drift ratios (b) Global and local responses



(c) Drift-base shear comparisons

Figure 4.3. Global and Local Response Curves and Cracking of Specimens SP2, Cracks at Different Drift Ratios and (b) Lateral Displacement-Base Shear and Interface Opening Responses for Corresponding LVDT Labels for the Specimen SP2 and (c) Drift-Base Shear Curve Comparisons for Bare Frame and Infill Walls as Binici et al. (2019), SP1, SP2

4.1.2 Tests in Literature

In addition to tests conducted within the scope of this study, two additional unreinforced AAC masonry infilled frames tested respectively, by Binici et al. (2019) and Penna and Calvi (2006) (Figure 4.1c,d) were used to compare the global responses for different types of interactions and to validate the models. The dimensions of the test frame used in our experiments are the same as those used by Binici et al. (2019), labeled as METU specimens (Figure 3.18a). The same loading protocol was employed, i.e. axial forces on the columns and distributed load on the slabs were performed with a magnitude of 180 kN and 10.25 kN/m, respectively. The only difference with respect to specimens SP1 and SP2 was observed in the region between the wall and frame. In Binici et al. (2019), foam was placed on all three sides instead of only on the upper side as in the experiments conducted in this study. Also, the gap between the beam and the infill wall, which was 2 cm in the study by Binici et al. (2019), was twice the thickness of the gap in SP1 and SP2. On the contrary, the test specimen proposed by Penna and Calvi (2006), using the same RC frame of the research by Calvi and Bolognini (2001) (Figure 3.18b), had no gap between the concrete and wall. In their study, single-bay and single-story full-scaled AAC infilled wall was subjected to in-plane tests under constant axial load and increasing cyclic lateral displacement excursions. While the axial load applied on the columns was 400 kN, the beam had no distributed load.

In summary, four different AAC-infilled wall specimens were used for the simulations in this study. Two experimental campaigns composed of two different types of AAC masonries and bare frames were used. The first batch was the experiments tested at the Middle East Technical University (METU), while the second batch was carried out at the University of Pavia (Pavia). Material properties of used AAC masonries are given in Table 2.4. It should be noted that “batch” term refers to a set of one AAC wall and one RC frame in this study.

Envelope curves of three cyclic experiments, SP1, SP2, Binici et al. (2019) and corresponding bare frame capacity results, are provided in Figure 4.3c in order to

discuss wall contributions for batch 1. Different types of frame-infill interaction properties affect the contributions as expected. For example, using leveling mortar at the vertical interaction regions enabled a stiffer response at the drift ratio value of about 0.5% than the specimen with foam interfaces despite the similar initial stiffness. The reason for obtaining a lower capacity of SP1 than the specimen tested by Binici et al. (2019) can be attributed to different concrete strengths on the day of the experiments or the mechanical properties of steel. The softer response of SP2 was observed as expected since the same frame was used after using for SP1. Moreover, the contribution of the wall with the opening on global response was negligibly small. This can be attributed to the opening in the wall of SP2, which prevents the development of a proper strut formation. The results of the Pavia tests are provided in the numerical validation section.

4.2 AAC Infilled Frames Simulations

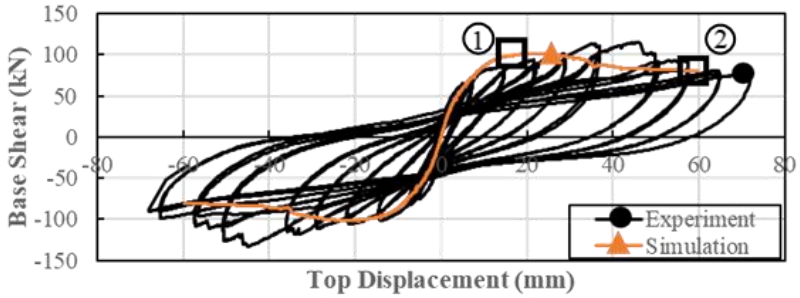
In this section, simulations of four AAC-infilled portal frames, discussed in the previous section, labeled as Pavia Test and METU Tests, consisting of the tests Binici et al. (2019), SP1, SP2 and Penna and Calvi (2006) were conducted with the lattice models described in Section 2.8. Based on the calibrations and validations at the material level in Section 2.5.3, the G_f, a_1, a_2 a_3 and R_{max}/d values were established for concrete and masonry, as shown in Table 2.4 and Table 3.6. Dimensions of infill specimens and mechanical properties are given in Figure 4.1, Figure 3.18, Table 2.4, and Table 3.6. Used frames in the infill walls are described in the previous section, and their properties are discussed in Section 3.2. The same lattice model used in Section 3.2 for the frames was employed in these four infill walls. Various interaction types of frames and walls, such that 1 cm and 2 cm gaps with foam or leveling mortar, were modeled with special interaction elements explained in Section 2.8. E_i, m_t and n values for foam elements were selected as 2, 50 and 10, respectively. The bottoms of both columns were fixed. On the other hand, the bottom of the wall was released in the lateral direction due to the low shear

resistance of mortar in that place. The lateral load was applied as a uniformly distributed load by using PID control to avoid stress localization after applying axial load on the related top nodes. The imposed lateral displacement was increased monotonically. The grid sizes were utilized the same as in the portal bare frame simulations. The lines on the estimated cracking images of infill walls at the end of the simulation in the figures represent the observed cracks during the tests.

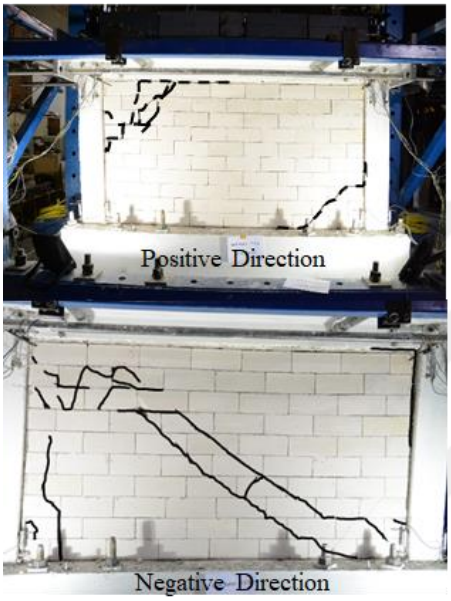
4.2.1 Infilled Frame (Binici et al. 2019)

The grid sizes for infilled frame specimens tested at METU were selected as 20 mm. The foam elements were placed on all interaction regions between columns, beam, and wall. The lateral load-deflection curve with the axial load of 180 kN on the columns is shown in Figure 4.4a. Initial stiffness and capacity were estimated with sufficient accuracy. The capacity was reached at a smaller displacement demand than the experimental measurement. Also, the capacity loss was simulated earlier than observed experimentally. The reason can be attributed to the absence of the cyclic loading in the simulation and improper strut formation in the positive direction in the experiment. However, the residual strength capacity was estimated close to the experimental result at the displacement value of about 55 mm and also, the global response in the simulation was in between the positive and negative responses of the experiment.

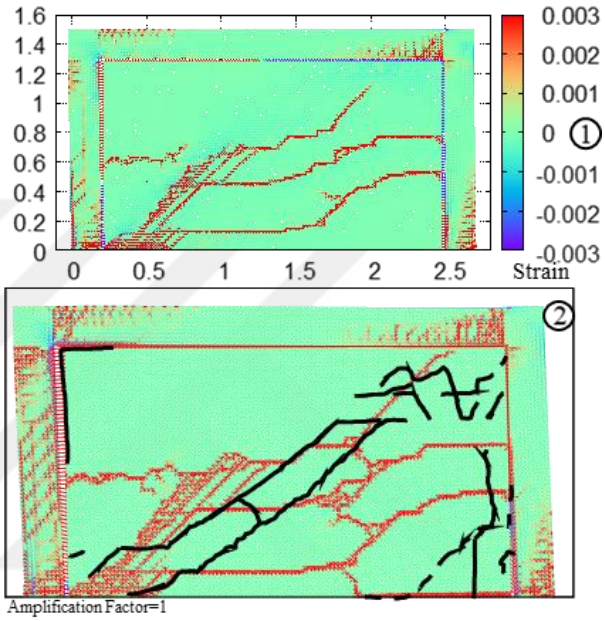
The cracks in the experiment at positive and negative drift ratio values of 3.0% and 3.5%, respectively and in the simulation at 1.32% and 4.00% lateral drift ratios are compared in Figure 4.4b,c. Diagonal struts and corresponding splitting cracks were visible in the experiment and also observed in the simulations. The corner cracks reported in the test were also simulated by correctly representing the contact behavior.



(a) Base Shear – Top Displacement Curve



(b) Cracking in Experiment



(c) Cracking in Simulation

Figure 4.4. Experiment and Simulations Results of Infill Test (Binici et al. 2019): (a) Base Shear – Top Displacement Responses, and Cracks (b) in Experiment at Positive (3.0% Drift Ratio) and Negative (3.5% Drift Ratio) Directions, (C) in Simulation at 1.32% and 4.00% Lateral Drift Ratios with Observed Experimental Cracks

4.2.2 Infilled Frames in This Study

SP1 and SP2 explained in Section 4.1 were simulated with the proposed lattice model. The grid sizes for specimens were chosen as 20 mm. The foam elements were

placed at only the top of the wall. Brittle AAC elements were placed at the left and right interaction regions.

Lateral load-deflection curves from the simulation and experiment of SP1 are shown in Figure 4.5a. Initial stiffness, strength, and load-deformation response were estimated with reasonable agreement, along with the deformation capacity, when the simulation results were compared with the envelope response of the experiment. Moreover, interface responses at the ends of the beam from the simulation and experiment are shown in Figure 4.5b. LVDT numbering corresponds to the measurement regions proposed in Figure 4.1a. The results proposed from the simulation at the related location of LVDTs are in good agreement with the experimental results based on the estimation of interaction response. Major strain distribution, in addition to the displacements in the lateral direction of nodes observed in DIC from the experiment and cracks in simulation at 1.39% and 2.92% lateral drift ratios are shown in Figure 4.5c. In the figure, cracks observed in the experiment, as shown in Figure 4.2a, are sketched on the simulation result at 42 mm lateral displacement. The estimated crack locations were in good agreement with the test results. The DIC results indicated the partitioning of horizontal wall segments. The lateral movements between segments were successfully captured with the proposed lattice model.

It should be clarified that after using the undamaged frame for SP1 until a 3.0% drift ratio, the same but the damaged frame was used for SP2, as mentioned in Section 4.1. After the SP1 experiment was conducted, the wall was removed, and a new AAC wall with an opening was placed in the damaged frame to prepare the SP2. In order to simulate the damaged frame, the simulated cumulated damage after unloading specimen SP1 was recorded and input as a pre-damage of the frame of specimen SP2. Fully elastic AAC elements were assigned at the region of the lintel. The load-deflection curve of SP2 is shown in Figure 4.6a. Simulations of the initial stiffness and subsequent softening of the specimen with the damaged frame were accurate. The lateral strength was slightly overestimated, beyond the peak displacement of about 40 mm.

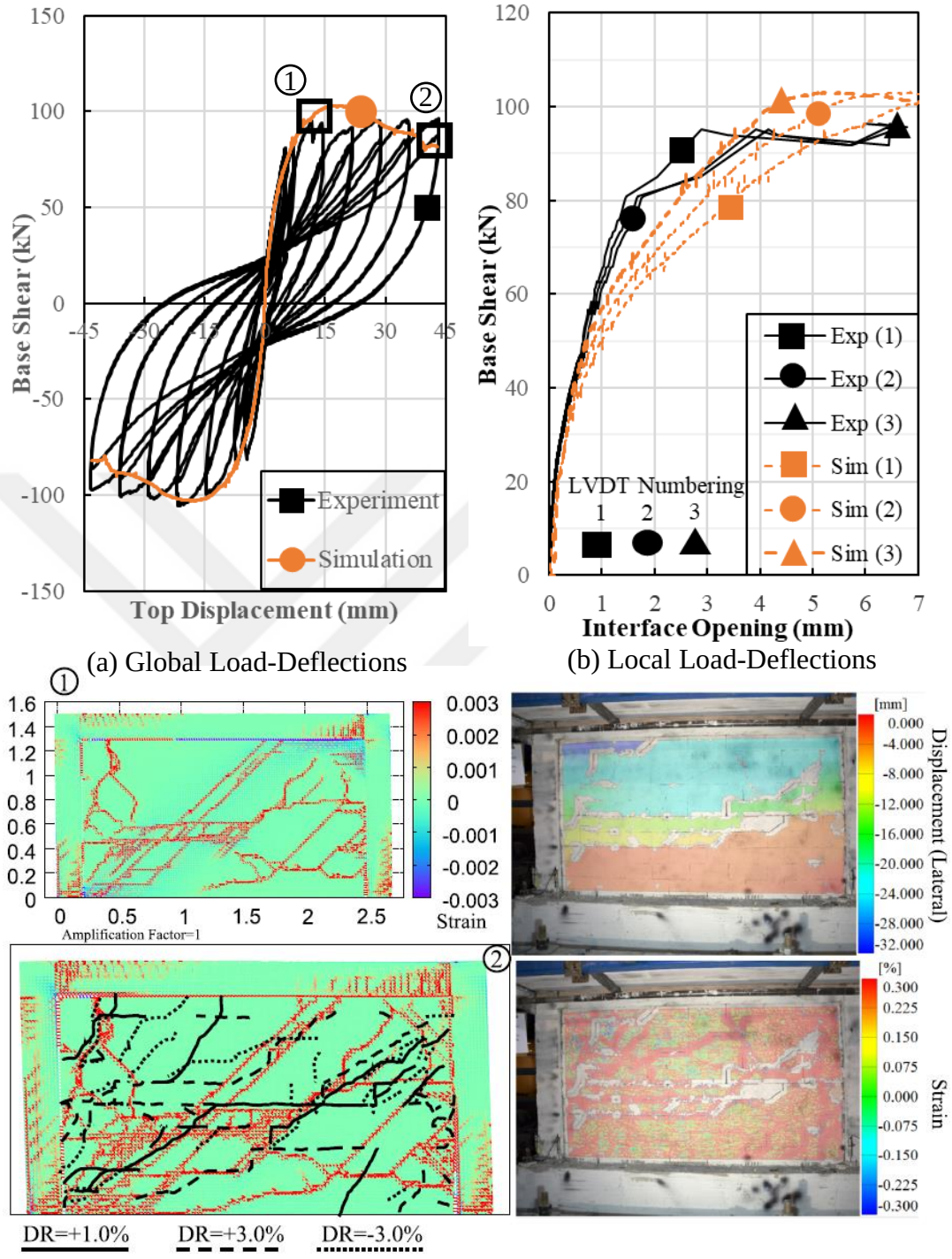
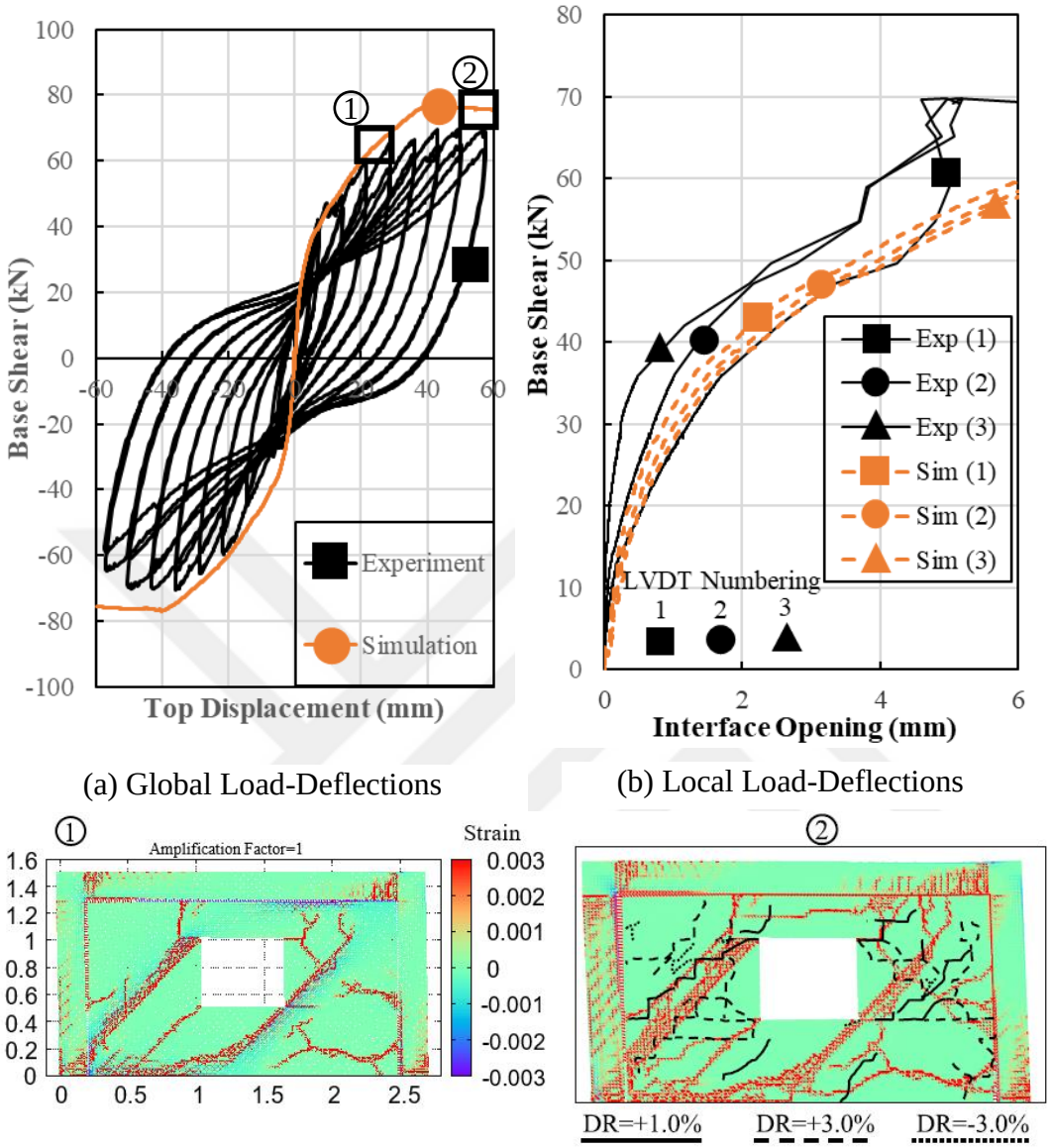


Figure 4.5. Experiment and Simulation Results of SP1: (a) Base Shear – Top Displacement Responses and (b) Interface Openings of Corresponding Lvdts and (c) Cracks in Simulation at 1.39% And 2.92% Lateral Drift Ratios with Observed Experimental Cracks at Different Drift Ratios and DIC Results



(a) Global Load-Deflections

(b) Local Load-Deflections

(b) Cracking in Simulation

Figure 4.6. Experiment and Simulation Results of SP2: (a) Base Shear – Top Displacement Responses and Interface Openings of Corresponding Lvdts and (b) Cracks in Simulation at 1.60% and 4.00% Lateral Drift Ratios with Observed Experimental Cracks at Different Drift Ratios

Furthermore, comparisons of the interaction region are shown in Figure 4.6b, which shows an accurate interface response. The cracks in simulation at 1.60% and 4.00% lateral drift ratios are shown in Figure 4.6c, with representative experimental

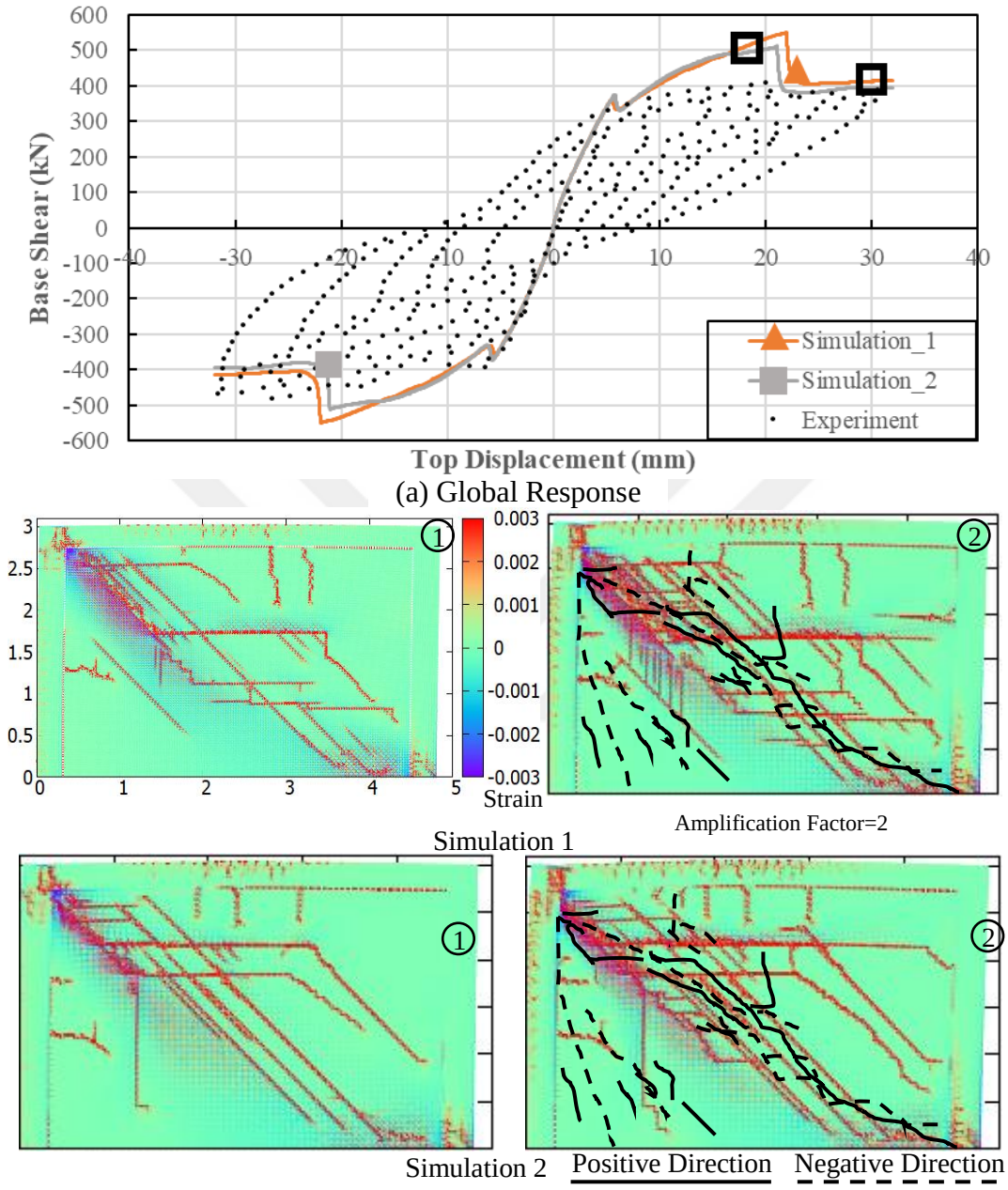
cracking lines corresponding to the results proposed in Figure 4.3a. There is a reasonable agreement in the main crack directions, while additional micro-cracks were noted in the simulation. Two struts in the wall around the opening were simulated. The same observation was also found in the experiments, as shown in Figure 4.3a.

4.2.3 Pavia Test

Finally, the AAC infilled wall tested by Penna and Calvi (2006) was simulated with a grid size value of 30 mm. In this specimen, no gaps between the concrete and wall are present, as mentioned in section 4.1. The interface mortar was modeled with the same mechanical properties of the brittle AAC elements with the reported and calibrated tensile strength value of 0.1 MPa by Milanesi et al. (2018). Lateral load-top deflection curve comparisons of two different grid perturbation instances with calibrated R_{max}/d values and experiment results are provided in Figure 4.7a. The initial stiffness was in perfect agreement with the test results. The first softening region at the displacement value of about 5 mm was captured in the simulation with a slight strength degradation. A higher capacity was simulated after a displacement of about 10 mm in the positive direction. At 20 mm, a considerable strength degradation was observed in the simulation, and the capacity was close to the test results. Besides, the effect of using a two different realization of node perturbation with the same R_{max}/d, was insignificant.

The crack pattern estimation with the lattice model is shown in Figure 4.7. In the figure, lines on images of strain distribution in the simulation represent the cracks observed at the near end of the experiment at positive and negative lateral directions. The two simulation results generally agreed with the observation of Penna and Calvi (2006). Diagonal struts were observed to be starting from the left top corner extending towards the right bottom of the wall. The splitting cracks were also captured in the simulations. Although the two simulations resulted in marginal

differences in the load-deflection responses, minor differences in the crack predictions were observed.



(a) Global Response

(b) Cracking in simulations

Figure 4.7. Experiment and Simulation Results of Pavia Infill Test (Penna and Calvi 2006): (a) Base Shear – Top Displacement Curve and (b) Cracks for Two Simulations at 0.66% and 1.11% Lateral Drift Ratios with Observed Experimental Cracks at Directions

4.2.4 Discussion of Results

The envelope curves shown in Figure 4.4-Figure 4.7 are within 5% in terms of strength estimations except for the Pavia test. In the Pavia test, the strength was overestimated by 25 to 35% in the positive and 6 to 13% in the negative direction. This result can be attributed to the variation of material strength in the test or small deviations of longitudinal bar placement. In order to obtain fully conservative results, the use of characteristic strength values instead of mean strength can be a viable approach, as usually used in the design.

Overall, load-deflection responses and crack patterns of masonry simulations were in reasonable agreement with the test results. Simulations with different residual bond strengths showed that the effect of the residual bond strength on the lateral load-top displacement response was significant. Residual bond strength was selected, which also led to reasonable crack predictions. Also, cover spalling and rebar buckling, as reported by Binici et al. (2019), were simulated at a drift ratio of about 3%. Results from the simulations using different realizations of the same node perturbance R_{max}/d was relatively close as shown in Pavia test. Diagonal struts and corresponding splitting cracks, and two struts due to an opening in the wall, were simulated with the proposed model. Using special interface truss elements, the interaction between walls and frames was simulated realistically.

It is well known that such computational demanding mesoscale models are not employed in full building design due to high computational effort. However, there are two possible ways to employ our approach in design. The damage limit states of infill walls can be predicted by using the lattice approach in infilled walls of RC frame buildings. For this purpose, a substructure lattice model composed of one bay one-story frame can be constructed, and building demands can be imposed on this model for the performance check of the infill walls. The other approach is resorting to classical truss-based strut models by using the contact lengths given in the later section.

4.3 Parametric Study

The local behavior affects the global response of the infilled frames, such as the reduction of clear high of the column, resulting from partial contact with masonry infill, or increasing shear demands with diagonal struts in full contact with the frame. The contact length represents the connection length of the diagonal strut at the column part (Figure 4.8). Considerable analytical formulations have been provided for the estimation the contact length and strut width, by many researchers and corresponding codes. Asteris et al. (2013) and Morandi et al. (2018) proposed further details about the simplified approaches. In this study, contact length results estimated with the proposed lattice model were compared with results found with formulations proposed by FEMA-306 (1998) as popular formulation and Pauley and Priestley (1992) conservative approach, for the infill walls with different length scale (L/H) values and interface properties. FEMA-306 estimates the width on the basis of experimental and analytical data by including the slenderness of the infill (λ). The effective width of the strut (b_w) is found with the following equation;

$$b_w = 0.175 d_w (\lambda h)^{-0.4} \tag{3.1}$$

Where d_w is diagonal length of infill wall, and h is column centerline height of the columns (Figure 4.8).

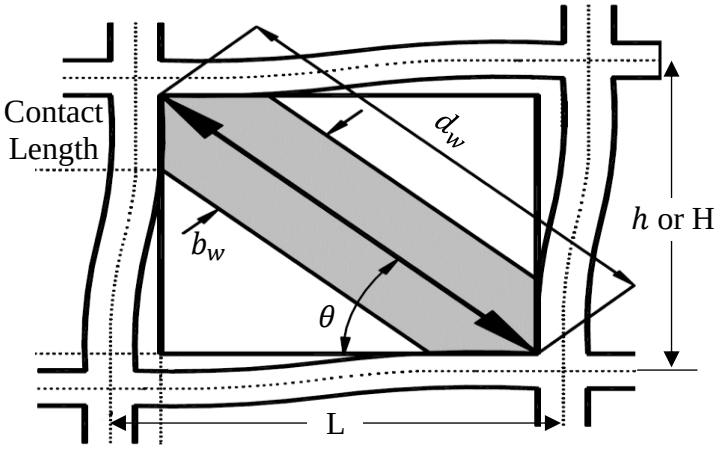


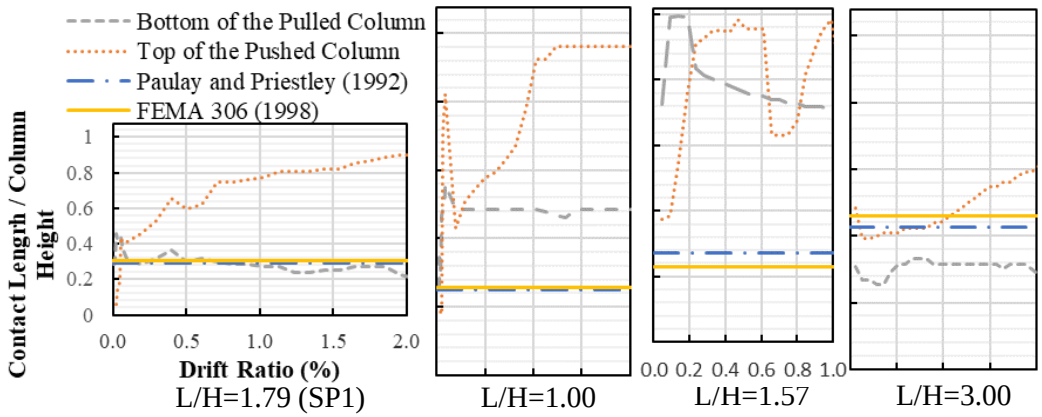
Figure 4.8. Masonry Infilled Wall and RC Frame Assemblage

On the other hand, Pauley and Priestley (1992) assumes one-quarter of diagonal length of infill wall (d_w) as the strut width (b_w). In both approaches, strut thickness is assumed same as the wall thickness. L/H values were chosen as 1.00, 1.57 (Pavia Test), 1.79 (SP1), and 3.00, and interface properties were similar to infill walls of SP1 (only upper side foam), Pavia Test (2006) (no foam) and Binici et al. (2019) (all sides foam). Contact length was assumed as the vertical component of equivalent strut width. The variation of contact lengths through the lateral displacement demands is shown in Figure 4.9.

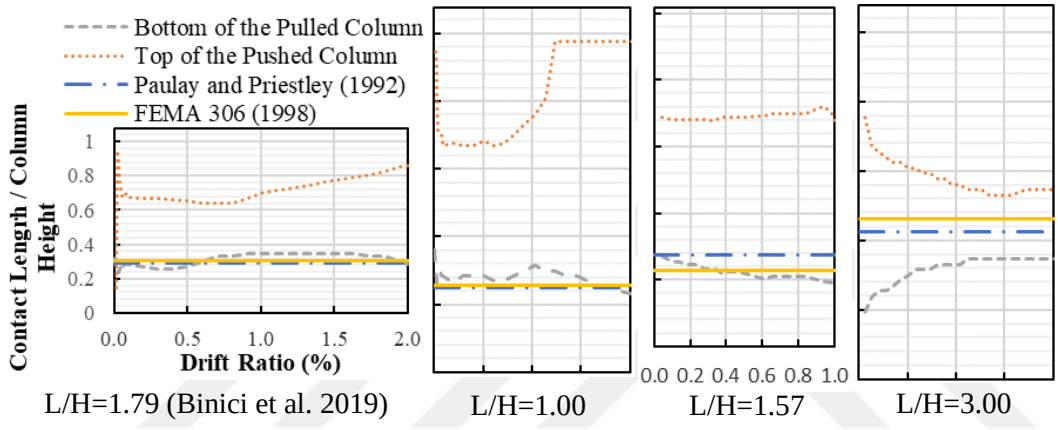
The compression regions were observed from the top of the loaded column and from the bottom of the pulled column, as shown in the previous section. The contact length was calculated by monitoring the relative distance of the element nodes in the interaction region. As can be seen from the figure, the results of the two simplified approaches were so close to each other.

Contact ratios (contact length/column height) at the two columns were different from each other, especially with more foam regions, as expected, even though the bottom of the pulled and top of the pushed column are related to the front and end of the same strut. Minimum differences were obtained from the lowest aspect ratio of the infill wall with no foam since the differences increased with more foam regions, as expected.

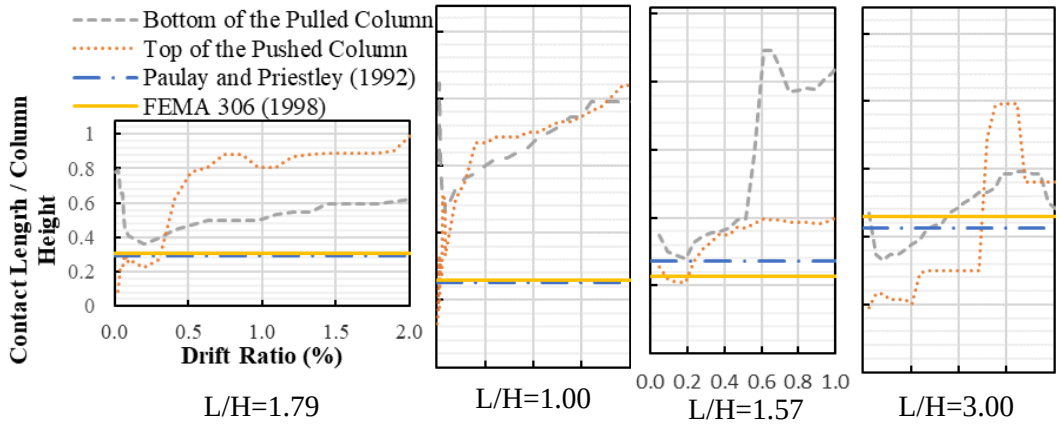
It can be realized from the curves that there existed no dominant trend for all infill wall types about the connection of drift ratio and contact ratio, but individual differences can be obtained from the simulations. For example, for low inter-story drift ratios, the average contact ratio results were close to the results of both simplified approaches for the infill walls with no foam. Complicated behavior was obtained for higher drift demand ratios.



(a) Only Upper Side Foam



(b) All Sides Foam



(c) No Foam

Figure 4.9. Contact Length in Columns and Drift Ratio Curves for Different Length Scales (L/H) And Interface Properties of (a) SP1 (Only Upper Side Foam), (b) Binici et al. (2019) (All Sides Foam), (c) Pavia Test (2006) (No Foam)

On the other hand, for all sides of foam infill walls, contact ratio estimation at the bottom of the strut was similar to simplified methods for small aspect ratios while higher contact length was desired from the loaded column as expected since there was no resistance for low inter-story drift ratios. The contact ratio at the bottom of the strut remained almost constant with increasing drift ratios. In addition, the average strut width ratio obtained from the front and end contact ratio was close to the simplified approaches for L/H=3.00.

For the infill walls with only upper-side foam, the combined response of the other two types of infill walls was obtained. While the contact length estimation of the model at both sides of the strut was close to the results calculated from simplified methods for L/H=3.00, smaller length scales walls needed much more contact demands. The contact length estimation of the bottom part of the pulled column for the SP1 specimen was approximately the same results with the two approaches.

To sum up, complicated behavior was obtained after cracking, and the contact length at the loaded column increased, although not monotonically, with an increasing drift ratio. Different types of interface regions and length scales of the walls affected the contact length behavior significantly, and it also depended on the drift demand values. This phenomenon is not addressed in the existing simple strut models. It can be observed that as the aspect ratio of the infill wall increased the estimation of the models tend to be closer to the simplified strut widths. The estimated contact lengths in the strut top and bottom were different.

CHAPTER 5

CONCLUSION

5.1 Summary

In this study, the two-dimensional mesoscale truss-based lattice modeling approach solved with sequentially linear analysis in static and an explicit time integration technique in a dynamic manner was proposed. Tension-only modeling with few parameters and ease of implementation are the novel features of the proposed lattice models. Moreover, the compressive behavior of a truss-based lattice model was investigated numerically. In such models where there is only tension failure, for structured grids with uniformly distributed nodes, it is known that locking mechanisms arise, resulting in an overestimation of strength. This locking problem was handled by introducing grid perturbation. Thus, a compression calibration methodology was proposed for concrete and AAC wall elements by using uniaxial compression tests. The methodology was validated for concrete elements by using uniaxial compression and compression strut tests on plain concrete struts loaded in uniaxial compression from two experimental campaign. Different uniaxial compression test specimens with different length/width ratio were also simulated. Three AAC masonry wallettes have been tested for uniaxial compression response by using DIC monitoring and these results were used to calibrate and validate the proposed lattice model to use the model for AAC infill walls. Diagonal compression tests for AAC walls were also simulated. Properties of special bond and foam elements connecting concrete nodes with steel and wall nodes were defined for RC and infill wall simulations, respectively. Explicit time integration scheme to solve all simulations presented in this study was enhanced by implementing a PID control algorithm.

In Chapter 3, calibrated lattice model was used to estimate the nonlinear response of RC specimens and members. Numerous validation studies were conducted for RC members, i.e. columns, beams and walls tested by many researchers with various failure modes including flexural, shear, tensile, compressive failures and combination of them. Two single-bay and single-story RC frames were chosen to validate the model within the scope of this study. Estimated crack patterns and force-displacement responses with different grid and horizon sizes were compared with experimental results. The sensitivity of the model was investigated with many different aspects including the effect of input variables, loading rates, and mesh rotation.

In Chapter 4, two single-bay, single-story half-scaled AAC-infilled portal frames experiments were carried out to investigate the interaction of AAC wall and frame with and without opening in the wall. Local behavior and global response of the specimens was observed by using LVDT and DIC measurements. Two additional AAC-infilled frame tests were used from the literature to achieve validation benchmarks for the proposed model. Thus, the four AAC masonry infilled RC frames, which are a combination of RC and masonry (bi-material), with different interaction region properties between RC frame and AAC wall were modeled to validate the proposed numerical approach for the first time in the literature to the best of author' knowledge. Furthermore, in a parametric study the evolution of the contact length was simulated for different aspect ratios of the walls. The results were presented and compared with simplified approaches.

5.2 Concluding Remarks

The following key conclusions can be drawn based on properties and compression response of the proposed lattice model:

- The uniaxial compressive response is imitated with indirect tension behavior with sufficient accuracy by using meso-scale lattice model without using non-linear compression behavior.
- The proposed lattice approach is capable of modeling uniaxial compression tests with different boundary conditions affecting significantly the strength and softening regime of concrete.
- Uniaxial compression behavior simulations indicate that there is a unique grid perturbance magnitude for a target compressive strength value. A calibration methodology that allows one to select R_{max}/d value for a given compressive strength and tensile fracture energy has been developed. Thus, it was concluded that compressive strength within a specific tensile fracture energy value corresponds to a specific magnitude of the perturbation. This aspect of the proposed modeling approach is one of the key novelty of the current research.
- The novel calibration technique for tension and compression at the meso-scale enables to successfully match the macro-scale response. The tension-only modeling with few parameters has the ability to simulate the macro-scale behavior.
- Sensitivities of the model to grid orientation and size effect in compression were investigated numerically. Tensile fracture energy enables the model to be insensitive to the grid refinement, but grid orientation affects the results slightly as can be seen at uniaxial compression simulations.
- The proposed model has the ability to capture the slenderness effect.
- The softening in compression is underestimated as same with other types of lattice models. The reason can be the cohesionless behavior of the model. However, compression softening behavior is directly related with tensile softening behavior.
- The load-deflection and crack pattern of uniaxial and diagonal compression AAC masonry and of uniaxial compression concrete tests are estimated as sufficiently reasonable.

- The proposed lattice simulation employs less number of parameters compared to continuum-based finite element models with nonlinear concrete constitutive models. The fact that cracks are represented with the fracture of lattice elements is a further important advantage over existing nonlinear finite element models.
- An explicit time integration is enhanced with a novel PID-controlled algorithm to make the system stabilize under monotonic loading.

Based on RC simulation results:

- It can be stated from the simulation results of RC members and frames that the overall load-deformation response, crack patterns and spacing estimations are in reasonable agreement.
- Reducing the grid size of the model appeared to result in more accurate estimations of strength and deformation capacity for RC simulations.
- Using smaller horizon sizes seems to be the better choice for the overall estimation of the experiments based on computational expense and load-deflection response.
- In additional to sufficiently accurate results for predicting compressive strength, the compression failure as a local instability is obtained in validation studies for over-reinforced beams by using the proposed lattice model.
- The robustness of the proposed model was shown by deterministic sensitivity analysis. The response estimations are affected no more than 10% by the expected uncertainty in the input parameters of the model thanks to the tensile fracture energy regularization.
- Mesh objectivity is proven by comparing the simulation results with numerous experiments having different failure types with different grid sizes.
- Residual bond strength affects the force-top displacement response of the portal frame significantly. However, the analytical formulation works well in terms of load-displacement response and crack prediction, cover spalling and rebar buckling.

Based on AAC-infilled frame experimental and numerical results:

- The AAC-infilled frame experiment results show that interaction properties affect the global response based on the rigidity and strength of infill walls.
- Load deflection and crack propagation gave close simulations of the experimental results. The maximum difference between the simulated and experimental lateral load capacity was found for the Pavia test (13%). Also, using different distributions of the same node perturbance R_{max}/d does not affect the simulation results.
- The infill wall-frame contact length depends on lateral deformation demands. It can be achieved with the proposed lattice approach.

In conclusion, the lattice approach appears to be a viable and easy to implement an alternative to simulate the response of concrete, AAC masonry, RC members and frame structures, and AAC-infilled frames, in which load-deformation or crack spacing estimations are needed with engineering accuracy. In other words, it appears that the lattice approach provides a practical and efficient model to simulate infill walls and their components. Both global and local behavior are simulated sufficiently accurate. The modeling approach, including an extended calibration procedure, can be consistently applied for a range of experiments. In addition, the model is robust from a computational view, insensitive to modeling parameters (Sensitivity Analysis Section) and can simulate the nonlinear response of concrete, RC structures, and their combination (bi-material) with reasonable accuracy (Validation Sections).

5.3 Future Works

The findings of the study point out that the increasing computation power allowing large-scale particle-based simulations may be used in the future to simulate the response of structures for which estimation of cracking and crushing deformations are crucial for design. In the near future, as the model has the ability to estimate cracking behavior and global response of structural members sufficiently accurately,

the lattice model has great potential to be used for parts of structures to describe nonlinearity in plastic regions. Infrastructures such as concrete dams, bridges, and tunnels are potential application areas for lattice simulations to describe the response of plasticity in specific regions on them, which require simpler tension-only models.

Application of the lattice models in building design is a challenging issue due to high computational efforts. However, lattice models can be employed within a substructure framework where the building inter-story demands can be imposed on the one bay one-story infilled RC frame to estimate the damage limit state of infill walls. The research outcome from this work can help in estimating damage limit state of infill walls at different deformation levels. For this purpose, a substructure lattice model composed of one bay one-story infilled RC frame can be constructed and inter-story deformations can be imposed on this model to estimate the damage limit state of the infill walls. A complete crack formation in an infill wall estimated with the lattice model can be considered as high damage whereas limited cracking can be considered as low damage. Alternatively, the findings on infill wall frame contact length can be used to create classical truss based compression only strut models. Further work is needed for establishing design oriented lattice-based approaches.

The work presented herein was limited to two-dimensional modeling without loss of generality. One important outcome of this study is establishing a novel calibration methodology for lattice models in tension and compression. A similar approach can be followed for the three-dimensional modeling of concrete and AAC masonry behavior, which is the scope of future work. For tension calibration, simulation of direct tension tests can be conducted in a three-dimensional domain to find the softening parameters while the nodes would be disturbed in a sphere instead of a circle to determine the perturbation value under compression loading.

REFERENCES

AASHTO LRFD *Bridge Design Specifications*, (1994), First Edition, American Association of State Highway and Transportation Officials, Washington, D.C., 1994.

AASHTO LRFD *Bridge Design Specifications*, (2014), Seventh Edition with 2016 Interim Revisions, American Association of State Highway and Transportation Officials, Washington, D.C., 2014.

ACI (American Concrete Institute) (2002) ACI 318-02 "Building code requirements for structural concrete." American Concrete Institute, Farmington Hills, MI, USA.

ACI (American Concrete Institute) (2011) ACI 318-11. "Building code requirements for structural concrete and commentary." American Concrete Institute, Detroit.

ACI (American Concrete Institute) (2016) ACI 318-14: Building Code Requirements for Structural Concrete. American Concrete Institute, Farmington Hills, MI, USA.

ACI (American Concrete Institute) (2019) ACI 318-19: Building Code Requirements for Structural Concrete. American Concrete Institute, Farmington Hills, MI, USA.

Acun, B. (2010) "Energy based seismic performance assessment of reinforced concrete columns," Ph.D Thesis, Middle East Technical University, Ankara.

Acun, B. and Sucuoglu, H. (2010) 'Performance of reinforced concrete columns designed for flexure under severe displacement cycles', *ACI Structural Journal*, 107(3), p. 364.

Aldemir, A., Binici, B. and Canbay, E. (2017) 'Cyclic Testing of Reinforced Concrete Double Walls.', *ACI Structural Journal*, 114(2).

Alfaiate, J. and Sluys, L.J. (2018) 'On the use of non-iterative methods in cohesive fracture', *International Journal of Fracture*, 210(1), pp. 167–186.

Alfano, G. and Sacco, E. (2006) 'Combining Interface Damage and Friction in a Cohesive-Zone Model', *International Journal for Numerical Methods in Engineering*, 68(5), pp. 542–582.

Alnaggar, M., Pelessone, D. and Cusatis, G. (2019) 'Lattice discrete particle modeling of reinforced concrete flexural behavior', *Journal of Structural Engineering ASCE*, 145(1), p. 04018231.

Alwashali, H., Sen, D., Jin, K. and Maeda, M. (2019) 'Experimental investigation of influences of several parameters on seismic capacity of masonry infilled reinforced concrete frame', *Engineering Structures*, 189, pp. 11–24.

Amato, G., Cavaleri, L., Fossetti, M. and Papia, M. (2008) 'Infilled frames: influence of vertical loads on the equivalent diagonal strut model', in *The 14th world conference on earthquake engineering*. Beijing, China.

American Society for Civil Engineers – American Concrete Institute (ASCE-ACI) Committee 445. (1998). "Recent approaches to shear design of structural concrete." *J. Struct. Eng.*, 124(12), 1375–1417.

Angiolilli, M., Gregori, A., Pathirage, M. and Cusatis, G. (2020) 'Fiber Reinforced Cementitious Matrix (FRCM) for strengthening historical stone masonry structures: Experiments and computations', *Engineering Structures*, 224, p. 111102.

Angiolilli, M., Pathirage, M., Gregori, A. and Cusatis, G. (2021) 'Lattice discrete particle model for the simulation of irregular stone masonry', *Journal of Structural Engineering*, 147(9), p. 4021123.

Askari, E., Bobaru, F., Lehoucq, R.B., Parks, M.L., Silling, S.A. and Weckner, O. (2008) 'Peridynamics for multiscale materials modeling', in *Journal of Physics: Conference Series*. IOP Publishing, p. 12078.

Asteris, P., Cotsovos, D., Chrysostomou, C., Mohebkhah, A. and Al-Chaar, G. (2013) 'Mathematical micromodeling of infilled frames: state of the art', *Eng Struct*, 56, pp. 1905–1921.

Asteris, P.G. (2003) 'Lateral stiffness of brick masonry infilled plane frames', *Journal of structural engineering*, 129(8), pp. 1071–1079.

Asteris, PG., Kakaletsis, DJ., Chrysostomou, CZ. and Smyrou E.E. (2011), "Failure modes of infilled frames" Electronic Journal of Structural Engineering 11(1):11-2011.

ASTM E519-10 (2010), Standard test method for diagonal tension (shear) in masonry assemblages.

ASTM Standard C192/C192M (2002). Making and curing concrete test specimens in the laboratory. ASTM International, West Conshohocken, PA, USA.

ASTM Standard C617/C617M (2012). Standard Practice for Capping Cylindrical Concrete Specimens. ASTM International, West Conshohocken, PA.

Aydin, B. B. (2017). "Overlapping lattice modeling for concrete fracture simulations using sequentially linear analysis," Master's Thesis, Middle East Technical University, Ankara.

Aydin, B., Tuncay, K. and Binici, B. (2018) 'Overlapping lattice modeling for concrete fracture simulations using sequentially linear analysis', *Structural Concrete*, 19(2), pp. 568–581.

Aziz A (2014) Simulation of fracture of concrete using micropolar peridynamics. Master's thesis, the University of New Mexico, New Mexico, USA. https://digitalrepository.unm.edu/ce_etds/97/

Balan, T.A., Filippou, F.C. and Popov, E.P. (1997) 'Constitutive model for 3D cyclic analysis of concrete structures', *Journal of Engineering Mechanics*, 123(2), pp. 143–153.

Baudet V, Beuve M, Jaillet F et al. (2007) New mass-spring system integrating elasticity parameters in 2D. Tech. Rep. RR-LIRIS-2007-003, LIRIS, Universite Lyon. https://hal.archives-ouvertes.fr/hal-01493734/document

Bažant, Z.P. and Oh, B.H. (1983) 'Crack band theory for fracture of concrete', *Matériaux et construction*, 16(3), pp. 155–177.

Bazant, Z.P. and Planas, J. (2019) *Fracture and size effect in concrete and other quasibrittle materials*. Routledge.

Bažant, Z.P. and Xiang, Y. (1997) 'Size effect in compression fracture: splitting crack band propagation', *Journal of engineering mechanics*, 123(2), pp. 162–172.

Bažant, Z.P., Lin, F. and Lippmann, H. (1993) 'Fracture energy release and size effect in borehole breakout', *International Journal for Numerical and Analytical Methods in Geomechanics*, 17(1), pp. 1–14.

Bažant, Z.P., Tabbara, M.R., Kazemi, M.T. and Pijaudier-Cabot, G. (1990) 'Random particle model for fracture of aggregate or fiber composites', *Journal of engineering mechanics*, 116(8), pp. 1686–1705.

Beale, P.D. and Srolovitz, D.J. (1988) 'Elastic fracture in random materials', *Physical Review B*, 37(10), p. 5500.

Belgin, Ç.M. and Şener, S. (2008) 'Size effect on failure of overreinforced concrete beams', *Engineering Fracture Mechanics*, 75(8), pp. 2308–2319.

Binici, B. (2005) 'An analytical model for stress–strain behavior of confined concrete', *Engineering structures*, 27(7), pp. 1040–1051.

Binici, B., Canbay, E., Aldemir, A., Demirel, I., Uzgan, U., Eryurtlu, Z. and Al, E. (2019) 'Seismic behavior and improvement of autoclaved aerated concrete infill walls', *Eng Struct*, 193, pp. 68–81.

Binici, B., Yakut, A. and Gülkan P (2012) "Van Depremine Yerleşimler Açısından Bakış ve Tavsiyeler", Bilim ve Teknik Dergisi January, 26-31.

Birck, G., Iturrioz, I., Lacidogna, G. and Carpinteri, A. (2016) 'Damage process in heterogeneous materials analyzed by a lattice model simulation', *Eng Fail Anal*, 70, pp. 157–176.

Birrcher, D., Tuchscherer, R., Huizinga, M., Bayrak, O., Wood, S.L. and Jirsa, J.O. (2009) *Strength and serviceability design of reinforced concrete deep beams*.

Blacklock, J.R. and Richard, R.M.(1969) 'Finite element analysis of inelastic structures.', *AIAA Journal*, 7(3), pp. 432–438.

Bobaru, F., Ha, Y.D. and Hu, W. (2012) 'Damage progression from impact in layered glass modeled with peridynamics', *Central European Journal of Engineering*, 2(4), pp. 551–561.

Bolander, J.E. and Sukumar, N. (2005) 'Irregular lattice model for quasistatic crack propagation', *Physical Review B*, 71(9), p. 94106.

Braga, F., Manfredi, V., Masi, A., Salvatori, A. and Vona, M. (2011) 'Performance of non-structural elements in RC buildings during the L'Aquila, 2009 earthquake', *Bulletin of Earthquake Engineering*, 9(1), pp. 307–324.

Brown, M.D., Sankovich, C.L., Bayrak, O. and Jirsa, J.O. (2006) 'Behavior and efficiency of bottle-shaped struts', *ACI Structural Journal*, 103(3), p. 348.

Brown, M.D., Sankovich, C.L., Bayrak, O., Jirsa, J.O., Breen, J.E. and Wood, S.L. (2006) *Design for shear in reinforced concrete using strut-and-tie models*.

Burt, N.J. and Dougill, J.W. (1977) 'Progressive failure in a model heterogeneous medium', *Journal of the Engineering Mechanics Division*, 103(3), pp. 365–376.

Caballero, A., Carol, I. and López, C.M. (2006) 'A meso-level approach to the 3D numerical analysis of cracking and fracture of concrete materials', *Fatigue & Fracture of Engineering Materials & Structures*, 29(12), pp. 979–991.

Caldarelli, G., Castellano, C. and Petri, A. (1999) 'Criticality in models for fracture in disordered media', *Physica A: Statistical Mechanics and its Applications*, 270(1–2), pp. 15–20.

Calvi, GM. and Bolognini, D. (2001) "Seismic response of R.C. frames infilled with weakly reinforced hollow masonry panels" Journal of Earthquake Engineering 2001;5(2):153–185.

Canadian Concrete Masonry Producers Association. CCMPA. (2009) Seismic design guide for masonry buildings. Toronto (Canada): CCMPA.

Carol, I., Prat, P.C. and López, C.M. (1997) 'Normal/Shear Cracking Model: Application to Discrete Crack Analysis', *Journal of Engineering Mechanics*, 123(8), pp. 765–773. Available at: https://doi.org/10.1061/(ASCE)0733-9399(1997)123:8(765).

Cauchy, A.-L. (1828) "Sur les équations qui expriment les conditions d'équilibre ou les lois du mouvement intérieur d'un corps solide, élastique ou nonélastique", Exerc. Math. 3, 160–187 (1828)

Cavaleri, L., Fossetti, M. and Papia, M. (2009) 'Modeling of out-of-plane behavior of masonry walls', *Journal of structural engineering*, 135(12), pp. 1522–1532.

CEB-FIP model code 1990 (1993) Comité euro-international du béton, and Fédération Internationale de la Précontrainte. CEB-FIP model code 1990: Design code (Vol. 1993). Thomas Telford Publishing.

Ceccato, C., Salviato, M., Pellegrino, C. and Cusatis, G. (2017) 'Simulation of concrete failure and fiber reinforced polymer fracture in confined columns with different cross sectional shape', *International Journal of Solids and Structures*, 108, pp. 216–229.

Červenka, J. and Papanikolaou, V.K. (2008) 'Three dimensional combined fracture–plastic material model for concrete', *International journal of plasticity*, 24(12), pp. 2192–2220.

Chang, Z., Zhang, H., SCHLANGEN, E. and Šavija, B. (2019) 'Lattice model for numerical analysis of fracture process of concrete material under various loading conditions', in *Proceedings of the 10th International Conference on Fracture Mechanics of Concrete and Concrete Structures*.

Chen, W.-F. and Han, D.-J. (2007) *Plasticity for structural engineers*. J. Ross Publishing.

Choi, S., Thienel, K.-C. and Shah, S.P. (1996) 'Strain softening of concrete in compression under different end constraints', *Magazine of Concrete Research*, 48(175), pp. 103–115.

Chrysostomou, C., Gergely, P. and Abel, J. (2002) 'A six-strut model for nonlinear dynamic analysis of steel infilled frames', *International Journal of Structural Stability and Dynamics*, 2(3), pp. 335–353.

Chrysostomou, C.Z. and Asteris, P.G. (2012) 'On the in-plane properties and capacities of infilled frames', *Engineering structures*, 41, pp. 385–402.

Chung, J. and Lee, J.M. (1994) 'A new family of explicit time integration methods for linear and non-linear structural dynamics', *International Journal for Numerical Methods in Engineering*, 37(23), pp. 3961–3976.

Clemen, R. T. (1996) Making Hard Decisions: An Introduction to Decision Analysis, 2nd edn. Edited by C. Belmont. Duxbury.

Clough, R.W. and Johnston, S.B. (1966) 'Effect of stiffness degradation on earthquake ductility requirements. Report 66-16, Structural and Materials Research', *Structural Engineering Laboratory, University of California, Berkeley, Calif* [Preprint].

Coleman, J. and Spacone, E. (2001) 'Localization issues in force-based frame elements', *Journal of Structural Engineering*, 127(11), pp. 1257–1265.

Collins M.P., and Mitchell, D. (1991). Prestressed Concrete Structures. Englewood Cliffs, Prentice Hall, New Jersey.

Cornelissen, H., Hordijk, D. and Reinhardt, H. (1986) 'Experimental determination of crack softening characteristics of normalweight and lightweight', *Heron*, 31(2), pp. 45–46.

Costa, AA. (2007) Experimental testing of lateral capacity of masonry piers. An application to seismic assessment of aac masonry buildings. MSc Dissertation, ROSE School, IUSS Pavia, Italy.

Cundall, P.A. (1971) 'A computer model for simulating progressive, large-scale movement in blocky rock system', in *Proceedings of the International Symposium on Rock Mechanics, 1971*.

Cusatis G and Pelessone D (2006) Mesolevel simulation of reinforced concrete structures under impact loadings. In Proceedings of the EURO-C 2006 Conference on Computational Modelling of Concrete Structures, Tyrol, Austria, 63-70.

Cusatis, G., Bažant, Z.P. and Cedolin, L. (2003) 'Confinement-Shear Lattice Model for Concrete Damage in Tension and Compression: I. Theory', *Journal of Engineering Mechanics*, 129(12), pp. 1439–1448. Available at: https://doi.org/10.1061/(ASCE)0733-9399(2003)129:12(1439).

Cusatis, G., Bažant, Z.P. and Cedolin, L. (2006) 'Confinement-shear lattice CSL model for fracture propagation in concrete', *Computer methods in applied mechanics and engineering*, 195(52), pp. 7154–7171.

Cusatis, G., Pelessone, D. and Mencarelli, A. (2011a) 'Lattice discrete particle model (LDPM) for failure behavior of concrete. I: Theory', *Cement and Concrete Composites*, 33(9), pp. 881–890.

Cusatis, G., Mencarelli, A., Pelessone, D. and Baylot, J. (2011b) 'Lattice discrete particle model (LDPM) for failure behavior of concrete. II: Calibration and validation', *Cement and Concrete composites*, 33(9), pp. 891–905.

DeJong, M.J., Hendriks, M.A.N. and Rots, J.G. (2008) 'Sequentially linear analysis of fracture under non-proportional loading', *Engineering Fracture Mechanics*, 75(18), pp. 5042–5056.

Demirel, I.O., Canbay, E., Binici, B., Yakut, A. and Eryurtlu, Z. (2015) 'Gazbeton dolgulu betonarme çerçevelerin deprem performansi üzerine deneysel çalişma', *3 Türkiye Deprem Mühendisliği ve Sismoloji Konferansı (3TDMSK)*, İzmir, Turkey, pp. 14–16.

Dialer, C. (1992) 'A distinct element approach for the deformation behaviour of shear stressed masonry panels', in *Proceedings of the 6th Canadian masonry symposium*, pp. 765–776.

Dolatshahi, K. and Aref, A. (2011) 'Two-dimensional computational framework of meso-scale rigid and line interface elements for masonry structures', *Engineering Structures*, 33(12), pp. 3657–3667.

Donzé, F. and Magnier, S. (1995) 'Formulation of a 3-D numerical model of brittle behaviour', *Geophysical Journal International*, 122(3), pp. 790–802.

Dzik, E.J. and Lajtai, E.Z. (1996) 'Primary fracture propagation from circular cavities loaded in compression', *International journal of fracture*, 79(1), pp. 49–64.

El-Dakhakhni, W., Elgaaly, M. and Hamid, A. (2003) 'Three-strut model for concrete masonry-infilled steel frames', *J Struct Eng*, 129(2), pp. 177–185.

Eliáš, J., Vořechovský, M. and Le, J.-L. (2013) 'Lattice modeling of concrete fracture including material spatial randomness', *Eng. Mech*, 20(5), pp. 413–426.

Elwood, K.J. (2004) 'Modelling failures in existing reinforced concrete columns', *Canadian Journal of Civil Engineering*, 31(5), pp. 846–859.

Eringen, A.C. (1992) 'Vistas of nonlocal continuum physics', *International journal of engineering science*, 30(10), pp. 1551–1565.

Eurocode 2 (2002): Design of Concrete Structures.

Fantilli, A.P., Ferretti, D., Iori, I. and Vallini, P. (2002) 'Mechanical model for failure of compressed concrete in reinforced concrete beams', *Journal of Structural Engineering*, 128(5), pp. 637–645.

Fascetti, A., Feo, L., Nisticò, N. and Penna, R. (2016) 'Web-flange behavior of pultruded GFRP I-beams: A lattice model for the interpretation of experimental results', *Composites Part B: Engineering*, 100, pp. 257–269.

Federal Emergency Management Agency (1998) FEMA 306: evaluation of earthquake damaged concrete and masonry wall buildings-basic procedures manual. Washington DC: Applied Technology Council (ATC-43 project).

Federal Emergency Management Agency. FEMA. (2000) Prestandard and commentary for the seismic rehabilitation of buildings. Report no. FEMA 356. Washington (DC): FEMA.

Fédération Internationle de la Précontrainte (FIP). (1996). *Recommendation—Practical design of structural concrete*, London.

Fenerci, A., Binici, B., Ezzatfar, P., Canbay, E. and Ozcebe, G. (2016) 'The effect of infill walls on the seismic behavior of boundary columns in RC frames', *Earthq. Struct.*, 10(3), pp. 539–562.

Foster, S. J., and Gilbert, R. I. (1996) "Tests on high strength concrete deep beams." UNICIV Report No. R-354, University of New South Wales, Sydney, Australia.

Foster, S.J. and Gilbert, R.I. (1998) 'Experimental studies on high-strength concrete deep beams', *Structural Journal*, 95(4), pp. 382–390.

Fouchal, F., Lebon, F. and Titeux, I. (2009) 'Contribution to the modelling of interfaces in masonry construction', *Constr Build Mater*, 23, pp. 2428–2441.

Furtado, A., Ramos, T., Rodrigues, H., Arêde, A., Varum, H. and Tavares, P. (2015) 'In-plane response of masonry infill walls: experimental study using digital image correlation', *Procedia Engineering*, 114, pp. 870–876.

Galli, M. (2006) 'Evaluation of the seismic response of existing RC frame buildings with masonry infills', *Master Degree in Earthquake Engineering Master Thesis, European School of Advanced Studies in Reduction of Seismic Risk (ROSE School), ROSE School, Pavia* [Preprint].

Gambarotta, L. and Lagomarsino, S. (1997) 'Damage Models for the Seismic Response of Brick Masonry Shear Walls. Part I: The Mortar Joint Model and Its Applications', *Earthquake Engineering & Structural Dynamics*, 26(4), pp. 423–439.

Ganzenmüller, G.C., Hiermaier, S. and May, M. (2015) 'On the similarity of meshless discretizations of peridynamics and smooth-particle hydrodynamics', *Computers & Structures*, 150, pp. 71–78.

Gerstle, W., and Sau, N. (2004). "Peridynamic modeling of concrete structures." in Li, L., Willam, K., and Billington, S. (eds) *Proceedings of the Fifth International Conference on Fracture Mechanics of Concrete Structures*, Ia-FRAMCOS, 949–956.

Gerstle, W., Geitanbaf, H.H. and Asadollahi, A. (2013) 'Computational simulation of reinforced concrete using the micropolar state-based peridynamic hexagonal lattice model', in *8th international conference on fracture mechanics of concrete and concrete structures, Barcelona, Spain*, pp. 261–270.

Gerstle, W.H. (2015) *Introduction to practical peridynamics: computational solid mechanics without stress and strain*. World Scientific Publishing Company.

Ghaboussi, J. and Barbosa, R. (1990) ‘Three-dimensional discrete element method for granular materials’, *International Journal for Numerical and Analytical Methods in Geomechanics*, 14(7), pp. 451–472.

Ghajari, M., Iannucci, L. and Curtis, P. (2014) ‘A peridynamic material model for the analysis of dynamic crack propagation in orthotropic media’, *Computer Methods in Applied Mechanics and Engineering*, 276, pp. 431–452.

Giambanco, G. and Di Gati, L. (1997) ‘A cohesive interface model for the structural mechanics of block masonry’, *Mechanics Research Communications*, 24(5), pp. 503–512.

Giberson, M.F. (1969) ‘Two nonlinear beams with definitions of ductility’, *Journal of the Structural Division*, 95(2), pp. 137–157.

Glucklich, J. (1963) ‘Fracture of plain concrete’, *Journal of the Engineering Mechanics Division*, 89(6), pp. 127–138.

Grassl, P. and Jirásek, M. (2010) ‘Meso-scale approach to modelling the fracture process zone of concrete subjected to uniaxial tension’, *International Journal of Solids and Structures*, 47(7–8), pp. 957–968.

Griffith, A. (1924) ‘The theory of rupture’, in *First Int. Cong. Appl. Mech*, pp. 55–63.

Griffiths, D. and Mustoe, G. (2001) ‘Modelling of elastic continua using a grillage of structural elements based on discrete element concepts’, *International Journal for Numerical Methods in Engineering2*, 50(7), pp. 1759–1775.

Guner, S. and Vecchio, F.J. (2011) ‘Analysis of shear-critical reinforced concrete plane frame elements under cyclic loading’, *Journal of Structural Engineering*, 137(8), pp. 834–843.

Ha, Y.D. and Bobaru, F. (2010) ‘Studies of dynamic crack propagation and crack branching with peridynamics’, *International Journal of Fracture*, 162(1), pp. 229–244.

Ha, Y.D. and Bobaru, F. (2011) 'Characteristics of dynamic brittle fracture captured with peridynamics', *Engineering Fracture Mechanics*, 78(6), pp. 1156–1168.

Häfner, S., Eckardt, S., Luther, T. and Könke, C. (2006) 'Mesoscale modeling of concrete: Geometry and numerics', *Computers & structures*, 84(7), pp. 450–461.

Han, L., Pathirage, M., Akono, A.-T. and Cusatis, G. (2021) 'Lattice discrete particle modeling of size effect in slab scratch tests', *Journal of Applied Mechanics*, 88(2).

Hillerborg, A., Modéer, M. and Petersson, P.E. (1976) 'Analysis of crack formation and crack growth in concrete by means of fracture mechanics and finite elements', *Cement and Concrete Research*, 6(6), pp. 773–781. Available at: https://doi.org/10.1016/0008-8846(76)90007-7.

Hognestad, E. (1951) *Study of combined bending and axial load in reinforced concrete members*. Bulletin Series No. 399, University of Illinois at Urbana Champaign, College of Engineering. Engineering Experiment Station, 43-46. http://www.ideals.illinois.edu/bitstream/handle/2142/4360/engineeringexperv00000i00399.pdf?sequence=3

Hordijk, D.A. (1993) *Local approach to fatigue of concrete. Doctoral dissertation, Delft University of Technology, Delft, Netherlands. https://repository.tudelft.nl/islandora/object/uuid%3Afa87147b-8201-47ed-83d7-b812b09c5fbb*

Hrennikoff, A. (1941) 'Solution of problems of elasticity by the framework method', J. Appl. Mech. Tech. Phys. 12: 169-175.

Hsu, T.T.C. and Mo, Y.-L. (2010) *Unified theory of concrete structures*. Hoboken, NJ, John Wiley & Sons.

Hsu, T.T.C., Slate, F.O., Sturman, G.M. and Winter, G. (1963) 'Microcracking of plain concrete and the shape of the stress-strain curve', ACI Journal Proceedings 60(2): 209-224. https://doi.org/10.14359/7852

Hu, W., Ha, Y.D. and Bobaru, F. (2012) 'Peridynamic model for dynamic fracture in unidirectional fiber-reinforced composites', *Computer Methods in Applied Mechanics and Engineering*, 217, pp. 247–261.

Iskander, M. and Shrive, N. (2018) 'Fracture of brittle and quasi-brittle materials in compression: A review of the current state of knowledge and a different approach', *Theoretical and Applied Fracture Mechanics*, 97, pp. 250–257.

Itasca consulting group. Inc. UDEC- Universal distinct element code. (2004) Version 4.0- User's manual. Minneapolis (MN, USA).

Jansen, D.C. and Shah, S.P. (1997) 'Effect of length on compressive strain softening of concrete', *Journal of engineering mechanics*, 123(1), p. 25.

Jirásek, M. and Bažant, Z.P. (1995) 'Particle model for quasibrittle fracture and application to sea ice', *Journal of engineering mechanics*, 121(9), pp. 1016–1025.

Kadysiewski, S. and Mosalam, K.M. (2009) *Modeling of unreinforced masonry infill walls considering in-plane and out-of-plane interaction*. Pacific Earthquake Engineering Research Center Berkeley.

Kaplan, M.F. (1961) 'Crack propagation and the fracture of concrete', in *Journal Proceedings*, pp. 591–610.

Karihaloo, B., Shao, P. and Xiao, Q. (2003) 'Lattice modelling of the failure of particle composites', *Engineering Fracture Mechanics*, 70(17), pp. 2385–2406.

Kawai, T. (1978) 'New discrete models and their application to seismic response analysis of structures', *Nuclear Engng. Design*, 48, pp. 207–229.

Kendall, K. (1978) 'Complexities of compression failure', *Proceedings of the Royal Society of London. A. Mathematical and Physical Sciences*, 361(1705), pp. 245–263.

Khojasteh, A. (2017) *Nonlinear modelling of masonry infill walls in building structures subject to extreme loading*. Imperial College London.

Kilic, B., Agwai, A. and Madenci, E. (2009) 'Peridynamic theory for progressive damage prediction in center-cracked composite laminates', *Composite Structures*, 90(2), pp. 141–151.

Klingner, RE. and Bertero, VV. (1976) Infilled frames in earthquake-resistant construction. Report EERC/76-32, Earthquake Engineering Research Center, University of California, Berkeley, CA, USA.

Korswagen, P.A., Longo, M., Meulman, E. and Rots, J.G. (2019) 'Crack initiation and propagation in unreinforced masonry specimens subjected to repeated in-plane loading during light damage', *Bulletin of Earthquake Engineering*, 17(8), pp. 4651–4687.

Koutromanos, I. and Shing, P.B. (2012) 'Cohesive Crack Model to Simulate Cyclic Response of Concrete and Masonry Structures', *ACI Structural Journal*, 109(3), pp. 349–358. Available at: https://doi.org/10.14359/51683748.

Kumar, S.L., Aravind, H.B. and Hossiney, N. (2019) 'Digital image correlation (DIC) for measuring strain in brick masonry specimen using Ncorr open source 2D MATLAB program', *Results in Engineering*, 4, p. 100061.

Kunin, IA. (1982) Elastic Media with Microstructure. Berlin: Springer.

Kupfer, H., Hilsdorf, H.K. and Rusch, H. (1969) 'Behavior of concrete under biaxial stresses', *ACI Journal*, 66(8), 656-666.

Kwan, A.K.H., Wang, Z.M. and Chan, H.C. (1999) 'Mesoscopic study of concrete II: nonlinear finite element analysis', *Computers & structures*, 70(5), pp. 545–556.

Lai, X., Ren, B., Fan, H., Li, S., Wu, C.T., Regueiro, R.A. and Liu, L. (2015) 'Peridynamics simulations of geomaterial fragmentation by impulse loads',

International Journal for Numerical and Analytical Methods in Geomechanics, 39(12), pp. 1304–1330.

Lajtai, E.Z. (1971) 'A theoretical and experimental evaluation of the Griffith theory of brittle fracture', *Tectonophysics*, 11(2), pp. 129–156.

Larson, N., Gomez, E.F., Garber, D., Bayrak, O. and Ghannoum, W. (2013) *Strength and serviceability design of reinforced concrete inverted-T beams*.

Laughery, L. and Pujol, S. (2015) 'Compressive Strength of Unreinforced Struts.', *ACI Structural Journal*, 112(5).

Lee, D.H. and Elnashai, A.S. (2001) 'Seismic analysis of RC bridge columns with flexure-shear interaction', *Journal of Structural Engineering*, 127(5), pp. 546–553.

Lee, K.M. and Park, J.H. (2008) 'A numerical model for elastic modulus of concrete considering interfacial transition zone', *Cement and Concrete Research*, 38(3), pp. 396–402.

Lemos, J. V (2007) 'Discrete element modeling of masonry structures', *International Journal of Architectural Heritage*, 1(2), pp. 190–213.

Leu, L.-J., Huang, C.-W., Chen, C.-S. and Liao, Y.-P. (2006) 'Strut-and-tie design methodology for three-dimensional reinforced concrete structures', *JOURNAL OF STRUCTURAL ENGINEERING-NEW YORK-*, 132(6), p. 929.

Li, Y.R. and Jirsa, J.O. (1998) 'Nonlinear analyses of an instrumented structure damaged in the 1994 Northridge earthquake', *Earthquake Spectra*, 14(2), pp. 265–283.

Liang, Q.Q., Uy, B. and Steven, G.P. (2002) 'Performance-based optimization for strut-tie modeling of structural concrete'.

Liang, Q.Q., Xie, Y.M. and Steven, G.P. (2000) 'Topology optimization of strut-and-tie models in reinforced concrete structures using an evolutionary procedure'. American Concrete Institute.

Lilliu, G. and van Mier, J. (2003) '3D lattice type fracture model for concrete', *Eng Fract Mech*, 70(7–8), pp. 927–941.

Lim, J.C. and Ozbakkaloglu, T. (2015) 'Lateral strain-to-axial strain relationship of confined concrete', *Journal of Structural Engineering*, 141(5), p. 4014141.

Limkatanyu, S. and Spacone, E. (2002) 'Reinforced concrete frame element with bond interfaces. I: Displacement-based, force-based, and mixed formulations', *Journal of Structural Engineering*, 128(3), pp. 346–355.

Littlewood, D.J. (2010) 'Simulation of dynamic fracture using peridynamics, finite element modeling, and contact', in *ASME International Mechanical Engineering Congress and Exposition*, pp. 209–217.

Littlewood, D.J. (2011) 'A nonlocal approach to modeling crack nucleation in AA 7075-T651', in *ASME International Mechanical Engineering Congress and Exposition*, pp. 567–576.

Liu, J., Deng, S., Zhang, J. and Liang, N. (2007) 'Lattice type of fracture model for concrete', *Theoretical and Applied Fracture Mechanics*, 48(3), pp. 269–284.

López, C.M., Carol, I. and Aguado, A. (2008a) 'Meso-structural study of concrete fracture using interface elements. I: numerical model and tensile behavior', *Materials and structures*, 41(3), pp. 583–599.

López, C.M., Carol, I. and Aguado, A. (2008b) 'Meso-structural study of concrete fracture using interface elements. II: compression, biaxial and Brazilian test', *Materials and structures*, 41(3), pp. 601–620.

Lotfi, H. and Shing, P. (1994) 'Interface model applied to fracture of masonry structures', *J Struct Eng ASCE*, 120(1), pp. 63–80.

Lu, Y. and Panagiotou, M. (2014) ‘Three-dimensional cyclic beam-truss model for nonplanar reinforced concrete walls’, *Journal of Structural Engineering*, 140(3), p. 4013071.

Lucy, L.B. (1977) ‘A numerical approach to the testing of the fission hypothesis’, *The astronomical journal*, 82, pp. 1013–1024.

Lura, P., Plizzari, G.A. and Riva, P. (2002) ‘3D finite-element modelling of splitting crack propagation’, *Magazine of Concrete Research*, 54(6), pp. 481–493.

Macek, R.W. and Silling, S.A. (2007) ‘Peridynamics via finite element analysis’, *Finite elements in analysis and design*, 43(15), pp. 1169–1178.

Markeset, G. and Hillerborg, A. (1995) ‘Softening of concrete in compression—localization and size effects’, *Cement and concrete research*, 25(4), pp. 702–708.

Masonry Standards Joint Committee. MSJC. (2011) Building code requirements and specification for masonry structures and related commentaries. TMS 602-11/ACI 530.1-11/ASCE 6-11. Farmington Hills (MI, USA): American Concrete Institute

Mazars, J., Kotronis, P., Ragueneau, F. and Casaux, G. (2006) ‘Using multifiber beams to account for shear and torsion: Applications to concrete structural elements’, *Computer Methods in Applied Mechanics and Engineering*, 195(52), pp. 7264–7281.

Mehrabi, A.B. and Shing, P.B. (1997) ‘Finite element modeling of masonry-infilled RC frames’, *Journal of structural engineering*, 123(5), pp. 604–613.

Mehta, P.K. (1986) ‘Concrete. Structure, properties and materials’.

Mercuri, M., Pathirage, M., Gregori, A. and Cusatis, G. (2020) ‘Computational modeling of the out-of-plane behavior of unreinforced irregular masonry’, *Engineering Structures*, 223, p. 111181.

Milanesi, R., Morandi, P. and Magenes, G. (2018) 'Local effects on RC frames induced by AAC masonry infills through FEM simulation of in-plane tests', *Bull Earthq Eng*, 16(9), pp. 4053–4080.

Mirmiran, A. and Shahawy, M. (1997) 'Dilation characteristics of confined concrete', *Mechanics of Cohesive-frictional Materials: An International Journal on Experiments, Modelling and Computation of Materials and Structures*, 2(3), pp. 237–249.

Mirza, M.S. and Hsu, C.T. (1969) 'Progress report on code clauses for limit design (discussion)', *Journal of the American Concrete Institute*, 66(3), pp. 221–223.

Mirza, S.A. and MacGregor, J.G. (1979) 'Variability of mechanical properties of reinforcing bars', *ASCE Journal of the Structural Division*, 105(5), pp. 921–937.

Mirza, S.A., MacGregor, J.G. and Hatzinikolas, M. (1979) 'Statistical descriptions of strength of concrete', *ASCE Journal of the Structural Division*, 105(6), pp. 1021–1037.

Moharrami, M., Koutromanos, I., Panagiotou, M. and Girgin, S.C. (2015) 'Analysis of shear-dominated RC columns using the nonlinear truss analogy', *Earthquake Engineering & Structural Dynamics*, 44(5), pp. 677–694.

Mohebkhah, A. and A Tasnimi, A. (2012) 'Distinct element modeling of masonry-infilled steel frames with openings', *The Open Construction & Building Technology Journal*, 6(1).

Mohebkhah, A., Tasnimi, A.A. and Moghadam, H.A. (2008) 'Nonlinear analysis of masonry-infilled steel frames with openings using discrete element method', *Journal of constructional steel research*, 64(12), pp. 1463–1472.

Mojsilovic, N. and Salmanpour, AH. (2016) "Masonry walls subjected to in-plane cyclic loading: application of digital image correlation for deformation field measurement", International Journal of Masonry Research and Innovation;1(2):165-187.

Monette, L. and Anderson, M.P. (1994) ‘Elastic and fracture properties of the two-dimensional triangular and square lattices’, *Modelling and Simulation in Materials Science and Engineering*, 2(1), p. 53.

Morandi, P., Hak, S. and Magenes, G. (2018) ‘Performance-based interpretation of in-plane cyclic tests on RC frames with strong masonry infills’, *Engineering Structures*, 156, pp. 503–521.

Mosalam, K., White, R. and Gergely, P. (1997) ‘Static response of infilled frames using quasi-static experimentation’, *J Struct Eng ASCE*, 123(11), pp. 1462–1469.

Mostafaei, H. and Vecchio, F.J. (2008) ‘Uniaxial shear-flexure model for reinforced concrete elements’, *J. Eng. Struct* [Preprint].

Murcia-Delso, J. and Benson Shing, P. (2015) ‘Bond-slip model for detailed finite-element analysis of reinforced concrete structures’, *Journal of Structural Engineering*, 141(4), p. 4014125.

Nagai, K., Hayashi, D. and Eddy, L. (2014) ‘Numerical simulation of failure of anchorage with shifted mechanical anchorage bars by 3D discrete model’, *Advances in Structural Engineering*, 17(6), pp. 861–869.

Najafian, H.A., Vollum, R.L. and Fang, L. (2013) ‘Comparative assessment of finite-element and strut and tie based design methods for deep beams’, *Magazine of Concrete Research*, 65(16), pp. 970–986.

Navier, L. (1821), *Sur les lois de l' equi/ibre et du mouvement des corps solides elastiques,* Bulletin des sciences par 1a Soeiete Philomatique de Paris, 1823, pp. 177-181; abstract of the memoir presented to the Academie des Sciences on May 14, 1821 and published with the title *Memoire sur les lois de l' equilibre et du mouvement des corps solides elastiques,* Memoires de l'Institut National, voL 7, 1827, pp.375-393.

Nayfeh, A.H. and Hefzy, M.S. (1978) ‘Continuum modeling of three-dimensional truss-like space structures’, *Aiaa journal*, 16(8), pp. 779–787.

Negro, P. and Colombo, A. (1997) 'Irregularities induced by nonstructural masonry panels in framed buildings', *Eng Struct*, 19, pp. 576–585.

Neuenhofer, A. and Filippou, F.C. (1997) 'Evaluation of nonlinear frame finite-element models', *Journal of structural engineering*, 123(7), pp. 958–966.

New York Times Online, https://www.nytimes.com/2021/03/31/business/economy/biden-infrastructure-plan.html, last visited 01.11.2022.

Ngo, D. and Scordelis, A.C. (1967) 'Finite Element Analysis of Reinforced Concrete Beams', *Journal Proceedings*, 64(3), pp. 152–163. Available at: https://doi.org/10.14359/7551.

Nicola, T., Leandro, C., Guido, C. and Enrico, S. (2015) 'Masonry infilled frame structures: state-of-the-art review of numerical modelling', *Earthquakes and structures*, 8(3), pp. 733–759.

Nikravesh, S. and Gerstle, W. (2018) 'Improved state-based peridynamic lattice model including elasticity, plasticity and damage', *Computer Modeling in Engineering & Sciences*, 116(3), pp. 323–347.

Oliveira, D. V. and Lourenço, P.B. (2004) 'Implementation and Validation of a Constitutive Model for the Cyclic Behaviour of Interface Elements', *Computers & Structures*, 82(17–19), pp. 1451–1461.

Ostoja-Starzewski, M., Sheng, P.Y. and Alzebdeh, K. (1996) 'Spring network models in elasticity and fracture of composites and polycrystals', *Computational Materials Science*, 7(1–2), pp. 82–93.

Oterkus, E., Madenci, E., Weckner, O., Silling, S., Bogert, P. and Tessler, A. (2012) 'Combined finite element and peridynamic analyses for predicting failure in a stiffened composite curved panel with a central slot', *Composite Structures*, 94(3), pp. 839–850.

Ozcebe, G. and Saatcioglu, M. (1987) ‘Confinement of Concrete Columns for Seismic Loading’, *ACI Structural Journal*, 84(4), pp. 308–315. Available at: https://doi.org/10.14359/1660.

Papia, M., Cavaleri, L. and Fossetti, M. (2003) ‘Infilled frames: developments in the evaluation of the stiffening effect of infills’, *Structural engineering and mechanics*, 16(6), pp. 675–693.

Pari, M., Hendriks, M.A.N. and Rots, J.G. (2020) ‘Non-proportional loading in sequentially linear solution procedures for quasi-brittle fracture: A comparison and perspective on the mechanism of stress redistribution’, *Engineering Fracture Mechanics*, 230, p. 106960.

Pari, M., Van de Graaf, A., Hendriks, M. and Rots, J. (2021) ‘A multi-surface interface model for sequentially linear methods to analyse masonry structures’, *Eng Struct*, 238, p. 112123.

Parisi, A. and Caldarelli, G. (2000) ‘Self-affine properties of fractures in brittle materials’, *Physica A: Statistical Mechanics and its Applications*, 280(1–2), pp. 161–165.

Pathirage, M., Bousikhane, F., D’ambrosia, M., Alnaggar, M. and Cusatis, G. (2019) ‘Effect of alkali silica reaction on the mechanical properties of aging mortar bars: Experiments and numerical modeling’, *International Journal of Damage Mechanics*, 28(2), pp. 291–322.

Paulay, T. and Priestley, M.J.N. (1992) *Seismic design of reinforced concrete and masonry buildings*. Wiley New York.

Penna, A. and Calvi, G. (2006) *Campagna sperimentale su telai in c.a. con tamponamenti in Gasbeton (AAC) con diverse soluzioni di rinforzo*. Pavia,Italy.

Penna, A., Morandi, P., Rota, M., Manzini, C.F., Da Porto, F. and Magenes, G. (2014) ‘Performance of masonry buildings during the Emilia 2012 earthquake’, *Bulletin of Earthquake Engineering*, 12(5), pp. 2255–2273.

Polyakov, S. V. (1950) *Investigation of the Strength and of the Deformational Characteristics of Masonry Filler Walls and Facing on Framed Structures*, Construction Industry Institute 1950, No.3.

Polyakov, S. V. (1960) 'On the interaction between masonry filler walls and enclosing frame when loaded in the plane of the wall', *Transl Earthq Eng*, 2(3), pp. 36–42.

Popovics, S. (1973) 'A numerical approach to the complete stress-strain curve of concrete', *Cement and concrete research*, 3(5), pp. 583–599.

Qian, Z. (2012) Multiscale modeling of fracture processes in cementitious materials. Doctoral dissertation, Delft University of Technology, Delft, Netherlands. https://repository.tudelft.nl/islandora/object/uuid%3A734b276c-283a-4f7a-8db2-a184453e8dac

Rahman, A.S.M. (2012) "Lattice-based peridynamic modeling of linear elastic solids," Master's Thesis, the University of New Mexico, New Mexico.

Ramos, T., Furtado, A., Eslami, S., Alves, S., Rodrigues, H., Arêde, A., Tavares, P.J. and Moreira, P. (2015) '2D and 3D digital image correlation in civil engineering–measurements in a masonry wall', *Procedia Engineering*, 114, pp. 215–222.

Rashid, Y.R. (1968) 'Ultimate strength analysis of prestressed concrete pressure vessels', *Nuclear Engineering and Design*, 7(4), pp. 334–344. Available at: https://doi.org/https://doi.org/10.1016/0029-5493(68)90066-6.

Ricci, P., De Luca, F. and Verderame, G.M. (2011) '6th April 2009 L'Aquila earthquake, Italy: reinforced concrete building performance', *Bulletin of earthquake engineering*, 9(1), pp. 285–305.

Rizvi, Z., Sattari, A. and Wuttke, F. (2018) 'Meso scale modelling of infill foam concrete wall for earthquake loads', in *16th European Conference on Earthquake Engineering (16ECEE)*. Thessaloniki, Greece.

Roelfstra, P.E., Sadouki, H. and Wittmann, F.H. (1985) 'Le béton numérique', *Materials and Structures*, 18(5), pp. 327–335.

Roth, S.-N., Léger, P. and Soulaïmani, A. (2015) 'A combined XFEM–damage mechanics approach for concrete crack propagation', *Computer Methods in Applied Mechanics and Engineering*, 283, pp. 923–955.

Rots, J.G. (2001) 'Sequentially linear continuum model for concrete fracture', *Fracture mechanics of concrete structures*, 13, pp. 831–839.

Rots, J.G., Belletti, B. and Invernizzi, S. (2008) 'Robust modeling of RC structures with an "event-by-event" strategy', *Engineering Fracture Mechanics*, 75(3–4), pp. 590–614.

Rots, J.G., Invernizzi, S. and Belletti, B. (2006) 'Saw-tooth softening/stiffening-a stable computational procedure for RC structures', *Computers and Concrete*, 3(4), pp. 213–233.

Roufaiel, M.S.L. and Meyer, C. (1987) 'Analytical modeling of hysteretic behavior of R/C frames', *Journal of Structural Engineering*, 113(3), pp. 429–444.

Saatcioglu, M. and Razvi, S.R. (1992) 'Strength and ductility of confined concrete', *Journal of Structural engineering*, 118(6), pp. 1590–1607.

Sarhosis, V. and Sheng, Y. (2014) 'Identification of material parameters for low bond strength masonry', *Engineering Structures*, 60, pp. 100–110.

Saritas, A. and Filippou, F.C. (2009) 'Inelastic axial-flexure–shear coupling in a mixed formulation beam finite element', *International Journal of Non-Linear Mechanics*, 44(8), pp. 913–922.

Schauffert, E.A. and Cusatis, G. (2012) 'Lattice discrete particle model for fiber-reinforced concrete. I: Theory', *Journal of Engineering Mechanics*, 138(7), pp. 826–833.

Schauffert, E.A., Cusatis, G., Pelessone, D., O'Daniel, J.L. and Baylot, J.T. (2012) 'Lattice discrete particle model for fiber-reinforced concrete. II: Tensile fracture and multiaxial loading behavior', *Journal of engineering mechanics*, 138(7), pp. 834–841.

Schlaich, J., Schäfer, K. and Jennewein, M. (1987) 'Toward a consistent design of structural concrete', *PCI journal*, 32(3), pp. 74–150.

Schlangen, E. (1995) 'Experimental and numerical analysis of fracture processes in concrete.', Doctoral dissertation, Delft University of Technology, Delft, Netherlands. https://repository.tudelft.nl/islandora/object/uuid%3A8e0d58b0-b5d0-4471-89a3-607ee4d6f7da

Schlangen, E. and Garboczi, E.J. (1997) 'Fracture simulations of concrete using lattice models: computational aspects', *Engineering fracture mechanics*, 57(2–3), pp. 319–332.

Schlangen, E. and Qian, Z. (2009) '3D modeling of fracture in cement-based materials', *Journal of Multiscale Modelling*, 1(02), pp. 245–261.

Schlangen, E. and van Mier, J.G.M. (1992) 'Experimental and numerical analysis of micromechanisms of fracture of cement-based composites', *Cement and Concrete Composites*, 14(2), pp. 105–118. Available at: https://doi.org/10.1016/0958-9465(92)90004-F.

Schlangen, E. and Van Mier, J.G.M. (1992) 'Simple lattice model for numerical simulation of fracture of concrete materials and structures', *Materials and Structures*, 25(9), pp. 534–542.

Scott, M.H. and Fenves, G.L. (2006) 'Plastic hinge integration methods for force-based beam–column elements', *Journal of Structural Engineering*, 132(2), pp. 244–252.

Scott, R.M., Mander, J.B. and Bracci, J.M. (2012) 'Compatibility Strut-and-Tie Modeling: Part I--Formulation.', *ACI Structural Journal*, 109(5).

Seleson, P. and Parks, M. (2011) ‘On the role of the influence function in the peridynamic theory’, *International Journal for Multiscale Computational Engineering*, 9(6).

Shen, F., Zhang, Q. and Huang, D. (2013) ‘Damage and failure process of concrete structure under uniaxial compression based on peridynamics modeling’, *Mathematical Problems in Engineering*, 2013.

Sih, G.C. (1974) ‘Strain-energy-density factor applied to mixed mode crack problems’, *International Journal of fracture*, 10(3), pp. 305–321.

Silling, S.A. (2000) ‘Reformulation of elasticity theory for discontinuities and long-range forces’, *Journal of the Mechanics and Physics of Solids*, 48(1), pp. 175–209.

Silling, S.A. and Askari, E. (2005) ‘A meshfree method based on the peridynamic model of solid mechanics’, *Computers & structures*, 83(17–18), pp. 1526–1535.

Silling, S.A., Epton, M., Weckner, O., Xu, J. and Askari, E. (2007) ‘Peridynamic states and constitutive modeling’, *Journal of elasticity*, 88(2), pp. 151–184.

Silling, S.A., Weckner, O., Askari, E. and Bobaru, F. (2010) ‘Crack nucleation in a peridynamic solid’, *International Journal of Fracture*, 162(1), pp. 219–227.

Slobbe, A.T., Hendriks, M.A.N. and Rots, J.G. (2014) ‘Smoothing the propagation of smeared cracks’, *Engineering Fracture Mechanics*, 132, pp. 147–168.

Smith, BS. (1966) “Behaviour of Square Infilled Frames”, ASCE Journal of Structural Division, 92 ST1:381-403 February.

Spacone, E., Filippou, F.C. and Taucer, F.F. (1996) ‘Fibre beam–column model for non-linear analysis of R/C frames: Part I. Formulation’, *Earthquake Engineering & Structural Dynamics*, 25(7), pp. 711–725.

Stankowski, T. (1990) *Numerical simulation of progressive failure in particle composites*. University of Colorado at Boulder.

Sun, S. and Sundararaghavan, V. (2014) 'A peridynamic implementation of crystal plasticity', *International Journal of Solids and Structures*, 51(19–20), pp. 3350–3360.

Sutcliffe, D., Yu, H. and Page, A. (2001) 'Lower bound limit analysis of unreinforced masonry shear walls', *Computers and Structures*, 79, pp. 1295–1312.

Takayanagi, T. and Schnobrich, W.C. (1979) 'Non-linear analysis of coupled wall systems', *Earthquake Engineering & Structural Dynamics*, 7(1), pp. 1–22.

Tan, K.H., Cheng, G.H. and Cheong, H.K. (2005) 'Size effect in shear strength of large beams—Behaviour and finite element modelling', *Magazine of Concrete Research*, 57(8), pp. 497–509.

Tarque, N., Candido, L., Camata, G. and Spacone, E. (2015) "Masonry infilled frame structures : state-of-the-art review of numerical modelling", *Earthquakes Struct*, 8(1):225-51.

Taucer, F., Spacone, E. and Filippou, F.C. (1991) *A fiber beam-column element for seismic response analysis of reinforced concrete structures*. Earthquake Engineering Research Center, College of Engineering, University ….

TEC (2019) Turkish Earthquake Code: Specifications for Building Design Under Earthquake Effects. Ministry of interior disaster and emergency management presidency (AFAD), Ankara, Turkey.

Thomsen IV, J.H. and Wallace, J.W. (2004) 'Displacement-based design of slender reinforced concrete structural walls—experimental verification', *Journal of structural engineering*, 130(4), pp. 618–630.

Thomsen, J. H., and Wallace, J. W. (1995). "Displacement based design of reinforced concrete structural walls: An experimental investigation of walls

with rectangular and T-shaped cross-sections." Rep. No. CU/CEE-95-06, Clarkson Univ., Potsdam, NY.

Todorovic, L. (2019) Out of plane seismic performance of aac infill walls with openings. MSc dissertation, Middle East Technical University, Ankara, Turkey.

TS (2000) TS 500: Requirements for design and construction of reinforced concrete structures. Institute of Turkish Standard, Ankara, Turkey.

Tupek, M.R., Rimoli, J.J. and Radovitzky, R. (2013) 'An approach for incorporating classical continuum damage models in state-based peridynamics', *Computer methods in applied mechanics and engineering*, 263, pp. 20–26.

Turgay, T., Durmus, M., Binici, B. and Ozcebe, G. (2014) 'Evaluation of the predictive models for stiffness, strength, and deformation capacity of RC frames with masonry infill walls', *J Struct Eng*, 140(10), p. 06014003.

Turkish Earthquake Code (TEC) (2018), Regulations on Structures constructed in Disaster Regions, Prime Ministry Disaster and Emergency Management Authority Ankara Turkey.

Turkish Standardization Institute. TS EN 1052-1. (2000) Methods of test for masonry – Part 1: Determination of compressive strength, Ankara: Turkish Standards Institution.

Van Mier, J.G.M. (2013) *Concrete fracture: a multiscale approach*. . Boca Raton, Florida, USA, CRC Press.

Van Mier, J.G.M., van Vliet, M.R.A. and Wang, T.K. (2002) 'Fracture mechanisms in particle composites: statistical aspects in lattice type analysis', *Mechanics of Materials*, 34(11), pp. 705–724.

Van Mier, JGM. (1997) *Fracture Processes of Concrete*. Boca Raton, Florida, USA, CRC press.

van Vliet, M.R.A. and van Mier, J.G.M. (1996) 'Experimental investigation of concrete fracture under uniaxial compression', *Mechanics of Cohesive-frictional Materials: An International Journal on Experiments, Modelling and Computation of Materials and Structures*, 1(1), pp. 115–127.

Vecchio, F.J. and Collins, M.P. (1986) 'The modified compression-field theory for reinforced concrete elements subjected to shear.', *ACI J.*, 83(2), pp. 219–231.

Vecchio, FJ. and Collins, MP. (1982) Response of Reinforced Concrete to In Plane Shear and Normal Stresses. Publication No. 82-03, Department of Civil Engineering, University of Toronto.

Vicente, R.S., Rodrigues, H., Varum, H., Costa, A. and Mendes da Silva, J.A.R. (2012) 'Performance of masonry enclosure walls: lessons learned from recent earthquakes', *Earthquake engineering and engineering vibration*, 11(1), pp. 23–34.

Walraven, J. C. (1978) "The influence of depth on the shear strength of lightweight concrete beams without shear reinforcement." *Report no S-78-4*, Delft University, Delft.

Wang, E.Z. and Shrive, N.G. (1995) 'Brittle fracture in compression: mechanisms, models and criteria', *Engineering fracture mechanics*, 52(6), pp. 1107–1126.

Wang, Y. and Waisman, H. (2016) 'From diffuse damage to sharp cohesive cracks: A coupled XFEM framework for failure analysis of quasi-brittle materials', *Computer Methods in Applied Mechanics and Engineering*, 299, pp. 57–89.

Wang, Z.M., Kwan, A.K.H. and Chan, H.C. (1999) 'Mesoscopic study of concrete I: generation of random aggregate structure and finite element mesh', *Computers & structures*, 70(5), pp. 533–544.

Wight, JK. (2016) Reinforced concrete mechanics and design. New Jersey: Pearson Education Inc.

Willam, K., Stankowski, T., Runesson, K. and Sture, S. (1989) 'Simulation issues of distributed and localized failure computations', In: Mazars J, Bazant ZP (eds) *Cracking and Damage,* Elsevier, New York, USA, 363-378.

Williams, C., Deschenes, D. and Bayrak, O. (2012) *Strut-and-tie model design examples for bridges*.

Wittmann, F.H. (1983) 'Structure of concrete with respect to crack formation', *Fracture mechanics of concrete*, 43(5), p. 6.

Wriggers, P. and Moftah, S.O. (2006) 'Mesoscale models for concrete: Homogenisation and damage behaviour', *Finite elements in analysis and design*, 42(7), pp. 623–636.

Yang, B. (2019) 'Comparisons of implicit and explicit time integration methods in finite element analysis for linear elastic material and quasi-brittle material in dynamic problems'.

Yip, M., Mohle, J. and Bolander, J.E. (2005) 'Automated modeling of three-dimensional structural components using irregular lattices', *Computer-Aided Civil and Infrastructure Engineering*, 20(6), pp. 393–407.

Yu, C., Hoogenboom, P.C.J. and Rots, J.G. (2016) 'Algorithm for non-proportional loading in sequentially linear analysis', in *9th International conference on fracture mechanics of concrete and concrete structures, UC Berkeley*.

Yun, Y.M. (2000) 'Computer graphics for nonlinear strut-tie model approach', *Journal of Computing in Civil Engineering*, 14(2), pp. 127–133.

Ziegler, J.G. and Nichols, N.B. (1942) 'Optimum settings for automatic controllers', *trans. ASME,* 64(11) , 759–768.

Zohdi, T.I. and Wriggers, P. (2001) 'Computational micro-macro material testing', *Archives of Computational Methods in Engineering*, 8(2), pp. 131–228.

Zubelewicz, A. and Bazant, Z.P. (1987) ‘Interface element modeling oj· fracture in aggregate composites’, *Journal of Engineering Mechanics*, 113(11), pp. 1619–1630.

APPENDICES

A. Residual Bond Strength Parameter

The residual bond strength parameter ($\boldsymbol{a}$) can be obtained in closed form by equating ultimate bond force to bond elements. For this purpose, first displacement field in x direction is introduced to the middle steel node while keeping clamped for the other nodes in the Figure A1. The resistant force obtained from the bond behavior for the interaction between rebar and concrete at interface for deformed bar can be calculated as;

$$F_b = \tau_b \pi d_b d \tag{A1}$$

Where τ_b is the residual bond strength, d_b is longitudinal bar diameter, d is grid size. τ_b value is calculated as $0.78\sqrt{f_c}$ where f_c is compressive strength of concrete.

This force should equal the force employed by bond lattice elements as;

$$F = \boldsymbol{a} E_t A_t \varepsilon_{cr} \tag{A2}$$

Where $E_t A_t$ can be obtained in closed form as $0.621Edw$ for $1.5d$ horizon size from eq. 2.4.

Equating Eqns. A1 and A2, the $\boldsymbol{a}$ value is obtained as follows;

$$\boldsymbol{a} = \frac{\tau_b \pi d_b}{0.621 w f_t \sqrt{2}} = \frac{\pi d_b \sqrt{0.39 f_c}}{0.621 w f_t} \tag{A3}$$

Where f_t is tensile strength of concrete, w is the member thickness. It should be pointed out that, the formulation does not depend on grid size.

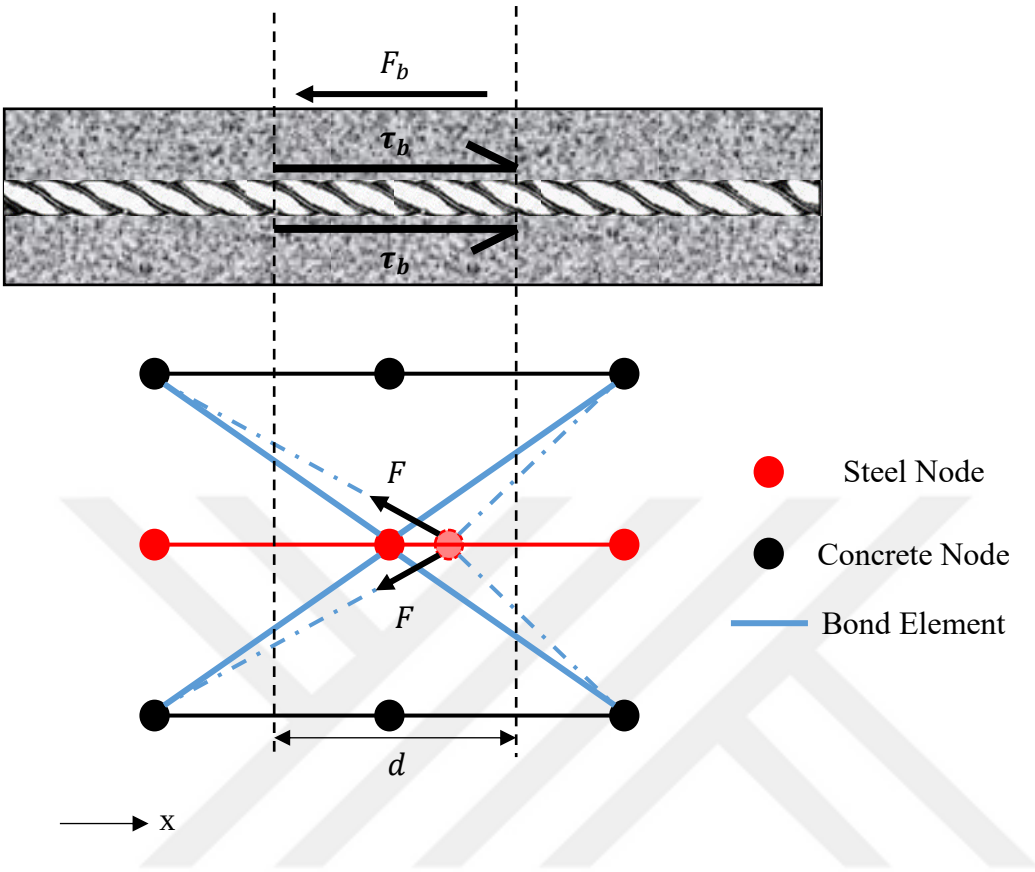


Figure A1. Interaction of Rebar and Concrete and Kinematics of the Lattice Model for Bond Behavior

CURRICULUM VITAE

PERSONAL INFORMATION

Surname, Name: Aydın, Beyazıt Bestami

EDUCATION

Degree	Institution	Year of Graduation
MS	METU Civil Engineering	2017
BS	METU Civil Engineering	2014
High School	Pertevniyal Anadolu High School, İstanbul	2009

WORK EXPERIENCE

Year	Place	Enrollment
2014-2022	METU	Teaching and Research Assistant
2022-2023	TU Delft	Visiting Researcher

FOREIGN LANGUAGES

Advanced English

PUBLICATIONS

Orcid Id: https://orcid.org/0000-0001-8613-623X

Google Scholar: https://scholar.google.com/citations?user=0QMDQEcAAAAJ

Journal Papers

1) Aydin, B. B., Binici, B., Hendriks, M. A. N. & Tuncay, K. (2022). "Lattice modeling and testing of aerated autoclaved concrete infilled frames" *Engineering Structures,* 251(part B). https://doi.org/10.1016/j.engstruct.2021.113467

2) Aydin, B. B., Binici, B., & Tuncay, K. (2021). "Lattice simulation of concrete compressive behaviour as indirect tension failure" *Magazine of Concrete Research, 73(8),* 394-409. https://doi.org/10.1680/jmacr.20.00206

3) Gul, S., Tuncay, K., Binici, B., & Aydin, B. B. (2020). “Transmission dynamics of Covid-19 in Italy, Germany and Turkey considering social distancing, testing and quarantine” *The Journal of Infection in Developing Countries, 14(7),* 713-720. https://doi.org/10.3855/jidc.12844

4) Aydin, B. B., Tuncay, K., & Binici, B. (2019). “Simulation of reinforced concrete member response using lattice model.” *Journal of Structural Engineering*, A*SCE, 145(9).* https://doi.org/10.1061/(ASCE)ST.1943-541X.0002381

5) Aydin, B. B., Tuncay, K., & Binici, B. (2018). “Overlapping Lattice Modeling for concrete fracture simulations using sequentially linear analysis” *Structural Concrete, 19*(2), 568-581. https://doi.org/10.1002/suco.201600196

Scholarships, Fundings and Projects

- Project from Ministry of Environment and Urbanization:

Project Number : 2020-03-03-2-01-086. Identifying Existing Buildings under High Gravity Collapse Probability under Service Level Earthquakes, 2020-2021

- Scholarship from Scientific and Technological Research Council of Turkey (TÜBİTAK):

TUBITAK BIDEB Supports. BEYAZIT BESTAMI AYDIN, 2214-A International Research Fellowship Programme for PhD Students, 2019 - 1.

- Project from Ministry of Environment and Urbanization:

Project Number : 2019-03-03-2-00-187. Construction principles of reinforced concrete formworks and carrier formworks scaffolds in buildings, 2018-2019

- Project from Multicon GmbH:

Dual Mixing Technology for Cement Reduction, 2017-2018

- Project from Scientific and Technological Research Council of Turkey (TÜBİTAK):

Project Number : 215M870, Examining reinforced concrete paving behavior in internal pressure concrete tunnels with innovative experimental and numerical approaches, 1001, ARDEB, 2016-2017

- Project from Turkish Union of Autoclaved Aerated Concrete Producers:

Design of Autoclaved Aerated Concrete Buildings in Seismic Zones, 2014-2015

International Conference Proceedings and Reports

1) Binici, B., Aydin, B.B., & Tuncay, K. (2022). “Estimation of Maximum Drift Demands Based on Residual Flexural Crack Widths from Post-Earthquake Damage Observations.” *Achieving Technical Excellence with Data Analytics in Materials, Structural Engineering and Construction (ASEA SEC 6),* Sydney, Australia.

2) İzmir-Seferihisar (Sisam) Earthquake (Mw=6.6) Investigation and Findings (2020). *Report no. ODTU/DMAM 2020-03*, METU, Ankara.

3) Aydin, B. B., Tuncay, K., & Binici, B. (2019). "Lattice Approach for Nonlinear Analysis for Reinforced Concrete Frames." *5th International Conference on Earthquake Engineering and Seismology (5ICEES)* , Ankara, Turkey.

4) Aydin, B. B., Tuncay, K., & Binici, B. (2018). "Overlapping Lattice Approach for Nonlinear Analysis of Reinforced Concrete Columns." *13th International Congress on Advances in Civil Engineering (ACE2018)*, İzmir, Turkey.

5) Aldemir, A. & Aydin, B. B. (2017). "Effect of Double-slotted Beams on the Frame Behavior." *17th International Scientific Conference (VSU2017)*, Sofia, Bulgaria.

6) Soysal, B. F., Aydin, B. B., Tuncay, K., Arici, Y. & Binici, B. (2017). "Overlapping Lattice Simulation Of Concrete Gravity Dam Collapse Scenarios" *6th International Conference on Computational Methods in Structural Dynamics and Earthquake Engineering (COMPDYN2017)*, Rhodes Island, Greece.

7) Aydin, B. B., Tuncay, K., & Binici, B. (2016). "Overlapping Lattice Modeling for Concrete Fracture Initiation and Propagation." *1st International Conference on Natural Hazards and Infrastructure: Protection, Design, Rehabilitation (ICONHIC2016),* Chania, Greece.

8) Aydin, B. B., Tuncay, K., & Binici, B. (2016). "Overlapping Lattice Modeling for Concrete Fracturing Using Sequentially Linear Analysis." *12th international congress on advances in civil engineering (ACE2016),* Istanbul, Turkey.